

1                   The Pennsylvania State University  
2                   The Graduate School  
3                   Eberly College of Science

4   **DEVELOPMENT OF SCALABLE APPROACHES TO NEUTRINO MASS**  
5                   **MEASUREMENT WITH THE PROJECT 8 EXPERIMENT**

6                   A Dissertation in  
7                   The Physics Department  
8                   by  
9                   Andrew Douglas Ziegler

10                  © 2023 Andrew Douglas Ziegler

11                  Submitted in Partial Fulfillment  
12                  of the Requirements  
13                  for the Degree of

14                  Doctor of Philosophy

15                  December 2023

<sup>16</sup> The dissertation of Andrew Douglas Ziegler was reviewed and approved\* by the following:

Luiz de Viveiros Souza  
Assistant Professor of Physics  
Thesis Advisor  
Chair of Committee

Carmen Carmona  
Assistant Professor of Physics

Doug Cowan  
Professor of Physics and Astrophysics

<sup>17</sup>

Xingjie Ni  
Associate Professor of Electrical Engineering

Stephanie Wissel  
Associate Professor of Physics

<sup>18</sup>

Mauricio Terrones  
George A. Margaret M. Downsborough Department Head  
Evan Pugh University Professor  
Professor of Physics, Chemistry and Material Science

<sup>19</sup> \*Signatures are on file in the Graduate School.

# <sup>20</sup> Abstract

21 Neutrinos are fundamental particles in the standard model and play an important role in  
22 the current understanding of the universe; however, the masses of the neutrinos, one of the  
23 most fundamental parameters for any particle, is currently unknown. This fact represents  
24 a gaping hole in our current knowledge of the universe that may provide clues to the  
25 energy scale of physics beyond the standard model. This dissertation summarizes research  
26 and development as a member of the Project 8 collaboration towards an experiment  
27 to measure the neutrino mass to a sensitivity below  $50 \text{ meV}/c^2$ , which is an order of  
28 magnitude less than the most sensitive direct measurements of the neutrino mass to date.  
29 Project 8 will perform this measurement using Cyclotron Radiation Emission Spectroscopy  
30 (CRES) to measure the beta-decay endpoint spectrum of atomic tritium. I present an  
31 analysis of the signal reconstruction performance of an antenna array system designed  
32 to perform large-scale CRES measurements. Next, I discuss an approach to calibrating  
33 an antenna array CRES experiment using a unique probe antenna designed to mimic  
34 radiation from CRES events. Finally, I present design studies for a resonant cavity that  
35 could be used to perform a CRES experiment with atomic tritium at multi-cubic-meter  
36 scales.

# Table of Contents

38	<b>List of Figures</b>	viii
39	<b>List of Tables</b>	xxvii
40	<b>Acknowledgments</b>	xxviii
41	<b>Chapter 1</b>	
42	<b>Introduction</b>	1
43	1.1 Summary . . . . .	1
44	1.2 Outline . . . . .	4
45	<b>Chapter 2</b>	
46	<b>Neutrinos and Neutrino Masses</b>	6
47	2.1 Introduction . . . . .	6
48	2.2 Neutrinos and Beta-decay . . . . .	6
49	2.3 Neutrino Oscillations . . . . .	8
50	2.4 Neutrino Masses in the Standard Model . . . . .	11
51	2.5 Neutrino Absolute Mass Scale . . . . .	13
52	2.5.1 Limits from Cosmology . . . . .	13
53	2.5.2 Limits from Neutrinoless Double Beta-decay Searches . . . . .	15
54	2.5.3 Limits from Beta-decay . . . . .	17
55	<b>Chapter 3</b>	
56	<b>Direct Measurement of the Neutrino Mass with Project 8</b>	21
57	3.1 Introduction . . . . .	21
58	3.2 Project 8 and Cyclotron Radiation Emission Spectroscopy . . . . .	22
59	3.2.1 Cyclotron Radiation Emission Spectroscopy — CRES . . . . .	22
60	3.2.2 Project 8 . . . . .	27
61	3.2.3 The Project 8 Phased Development Plan . . . . .	30
62	3.3 Phase II: First Tritium Beta Decay Spectrum and Neutrino Mass Measurement with CRES . . . . .	34
63	3.3.1 The Phase II CRES Apparatus . . . . .	34
64	3.3.2 CRES Track and Event Reconstruction . . . . .	39
65	3.3.3 Results from Phase II . . . . .	43
66	3.4 Phase III R&D: Antenna Array CRES . . . . .	47

68	3.4.1	The Basic Approach . . . . .	47
69	3.4.2	The FSCD: Free-space CRES Demonstrator . . . . .	48
70	3.5	Pilot-scale Experiments . . . . .	53
71	3.5.1	Choice of Frequency . . . . .	54
72	3.5.2	Pilot-scale Experiment Concepts . . . . .	56
73	3.6	Phase IV . . . . .	59

74	<b>Chapter 4</b>		
75	<b>Signal Reconstruction Techniques for Antenna Array CRES and the</b>		
76	<b>FSCD</b>		<b>61</b>
77	4.1	Introduction . . . . .	61
78	4.2	FSCD Simulations . . . . .	62
79	4.2.1	Kassiopeia . . . . .	63
80	4.2.2	Locust . . . . .	67
81	4.2.3	CRESana . . . . .	71
82	4.3	Signal Detection and Reconstruction Techniques for Antenna Array CRES	71
83	4.3.1	Digital Beamforming . . . . .	76
84	4.3.2	Matched Filtering . . . . .	85
85	4.3.3	Machine Learning . . . . .	97
86	4.4	Analysis of Signal Detection Algorithms for the FSCD . . . . .	102
87	4.4.1	Introduction . . . . .	103
88	4.4.2	Signal Detection with Antenna Array CRES . . . . .	104
89	4.4.2.1	Antenna Array and Data Rate Estimates . . . . .	104
90	4.4.2.2	Real-time Signal Detection . . . . .	106
91	4.4.3	Signal Detection Algorithms . . . . .	109
92	4.4.3.1	Power Threshold . . . . .	110
93	4.4.3.2	Matched Filtering . . . . .	112
94	4.4.3.3	Machine Learning . . . . .	116
95	4.4.4	Methods . . . . .	118
96	4.4.4.1	Data Generation . . . . .	118
97	4.4.4.2	Template Number and Match Estimation . . . . .	119
98	4.4.4.3	CNN Training and Data Augmentation . . . . .	120
99	4.4.5	Results and Discussion . . . . .	121
100	4.4.5.1	Trigger Classification Performance . . . . .	121
101	4.4.5.2	Computational Cost and Hardware Requirements . . . . .	123
102	4.4.6	Conclusion . . . . .	125

103	<b>Chapter 5</b>		
104	<b>Antenna and Antenna Measurement System Development for the</b>		
105	<b>Project 8 Experiment</b>		<b>127</b>
106	5.1	Introduction . . . . .	127
107	5.2	Antenna Measurements for CRES experiments . . . . .	128
108	5.2.1	Antenna Parameters . . . . .	128
109	5.2.1.1	Radiation Patterns . . . . .	128

110	5.2.1.2	Directivity and Gain . . . . .	129
111	5.2.1.3	Far-field and Near-field . . . . .	130
112	5.2.1.4	Polarization . . . . .	131
113	5.2.1.5	Antenna Factor and Effective Aperture . . . . .	132
114	5.2.2	Antenna Measurement Fundamentals . . . . .	134
115	5.2.2.1	Friis Transmission Equation . . . . .	134
116	5.2.2.2	S-Parameters and Network Analyzers . . . . .	135
117	5.2.2.3	Antenna Array Commissioning and Calibration Measurements . . . . .	136
119	5.2.3	The Penn State Antenna Measurement System . . . . .	137
120	5.3	Development of a Synthetic Cyclotron Antenna (SYNCA) for Antenna Array Calibration . . . . .	140
121	5.3.1	Introduction . . . . .	141
123	5.3.2	Cyclotron Radiation Phenomenology . . . . .	143
124	5.3.3	SYNCA Simulations and Design . . . . .	149
125	5.3.4	Characterization of the SYNCA . . . . .	155
126	5.3.5	Beamforming Measurements with the SYNCA . . . . .	159
127	5.3.6	Conclusions . . . . .	163
128	5.4	FSCD Antenna Array Measurements with the SYNCA . . . . .	164
129	5.4.1	Introduction . . . . .	164
130	5.4.2	Measurement Setups . . . . .	165
131	5.4.2.1	FSCD Array Setup . . . . .	165
132	5.4.2.2	Synthetic Array Setup . . . . .	167
133	5.4.3	Simulations, Analysis, and Results . . . . .	167
134	5.4.3.1	Simulations . . . . .	168
135	5.4.3.2	Phase Analysis . . . . .	169
136	5.4.3.3	Magnitude Analysis . . . . .	173
137	5.4.3.4	Beamforming Characterization . . . . .	174
138	5.4.4	Conclusions . . . . .	176

139	<b>Chapter 6</b>		
140	<b>Development of Resonant Cavities for Large Volume CRES Measurements</b>	<b>182</b>	
141	6.1	Introduction . . . . .	182
142	6.2	Cylindrical Resonant Cavities . . . . .	183
143	6.2.1	General Field Solutions . . . . .	183
144	6.2.2	TE and TM Modes . . . . .	184
145	6.2.3	Resonant Frequencies of a Cylindrical Cavity . . . . .	186
146	6.2.4	Cavity Q-factors . . . . .	188
147	6.3	The Cavity Approach to CRES . . . . .	192
148	6.3.1	A Sketch of a Molecular Tritium Cavity CRES Experiment . . . . .	192
149	6.3.2	Magnetic Field, Cavity Geometry, and Resonant Modes . . . . .	194
150	6.3.3	Trade-offs Between the Antenna and Cavity Approaches . . . . .	197
152	6.4	Single-mode Resonant Cavity Design and Simulations . . . . .	199

153	6.4.1	Open Cylindrical Cavities with Coaxial Terminations . . . . .	199
154	6.4.2	Mode Filtering . . . . .	203
155	6.4.3	Simulations of Open, Mode-filtered Cavities . . . . .	204
156	6.5	Single-mode Resonant Cavity Measurements . . . . .	207
157	6.5.1	Cavities and Setup . . . . .	207
158	6.5.2	Results and Discussion . . . . .	210
159	<b>Chapter 7</b>		
160	<b>Conclusion and Future Prospects</b>		<b>214</b>
161	<b>Bibliography</b>		<b>217</b>

# **List of Figures**

162	2.1	A diagram of two different neutrino mass ordering scenarios [1]. In the inverted hierarchy (inverted mass ordering) the lightest neutrino mass is $m_3$ , whereas, in the normal hierarchy (normal mass ordering) $m_1$ is the lightest neutrino. What cannot be measured by neutrino oscillations is the neutrino absolute mass scale, which is essentially the mass of the lightest neutrino mass eigenstate. . . . .	9
163	2.2	The masses of the neutrinos as a function of the lightest neutrino mass in both the normal (a) and inverted (b) mass ordering regimes. . . . .	10
164	2.3	The neutrino mass observable measured by cosmology as a function of the lightest neutrino mass eigenstate. . . . .	14
165	2.4	Feynman diagrams for double beta-decay (a) and $0\nu\beta\beta$ (b). . . . .	15
166	2.5	The discovery probabilities for the future generation of $0\nu\beta\beta$ experiments as a function of $m_{\beta\beta}$ and $m_{least}$ . Figure from [2]. . . . .	16
167	2.6	A Feynman diagram of beta decay . . . . .	17
168	2.7	A figure from Fermi's 1934 paper on a theory of beta-decay depicting the kinetic energy spectrum of the emitted electron. The effect of the neutrino mass, written as $\mu$ , is to distort the shape of the spectrum near the endpoint from the zero-mass spectrum. . . . .	17
169	2.8	The tritium beta-decay spectrum. The effect of a massive neutrino on the spectrum is to change its shape near the endpoint by an amount proportional to the size of the neutrino mass. A sufficiently high-statistic and high-resolution measurement of the spectrum endpoint would be able to measure the neutrino mass. . . . .	19
170			
171			
172			
173			
174			
175			
176			
177			
178			
179			
180			
181			
182			
183			
184			
185			

186	3.1	A cartoon illustration of the CRES technique. An electron is contained in 187 a magnetic trap, which is a local minimum in the magnetic field, so that 188 its cyclotron radiation can be detected by an array of antennas. Detecting 189 the cyclotron radiation allows one to measure its cyclotron frequency and 190 determine its kinetic energy. . . . .	23
191	3.2	An illustration of an electron in a bathtub magnetic trap generated by 192 two well-separated coils. . . . .	24
193	3.3	A plot of the main components of an electron's trajectory in a cylindrically 194 symmetric trap. . . . .	26
195	3.4	A plot of the final state distributions of atomic and molecular tritium. The 196 final state distribution provides the primary contribution to the width of 197 the molecular spectrum whereas thermal doppler broadening is responsible 198 for the width of the atomic spectrum. . . . .	27
199	3.5	Neutrino mass exclusion plot including limits from cosmological measure- 200 ments and the KATRIN experiment. Allowed ranges for neutrino masses 201 under the normal and inverted hierarchies are shown as the blue and 202 orange lines respectively. The black dashed line shows Project 8's goal 203 neutrino mass sensitivity for the Phase IV experiment. . . . .	30
204	3.6	Sensitivity calculations for a cavity based CRES experiment that demon- 205 strate the neutrino mass measurement goals of Project 8 throughout the 206 phased development plan. The blue curves indicate molecular tritium 207 sources and the red curves indicate atomic tritium sources. In the current 208 plan, Phase III contains two tritium experiments. The first is the Low- 209 frequency Apparatus (LFA), which is a molecular tritium experiment, and 210 the second is the atomic tritium pilot-scale experiment that officially ends 211 Phase III. The sensitivity of these experiments is primarily a function 212 of statistics; however, there is a critical density beyond which CRES 213 electrons do not have enough time to radiate between collisions for a 214 high-resolution frequency measurement leading to worse sensitivity. . . .	31
215	3.7	The Phase II CRES apparatus used to perform the first measurement of 216 the tritium beta-decay spectrum using CRES. . . . .	35
217	3.8	Diagram of the CRES cell portion of the Phase II apparatus. . . . .	36
218	3.9	RF system diagram for the Phase II apparatus. . . . .	38

219	3.10 The time-frequency spectrogram of a tritium CRES event in the Phase II 220 apparatus. . . . .	39
221	3.11 The sparse spectrogram obtained by placing a power cut on the raw 222 spectrogram shown in Figure 3.10. . . . .	41
223	3.12 Fits to the measured 17.8-keV $^{83m}\text{Kr}$ conversion line using the deep and 224 shallow trap configurations. . . . .	44
225	3.13 Measurements of the 17.8-keV $^{83m}\text{Kr}$ line using the deep trap configuration 226 for different values of the magnetic field from the field shifting solenoid. .	45
227	3.14 The measured tritium spectrum from Phase II with Bayesian and frequen- 228 tist fits. . . . .	46
229	3.15 A cartoon illustration of the basics of the antenna array CRES technique.	47
230	3.16 An image of the MRI magnet installed in the Project 8 laboratory at the 231 University of Washington, Seattle. . . . .	49
232	3.17 (a) A model of the FSCD antenna array, magnetic trap, and tritium 233 containment vessel design.(b) A more detailed model of a prototype 234 design for the 5-slot waveguide antenna design. . . . .	51
235	3.18 (a) A plot of the decay rate for the two-body dipolar spin exchange 236 interaction for cc and dd state. (b) A plot of the decay rate of the dipolar 237 spin exchange interaction for d+d states as a function of magnetic field 238 magnitude. Lowering the magnetic field is key for reducing the losses 239 from this interaction. . . . .	55
240	3.19 A conceptual sketch of a large-volume antenna array based CRES experi- 241 ment to measure the neutrino mass. . . . .	57
242	3.20 A conceptual sketch of a pilot-scale cavity CRES experiment with an 243 atomic tritium beamline. . . . .	58

244	3.21 An illustration of a possible arrangement of ten pilot-scale cavity experiments for Phase IV. The experiments are arranged in a circle with an approximate diameter of 50 meters. Each atomic beamline connected to the bottom of each cavity is approximately 10 m in length. The cavities themselves are designed to operate at 325 MHz and are approximately 11 m tall. The circular arrangement of cavities has some advantages when it comes to cancellation of fringe fields from neighboring magnets, which is important due to the small magnetic field magnitudes consistent with these CRES frequencies. The advantage of ten independent atomic sources and cavities is that there is no single point of failure for the experiment. If an experiment goes down for repairs the other nine may continue running. Figure courtesy of Michael Huehn at UW-Seattle. . . . .	60
256	4.1 The geometry and parameters of the coils used to simulate the FSCD magnetic trap in Kassiopeia. Some axial profiles of the magnetic trap at different radial positions are shown to demonstrate the shape of the magnetic field and trap depth as a function of position. Calculation of the magnetic field profiles was graciously done by René Reimann. . . . .	64
261	4.2 A map of the average $\nabla B$ -drift frequency for electrons trapped in the prototype FSCD trap shown in Figure 4.1. Negative drift frequencies indicate electrons that are drifting opposite to the standard direction, which means that they are close to escaping the magnetic trap. . . . .	66
265	4.3 The receiver chain used by Locust when simulating CRES events in the FSCD. . . . .	69
267	4.4 A high-level diagram depicting the process of CRES event reconstruction. The first step consists of identifying the presence of a signal in the data. This step is necessary to avoid the danger of performing a reconstruction of a false event, which would constitute a background contribution to the tritium spectrum measured by CRES. . . . .	73
272	4.5 An illustration of two PDFs associated a binary hypothesis test. The decision threshold is represented by the vertical line that partitions both distributions. The orange and red areas correspond to the true negative and false positive probabilities and the blue and green areas correspond to the false negative and true positive probabilities respectively. To decide between the two hypotheses the likelihood ratio test specified by the Neyman-Pearson theorem is applied. This approach achieves the highest true positive probability for a given false positive probability. . . . .	74

280	4.6 An example ROC curve formed by computing the $P_{\text{FP}}$ and the $P_{\text{TP}}$ for 281 a given likelihood ratio test. As the decision threshold is increased $P_{\text{FP}}$ 282 decreases at the expense of a lower $P_{\text{TP}}$ . The black dashed line indicates 283 the lower bound ROC curve obtained by randomly deciding between $\mathcal{H}_0$ 284 and $\mathcal{H}_1$ . . . . .	75
285	4.7 An illustration of the constructive interference condition which is the 286 operating principle of digital beamforming using a uniform linear array 287 as an example. . . . .	77
288	4.8 A system level diagram of the laboratory setup used for beamforming 289 demonstrations at Penn State. For more information on this system see 290 Chapter 5. Signals near 26 GHz are fed to a dipole antenna using an 291 arbitrary waveform generator (AWG) and vector network analyzer (VNA), 292 which drive a mixer. The dipole radiation is collected by an array of 293 antennas connected to the digitizer data acquisition (DAQ) system. . . . .	78
294	4.9 Photographs of the beamforming demonstration setup. In (a) I show a 295 top-down view of the dipole antenna and the array of eight horn antennas. 296 Manual repositioning of the horn antennas allows one to synthesize a full- 297 circular antenna array. The dipole antenna is mounted on a camera tripod 298 mount that allows for manual position tuning. (b) is a close up image of 299 the dipole, which is manufactured from two segments of semi-rigid coaxial 300 cable. (c) is another image of the dipole and array. . . . .	79
301	4.10 An example of digital beamforming reconstruction of a dipole antenna 302 using a synthetic array of horn antennas. The beamforming image on 303 the right is constructed by computing the time-averaged power of the 304 summed signals for a two-dimensional grid of beamforming positions. In 305 the image, one can see a clear maximum that corresponds to the position 306 of the dipole antenna. On the left I show the frequency spectrum of the 307 time-series at the maximum power pixel. White Gaussian noise is added 308 to the signal to mimic a more realistic signal-to-noise-ratio. The signal 309 emitted by the dipole is clearly visible as the high power peak in the 310 frequency spectrum. . . . .	80
311	4.11 Beamforming images visualizing the reconstruction of an electron without 312 (a) and with (b) the cyclotron phase correction. The images were generated 313 using data from Locust simulations. The cyclotron phase refers to a phase 314 offset equal to the relative azimuthal position of an antenna in the array. 315 This phase offset is caused by the circular electron orbit and must be 316 corrected for during reconstruction. . . . .	81

317	4.12 Beamforming images visualizing the reconstruction of an electron located 318 off the central axis of the FSCD trap. In (a) beamforming is being 319 performed without the $\nabla B$ -drift correction, and in (b) it is included. . . . .	82
320	4.13 A plot of a typical frequency spectrum obtained by applying a Fourier 321 transform to the time-series obtained from beamforming. The frequency 322 spectra are plotted without noise on top of an example of a typical noise 323 spectrum to visualize a realistic signal-to-noise ratio. In the example, 324 without beamforming it would not be possible to detect anything since 325 the signal amplitudes would be reduced by a factor of sixty relative to 326 the noise. Additionally, it is clear the $\nabla B$ -drift correction is needed to 327 detect this electron in the presence of noise. . . . .	84
328	4.14 A plot of the total signal power received by the FSCD array from trapped 329 electrons with different radial positions and pitch angles generated using 330 Locust simulations. The lines on the plot indicate a 10 dB detection 331 threshold above the mean value of the noise in the frequency spectrum. 332 With static beamforming electrons with radial positions larger than about 333 two centimeters are undetectable due to the change in the electron's 334 position over time causing losses from beamforming phase mismatch. This 335 is corrected by including $\nabla B$ -drift frequencies in the beamforming phases. 336 Both beamforming techniques fail to detect electrons below $\approx 88.0^\circ$ , since 337 these signals are composed of several relatively weak sidebands that are 338 comparable to the noise. . . . .	85
339	4.15 Example of a convolution of a CRES signal template with a segment of 340 noisy data. A simulated CRES signal was simulated using Locust and 341 normalized to create a matched filter template. When this template is 342 convolved with noisy data the convolution output increases dramatically compared to data with only noise. 343 The decreasing convolution output as the time offset of the convolution 344 increases is caused by zero-padding of the data and template. . . . .	86
345	4.16 An example two-dimensional parameter distribution of a matched filter 346 template bank and random test signals. $\theta$ refers to the pitch angle of 347 the electron and $E$ is the kinetic energy. The template bank forms a 348 regular grid of in pitch angle and energy; whereas, the test signals are 349 uniformly distributed in pitch angle and follow the tritium beta-decay 350 kinetic energy distribution. This is why there are fewer test signals at 351 higher energies. The need for high match across the full parameter space 352 prevents one from reducing the density of templates in this low activity 353 region. A zoomed in version of the template bank illustrates the relative 354 density of templates and signals needed for match > 90%. . . . .	89

356	4.17 The matched filter scores of a dense grid of templates in pitch angle energy 357 space. Dense template grids allow one to estimate the kinetic energy of 358 the electron by identifying the best matching template. The uncertainty 359 on this value is proportional to the space of templates that also match 360 the test signal well. In the worst case matched filter templates can be 361 completely degenerate where templates with different parameters match 362 a signal with equal likelihood. . . . .	90
363	4.18 The mean match of the dense template grid shown in Figure 4.17 for 364 different numbers of templates. Grids of different sizes were obtained by 365 decimating a dense grid of templates and the average match for each grid 366 was computed using the same set of randomly distributed test signals. 367 Plotting the mean match against the size of the grid allows one to visualize 368 the exponential relationship between match and template bank size. The 369 noise in each curve is caused by sampling effects from the decimation 370 algorithm. In general, longer templates are harder to match than shorter 371 templates. . . . .	91
372	4.19 Matched filter template bank ROC curves as a function of mean match. 373 One can see that for low match a matched filter is on average worse than 374 the more straight forward beamforming detection approach. . . . .	91
375	4.20 Boundaries of detectable electrons in pitch angle kinetic energy space 376 for a series of different signal detection algorithms. A detectable signal 377 is defined as a signal that is above a consistent decision with at least 378 50% probability. This non-rigorous treatment of detection probability is 379 primarily useful for the visualization the relative increases in detection 380 performance provided by the different algorithms. The static beamforming 381 (Static-BF) algorithm is the digital beamforming algorithm introduced 382 above without the $\nabla B$ -drift correction. The DNN algorithm refers to a 383 convolutional neural network classifier trained to detect CRES signals 384 (see Section 4.3.3). . . . .	92
385	4.21 Two example illustrations of the correlation between kinetic energy and 386 pitch angle imparted by the shape of the FSCD magnetic trap. The 387 correlations manifest themselves as degeneracies in the matched filter 388 score where multiple matched filter templates have the same matched filter 389 for a particular signal. These degeneracies are a sign that the magnetic 390 trap must be redesigned in order to break the correlation between pitch 391 angle and kinetic energy. . . . .	96

392	4.22 A visualization of the correlation between energy and pitch angle in the FSCD magnetic trap. The image is formed by computing the match of the best template from a grid consisting of pitch angles from 84 to 90 degrees in steps of 0.05 degrees, kinetic energies from 17574 to 18574 eV, located at 2 cm from the central axis, and simulated for a length of three FSCD time-slices. The signals used to compute the best matching template consisted of a grid from 84 to 90 degrees in steps of 0.05 degrees, kinetic energies from 18550 to 18575 eV in steps of 0.25 eV, located 2 cm from the central axis, and simulated for three FSCD time-slices. The colored regions of the plot show how well signals with lower energy can match those of higher energy for the FSCD magnetic trap, which is proportional to the achievable energy resolution of the FSCD design. . . . .	97
404	4.23 A representation of a matched filter template bank as a convolutional neural network. The network has a single layer composed of the templates, which act as convolutional filters. The activation of the neural network is an absolute value followed by a max operator. . . . .	100
408	4.24 A graphical depiction of CRES signal detection using a CNN. A noisy segment of data is converted to a frequency series using digital beamforming and a FFT. The complex-valued frequency series is input into a trained CNN model that classifies the data as signal or noise using a decision threshold on the CNN output. . . . .	101
413	4.25 The detection efficiency and false alarm rate (false positive rate) as a function of the decision threshold for different values of the noise temperature. The model is trained to output a value close to one for data that contains a signal and outputs a value near zero when the data contains only noise. One sees that a lower decision threshold will have a high detection efficiency at the cost of a high rate of false alarms. . . . .	102
419	4.26 ROC curves for a CNN model classifying CRES signals. One can see that the area under the curve, which is a figure of merit that describes the performance of the classifier, is roughly linearly dependent with the noise temperature. . . . .	103

423	4.27 An illustration of the conceptual design for an antenna array CRES	
424	tritium beta-decay spectrum measurement. The antenna array geometry	
425	consists of a 20 cm interior diameter with 60 independent antenna channels	
426	arranged evenly around the circumference. The nominal antenna design	
427	is sensitive to radiation in the frequency range of 25-26 GHz, which	
428	corresponds to the cyclotron frequency of electrons emitted near the	
429	tritium beta-spectrum endpoint in a 0.96 T magnetic field. The array is	
430	located at the center of the magnetic trap produced by a set of current-	
431	carrying coils. The nominal magnetic trap design is capable of trapping	
432	electrons up to 5 cm away from the central axis of the array and traps	
433	electrons within an approximately 6 cm long axial region centered on the	
434	antenna array. . . . .	105
435	4.28 A block diagram illustration of the real-time triggering algorithm proposed	
436	for antenna array CRES reconstruction. . . . .	106
437	4.29 An illustration of the digital beamforming procedure. The blue lines	
438	indicate the distances from the beamforming position to each antenna.	
439	In the situation depicted the actual position of the electron matches the	
440	beamforming position; therefore, one expects constructive interference	
441	when the phase shifted signals are summed. To prevent the electron's	
442	$\nabla B$ -motion from moving the electron off of the beamforming position,	
443	the beamforming phases include time-dependence to follow the trajectory	
444	of the electron in the magnetic trap. . . . .	107
445	4.30 Frequency spectra of simulated CRES events in the FSCD magnetic	
446	trap after beamforming. The signal of a 90° electron consists of a single	
447	frequency component that is clearly detectable using a power threshold	
448	on the frequency spectrum. This power threshold remains effective for	
449	signals with relatively large pitch angles such as 89.0° and 88.75°, which	
450	are composed of a main carrier and a few small sidebands. Signals with	
451	smaller pitch angles, below about 88.5°, are dominated by sidebands such	
452	that no single frequency component can be reliably distinguished from	
453	the noise with a power threshold. . . . .	109
454	4.31 PDFs of the power threshold test statistic for CRES signals with various	
455	pitch angles as well as the PDF for the noise-only signal case. The average	
456	PDF computed for pitch angles ranging from 85.5 to 88.5° is also shown.	
457	As the pitch angle is decreased the signal PDF converges towards the	
458	noise PDF which indicates that the power threshold trigger is unable to	
459	distinguish between small pitch angle signals and noise. . . . .	112

460	4.32 Plots of PDFs that describe the matched filter template bank test statistic for CRES signals with various pitch angles, as well as the estimated PDF for the noise only case. $10^5$ matched filter templates are used and perfect match between signal and template i.e. $\Gamma_{\text{best}} = 1$ is assumed. The mean PDF includes signals ranging from $85.5 - 88.5^\circ$ in pitch angle. There is a larger distinction between the signal PDFs at small pitch angles compared to the power threshold, which indicates a higher detection efficiency for these signals. . . . .	116
468	4.33 The mean match of the matched filter template bank to a test set of randomly parameterized signals as a function of the number or density of templates. The parameter space includes pitch angles from $85.5 - 88.5^\circ$ and energies from $18575 - 18580$ eV. . . . .	119
472	4.34 Histograms of the trained CNN model output from the test dataset. The blue histogram shows the model outputs for signal data. The oddly shaped peak near the end is the result of the softmax function mapping the long tail of the raw output distribution to the range $[0, 1]$ . . . . .	121
476	4.35 ROC curves describing the detection efficiency or true positive rates for the three signal classification algorithms examined in this paper. The matched filter (MF) and Power Threshold curves are computed analytically using the distribution functions introduced in Section 4.4.3, and the CNN curve is computed numerically using the classification results on the test dataset. The percent match indicated in the legend refers to the mean match of the classifier. . . . .	122
483	5.1 An example radiation pattern generated using HFSS simulations. The color and radial distance of the surface from the origin indicate the relative magnitude of radiation power emitted by the antenna in that direction. The primary goal of most antenna measurements is typically to measure the antenna pattern, which is used to derive many useful antenna performance parameters. . . . .	128

489	5.2 An illustration of the three field regions important for the analysis of 490 an antenna system. Very close to the antenna the electric fields are 491 primarily reactive so there is no radiation. If a receiving antenna were 492 placed in this region most of the energy would be reflected back to the 493 transmitter. Outside of the reactive near-field is the radiative near field. 494 At these distances the antenna does radiate, but the radiation pattern is 495 not well-defined since it changes based on the distance of the receiving 496 antenna. It is only in the far-field region where the radiation pattern 497 becomes constant as a function of distance, which is where the majority 498 of antenna engineering is assumed to take place. The antenna arrays 499 developed by Project 8 for CRES measurements operate in the radiative 500 near-field due to the importance of limiting power loss from free-space 501 propagation, which complicates the design of the antenna system. . . . .	130
502	5.3 An illustration of the Friis measurement technique commonly used for 503 antenna characterization measurements. . . . .	134
504	5.4 Illustration of a two-port S-parameter measurement setup. S-parameters 505 characterize how incoming waves of voltage or power scatter off of the RF 506 device under test. This allows you to measure important properties of the 507 device. In particular, this framework can be used to model a two antenna 508 radiation pattern measurement, which can be automated using a VNA. . .	135
509	5.5 Two measurement approaches to characterizing an antenna array for CRES 510 measurements. The full-array approach (a) requires a complete antenna 511 array with all the associated hardware. The synthetic array approach 512 (b) utilizes a single antenna and a set of rotation/translation stages to 513 reposition the transmitter or the receiving antenna to synthesize the signals 514 that would be received by the full-array. This approach reduces the cost 515 and complexity of array measurements. A down-side of the synthetic 516 array approach is that multi-channel effects such as reflections cannot 517 be measured. Utilizing both the full-array and the synthetic array is a 518 powerful way to quantify the impact of errors from the multi-channel array.	136
519	5.6 Illustration of the antenna measurement system developed for the Project 520 8 Collaboration. The reference and test antennas can be connected to 521 different data acquisition configurations depending on the measurement 522 goals. The reference antenna is typically a standard horn antenna and 523 the test antenna is mounted on a set of translation stages for positioning. 524 Automated translation stages allow for relatively painless data-taking enabling 525 synthetic antenna array measurements using only a single receiving 526 antenna. Anechoic form designed to mitigate RF reflections surrounds 527 the setup. . . . .	138

528	5.7	Diagrams of two measurement system configurations. Configuration (a) utilizes a VNA and is more suited to antenna characterization. Configuration (b) utilizes an AWG (arbitrary waveform generator) and VNA as a signal generation system and digitizer to collect measurement data, which is more suited to simulating CRES measurements. The transmission chain utilizes a quadrature hybrid and a pair of baluns to drive the cross-dipole variant test antenna developed for synthetic CRES measurements. . . . .	139
535	5.8	A sketch of an antenna array large-volume CRES experiment. Electrons from $\beta$ -decays are confined in a magnetic field using a set of trap coils. The cyclotron radiation produced by the motion of the trapped electrons can be detected by a surrounding antenna array to determine the electron energies. Measuring the energies of many electrons produces a $\beta$ -decay spectrum. . . . .	141
541	5.9	A schematic of the antenna array test stand. The circular antenna array has a radius of 10 cm with 60 independent channels (limited number shown for clarity). The test stand includes an arbitrary waveform generator (AWG), local oscillator (LO), and data acquisition (DAQ) hardware. Finally, a specialized Synthetic Cyclotron Antenna (SYNCA) is used to inject signals to test the antenna array. . . . .	142
547	5.10	An electron (red dot) performing cyclotron motion in the x-y plane. The resulting cyclotron radiation is observed by an antenna located at the field point of interest. . . . .	143
550	5.11	A plot of the numeric solution to Equation 5.30. The time-domain representation of the signal (a) is composed of a zero frequency term and a series of harmonics separated by the main cyclotron frequency as shown in the plot of the frequency spectrum (b). We can see that the relative amplitude of the harmonics beyond $k = 7$ are smaller than the main carrier by a factor of about $10^{-5}$ and are completely negligible. . . . .	146
556	5.12	The amplitude maxima of the cyclotron radiation form an Archimedean spiral as the radiation propagates outward from the cyclotron orbit center (a). A circular antenna array located at a fixed radius from the orbit center will receive electric fields with equal magnitude in each of its channels, but the phase of the electric field incident on each array channel will be linearly out of phase from its neighbor antennas by an amount equal to the angular separation of the two channels (b). . . . .	148

563	5.13 Images of an early prototype crossed-dipole antenna manufactured by hand and the first measurement setup. The antenna was constructed by hand using four stripped coaxial cables. The antenna was connected to one port of the VNA, and the remaining three ports on the VNA were connected to horn antenna arranged with 90 deg offsets around the crossed-dipole. The measured unwrapped S-parameter phases exhibit the desired relative phase behavior for a SYNCA. These early measurements were the first laboratory proof-of-principle for the crossed-dipole SYNCA.	150
571	5.14 An early iteration of a crossed-dipole SYNCA antenna simulated in HFSS. The antenna is electrically small at 26 GHz, which requires dipole arms on the order of 1 mm long. This design is limited by the minimum achievable distance between the dipole arms caused by the available diameters of coaxial cables. The assumed termination scheme for the coaxial cables to the antenna is hand-soldering, which introduces random variation in the antenna pattern from the inevitable blobs of solder left on the surface of the PCB.	151
579	5.15 An idealized crossed-dipole antenna consists of two electric dipole antennas oriented perpendicular to each other and is fed with four signals with a quadrature phase relationship. An example antenna feed circuit is shown which is composed of a chained combination of a quadrature hybrid-coupler (Quad) and two baluns.	152
584	5.16 A model of the PCB crossed-dipole antenna with dimensions. The design has an inside diameter of 2.16 mm for the central circular trace, which is 0.13 mm wide. The dipole arms each have a width of 1.27 mm and protrude beyond the circular trace by 1.40 mm, which gives an overall width of 4.96 mm for the length of the antenna PCB trace from end-to- end. The overall size of the antenna is 20.0 mm the majority of which is the PCB dielectric material. This design was observed in simulation to maintain the field characteristics of the idealized crossed-dipole while being simpler to fabricate due to the increased size of the antenna.	153
593	5.17 A comparison of the electric field magnitudes, normalized by the maximum value of the electric field in each simulation, plotted on a 10 cm square to visualize the Archimedean spirals formed by the electron (a), the crossed- dipole antenna (b), and a PCB crossed-dipole antenna (c). The matching patterns indicate that the electric fields have similar phase characteristics. These images were generated using Locust simulations for the electron and ANSYS HFSS for both antennas.	154

600	5.18 A comparison of the normalized electric field magnitudes for the ideal		
601	crossed-dipole, PCB crossed-dipole, and a simulated electron as a function		
602	of the polar angle ( $\theta$ ). (a) Shows the total electric field, (b) shows the		
603	$\phi$ -polarized electric field component, and (c) shows the $\theta$ -polarized electric		
604	field component. These images were generated using Locust simulations		
605	for the electron and ANSYS HFSS for both antennas. . . . .	155	
606	5.19 A comparison of the normalized electric field magnitudes for the crossed-		
607	dipole, PCB crossed-dipole, and a simulated electron as a function of the		
608	azimuthal angle ( $\phi$ ) evaluated at $\theta = 90^\circ$ . This image was generated using		
609	Locust simulations for the electron and ANSYS HFSS for both antennas.	156	
610	5.20 (a) A cartoon schematic which highlights the routing of the semi-rigid		
611	coax transmission lines. (b) A photograph of a SYNCA constructed		
612	using the modified crossed-dipole PCB antenna design. Visible in the		
613	photograph of the SYNCA are four blobs of solder which are an artifact		
614	of the SYNCA's hand-soldered construction. These solder blobs are the		
615	most significant deviation from the SYNCA design shown in Figure 5.16		
616	and are responsible for a significant fraction of the irregularities seen in		
617	the antenna pattern. . . . .	157	
618	5.21 A schematic of the VNA characterization measurements (a). This setup		
619	allows for antenna gain and phase measurements across a full $360^\circ$ of		
620	azimuthal angles using a motorized rotation stage and control of the radial		
621	position of the SYNCA using a translation stage. A photo of the setup in		
622	the lab is shown in (b). . . . .	158	
623	5.22 Linear interpolations of the measured electric field magnitude (a) and		
624	phase (b). The data was acquired using a VNA at 120 points spaced		
625	by 3 degrees from 0 to $357^\circ$ of azimuthal angle. The different		
626	color lines indicate the vertical offset of the horn antenna relative to the		
627	SYNCA PCB and the dashed line shows the expected shape from electron		
628	simulations. No significant difference in the antenna pattern is observed		
629	for the measured vertical offsets. . . . .	159	
630	5.23 (a) A depiction of the relative phase differences for signals received by a		
631	circular antenna array from an isotropic source. The phases correspond to		
632	a unique spatial position. (b) A schematic of the setup used to perform		
633	digital beamforming. . . . .	160	

634	5.24 Digital beamforming maps generated using a simulated 60 channel array and electron simulated using the Locust package. (a) and (b) show the beamforming maps for simulated electrons without the cyclotron spiral phases and with the cyclotron spiral phases respectively. (c) and (d) show the beamforming maps produced from SYNCA measurements. We observe good agreement between simulated electrons and the SYNCA measurements. . . . .	161
641	5.25 A plot of the SYNCA's reconstructed position using the synthesized horn- antenna array and digital beamforming. (a) Shows the reconstructed position of the SYNCA compared with the target position indicated by the positioning system readout. (b) Shows the reconstruction error, which is the difference between the target and reconstructed positions. The error bars in (b) are the uncertainty in the mean position of the 2D Gaussian used to fit the digital beamforming reconstruction peak obtained from the fit covariance matrix. The mean fit position uncertainty of 0.02 mm is an order of magnitude smaller than the typical reconstruction error of 0.3 mm obtained by calculating the standard deviation of the difference between the reconstructed and target position. . . . .	162
652	5.26 A diagram of the array measurement system used to test the prototype FSCD antenna array. A VNA is used as the primary measurement tool, which is connected to the array through a series of switches. The other port of the VNA connects to the SYNCA through the quad-balun chain used to provide the SYNCA feed signals. During measurements the SYNCA is positioned inside the center of the antenna array and translated to different radial and axial positions using a 3-axis manual translation stage setup. . . . .	164
660	5.27 Photos of the prototype FSCD antenna (a), the FSCD array and SYNCA (b), and the translation stages and coordinate system used to position the SYNCA (c). . . . .	166
663	5.28 A photo of the FSCD antenna and the SYNCA in the synthetic array measurement setup at Penn State. . . . .	168
665	5.29 The unwrapped phases of signals received by the FSCD antenna array from an electron with a 90° pitch angle located in the plane of the antenna array. The data points indicated the phases extracted from simulation and the dashed lines show the model predictions. . . . .	169

669	5.30 Plots of the measured unwrapped phases from the FSCD array (a) and the 670 synthetic array (b) compared to the model predictions for a series of radial 671 positions. The different phases of the sinusoidal phase oscillations in the 672 two plots reflects differences in the coordinate systems of the measurements.	170
673	5.31 The phase errors between the measurement and model for the synthetic 674 array (blue) and the FSCD array (orange) for a series of radial positions. 675 The label JUGAAD refers to an alternative name for the FSCD array 676 setup. As the SYNCA is translated off-axis phase errors with progressively 677 higher oscillation frequency enter into the measurements. . . . .	171
678	5.32 Two dimensional plots of the phase errors for the synthetic array (a) 679 and the FSCD (JUGAAD) array (b). In both plots there is evidence 680 of a similar diffraction pattern with bilateral symmetry, but the FSCD 681 array measurments have an additional phase error contribution from the 682 different antennas and paths through the switch network. . . . .	177
683	5.33 The amplitude of the signals from CREsana for the FSCD array from a 684 $90^\circ$ electron. As the electron is moved from $R = 0$ the signals begin to 685 have unequal amplitudes depending on the distance from the electron to 686 the antenna. . . . .	178
687	5.34 The normalized magnitudes of the S21 parameters measured in the FSCD 688 (orange) and synthetic array (blue) setups. The dominant observed 689 behavior as a function of radius is the increase in the number of magnitude 690 peaks, which was noted in the phase error curves. There does not appear 691 to be a strong change in the relative amplitude of a group of antennas as 692 predicted by CREsana. . . . .	178
693	5.35 . . . . .	179
694	5.36 Beamforming images from the synthetic array (a) and FSCD array (b) 695 setups with the SYNCA positioned 15 mm off the central axis. In both 696 images, there is a clear maxima that corresponds to the true SYNCA 697 position. However, in the FSCD array there is an additional faint peak 698 located at the opposite position of the beamforming maximum. This 699 additional peak is the mirror of the true peak and is the result of reflections 700 between antennas in the FSCD array. . . . .	180

701	5.37 A comparison of the maximum signal amplitude obtained by beamforming 702 to the signal amplitude obtained with an ideal summation as a function of 703 the radial position of the SYNCA. The amplitudes for the synthetic array 704 are shown in (a) and the FSCD array are shown in (b). In both setups, 705 the signal amplitudes obtained from beamforming are smaller than the 706 signal amplitude that could be attained with the ideal summation without 707 phase mismatch. . . . .	180
708	5.38 The ratio of the beamforming signal amplitude to the ideal signal ampli- 709 tude for the FSCD and synthetic arrays. The FSCD array has a larger 710 power loss from phase error compared to the synthetic array which indi- 711 cates that calibration errors associated with the multiple channels as well 712 as reflections are impacting the signal reconstruction. . . . .	181
713	6.1 Geometry of a cylindrical waveguide with radius $b$ . . . . .	183
714	6.2 The geometry of a cylindrical cavity with length $L$ and radius $b$ . . . . .	186
715	6.3 Relation of mode frequency to cavity length for a cylindrical cavity with 716 a radius of 18.32 cm. . . . .	187
717	6.4 A series RLC circuit. . . . .	188
718	6.5 Illustration of the behavior of the input impedance of the series RLC 719 circuit as a function of the driving frequency. The BW is proportion to 720 the width of the resonance, which is inversely proportional to Q. . . . .	190
721	6.6 A series RLC circuit coupled to an external circuit with input impedance 722 $R_L$ . . . . .	191
723	6.7 A cartoon depiction of a cavity CRES experiment. A metallic cavity filled 724 with tritium gas is inserted into a uniform background magnetic field 725 to perform CRES measurements. Electrons from beta-decays inside the 726 cavity can be trapped and used to excite a resonant mode(s). By coupling 727 to the cavity mode with a suitable probe one can measure the cyclotron 728 frequency of the electron and perform CRES. . . . .	192

729	6.8 Examples of the resonant mode frequencies of a cylindrical cavity. This 730 cavity has a radius of 18.32 cm and a length to diameter ratio of 4.55. Sev- 731 eral families of resonant modes are relevant in the $\approx 800$ MHz bandwidth 732 of (a); however, after zooming in to a $\sim 80$ MHz bandwidth centered 733 on TE011 one sees that only a handful of resonant modes have frequen- 734 cies close to TE011. Since the bandwidth required for a cavity CRES 735 experiment is $O(10)$ 's MHz, a significant number of resonant modes can 736 be safely ignored since their resonant frequencies are far from the CRES 737 bandwidth. . . . .	196
738	6.9 An image of an open cavity with coaxial terminations used for dielectric 739 constant measurements. Figure from [3]. . . . .	200
740	6.10 The simplified geometry of an open cavity with coaxial terminations. 741 Figure from [4]. . . . .	201
742	6.11 Electric field regions for the open cavity boundary value problem. Figure 743 from [4]. . . . .	201
744	6.12 Two mode filtering concepts to break the degeneracy of TE <sub>01</sub> and TM <sub>11</sub> 745 modes. The resistive approach uses dielectric materials to impede currents 746 that travel vertically along the cavity while leaving azimuthal currents 747 unperturbed. An alternative approach is to impede the currents using 748 grooves cut into the cavity wall, which achieve the same effect with an 749 inductive impedance. . . . .	204
750	6.13 Four cavity design variations. (a) is a standard sealed cylindrical cavity, 751 (b) is an open cavity with smooth walls, (c) is an open cavity with walls 752 made of alternating conductor and dielectric, and (d) is an open cavity 753 with grooved walls. The main cavity and coaxial terminator parameter 754 are identical for all four cavities. . . . .	205
755	6.14 The frequencies and Q-factors of the resonant modes identified by HFSS 756 for the cavity variations shown in Figure 6.13. The fully-sealed cavity with 757 smooth walls has several high-Q modes near the TE <sub>011</sub> resonance. Intro- 758 ducing the open-termination preserves the Q-factors of the TE <sub>01ℓ</sub> modes 759 and suppresses the Q-factors of the modes whose boundary conditions do 760 not match the cylindrical partition. Both the resistive and grooved wall 761 perturbations shift the resonant frequencies of the TM modes away from 762 the TE <sub>011</sub> mode. By properly tuning the geometry of the grooves or the 763 resistive spacers several MHz of frequency separation can be achieved. . .	206

764	6.15 A cartoon depicting the design of the open-ended cavity prototype designed 765 to operate at approximately 6 GHz. The main cavity wall was composed of 766 a single copper pipe. A mode-filtered version of this cavity was constructed 767 by . . . . .	208
768	6.16 Images depicting the measurement of the filtered and non-filtered open 769 cavities using the VNA. The coupling loop in the figure is shown in the 770 TE orientation. . . . .	209
771	6.17 HFSS simulation results for the as-built cavity with the coaxial terminators 772 removed. The $\text{TE}_{011}/\text{TM}_{111}$ frequency is approximately 5.78 GHz. . . . .	210
773	6.18 Measurements of the filtered and non-filtered prototype cavities acquired 774 with the VNA. . . . .	211

# **List of Tables**

775	4.1	A summary of the CNN model layers and parameters. The output of each 1D-Convolution and Fully Connected layer is passed through a LeakyReLU activation function and re-normalized using batch normalization before being passed to the next layer in the model. The output of the final Fully Connected layer in the model is left without activation so that the model outputs can be directly passed to the Binary Cross-entropy loss function used during training. The first layer in the network has two input channels for the real and imaginary components of the spectrum. . .	117
784	6.1	A table of the values of $p'_{nm}$ . . . . .	185
785	6.2	A table of the values of $p_{nm}$ . . . . .	186
786	6.3	A table of cavity design parameters used for HFSS simulations. . . . .	205
787	6.4	A table of parameters describing the cavity prototypes. Certain values such as the cavity length and the distance between dielectric spacers are approximate due to variation in the machining of the copper. In particular, the filtered cavity was constructed from conducting copper segments that varied in size from 1.50" to 1.85". . . . .	208

## <sup>792</sup> **Acknowledgments**

<sup>793</sup> First, thank you to my advisor, Luiz de Viveiros. During these past years I have been  
<sup>794</sup> deeply grateful for the freedom to pursue my own research paths, his patience and support  
<sup>795</sup> when, inevitably, things do not go right the first time, and the reminders to keep the big  
<sup>796</sup> picture in mind.

<sup>797</sup> Second, thank you to my friends in colleagues in the Project 8 Collaboration, who  
<sup>798</sup> have been a genuine pleasure to work with and have contributed in enumerable ways to  
<sup>799</sup> my dissertation and ability as a scientist. I am honored to have been a member of this  
<sup>800</sup> team.

<sup>801</sup> This material is based upon work supported by the U.S. Department of Energy Office  
<sup>802</sup> of Science, Office of Nuclear Physics under Early Career Award No. DE-SC0019088 to  
<sup>803</sup> Pennsylvania State University. The findings and conclusions of this dissertation do not  
<sup>804</sup> necessarily reflect the views of the U.S. Department of Energy Office of Science.

<sup>805</sup> **Dedication**

<sup>806</sup> To my parents, Chris and Doug, and my sister, Hannah. And to all those friends and  
<sup>807</sup> mentors who have shared this strange and beautiful thing called "life" with me.

808 **Chapter 1** |  
809 **Introduction**

810 **1.1 Summary**

811 Neutrinos are one of the fundamental particles in the standard model of particle physics  
812 and account for a significant fraction of the matter in the universe. Neutrinos are the  
813 most abundant fermions in the universe, but due to their weak interactions neutrinos  
814 seldom interact with other particles. Regardless, neutrinos play a unique role in the  
815 evolution of the early-universe, and a detailed understanding of the properties of the  
816 neutrino is key to understanding the universe at the cosmological scale as well as the  
817 smallest particle physics regime.

818 It was uncertain that neutrinos had nonzero mass until vacuum neutrino flavor  
819 oscillations were observed in the late 90's and early 00's. A simple relativistic argument  
820 as to why oscillations are evidence for neutrino masses is that oscillations imply neutrinos  
821 experience time, which means that they do not propagate at the speed of light, therefore  
822 the masses of the neutrinos must be non-zero. Current neutrino oscillation data supports  
823 that neutrino flavor states are actually a superposition of three separate neutrino states  
824 with well-defined masses. Measurements of neutrino oscillations that have taken place  
825 over the past couple of decades have measured the differences between neutrino mass  
826 eigenstates with increasing precision. However, oscillation measurements cannot tell  
827 us the mass scale of the neutrinos, which is required in order to measure the absolute  
828 neutrino masses.

829 The neutrino mass scale remains an unknown quantity in the standard model of  
830 particle physics. The value of the neutrino mass influences the evolution of the early  
831 universe and is likely relevant to the energy-scale of new physics responsible for the factor  
832 of  $10^{-6}$  difference between the neutrino and electron masses. A model-independent way  
833 to measure the neutrino mass is to measure the tritium beta-decay spectrum near its  
834 endpoint. Energy conservation requires that the neutrino mass carry away some kinetic

835 energy from the beta-decay electron in the form of its mass, which causes a distortion in  
836 the shape of the tritium beta-decay spectrum near the endpoint. The isotope tritium has  
837 many advantages for this measurement, and has been used by the KATRIN collaboration  
838 to perform the most sensitive direct neutrino mass measurement to date.

839 KATRIN represents the state-of-the-art in the current generation of neutrino mass  
840 direct measurement experiments with a projected neutrino mass sensitivity of  $m_\nu < 200$  meV.  
841 This sensitivity does not fully exhaust the allowed parameter space of neutrino  
842 masses under the normal and inverted neutrino mass ordering scenarios, which motivates  
843 the development of a next generation of neutrino mass measurement experiments.

844 The Project 8 collaboration is developing a next-generation neutrino mass experiment  
845 with a goal neutrino mass sensitivity of  $m_\nu < 40$  meV. This sensitivity is sufficient to  
846 exhaust the range of neutrino masses allowed under the inverted mass ordering regime.  
847 Project 8 intends to achieve its sensitivity goal utilizing two technologies that are novel  
848 to the space of direct neutrino mass measurements — atomic tritium and cyclotron  
849 radiation emission spectroscopy (CRES). Atomic tritium is required in order to avoid  
850 systematic broadening the tritium beta-decay spectrum caused by the final state of the  
851  $^3\text{He}^+ - \text{T}$  molecule, and the CRES technique enables a differential measurement of the  
852 tritium spectrum that is background-free and able to be directly integrated with the  
853 atomic tritium source.

854 The Project 8 collaboration is currently engaged in a research and development  
855 program intended to simultaneously develop the atomic tritium and CRES technologies  
856 so that they can be combined in a next-generation experiment. This past year (2022)  
857 Project 8 has used the CRES technique to measure the molecular tritium beta-decay  
858 spectrum and place an upper limit on the neutrino mass:  $m_\beta \leq 152$  eV. This measurement,  
859 while not competitive scientifically, represents the first proof-of-principle that the CRES  
860 technique can be used to measure the neutrino mass.

861 The future goals of the Project 8 collaboration are to develop the technologies  
862 and techniques necessary to scale-up the volume in which CRES measurements can  
863 be performed. Project 8's first neutrino mass measurement with CRES utilized a  
864 measurement volume on the cubic-centimeter scale, however, sensitivity calculations  
865 estimate that an experiment sensitive to neutrino masses of 40 meV will require several  
866 tens of cubic-meters of experiment volume filled with atomic tritium. Developing a new  
867 approach to performing CRES measurements that can be successfully scaled to these  
868 volumes is a necessary step towards Project 8's neutrino mass measurement goal, and is  
869 the primary topic of my dissertation research.

870 A parallel development is the technology necessary to produce, cool, trap, and  
871 recirculate a supply of atomic tritium that is compatible with CRES measurements. The  
872 atomic tritium system is equally important as the large-volume CRES measurement  
873 technology, but will not be discussed at depth here.

874 The Project 8 collaboration has identified two scalable approaches to neutrino mass  
875 measurement using the CRES technique. One approach is to use an array of antennas  
876 that surrounds a volume of trapped atomic tritium that can perform CRES measurements  
877 by collection the cyclotron radiation emitted by beta-decay electrons into free-space. The  
878 other approach uses a resonant cavity filled with atomic tritium to perform CRES by  
879 measuring the excitation of resonant cavity modes caused by the motion of electrons  
880 trapped inside the cavity volume.

881 The cavity and antenna approaches to CRES have been studied in detail over the past  
882 five years, and, while both approaches offer a physically viable path towards a 40 meV  
883 neutrino mass measurement, the collaboration has elected to pursue the cavity approach  
884 for the foreseeable future. The major advantage of the cavity approach is a significant  
885 reduction in the cost and complexity of the experiment design and data analysis, which  
886 provides a lower risk path to Project 8’s scientific goals.

887 In this dissertation I summarize my most impactful contributions to the research and  
888 development of antenna array and cavity CRES. In short these contributions are

- 889 • the development and analysis of signal reconstruction algorithms for antenna array  
890 CRES, which provide key inputs to sensitivity analyses of antenna array CRES  
891 experiments.
- 892 • The development of a specialized antenna, designed to synthesize fake CRES  
893 radiation, which enables bench-top testing and validation of the antenna array  
894 CRES technique.
- 895 • The development of an open-cavity design for CRES measurement, whose mode  
896 structure can be tuned using perturbations that modify the impedance of the cavity  
897 walls. The development of this cavity concept was one of many developments that  
898 eventually lead to the adoption of cavities as the CRES technology of choice for  
899 the future of Project 8.

## 900 1.2 Outline

901 The outline of this dissertation is as follows. In Chapter 2 I provide an introduction to  
902 the basic physics of neutrinos and beta-decay, which provides context for a discussion of  
903 various methods to measure the neutrino absolute mass scale.

904 Chapter 3 is an overview of the CRES technique and the Project 8 collaboration.  
905 Project 8's experimental program is organized into four phases. The first phase completed  
906 in 2015 before I began my dissertation work, so I begin by highlighting the Project 8's first  
907 measurement of the tritium beta-decay spectrum with CRES. Next, I discuss the planned  
908 research and development for an antenna array CRES experiment for the upcoming phase  
909 of Project 8's experimental program. I end Chapter 3 with a discussion of Project 8's  
910 pilot-scale and final phase experiments, that will combine a scalable CRES measurement  
911 technology with atomic tritium and measure the neutrino mass with 40 meV sensitivity.

912 Chapter 4 discusses the first of my contributions mentioned above, which is the  
913 development of signal reconstruction techniques for antenna array CRES and an antenna  
914 array demonstrator experiment called the FSCD. I discuss the key tools that Project 8  
915 uses to simulate antenna array CRES before introducing signal reconstruction algorithms  
916 that can be used to detect CRES signals using the array. I end Chapter 4 with a  
917 detailed analysis and comparison of the signal detection performance of each algorithm,  
918 as reported in a paper I have authored.

919 Chapter 5 describes my contributions to the development of antennas and an antenna  
920 measurement system for Project 8, which is the second major contribution of this  
921 dissertation. I begin with a general overview of basic principle of antennas and antenna  
922 measurements, and describe the development, as reported in another paper I have  
923 authored, of unique antenna designed to mimic the cyclotron radiation emitted by  
924 electrons in free-space. I call this antenna the synthetic cyclotron radiation antenna  
925 (SYNCA) and its main purpose is to serve as a fake electron for laboratory validation  
926 measurements of Project 8's antenna array CRES simulations. Chapter 5 ends with an  
927 overview of laboratory measurements of a prototype antenna array using the SYNCA,  
928 which were compared with simulations to provide upper bounds on reconstruction errors  
929 caused by imperfections in real-life measurements.

930 Chapter 6 discusses the cavity approach to CRES, which was adopted as the preferred  
931 CRES technology for Phase IV late into my dissertation work. The chapter starts by  
932 discussing resonant cavities in general before introducing the operating principles of the  
933 cavity approach to CRES. I end the chapter by discussing a study of and open-cavity

<sup>934</sup> design that could be used for CRES measurements and integrated with atomic tritium  
<sup>935</sup> and an electron gun calibration source for the pilot-scale and Phase IV experiments.

<sup>936</sup> Finally, in Chapter 7 I conclude by briefly discussing the future directions of Project  
<sup>937</sup> 8 as development proceeds towards a direct measurement of the neutrino mass.

938 **Chapter 2 |**

939 **Neutrinos and Neutrino Masses**

940 **2.1 Introduction**

941 In this chapter I provide a cursory overview of background information relevant to  
942 neutrinos and neutrino mass measurements.

943 In Section 2.2 I provide background information on the history of neutrinos and beta-  
944 decay. In Section 2.3 I describe the discovery of neutrino oscillations, which demonstrated  
945 unambiguously that neutrinos have non-zero masses. In Section 2.4 I discuss the current  
946 state of the theoretical understanding of neutrino masses in the standard model. Lastly,  
947 in Section 2.5 I discuss a few methods for measuring the absolute scale of the neutrino  
948 mass.

949 **2.2 Neutrinos and Beta-decay**

950 Late in the 19th century the phenomena of radioactivity was first observed in experiments  
951 performed by Henri Becquerel with uranium, and further studied using thorium and  
952 radium by Marie and Pierre Curie [5,6]. Early work in radioactivity classified different  
953 forms of radiation based on its ability to penetrate different materials. Rutherford was  
954 the first to separate radioactive emissions into two types, alpha and beta radiation [7].  
955 Alpha rays were easily stopped by a piece of paper or thin foil of metal, whereas beta  
956 radiation could penetrate metal several millimeters thick. Later a third form of radiation  
957 was identified by Villard [8], which was still more penetrating, later termed gamma  
958 radiation by Rutherford.

959 When these forms of radioactivity were first discovered, it was unclear what physically  
960 constituted an alpha, beta, or gamma particle. Experiments with radioactivity in magnetic  
961 fields were eventually able to identify the charge composition of the different forms of

radiation. In particular, experiments by Becquerel identified [9] that beta radiation had an identical charge-to-mass ratio to the electron. This was strongly suggestive that beta particles were indeed electrons.

Studies of beta radiation lead to the discovery that radioactivity resulted in the transmutation of elements [10] caused by the decay of a heavier nucleus to a lighter species. A decay that produces beta-radiation is called a beta-decay. One feature of beta radiation that differentiated it from alpha and gamma radiation is that the electrons produced by beta-decay have a continuous spectrum of kinetic energies, whereas, alpha and gamma particles are emitted with discrete energies. This feature of beta-decay was first observed by Chadwick in 1914 [11], and was extremely puzzling at the time, since the continuous spectrum apparently violates energy conservation [12].

Famously, in 1930 Pauli proposed the existence of a new neutral particle, which he termed the "neutron", that was also produced during beta-decay to resolve the missing energy problem posed by the beta-decay spectrum [13]. Because this particle carried no charge, it was hypothesized that it had simply not been observed in any previous experiments. This "neutron", which was initially estimated to have a mass no larger than that of an electron, was eventually renamed the "neutrino" by Fermi [14] after the discovery of the neutron by Chadwick in 1932 [15]. Later, in 1933, Fermi developed a quantum mechanical theory for beta-decay in which an electron and neutrino are produced by the decay of a neutron to a proton inside the radioactive nucleus [16].

Little more than a speculation when first introduced, indirect evidence for the existence of neutrinos was obtained in 1938 by the simultaneous observation of the electron and recoiling nucleus in cloud chambers by Crane and Halpern [17]. However, it wasn't until the Cowan-Reines experiment [18] in 1956 that direct evidence for the existence of neutrinos was observed through the observation of inverse beta-decays caused by neutrinos from a nuclear reactor interacting with protons contained in water molecules. The difficulty in detecting neutrinos is caused by their weak interactions with other particles. Later experiments revealed the existence of different types or flavors of neutrinos based on the nature of the leptons produced in neutrino charged-current interactions [19], but the existence of nonzero neutrino mass remained an open question that would take more than 40 years to resolve.

## 993 2.3 Neutrino Oscillations

994 One of the first clues that neutrino flavor transitions or neutrino oscillations were occurring  
 995 was the solar neutrino problem. The solar neutrino problem is a discrepancy between  
 996 the measured and predicted flux of  $\nu_e$  from the sun. The solar neutrino problem was  
 997 famously observed by Ray Davis Jr. and collaborators in the 1960s [20] at the Homestake  
 998 mine in South Dakota. In the early 2000s, the SNO experiment was able to resolve the  
 999 solar neutrino problem by identifying neutrino oscillations as the cause of the observed  
 1000 deficit [21]. Furthermore, measurements of the atmospheric flux of neutrinos by the  
 1001 Super-Kamiokande experiment and others revealed that fewer muon-type neutrinos  
 1002 survived passage through the earth than expected, providing strong evidence for neutrino  
 1003 oscillations for both flavors [22].

1004 Neutrino oscillations occur because the neutrino flavor eigenstates are distinct from  
 1005 the mass eigenstates [23]. The neutrino mass eigenstates represent physical particles in  
 1006 that they are solutions to the free-particle Hamiltonian; whereas, the neutrino flavor  
 1007 eigenstates correspond to the neutrino states that interact via the weak charged-current  
 1008 interaction. The neutrino flavor eigenstates are a linear superposition of the neutrino  
 1009 mass eigenstates

$$1004 \quad \nu_\ell = \sum_i U_{\ell i} \nu_i, \tag{2.1}$$

1010 where  $\ell = e, \mu, \tau$  and  $i = 1, 2, 3$ . The matrix elements  $U_{\ell i}$  are the elements of the  
 1011 Pontecorvo-Maki-Nakagawa-Sakata (PMNS) matrix that describes the mixing between  
 1012 the neutrino flavor and mass states.

1013 A standard parameterization [24] of the PMNS matrix is

$$1013 \quad U_{PMNS} = \begin{bmatrix} U_{e1} & U_{e2} & U_{e3} \\ U_{\mu 1} & U_{\mu 2} & U_{\mu 3} \\ U_{\tau 1} & U_{\tau 2} & U_{\tau 3} \end{bmatrix} = \begin{bmatrix} 1 & 0 & 0 \\ 0 & c_{23} & s_{23} \\ 0 & -s_{23} & c_{23} \end{bmatrix} \begin{bmatrix} c_{13} & 0 & s_{13}e^{-i\delta} \\ 0 & 1 & 0 \\ -s_{13}e^{i\delta} & 0 & c_{13} \end{bmatrix} \begin{bmatrix} c_{12} & s_{12} & 0 \\ -s_{12} & c_{12} & 0 \\ 0 & 0 & 1 \end{bmatrix} \times \begin{bmatrix} e^{i\alpha_1/2} & 0 & 0 \\ 0 & e^{i\alpha_2/2} & 0 \\ 0 & 0 & 1 \end{bmatrix}, \tag{2.2}$$

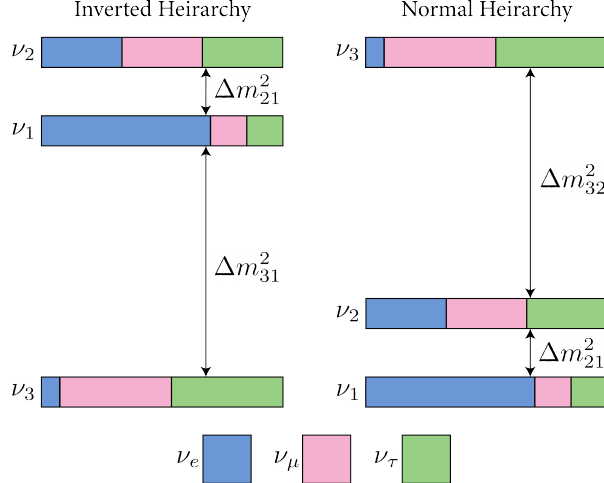


**Figure 2.1.** A diagram of two different neutrino mass ordering scenarios [1]. In the inverted hierarchy (inverted mass ordering) the lightest neutrino mass is  $m_3$ , whereas, in the normal hierarchy (normal mass ordering)  $m_1$  is the lightest neutrino. What cannot be measured by neutrino oscillations is the neutrino absolute mass scale, which is essentially the mass of the lightest neutrino mass eigenstate.

where  $c_{ij} = \cos \theta_{ij}$  and  $s_{ij} = \sin \theta_{ij}$ . The parameters  $\alpha_1$  and  $\alpha_2$  are only included in the PNMS matrix if neutrinos are Majorana particles, something which represents a current area of research in neutrino physics. The phase  $\delta$  quantifies the degree of CP-violation in the neutrino sector. Including the Majorana phases, the PMNS matrix contains six independent parameters. Neutrino oscillation probabilities also depend on the squared mass differences between neutrino mass eigenstates

$$\Delta m_{ij}^2 = m_i^2 - m_j^2, \quad (2.3)$$

where  $ij = 12, 32, 31$  respectively. Because  $\Delta m_{32}^2 = \Delta m_{31}^2 - \Delta m_{21}^2$ , this adds an additional two parameters that must be constrained by neutrino oscillations.

A large experimental effort over the past few decades has greatly constrained the majority of parameters in the PMNS matrix, many to relative uncertainties of only a few percent. However, certain ambiguities remain, which is the origin of the current uncertainty in the ordering of the neutrino masses (see Figure 2.1). Current neutrino oscillation data supports that  $m_2 > m_1$ ; however, the sign of  $\Delta m_{32}^2$  is still unknown. Therefore, two mass-ordering scenarios are allowed, one where neutrino masses are arranged  $m_3 > m_2 > m_1$ , which is called the normal mass ordering (NMO), or alternatively neutrino masses may be ordered  $m_2 > m_1 > m_3$ , which is called the inverted mass ordering (IMO). Next-generation neutrino oscillation experiments such as JUNO [25],

1031 Hyper-Kamiokande [26], and DUNE [27] are poised to resolve this ambiguity in the  
 1032 coming years.

1033 Neutrino oscillation probabilities are sensitive to the neutrino masses via the squared  
 1034 mass differences. Therefore, oscillation probabilities are unaffected by the absolute scale  
 1035 of the neutrino mass. However, oscillations can be used to obtain a lower bound on the  
 1036 neutrino masses by setting the mass of the lightest neutrino mass state to zero. This  
 1037 results in different lower limits depending on the ordering of the neutrino mass states.  
 1038 Current best-fit values [24] with  $1\sigma$ -uncertainties for the squared mass differences are

$$\Delta m_{21}^2 = (7.42^{+0.21}_{-0.20}) \times 10^{-5} \text{ eV}^2, \quad (2.4)$$

$$\Delta m_{31}^2 = (2.5176^{+0.026}_{-0.028}) \times 10^{-3} \text{ eV}^2 \text{ (NMO)}, \quad (2.5)$$

1039 for the normal mass ordering, and for the inverted ordering the limit is

$$\Delta m_{32}^2 = (-2.498^{+0.028}_{-0.028}) \times 10^{-3} \text{ eV}^2 \text{ (IMO).} \quad (2.6)$$

1040 The parameter  $\Delta m_{21}^2$  is the same in the NMO and the IMO. By allowing the lightest  
 1041 neutrino mass in each ordering scenario ( $m_{\text{least}}$ ) to take on a range of values, one can  
 1042 visualize the relative masses of the neutrinos as a function of  $m_{\text{least}}$  (see Figure 2.2). The  
 1043 absolute neutrino mass scale is effectively the value of this  $m_{\text{least}}$  parameter.

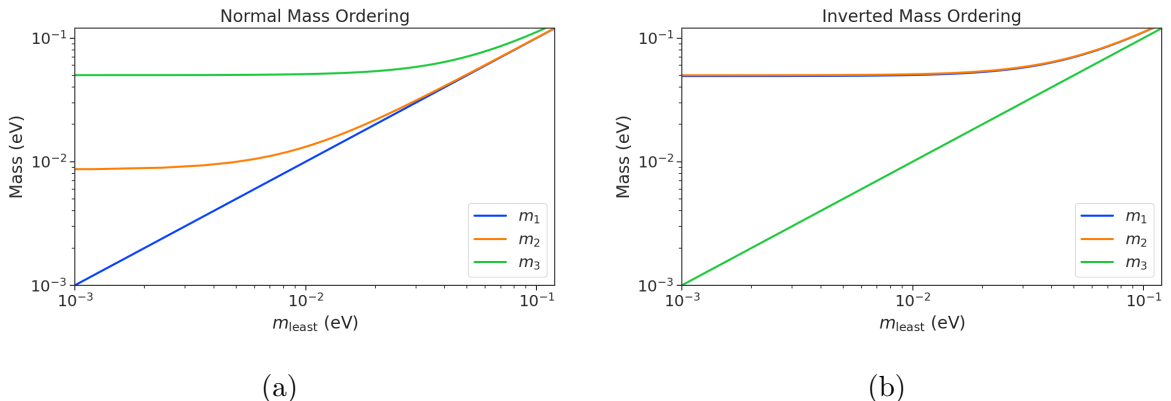


**Figure 2.2.** The masses of the neutrinos as a function of the lightest neutrino mass in both the normal (a) and inverted (b) mass ordering regimes.

## 2.4 Neutrino Masses in the Standard Model

In this section, I briefly summarize the current theoretical understanding of neutrino masses in the standard model [28–30]. Neutrinos are spin 1/2 particles, which are described using the Dirac equation.

$$(i\hbar\gamma^\mu\partial_\mu - mc)\psi(x) = 0, \quad (2.7)$$

where the field that describes the particle is denoted as  $\psi(x)$ . In the standard model fermions acquire mass through the Yukawa interaction, which add to the standard model Lagrangian terms of the form

$$\mathcal{L}_{\text{Yukawa}} = -Y_{ij}^\ell \bar{L}_{Li} \phi E_{Rj} + \text{h.c.}, \quad (2.8)$$

where  $Y_{ij}^\ell$  is an element of the  $3 \times 3$  Yukawa coupling matrix for leptons,  $L_{Li}$  is the left-handed lepton doublet for generation  $i$ ,  $\phi$  is the Higgs doublet, and  $E_{Rj}$  is the right-handed lepton field for generation  $j$ . Neutrinos are represented only as left-handed neutrinos and right-handed antineutrinos in the standard model, which is consistent with experimental observations. Since there are no right-handed neutrino singlet fields, there are no Yukawa interaction terms, thus neutrinos in the standard model are strictly massless. Therefore, non-zero neutrino mass is evidence for physics beyond the standard model.

For the charged leptons, the Yukawa interaction leads to masses of the form

$$m_{ij}^\ell = Y_{ij}^\ell \frac{v}{\sqrt{2}}, \quad (2.9)$$

where  $v$  is the Higgs vacuum expectation value. The observation of massive neutrinos motivates the extension of the standard model to explain the origin of neutrino masses, which can be approached in different ways, but all approaches add additional degrees of freedom to the standard model.

One approach is to introduce to the standard model a right-handed neutrino field that allows one to include Yukawa terms of the form

$$\mathcal{L}_{\nu \text{Yukawa}} = -Y_{ij}^\ell \bar{L}_{Li} \phi \nu_{Rj} + \text{h.c.} \quad (2.10)$$

where  $\nu_{Rj}$  is the right-handed neutrino singlet. Because experimental evidence strongly

1067 predicts only three active neutrinos, these additional neutrinos are "sterile", in that they  
1068 do not interact via the strong, weak, or electromagnetic interactions. After spontaneous  
1069 symmetry breaking, the Yukawa interaction leads to mass terms given by

$$\mathcal{L}_D = -M_{Dij}\bar{\nu}_{Ri}\nu_{Lj} + \text{h.c.}, \quad (2.11)$$

1070 which is called a Dirac mass term. One of the issues with constructing neutrino masses  
1071 in this way is that the required Yukawa couplings are at least a factor of  $10^6$  smaller than  
1072 that of an electron, which begs the question: why are the Yukawa couplings so small for  
1073 the neutrinos?

1074 An alternative approach is to allow the neutrinos to have a Majorana mass, which is  
1075 possible because neutrinos are electrically neutral particles. The Majorana mass terms  
1076 for neutrinos have the form

$$\mathcal{L}_M = -\frac{1}{2}(M_{Rij}\bar{\nu}_{Ri}\nu_{Rj}^c M_{Lij}\bar{\nu}_{Li}\nu_{Lj}^c) + \text{h.c.}, \quad (2.12)$$

1077 where  $M_{Rij}$  and  $M_{Lij}$  are right-handed and left-handed Majorana mass matrices. A  
1078 consequence of neutrinos being Majorana particles is lepton number violation, which  
1079 predicts the occurrence of neutrino-less double beta-decay at a rate proportional to the  
1080 neutrino mass.

1081 In the most general case neutrinos have both Dirac and Majorana mass terms, which  
1082 allows one to generate neutrino masses with Yukawa couplings similar to the rest of the  
1083 standard model. Considering a single generation of neutrinos for demonstration, the  
1084 combined neutrino mass Lagrangian can be written as

$$\mathcal{L}_{D+M} = -m_D\bar{\nu}_R\nu_L - \frac{1}{2}(m_L\bar{\nu}_L\nu_L^c + m_R\bar{\nu}_R\nu_R^c) + \text{h.c.}, \quad (2.13)$$

1085 or equivalently,

$$\mathcal{L}_{D+M} = -\frac{1}{2} \begin{bmatrix} \bar{\nu}_L & \bar{\nu}_R^c \end{bmatrix} \begin{bmatrix} m_L & m_D \\ m_D & m_R \end{bmatrix} \begin{bmatrix} \nu_L^c \\ \nu_R \end{bmatrix} + \text{h.c..} \quad (2.14)$$

1086 An example mass generation mechanism with this approach is the Type-I see-saw  
1087 mechanism [31], in which one takes  $m_L = 0$  and  $m_R \gg m_D$ . By diagonalizing Equation  
1088 2.14 one obtains the mass eigenvalues that represent the physical masses of the neutrinos.  
1089 The light neutrino mass eigenstate, which represents the observed neutrino mass, has a  
1090 mass given by

$$m_1 \approx \frac{m_D^2}{m_R}, \quad (2.15)$$

1091 and the heavy neutrino mass eigenstate, which represents the unobserved sterile neutrino,  
1092 has a mass

$$m_2 \approx m_R. \quad (2.16)$$

1093 For  $m_D$  similar to the other quark or lepton masses, one obtains physical neutrino masses  
1094 consistent with observations from sterile neutrino masses of  $m_R \approx O(10^{15})$  GeV. This  
1095 mass scale is well beyond the capabilities of modern particle accelerators to probe.

## 1096 2.5 Neutrino Absolute Mass Scale

1097 The neutrino absolute mass scale or simply "neutrino mass" cannot be probed with  
1098 neutrino oscillations, since oscillation probabilities are determined by the squared mass  
1099 differences between neutrino mass eigenstates, therefore, alternative techniques are needed  
1100 to perform an effective measurement of the neutrino mass.

### 1101 2.5.1 Limits from Cosmology

1102 The  $\Lambda$ CDM model summarizes the current cosmological understanding of the universe [24].  
1103  $\Lambda$ CDM predicts that the universe originated from a single expansion event colloquially  
1104 called the "Big Bang". During the Big Bang, the universe originated as a hot spacetime  
1105 singularity, which abruptly experienced rapid expansion in a process known as inflation.  
1106 After expansion the inflationary field eventually decayed into a population of quarks,  
1107 gluons, leptons, and photons, which were kept in thermal equilibrium by the high-  
1108 temperatures of the early universe.

1109 As the universe continued to expand its density and temperature decreased until  
1110 the formation of neutral atoms, primarily hydrogen, was possible. At which point the  
1111 population of photons produced during the Big Bang decoupled from the primordial  
1112 universe and began to freely propagate. A direct prediction of the  $\Lambda$ CDM model is that  
1113 this population of photons is still present, but with a significantly reduced temperature  
1114 due to the subsequent expansion of the universe. This is consistent with the observation of  
1115 the CMB (cosmic microwave background), which is a population of microwave radiation  
1116 with a blackbody temperature of 2.7 K. The CMB is extremely uniform in all directions  
1117 with slight anisotropies that can be analyzed to study the evolution of the early universe.  
1118 A series of experiments have measured the CMB with increasing levels of precision, which  
1119 has lead to a significant increase in our current understanding of cosmology.

1120 In addition to the CMB, inflation predicts the existence of a  $C\nu B$  (cosmic neutrino

background) [32], which are the remnant neutrinos produced during the Big Bang. Since neutrinos only interact via the weak force, they decouple from the Big Bang plasma at an earlier time than the CMB photons. The temperature at which the C $\nu$ B decouples depends on the neutrino rest mass. Neutrinos play a unique role in the  $\Lambda$ CDM model, due to the fact that neutrinos act as radiation early in the universe but as matter in the late universe. This leads to specific signatures that impact the expected anisotropies of the CMB as well as the distribution of matter in the universe [33]. By combining measurements of the CMB with measurements of the large-scale structure (LSS) of the universe one can constrain the neutrino mass scale by fitting these datasets with the  $\Lambda$ CDM model. This analysis results in some of the most stringent constraints on the neutrino mass. Recent analyses [24] have been able to constrain the neutrino mass scale to

$$\Sigma_{m_\nu} \equiv \sum_i m_i < 0.11 \text{ eV}, \quad (2.17)$$

where  $m_i$  are the neutrino mass eigenstates.

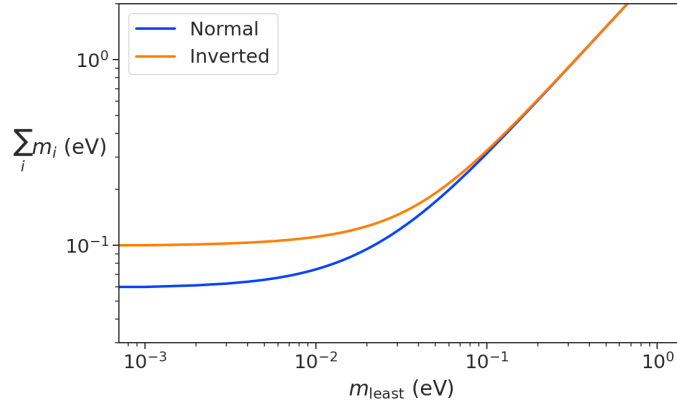


**Figure 2.3.** The neutrino mass observable measured by cosmology as a function of the lightest neutrino mass eigenstate.

The observable  $\Sigma_{m_\nu}$  constrains the neutrino mass by setting the mass of the lightest neutrino mass eigenstate ( $m_{\text{least}}$ ) (see Figure 2.3). In the normal mass ordering  $\Sigma_{m_\nu}$  can be rewritten in the form

$$\Sigma_{m_\nu} = m_{\text{least}} + \sqrt{\Delta m_{21}^2 + m_{\text{least}}^2} + \sqrt{\Delta m_{32}^2 + m_{\text{least}}^2}, \quad (2.18)$$

where it is clear that a measurement of  $\Sigma_{m_\nu}$  effectively sets the neutrino mass scale

1138 through  $m_{\text{least}}$ . The analogous formula for the inverted mass ordering is

$$\Sigma_{m_\nu} = m_{\text{least}} + \sqrt{-\Delta m_{32}^2 + m_{\text{least}}^2} + \sqrt{-\Delta m_{31}^2 + m_{\text{least}}^2}. \quad (2.19)$$

1139 Upcoming experiments [34] are planned to refine measurements of the CMB, LSS,  
 1140 and other cosmological observables. With this additional data it is possible that in the  
 1141 near future cosmological measurements will be able to positively constrain the neutrino  
 1142 absolute mass scale. However, the strength of these limits strictly depend on the accuracy  
 1143 of the  $\Lambda$ CDM model, which highlights the need for direct experimental measurements of  
 1144 the neutrino mass to confirm the predictions of cosmology and to fix the neutrino mass  
 1145 parameter in future cosmological analyses.

### 1146 2.5.2 Limits from Neutrinoless Double Beta-decay Searches

1147 If neutrinos are Majorana fermions, then the neutrino is equivalent to its own antiparticle  
 1148 and lepton conservation is not an exact law of nature [35]. Limits on the rate of  
 1149 neutrinoless double beta-decay ( $0\nu\beta\beta$ ), are some of the most powerful current tests of  
 1150 lepton number conservation [24]. If  $0\nu\beta\beta$  were observed, it would be direct evidence that  
 1151 neutrinos are Majorana fermions and provide a method for measuring the neutrino mass  
 1152 scale.

1153 Standard double beta-decay occurs when two neutrons in an unstable nucleus spon-  
 1154 taneously decay into two protons, which results in the production of two electrons and  
 two neutrinos (see Figure 2.4). Whereas, during  $0\nu\beta\beta$  the two neutrinos self-annihilate

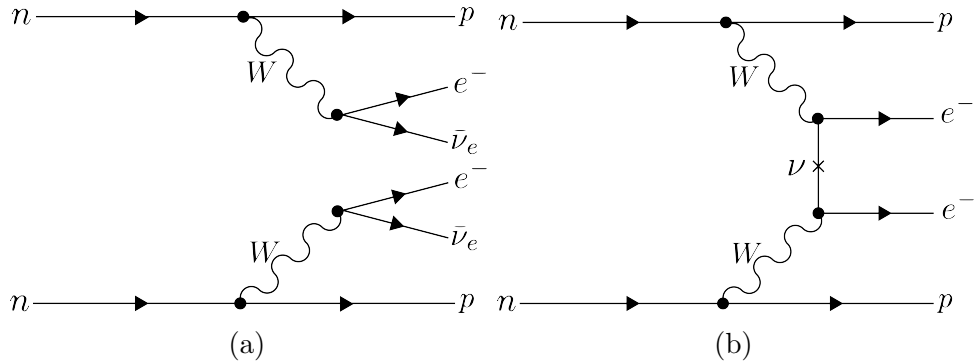


**Figure 2.4.** Feynman diagrams for double beta-decay (a) and  $0\nu\beta\beta$ (b).

1155  
 1156 producing only two electrons, which violates lepton number by two.

1157 Assuming that the exchange of two Majorana neutrinos is the dominant channel for  
 1158  $0\nu\beta\beta$ , then a measurement of the  $0\nu\beta\beta$  half-life for a particular isotope can be used to

1159 set the neutrino absolute mass scale [36]. The half-life is written in terms of the effective  
 1160 neutrino mass for  $0\nu\beta\beta$  ( $m_{\beta\beta}$ ) using the equation

$$T_{1/2}^{0\nu} = \frac{1}{G|\mathcal{M}|^2 m_{\beta\beta}^2}, \quad (2.20)$$

1161 where  $G$  is the phase-space factor for the decay and  $\mathcal{M}$  is the relevant nuclear matrix  
 1162 element.  $m_{\beta\beta}$  is given by an incoherent sum of the neutrino mass eigenstates weighted  
 1163 by the PMNS mixing matrix parameters,

$$m_{\beta\beta} = \left| \sum_i U_{ei}^2 m_i \right|. \quad (2.21)$$

1164 The information provided from  $0\nu\beta\beta$  on the neutrino mass scale can be visualized by  
 1165 expressing the value of  $m_{\beta\beta}$  in terms of  $m_{\text{least}}$  and two relative Majorana phases [2]. The  
 1166 allowed regions for  $m_{\beta\beta}$  as a function of  $m_{\text{least}}$  are shown in Figure 2.5 as the regions  
 1167 bounded by the black curves overlayed with the discovery probabilities of future  $0\nu\beta\beta$   
 decay experiments based on current neutrino data.

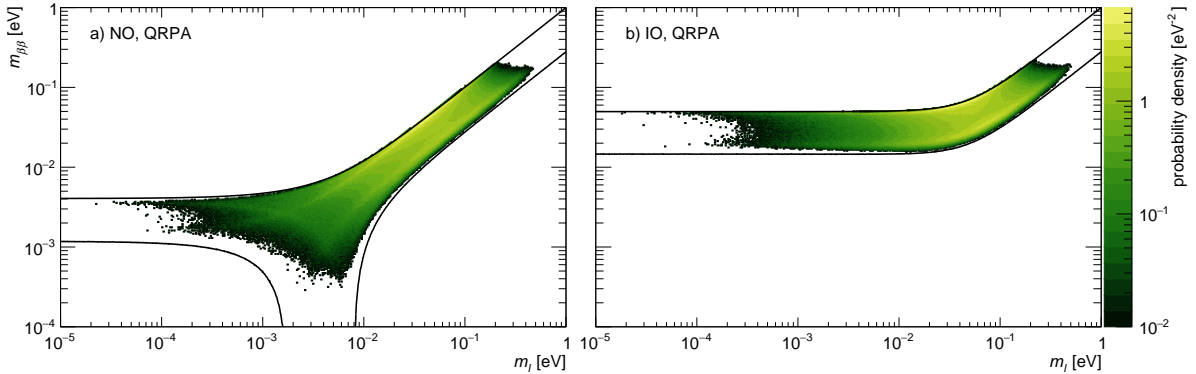


**Figure 2.5.** The discovery probabilities for the future generation of  $0\nu\beta\beta$  experiments as a function of  $m_{\beta\beta}$  and  $m_{\text{least}}$ . Figure from [2].

1168  
 1169 Because of the possibility of cancellation due to the unknown Majorana phases included  
 1170 in the sum specified by Equation 2.21, the neutrino mass information gained from  $0\nu\beta\beta$   
 1171 is necessarily imperfect. Additionally, theoretical uncertainties in the calculation of the  
 1172 nuclear matrix elements complicates the calculation of  $m_{\beta\beta}$  from a measurement of  $0\nu\beta\beta$   
 1173 half-life. Similar to cosmology, there is a high degree of complementarity between direct  
 1174 measurements of the neutrino mass and  $0\nu\beta\beta$ . In particular, a measurement of  $m_{\text{least}}$  to  
 1175 less than 0.1 eV sensitivity provides significant information for  $0\nu\beta\beta$  searches based on  
 1176 the discovery probabilities displayed in Figure 2.5.

### 2.5.3 Limits from Beta-decay

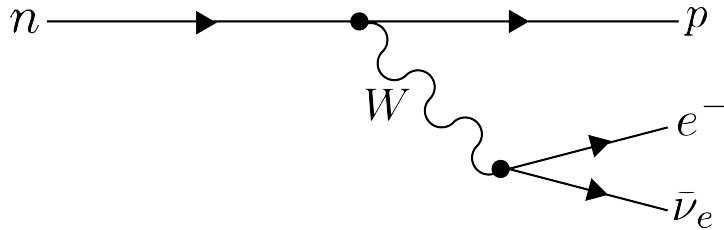


**Figure 2.6.** A Feynman diagram of beta decay

Certain processes involving neutrinos, in particular beta-decay (see Figure 2.6), have initial states with well-defined total energies and final states that can be measured with high accuracy and precision. Beta-decay involves the decay of an unstable isotope where a neutron spontaneously converts to a proton and emits an electron and anti-neutrino ("neutrino" for brevity) to conserve charge and lepton number [5]. Therefore, by applying the principles of energy and momentum conservation, a measurement of the kinematics of the final state can be used to constrain the neutrino mass [37].

Using beta-decay to measure the neutrino mass can be tied back to Fermi's original 1934 theory of nuclear beta-decay [16] (see Figure 2.7). Because the constraints on the

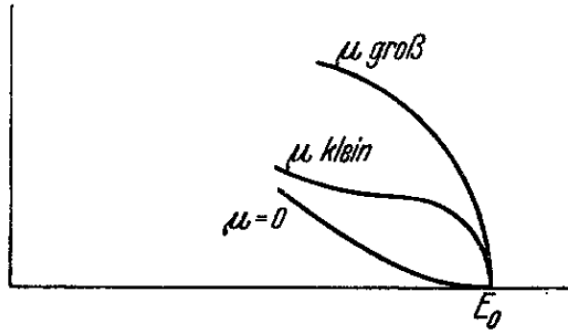


**Figure 2.7.** A figure from Fermi's 1934 paper on a theory of beta-decay depicting the kinetic energy spectrum of the emitted electron. The effect of the neutrino mass, written as  $\mu$ , is to distort the shape of the spectrum near the endpoint from the zero-mass spectrum.

neutrino mass from beta-decay depend only on the final state measurement capabilities and the principles of energy and momentum conservation, neutrino mass measurements with beta-decay are called direct measurements. A direct measurement like beta-decay contrasts with other neutrino mass measurements approaches that are model-dependent such as cosmology and  $0\nu\beta\beta$ , which provide complementary ways to study the physics of massive neutrinos.

1193     The isotope of choice for direct neutrino mass measurements with beta-decay has  
 1194     been tritium ( ${}^3H_2$ ) for many decades, because it conveniently fulfills many experimental  
 1195     requirements. Of upmost importance is a decay with a low Q-value, which is the available  
 1196     kinetic energy based on the mass difference between the initial and final states. The  
 1197     effect of a massive neutrino on the shape of the spectrum is magnified for low Q-values  
 1198     and tritium has an unusually low Q-value of 18.6 keV.

1199     Additionally, tritium beta-decay is super-allowed, which results in a relatively short  
 1200     half-life of 12.3 years. Therefore, high source activity can be obtained with a relatively  
 1201     small source mass. High-activity is desirable because of the low decay probability near  
 1202     the tritium spectrum endpoint. For tritium beta-decays, only a factor of  $3 \times 10^{-13}$  of the  
 1203     decays occur in the last 1 eV of the spectrum. Isotopes with Q-values lower than tritium  
 1204     are known [37], but this advantage is outweighed by exceedingly long half-lives leading  
 1205     to required source masses that are unobtainable.

1206     The endpoint measurement approach involves quantifying the effect of the neutrino's  
 1207     mass on shape of the electron's kinetic energy spectrum near the endpoint. The shape of  
 1208     the kinetic energy spectrum (see Figure 2.8) is given by

$$\frac{d\Gamma}{dE} = \frac{G_F^2 |V_{ud}|^2}{2\pi^3} (G_V^2 + 3G_A^2) F(Z, \beta) \beta (E + m_e)^2 (E_0 - E) \\ \times \sum_{i=1,2,3} |U_{ei}|^2 [(E_0 - E)^2 - m_i^2]^{1/2} \Theta(E_0 - E - m_i), \quad (2.22)$$

1209     where  $G_F$  is the Fermi coupling constant,  $V_{ud}$  is an element of the CKM matrix,  $E$   
 1210     is the kinetic energy of the electron,  $\beta$  is the velocity of the electron divided by the  
 1211     speed of light,  $E_0$  is the endpoint energy assuming zero neutrino mass,  $F(Z, \beta)$  is the  
 1212     Fermi function, and  $\Theta(E_0 - E - m_i)$  is the Heaviside function, which enforces energy  
 1213     conservation. One can see that the decay spectrum is actually a combination of three  
 1214     spectra with different endpoints based on the values of the neutrino mass eigenstates,  $m_i$ .  
 1215     This produces "kinks" in the spectrum shape due to overlapping spectra with different  
 1216     endpoint values, but such an effect would be nearly impossible to resolve given the finite  
 1217     energy resolution of a real experiment.

1218     The neutrino mass scale variable measured by beta-decay is given by

$$m_\beta^2 = \sum_i |U_{ei}|^2 m_i^2, \quad (2.23)$$

1219     where  $m_\beta$  is the electron-weighted neutrino mass or simply "neutrino mass" for brevity.

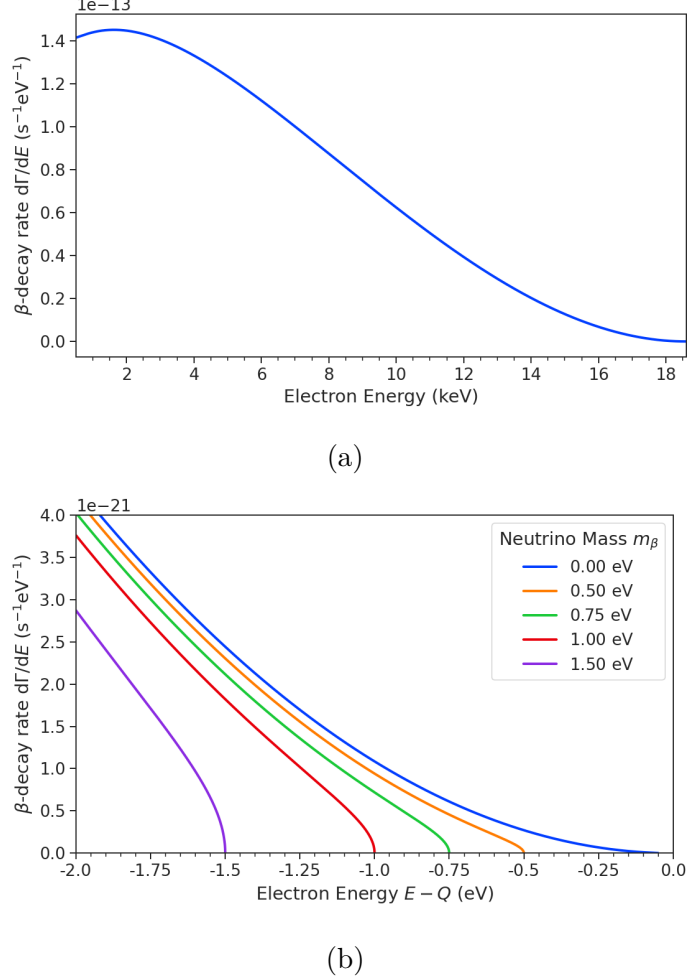


**Figure 2.8.** The tritium beta-decay spectrum. The effect of a massive neutrino on the spectrum is to change its shape near the endpoint by an amount proportional to the size of the neutrino mass. A sufficiently high-statistic and high-resolution measurement of the spectrum endpoint would be able to measure the neutrino mass.

1220 The quantity  $m_\beta$  corresponds to a particular weighted sum of the neutrino masses, which  
 1221 is distinct from effective neutrino masses such as  $m_{\beta\beta}$  [37]. Assuming unitarity, the  
 1222 neutrino mass can be expressed in terms of the PMNS matrix elements, squared mass  
 1223 differences, and the lightest neutrino mass eigenstate. For the normal mass ordering the  
 1224 equation is

$$m_\beta^2 = m_{\text{least}}^2 + |U_{e2}|^2 \Delta m_{21}^2 + |U_{e3}|^2 \Delta m_{31}^2, \quad (2.24)$$

1225 and for the inverted ordering the equation is

$$m_\beta^2 = m_{\text{least}}^2 + |U_{e1}|^2 (-\Delta m_{32}^2 - \Delta m_{21}^2) + |U_{e2}|^2 (-\Delta m_{32}^2). \quad (2.25)$$

1226 Therefore, a measurement of the neutrino mass in combination with neutrino mixing  
1227 parameters is effectively a measurement of  $m_{\text{least}}$ .

1228 Since the neutrino mass is small ( $< 1$  eV), its effect on the spectrum is limited to the  
1229 endpoint region. The affect of a non-zero neutrino mass on the endpoint spectrum is  
1230 plotted for the reader in Figure 2.8. Resolving the small changes in the spectrum shape  
1231 requires an experimental technique with high statistics, excellent energy resolution, and  
1232 low background activity.

1233 **Chapter 3 |**

1234 **Direct Measurement of the Neutrino Mass**

1235 **with Project 8**

1236 **3.1 Introduction**

1237 A promising technique for direct measurements of the neutrino mass beyond the projected  
1238 200 meV limit of the KATRIN experiment [38] is tritium beta-decay spectroscopy with  
1239 an atomic tritium source [39]. Atomic tritium, combined with a large-volume, high-  
1240 resolution energy measurement technique, is capable of measuring the neutrino mass  
1241 with sensitivity below the 50 meV, which exhausts the range of neutrino masses allowed  
1242 under the inverted hierarchy.

1243 Cyclotron Radiation Emission Spectroscopy (CRES) is a high-resolution energy  
1244 measurement technique compatible with atomic tritium production and storage that can  
1245 enable the next-generation of neutrino mass direct measurement experiments [40]. The  
1246 Project 8 collaboration is currently engaged in a program of research and development  
1247 (R&D) aimed at developing the technology necessary for a measurement of the neutrino  
1248 mass using CRES and atomic tritium with a sensitivity of 40 meV [41].

1249 In Section 3.2 I provide an introduction to the basics of the CRES technique as well as  
1250 the goals of the Project 8 experiment. Additionally, I sketch out the phased experiment  
1251 development plan being implemented by Project 8 to build towards a next-generation  
1252 neutrino mass experiment.

1253 In Section 3.3 I give an overview of Phase II of the Project 8 experiment [42,43], which  
1254 completed early in 2023. Although the bulk of the work presented in this dissertation is  
1255 relevant to designs of future Project 8 experiments, a description of the work in Phase II  
1256 provides useful context.

1257 In Section 3.4 I introduce a CRES measurement concept based on antenna arrays [44],  
1258 which could be the basis for the ultimate Project 8 neutrino mass experiment. A

1259 significant portion of the R&D efforts of Project 8 in Phase III were directed towards  
1260 simulating and modeling this experimental concept in order to understand the achievable  
1261 sensitivity to the neutrino mass.

1262 Lastly, in Section 3.5 I introduce conceptual designs of pilot-scale experiments and  
1263 Phase IV that combine atomic CRES with a large-volume CRES detection technique.  
1264 This includes a design concept for an antenna array based experiment, but also a design  
1265 for a resonant cavity based experiment. Resonant cavities are discussed in more depth in  
1266 Chapter 6 and have become the default choice for the Phase IV experiment.

## 1267 **3.2 Project 8 and Cyclotron Radiation Emission Spectroscopy**

### 1268 **3.2.1 Cyclotron Radiation Emission Spectroscopy — CRES**

1270 Time and frequency are two of the most precisely measured quantities in physics. Atomic  
1271 clocks, which operate by measuring the frequencies of various atomic transitions, have  
1272 been used to measure time with astounding relative uncertainties of  $10^{-18}$  seconds [45].  
1273 The extreme precision possible with frequency measurements is often summarized using  
1274 the famous quote from the Physicist Arthur Schawlow who said advise his students to  
1275 "Never measure anything but frequency!" [46].

1276 Neutrino mass measurements using tritium beta-decay require the measurement  
1277 of perturbations to the 18.6-keV tritium endpoint with a precision as small as 0.1 eV.  
1278 Therefore, a spectroscopic technique with extremely high resolution is required. Frequency  
1279 measurements are capable of such high-resolutions for the intuitive reason that they are  
1280 essentially digital counting measurements, which average the number of oscillations of a  
1281 physical system over time. By observing a rapidly oscillating system over a sufficient  
1282 length of time one can obtain essentially arbitrary precision on a frequency limited only  
1283 by the measurement time and signal-to-noise ratio (SNR) of the system.

1284 A method is required for translating a kinetic energy measurement into a frequency  
1285 measurement. A straightforward way to accomplish this is to place a gaseous supply of  
1286 tritium into a magnetic field; therefore, when a beta-decay occurs the resulting electron  
1287 will immediately begin to orbit around a magnetic field line at the cyclotron frequency,  
1288 proportional to its kinetic energy (see Figure 3.1). The acceleration caused by the orbit  
1289 leads to the emission of cyclotron radiation that can be detected using an array of  
1290 antennas or resonant cavity. The starting frequency of the radiation gives the electron's

1291 initial kinetic energy, which is used to build the beta-decay spectrum and measure  
 1292 the neutrino mass. The name for this measurement technique is Cyclotron Radiation  
 1293 Emission Spectroscopy or CRES [40].

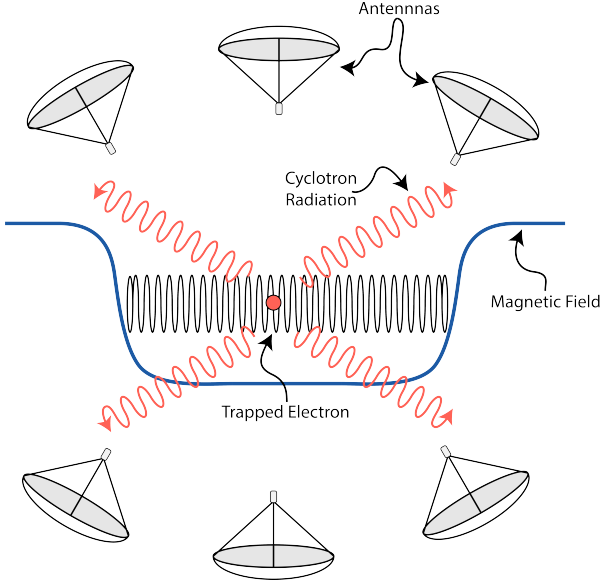


**Figure 3.1.** A cartoon illustration of the CRES technique. An electron is contained in a magnetic trap, which is a local minimum in the magnetic field, so that its cyclotron radiation can be detected by an array of antennas. Detecting the cyclotron radiation allows one to measure its cyclotron frequency and determine its kinetic energy.

1294 In the non-relativistic case, the cyclotron frequency is simply a function of the  
 1295 charge-to-mass ratio of the particle; however, the relativistic correction to the cyclotron  
 1296 frequency

$$f_c = \frac{qB}{2\pi m_e \gamma} = \frac{1}{2\pi} \frac{qB}{m_e + E_{\text{kin}}/c^2}, \quad (3.1)$$

1297 introduces a dependence of the kinetic energy ( $E_{\text{kin}}$ ) to the inverse of the cyclotron  
 1298 frequency ( $f_c$ ). Electrons with kinetic energies of 18.6 keV are in the weakly relativistic  
 1299 regime with  $\beta = \frac{v}{c} = 0.263$  and  $\gamma = 1.036$ .

1300 The frequency resolution of a CRES measurement can be estimated by differentiating  
 1301 Equation 3.1,

$$\frac{df_c}{dE_{\text{kin}}} = \frac{1}{2\pi} \frac{-qBc^2}{(m_e c^2 + E_{\text{kin}})^2}, \quad (3.2)$$

1302 from which one obtains the relationship between fractional differences in energy and  
 1303 frequency,

$$\frac{df_c}{f_c} = \frac{1 - \gamma}{\gamma} \frac{dE_{\text{kin}}}{E_{\text{kin}}}. \quad (3.3)$$

1304 Therefore, an energy precision of 1 eV for an 18.6 keV electron can be achieved with a  
 1305 frequency precision of approximately 2 ppm.

1306 The minimum observation time required to achieve this resolution can be estimated  
 1307 using the uncertainty principle as formulated by Gabor [47]. Electrons from tritium  
 1308 beta-decay experience random collisions with the background gas particles, which limits  
 1309 the uninterrupted radiation lifetime. The time between collision events, referred to as  
 1310 "track length", is an exponentially distributed variable. Differences in the track lengths  
 1311 of a population of mono-energetic electrons leads to an uncertainty or broadening in the  
 1312 distribution of measured frequencies, which is proportional to the mean track length,  $\tau_\lambda$ .  
 1313 The resulting frequency distribution has a Lorentzian profile, whose width is given by  
 1314 the Gabor limit,

$$\tau_\lambda \Delta f_c = \frac{1}{2\pi} \implies \Delta f_c = \frac{1}{2\pi\tau_\lambda}. \quad (3.4)$$

1315 The cyclotron frequency for a 18.6-keV electron in a 1 T field is approximately 27 GHz,  
 1316 consequently, the minimum observation time for a frequency resolution of 2 ppm is  
 1317 approximately 3  $\mu$ sec.

1318 Strictly speaking, the Gabor limit is not the true lower bound on the frequency  
 1319 resolution for a CRES signal, since it derives from the Fourier representation of a fixed  
 1320 length time-series using a basis of infinite duration sinusoids. If one takes the approach of  
 1321 fitting the CRES signal in the time-domain, then the lower limit on frequency precision  
 1322 is given by the Cramér-Rao lower bound (CRLB) [48], which depends on the track length  
 1323 and SNR. The CRLB is the minimum variance achievable by an unbiased estimator for  
 1324 an unknown but deterministic parameter, and, in general, the CRLB allows for better  
 1325 precision on the cyclotron frequency.

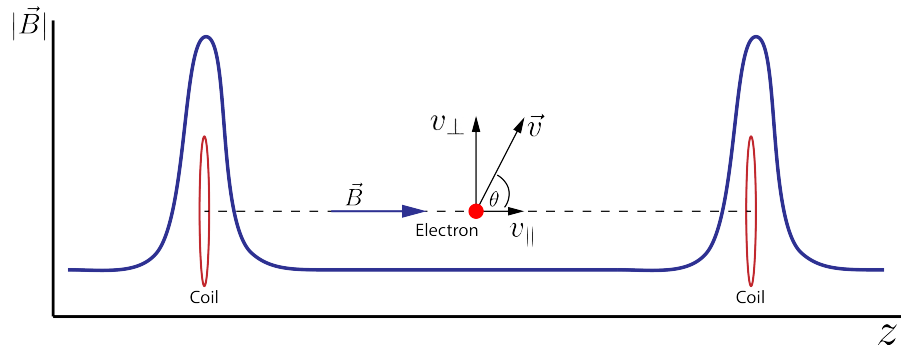


**Figure 3.2.** An illustration of an electron in a bathtub magnetic trap generated by two well-separated coils.

1326 Ensuring that an electron remains under observation long enough so that its frequency

1327 can be precisely measured requires a magnetic trap. A magnetic trap is a local minimum  
1328 in a background magnetic field generated an appropriate configuration of electromagnetic  
1329 coils. Since magnetic fields can do no work, there is no danger of the magnetic trap  
1330 affecting the kinetic energy of the electron after it is emitted from the beta-decay. One  
1331 common approach to creating a magnetic trap is the "bathtub" trap configuration, which  
1332 can be produced using two magnetic pinch coils aligned on a central axis that are  
1333 separated by a distance that is large compared to the coil radius (see Figure 3.2). This  
1334 configuration produces a trap with a uniform bottom and relatively steep walls, which is  
1335 ideal for CRES measurements.

1336 The electron's pitch angle is a useful parameter for describing its motion in the  
1337 magnetic trap. Pitch angle is defined in terms of the ratio between the component of the  
1338 electron's velocity perpendicular to the magnetic field and the component parallel to the  
1339 magnetic field

$$\tan \theta_p = \frac{v_{\perp}}{v_{\parallel}}. \quad (3.5)$$

1340 Electrons with pitch angles less than  $90^\circ$  oscillate back and forth in the magnetic trap,  
1341 which leads to variations in the cyclotron frequency caused by the changing value of  
1342 the magnetic field along the electron's path. This leads to frequency modulation that  
1343 produces sidebands in the cyclotron radiation spectrum. Resolving these sideband  
1344 frequency components is necessary for a complete reconstruction of the CRES signal in  
1345 the experiment.

1346 Electrons trapped in a cylindrically symmetric trap have three primary components of  
1347 motion (see Figure 3.3). The dominant component, typically with the highest frequency,  
1348 is the electron's cyclotron orbit, which encodes information on the electron's kinetic  
1349 energy. Axial motion from the electron's pitch angle leads to frequency modulation,  
1350 and a shift in the average magnetic field experienced by an electron. This leads to a  
1351 correlation between the kinetic energy of the electron and the pitch angle depending on  
1352 the particular shape of the magnetic trap, which can negatively impact energy resolution.  
1353 Generally, more variation in the magnetic field along the electron's trajectory leads to  
1354 a worse energy resolution. The magnetic trap can be engineered to have a flat bottom  
1355 with very steep walls to mitigate this effect. A bathtub trap design, where the distance  
1356 between the coils is much greater than the coil radius, is the trap that best approximates  
1357 this ideal design. Radial gradients in the trap leads to a third component of motion

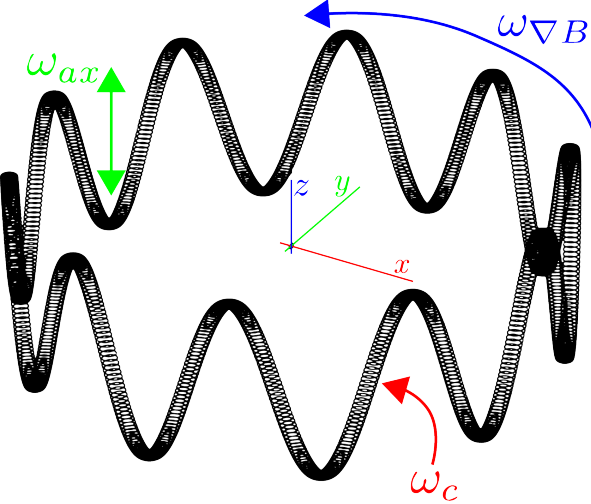


**Figure 3.3.** A plot of the main components of an electron's trajectory in a cylindrically symmetric trap.

1358 called grad-B drift [49]. The equation for the drift velocity is

$$\mathbf{v}_{\nabla B} = \frac{m_e v_{\perp}^2}{2qB} \frac{\mathbf{B} \times \nabla B}{B^2}. \quad (3.6)$$

1359 The total power of the radiation emitted by an electron in a free-space environment  
 1360 is given by the Larmor equation [50]

$$P(\gamma, \theta_p) = \frac{1}{4\pi\epsilon_0} \frac{2}{3} \frac{q^2 \omega_c^2}{c} (\gamma^2 - 1) \sin^2 \theta_p, \quad (3.7)$$

1361 where  $\omega_c$  is the cyclotron frequency multiplied by  $2\pi$  and  $\theta_p$  is the pitch angle to distinguish  
 1362 it from the spherical angle coordinate. A single electron with a  $90^\circ$  pitch angle and  
 1363 18.6 keV of kinetic energy in a 1 T magnetic field emits a total radiation power of 1.2 fW.  
 1364 Furthermore, one is typically only able to receive a fraction of this total power with an  
 1365 antenna or other detection system. Therefore, RF (radio-frequency) systems in CRES  
 1366 experiments must be operated at cryogenic temperatures to limit the noise power such  
 1367 that adequate SNR can be achieved for signal detection and reconstruction. Alternatively,  
 1368 longer tracks enable detection of weaker signals due to the increase in the total signal  
 1369 energy available for the detection algorithm.

### **1370 3.2.2 Project 8**

1371 The Project 8 collaboration<sup>1</sup> is a group of institutions in the United States and Germany  
1372 building an experiment to measure the neutrino mass by developing a novel spectrometer  
1373 technology based on CRES. In the ultimate Project 8 experiment, the CRES technique  
1374 will be used to measure the beta-decay spectrum using a large source of atomic tritium  
1375 sufficient to achieve the required statistics in the last  $O(10)$  eV of the decay spectrum.  
1376 Project 8 is targeting a neutrino mass sensitivity below 50 meV [51], which exhausts the  
1377 range of possible neutrino masses under the inverted hierarchy and is a factor of four less  
1378 than sensitivity projections for the ongoing KATRIN experiment.

1379 Project 8's proposed experiment requires the development of two novel technologies:  
1380 the production and trapping of a source of atomic tritium on cubic-meter scales and  
1381 technology to enable CRES measurements of individual electrons in the same volume.

#### **1382 Atomic Tritium**

1383 Previous measurements of the tritium beta-decay spectrum for neutrino mass measure-  
1384 ments have relied on sources of molecular tritium for their measurements [38, 52, 53] due  
1385 to the technical challenges associated with the production and storage of atomic tritium.

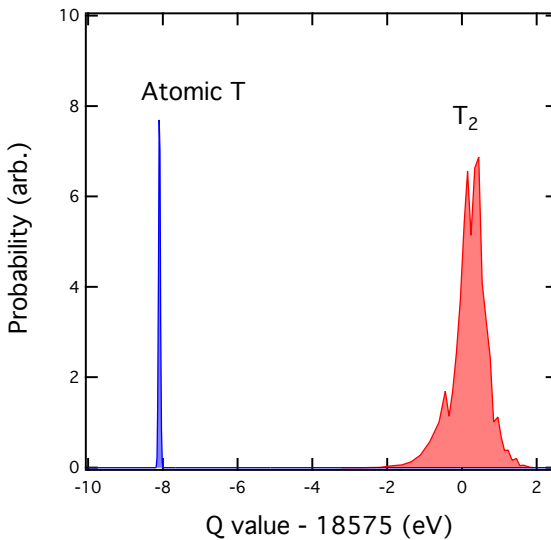


**Figure 3.4.** A plot of the final state distributions of atomic and molecular tritium. The final state distribution provides the primary contribution to the width of the molecular spectrum whereas thermal doppler broadening is responsible for the width of the atomic spectrum.

1386 One must supply sufficient energy to the tritium molecules to break the molecular

---

<sup>1</sup><https://www.project8.org/>

1387 bond and create atomic tritium. Common approaches include the use of hot coaxial  
1388 filament atom crackers as well as plasma sources. Both involve heating the tritium atoms  
1389 to temperatures of  $> 2500$  K, which must then be cooled to temperatures on the order  
1390 of a few mK so that the tritium atoms can be trapped. Cooling the atoms requires the  
1391 construction of a large tritium infrastructure and cooling system that can supply a source  
1392 of cold atoms to the trap.

1393 Once cold tritium atoms are produced they cannot make contact with any surfaces  
1394 to avoid recombination of the atoms to molecules. Therefore, a magnetic trap is required  
1395 to store the atoms for a sufficient length of time that they have a chance to decay before  
1396 escaping the trap. Trapping the atoms requires the construction of a large and complex  
1397 magnet system that must be cooled to cryogenic temperatures.

1398 The significant experimental complexity caused by atomic tritium makes a molecular  
1399 source the obvious choice from practical considerations. However, the drawback of  
1400 molecular tritium for neutrino mass measurement is the irreducible broadening in the  
1401 electron's kinetic energy due to the final state spectrum of molecular tritium (see Figure  
1402 3.4). The broadening of the final state spectra has a RMS amplitude of 436 meV [54, 55]  
1403 caused by variation in the final vibrational state of the daughter molecule.

1404 For atomic tritium, the primary sources of broadening in the final state spectrum are  
1405 magnetic hyperfine splittings (magnitude of  $O(10^{-5})$  eV) and thermal Doppler broadening  
1406 caused by the motion of the trapped atom. Atomic tritium at a temperature of 1 mK  
1407 has an energy broadening dominated by thermal Doppler component, providing about  
1408 1 meV RMS of broadening to the electron's kinetic energy.

1409 The larger energy broadening with molecular tritium leads to an irreducible statistical  
1410 uncertainty that limits the achievable sensitivity to approximately 100 meV at 90%  
1411 confidence. For previous direct measurements of the neutrino mass, this uncertainty is  
1412 an insignificant contribution to the overall uncertainty budget. However, for experiments  
1413 like Project 8 atomic tritium will become a key component to the success of the final  
1414 experiment.

## 1415 CRES for Neutrino Mass Measurement

1416 Several features of the CRES technique make it an attractive choice for a next generation  
1417 neutrino mass measurement experiment. Because CRES is a remote-sensing technique,  
1418 it is possible to observe the kinetic energy of the electron without altering its trajectory  
1419 or directly interacting with the particle; therefore, in a CRES experiment the source  
1420 gas volume can be the same as the CRES spectrometer volume. Tritium gas is also

1421 transparent to cyclotron radiation, which means that the kinetic energies of electrons can  
1422 be measured using a cavity or antenna array, located directly outside the atom trapping  
1423 volume.

1424 Because source and spectrometer can be colocated, CRES experiments have an  
1425 advantageous scaling law relative to the current state-of-the-art beta-decay spectroscopy  
1426 experiment, KATRIN. KATRIN utilizes the magnetic adiabatic collimation with an  
1427 electrostatic filter (MAC-E filter) technique to measure the beta-decay spectrum of  
1428 molecular tritium. In this approach, a source of molecular tritium is located outside the  
1429 spectrometer. When a beta-decay occurs the electron is guided out of the tritium source  
1430 using a magnetic field and is transported through the MAC-E filter before it is detected  
1431 on the other side of the filter using a charge sensor. The measurement statistics of the  
1432 MAC-E filter are limited by the transverse area ( $L^2$ ) of the tritium source and filter due  
1433 to the need to travel through the experiment without scattering. This scaling is less  
1434 favorable than the volumetric scaling ( $L^3$ ) of CRES due to the ability to colocate source  
1435 and detector.

1436 Another promising aspect of the CRES technique is the inherently high precision  
1437 of frequency based measurements. The endpoint of the molecular tritium beta-decay  
1438 spectrum is approximately 18.6 keV, which dwarfs the neutrino mass scale of  $< 1 \text{ eV}/c^2$   
1439 by at least a factor of  $10^5$ . Measuring the effect of such a small mass on a high energy  
1440 electron requires excellent energy resolution. Since frequency measurements are essentially  
1441 counting measurements, they are intrinsically accurate due to the ability to measure  
1442 the cyclotron frequency by effectively averaging over millions of cyclotron orbits. It  
1443 is possible to achieve part-per-million accuracy on the kinetic energy with the CRES  
1444 technique using the off-the-shelf RF components.

1445 CRES is also nearly immune to typical sources of backgrounds that can plague other  
1446 experiments. Since CRES operates via a non-destructive measurement of the electron's  
1447 cyclotron frequency, sources of background electrons are effectively filtered out by limiting  
1448 the frequency bandwidth of the measurement. The fiducial volume of the experiment is  
1449 free from any surfaces that could introduce stray electrons, and electrons from sources  
1450 outside the fiducial volume can be prevented from entering the experiment.

## 1451 Neutrino Mass Sensitivity Goals

1452 Project 8's ultimate goal is to combine CRES with atomic tritium to measure the neutrino  
1453 mass with 40 meV sensitivity at the 90% confidence level (see Figure 3.5). This sensitivity  
1454 is sufficient to fully exhaust the range of allowable neutrino masses under the inverted

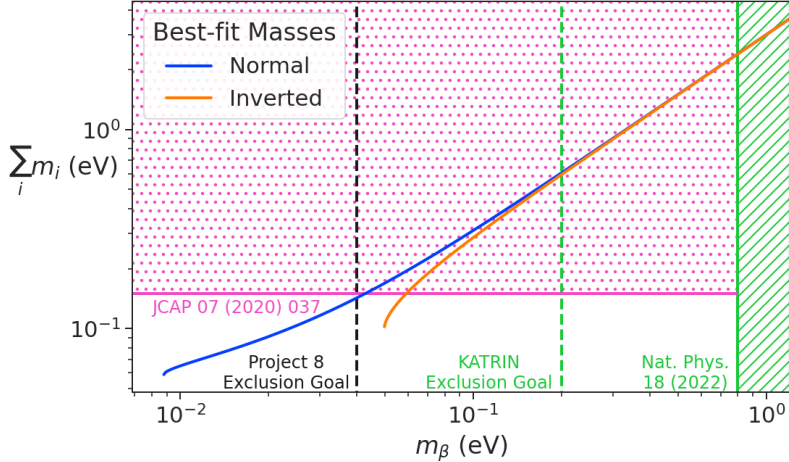


**Figure 3.5.** Neutrino mass exclusion plot including limits from cosmological measurements and the KATRIN experiment. Allowed ranges for neutrino masses under the normal and inverted hierarchies are shown as the blue and orange lines respectively. The black dashed line shows Project 8’s goal neutrino mass sensitivity for the Phase IV experiment.

neutrino mass ordering regime and is approximately an order of magnitude less than the projected final sensitivity of the KATRIN experiment. Excluding the full neutrino mass parameter space would require a sensitivity an order of magnitude lower than what is proposed by Project 8, which would require an experiment whose size and complexity are currently well beyond proposals for the next-generation of neutrino mass direct measurement experiments.

### 3.2.3 The Project 8 Phased Development Plan

Reaching 40 meV sensitivity requires the simultaneous development and eventually combination of CRES and atomic tritium. These technologies require a significant up-front R&D investment to build-out the required capabilities for a 40 meV CRES experiment. Therefore, Project 8 is following a phased experiment plan in which incremental progress can be made towards the ultimate goal of a 40 meV neutrino mass measurement with CRES.

Project 8’s experiment plan is divided into four phases. The first phase, called Phase I, consisted of a demonstration of the CRES technique and a measurement of the internal conversion spectrum of  $^{83m}\text{Kr}$ . Phase II was the first measurement of the tritium beta-decay spectrum and neutrino mass measurement with CRES. Currently, Project 8 is engaged in Phase III, which is R&D towards a scalable CRES measurement technique

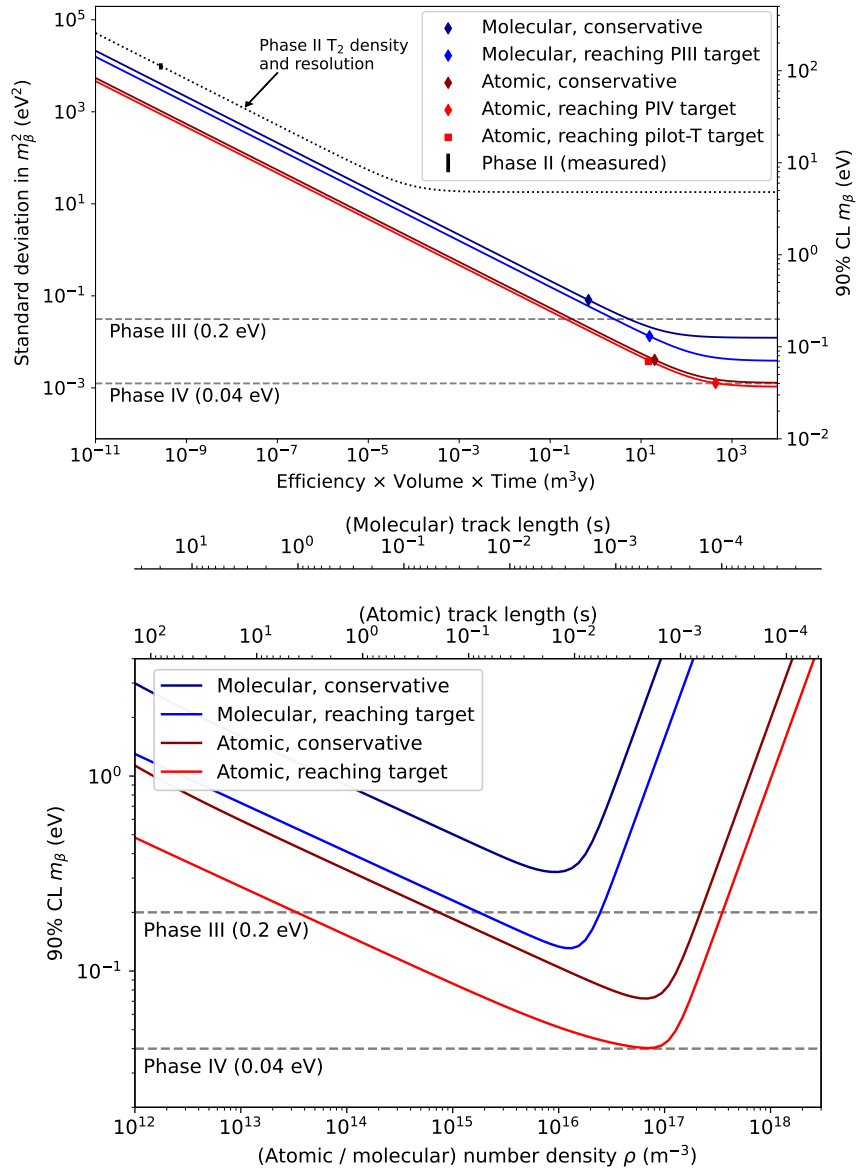


**Figure 3.6.** Sensitivity calculations for a cavity based CRES experiment that demonstrate the neutrino mass measurement goals of Project 8 throughout the phased development plan. The blue curves indicate molecular tritium sources and the red curves indicate atomic tritium sources. In the current plan, Phase III contains two tritium experiments. The first is the Low-frequency Apparatus (LFA), which is a molecular tritium experiment, and the second is the atomic tritium pilot-scale experiment that officially ends Phase III. The sensitivity of these experiments is primarily a function of statistics; however, there is a critical density beyond which CRES electrons do not have enough time to radiate between collisions for a high-resolution frequency measurement leading to worse sensitivity.

1473 and atomic tritium source for the final Project 8 experiment in Phase IV. Phase IV is  
1474 the ultimate experiment by Project 8 that will combine CRES with atomic tritium to  
1475 measure the neutrino mass with a sensitivity of 40 meV.

#### 1476 **Phase I and II: Proof of Principle and First Tritium Measurements**

1477 The earlier phases of the Project 8 experiment, Phase I and II, were focused on demon-  
1478 stration and development of the CRES technique itself as well as a proof-of-principle  
1479 measurement of the neutrino mass using the CRES technique.

1480 In Phase I, Project 8 performed a proof-of-principle measurement of the  $^{83m}\text{Kr}$   
1481 spectrum using CRES, which marked the first ever kinetic energy spectrum measurement  
1482 with CRES. The experiment included all the components of a basic CRES experiment.  
1483 An electron source consisting of a gas of  $^{83m}\text{Kr}$  was supplied to a waveguide gas cell  
1484 constructed out of a segment of WR-42 waveguide and sealed with Kapton windows at  
1485 the top and bottom. A magnetic trapping region was created in the waveguide cell using  
1486 a single electromagnetic coil wrapped around the waveguide which provided a trapping  
1487 volume on the order of a few cubic-millimeters. Detection of the cyclotron radiation was  
1488 performed by connecting the waveguide cell to an additional segment of waveguide that  
1489 transmitted the radiation to a cryogenic amplifier.

1490 Success in Phase I was achieved with the 2014 publication of the measured  $^{83m}\text{Kr}$   
1491 conversion spectrum [56], which contains a mono-energetic 17.8-keV line as well as several  
1492 other conversion lines at higher energies. Publication of this result marked the official  
1493 end of Phase I and the start of Phase II, in which Project 8 shifted its focus to the  
1494 demonstration of the first tritium beta-decay spectrum using CRES. Phase II is described  
1495 below in Section 3.3.

#### 1496 **Phase III: Research and Development and a Pilot-scale Experiment**

1497 After completing Phase II, Project 8 has shifted focus towards R&D aimed at the  
1498 construction of an experiment that demonstrates all the technologies required for a  
1499 40 meV measurement of the neutrino mass. The culmination of Phase III is a pilot-scale  
1500 experiment that successfully retires all technological and engineering risks associated  
1501 with the Phase IV experiment, while also being a scientifically interesting experiment in  
1502 its own right. Sensitivity estimates of the pilot-scale experiment predict a neutrino mass  
1503 sensitivity on par with the projected sensitivity of the KATRIN experiment.

1504 Phase III R&D is divided into two main efforts — atomic tritium and CRES detection  
1505 techniques. Atomic tritium development in Phase III must retire all risks associated

1506 with the atomic tritium system. This includes the production of tritium atoms, atomic  
1507 cooling and recirculation systems, purity and isotope concentration monitoring, and  
1508 atom trapping. Currently, Project 8 is operating small scale atom cracking demonstrator  
1509 systems to show that atom production at the estimated rates needed for Phase IV is  
1510 achievable. Future efforts will continue the current developments on atom production  
1511 and expand to include demonstrations of atomic cooling with an evaporative beam line  
1512 as well as atom trapping using Halbach magnet arrays.

1513 The need for new CRES detection techniques is driven by the drastic increase in scale  
1514 from Phase II to the pilot-scale experiments. The physical volume used for CRES in  
1515 Phase II was on the order of a few cubic-centimeters, and achieving Project 8's sensitivity  
1516 target of 40 meV requires an experiment volume on the multi-cubic meter scale. Therefore,  
1517 the waveguide gas cell CRES detection technique used in Phase II is not a feasible option  
1518 for the future of Project 8 due to its inability to scale to the required size.

1519 Two alternative CRES detection techniques have been proposed for the pilot-scale  
1520 experiment — antenna arrays and resonant cavities (see Section 3.4 and Chapter 6).  
1521 Both approaches have relative advantages and disadvantages; however, the improved  
1522 understanding of the antenna array and cavity approaches to CRES in the recent years  
1523 has led to cavities being the preferred technology for the pilot-scale experiment and  
1524 Phase IV due to the estimated reduced cost and complexity of this approach. Since  
1525 a large degree of the work presented in this dissertation is focused specifically on the  
1526 development of the antenna array CRES technique, I first describe the proposed R&D  
1527 plan for antenna array CRES in Section 3.4. A description of the cavity approach to  
1528 CRES can be found in Chapter 6, which summarizes the contribution of my dissertation  
1529 towards this effort.

1530 Cavity CRES R&D consists of a series of demonstrator experiments intended to  
1531 demonstrate cavity CRES at a variety of scales and magnetic fields. Radioactive source  
1532 gases include  $^{83m}\text{Kr}$  and molecular tritium, as well as electrons produced by an electron-  
1533 gun, which is a key calibration tool for future CRES experiments. The near-term cavity  
1534 effort in Project 8 is the cavity CRES apparatus (CCA), which is a small-scale cavity  
1535 experiment operating near 26 GHz. The CCA will perform the first CRES measurements  
1536 using a small cavity, and will pave the way towards larger scale cavity experiments in  
1537 preparation for the eventual pilot-scale tritium experiment.

1538 The pilot-scale experiment will be the first experiment to combine atomic tritium and  
1539 large-volume CRES detection. It will directly demonstrate all the technologies required  
1540 for Phase IV such that no technical risks remain for scaling the experiment to required

1541 scale. A robust approach to scaling the pilot-scale experiment is to simply build multiple  
1542 copies of it for the Phase IV experiment.

### 1543 **Phase IV: Project 8's Ultimate Neutrino Mass Experiment**

1544 The design of Phase IV should be a direct extension of the pilot-scale CRES experiment  
1545 that marks the official end of Phase III (see Section 3.5). The Phase IV experiment  
1546 represents the final experiment in the Project 8 neutrino mass measurement experiment  
1547 plan and will have sensitivity to neutrino masses of 40 meV.

## 1548 **3.3 Phase II: First Tritium Beta Decay Spectrum and 1549 Neutrino Mass Measurement with CRES**

1550 In Phase II, Project 8 demonstrated the first ever measurement of the tritium beta-decay  
1551 spectrum endpoint using the CRES technique, which lead to the first neutrino mass  
1552 measurement by Project 8. This milestone was made possible by many improvements  
1553 in the CRES technique and in the understanding of CRES systematics, which takes  
1554 an important first step towards larger scale measurements of the tritium beta-decay  
1555 spectrum with CRES. In this section, I briefly describe some important elements of the  
1556 Phase II experiment, with the goal of contextualizing the research and development  
1557 efforts for Phases III and IV of Project 8. For more complete descriptions of the work  
1558 that lead to Project 8's Phase II results, please refer to the relevant publications by the  
1559 collaboration [42, 43].

### 1560 **3.3.1 The Phase II CRES Apparatus**

#### 1561 **Magnet and Cryogenics**

1562 The magnetic field for the Phase II experiment is provided by a nuclear magnetic  
1563 resonance (NMR) spectroscopy magnet with a central bore diameter of 52 mm (see  
1564 Figure 3.7). The magnet produces a background magnetic field with an average value  
1565 of 0.959 T with a 10 ppm variation across the bore diameter achieved using several  
1566 shim coils built into the magnet. Using an external NMR field probe, the variation of  
1567 the magnetic field along the vertical axis of the magnet bore was measured to obtain  
1568 an accurate model of the magnetic field so that the CRES cell could be positioned for  
1569 optimal magnetic field uniformity.

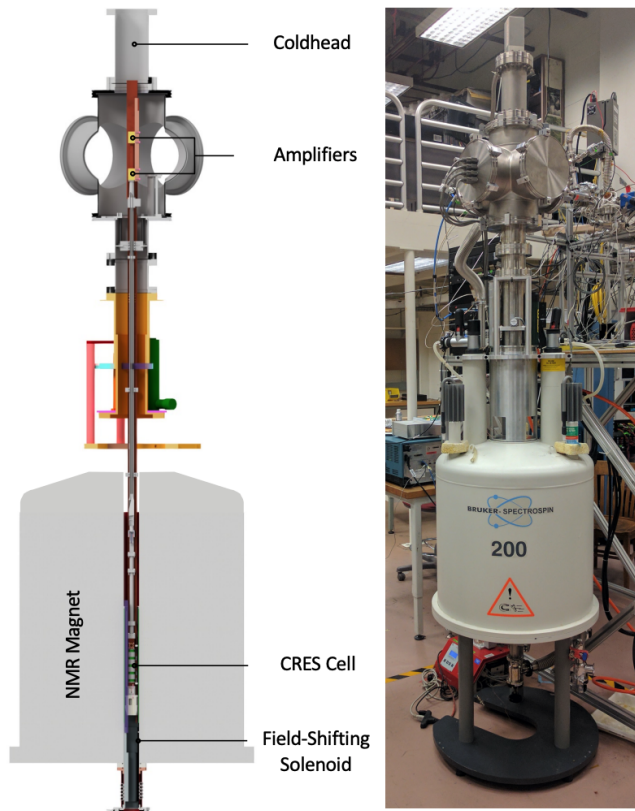


**Figure 3.7.** The Phase II CRES apparatus used to perform the first measurement of the tritium beta-decay spectrum using CRES.

1570 An external solenoid magnet was installed inside the magnet bore to provide the  
 1571 ability to shift the magnitude of the background magnetic field by a few mT. The solenoid  
 1572 has inside diameter of 46 mm and a length of 350 mm, which terminates in a vacuum  
 1573 flange that allows it to be inserted into the NMR magnet bore from the bottom. By  
 1574 shifting the value of the magnetic field by a few mT, the cyclotron frequencies of electrons  
 1575 produced by the 17.8 keV  $^{83m}\text{Kr}$  internal-conversion line [57] can be shifted by frequencies  
 1576 of  $\pm 100$  MHz. This allows one to study the frequency dependent behavior of several  
 1577 CRES systematics, such as detection efficiency, that directly affect the measured shape  
 1578 of the tritium spectrum.

1579 The inside of the magnet bore diameter was pumped down to a vacuum of less than  
 1580 10  $\mu\text{torr}$  using a turbomolecular pump, which allows for cryogenic cooling of the CRES  
 1581 cell and RF system. Cooling power was supplied to the Phase II apparatus using a  
 1582 cryopump with its coldhead mounted above the primary magnet and CRES cell. This  
 1583 arrangement allowed for sufficient cooling power to be delivered to the amplifiers to cool  
 1584 them to a temperature of  $\approx 40$  K, while keeping the amplifiers far enough from the

1585 magnet so as not to be damaged by the large field strength. Thermal contact between  
1586 the coldhead, amplifiers, RF system, and CRES cell is achieved using a copper bar that  
1587 runs the full length of the apparatus. To prevent freeze-out of  $^{83m}\text{Kr}$  on the walls of the  
1588 CRES cell a separate heater was installed to keep the CRES cell near a temperature of  
1589 85 K during the operation of the experiment.

## 1590 CRES Cell

1591 Located in the most uniform region of the magnetic field is the CRES cell, which is  
1592 the region of the apparatus where radioactive decays of  $^{83m}\text{Kr}$  and  $T_2$  produce electrons  
that can be trapped and measured using CRES (see Figure 3.8). The CRES cell is

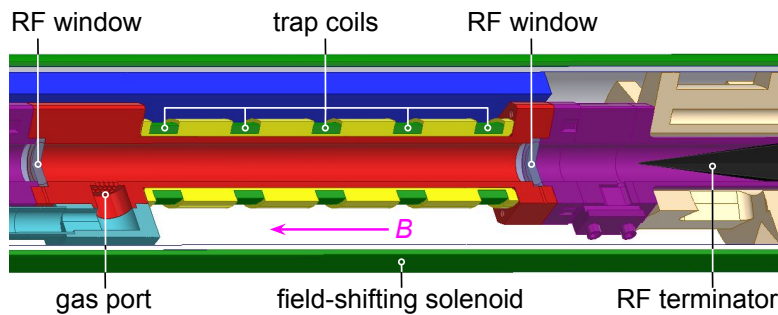


Figure 3.8. Diagram of the CRES cell portion of the Phase II apparatus.

1593  
1594 manufactured from a segment of cylindrical waveguide designed to operate at K-band  
1595 frequencies near 26 GHz. The diameter of the waveguide determines which resonant  
1596 modes of the waveguide will couple to the electron and transmit its radiation to the  
1597 amplifiers. For Phase II a waveguide diameter of 1 cm was selected, which allows electrons  
1598 to couple to the  $\text{TE}_{11}$  and  $\text{TM}_{01}$  cylindrical waveguide modes. To reduce complexity in  
1599 modeling and analyzing the CRES data, it is ideal to select a diameter that prevents  
1600 electrons from coupling to higher-order waveguide modes beyond the fundamental TE  
1601 and TM modes.

1602 Around the exterior of the cylindrical waveguide are several magnetic coils used to  
1603 produce magnetic traps inside the CRES cell volume. Without a magnetic trap electrons  
1604 produced from decays inside the CRES cell quickly impact the cell wall, which prevents a  
1605 measurement of their cyclotron frequency using CRES. Each coil along the length of the  
1606 waveguide produces a separate trap that is approximately harmonic. By independently  
1607 controlling the currents provided to each coil, the traps can be configured to have equal  
1608 values of the magnetic field at the trap bottom despite a non-uniform field from the  
1609 NMR magnet.

1610 Two primary magnetic trap configurations were used during the Phase II experiment.  
1611 The first was a shallow trap configuration used primarily for its high energy resolution  
1612 to study systematics using  $^{83m}\text{Kr}$  decays, and the second was a deeper trap that could  
1613 trap a higher percentage of pitch angles. The trade-off with the deeper trap is that the  
1614 higher trapping efficiency comes at the cost of lower energy resolution due to the greater  
1615 variation in pitch angle (see Section 3.2.1). The deep trap was the trap used to measure  
1616 the tritium beta-decay spectrum in Phase II.

1617 The source gases were delivered into the CRES cell through a gas port located near the  
1618 top end of the cylindrical waveguide. To prevent the gases from escaping the cell, vacuum  
1619 tight RF transparent windows are needed to contain the tritium and krypton source  
1620 gas across a 1 atm pressure differential, while still transmitting the cyclotron radiation  
1621 without distortion. The crystalline material,  $\text{CaF}_2$ , which has a thermal expansion  
1622 coefficient similar to that of copper, was used for this purpose in the CRES cell. Two  
1623 windows, each 2.4 mm thick, were used to seal off the ends of the CRES cell. The  
1624 thickness of 2.4 mm corresponds to half of a cyclotron wavelength when one accounts for  
1625 the permittivity of  $\text{CaF}_2$ .

1626 **RF System**

1627 The RF system in the Phase II apparatus propagates the cyclotron radiation from the  
1628 CRES cell to the receiver chain. The receiver chain performs the down-conversion and  
1629 digitization required to obtain signals that can be analyzed to determine the cyclotron  
1630 frequencies of electrons in the CRES cell (see Figure 3.9).

1631 Below the CRES cell, at the bottom of the Phase II apparatus, is a tickler port and  
1632 waveguide terminator. The tickler port is used to inject signals into the CRES cell and  
1633 RF system for testing and calibration purposes. The waveguide terminator is designed to  
1634 absorb cyclotron radiation emitted by electrons that transmits out of the bottom of the  
1635 CRES cell. This lowers the total power received from electrons in the CRES cell, since all  
1636 the energy radiated downwards is absorbed into the terminator. Earlier iterations of the  
1637 Phase II apparatus used an RF short in this location that reflected this power up towards  
1638 the amplifiers; however, interference between the upward traveling and reflected radiation  
1639 led to a disappearance in the signal carrier that made reconstruction impossible.

1640 Radiation traveling upward passes through the  $\text{CaF}_2$  window passes and a  $\lambda/4$  plate,  
1641 which transforms the circularly polarized cyclotron radiation into linear polarization.  
1642 The linearly polarized fields next travel through a segment of circular waveguide that  
1643 transitions into a long segment of WR-42 waveguide that carries the fields out of the

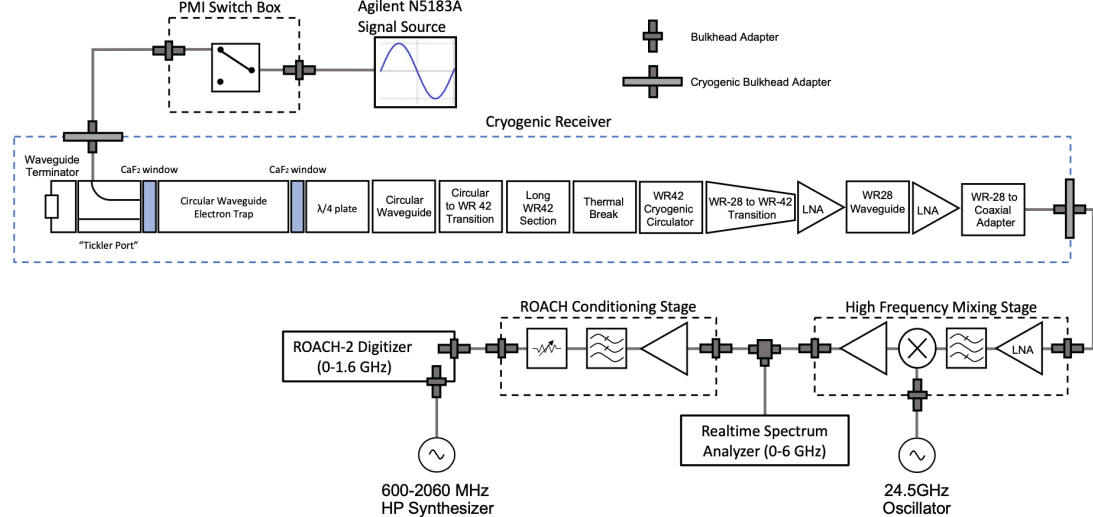


**Figure 3.9.** RF system diagram for the Phase II apparatus.

1644 high magnetic field region. A thermal break segment is included, which consists of a  
 1645 segment of gold-plated stainless steel WR-42 waveguide, to help thermally isolate the  
 1646 relatively warm CRES cell from the colder amplifiers. The radiation then passes through  
 1647 a cryogenic circulator, which prevents signals reflected from the amplifiers from interfering  
 1648 with the CRES cell before a WR-42 to WR-28 transition connects the waveguide to the  
 1649 first of the cyrogenic amplifiers. The radiation passes through two cyrogenic amplifiers  
 1650 before being coupled to a coaxial termination at the top of the Phase II apparatus.

1651 The coaxial cable transfers the cyclotron radiation signals to a high-frequency mixing  
 1652 stage that performs an analog frequency down-conversion using a 24.5 GHz LO. Two  
 1653 forms of digitization can be used at this stage to read out the CRES data. One is a  
 1654 real-time spectrum analyzer that digitizes the CRES signal data in time-domain and  
 1655 computes the frequency spectrum in real-time, which allows for direct visualization of  
 1656 CRES signal spectrograms as the experiment is running. The real-time spectrum analyzer  
 1657 is most useful for taking small amount of streamed data for debugging and analysis of  
 1658 the system. The other method, which was used to collect the majority of the CRES data  
 1659 in Phase II, is a ROACH-2 FPGA and digitizer system. The ROACH system consists  
 1660 of a fast ADC that samples the CRES signal data at 3.2 GSps. Internal digital down-  
 1661 conversion stages implemented in the FPGA perform a mixing operation that reduces  
 1662 the bandwidth of the CRES signals to 100 MHz. The FPGA implements a 4096 sample  
 1663 FFT and packetizes time and frequency domain records in parallel. The packetized data  
 1664 is then transferred from the ROACH to be analyzed by the data-processing pipeline.

### 1665 3.3.2 CRES Track and Event Reconstruction

#### 1666 Time-Frequency Spectrogram

1667 The online data-processing software uses a real-time triggering algorithm that identifies  
1668 interesting data that could contain CRES signals. Triggered data are collected into files  
1669 that are transferred to a server for offline processing and analysis. The data files contain  
1670 a continuous series of time-domain samples, broken into a set of records, which are 4096  
1671 samples long. The time-series is made up of 8-bit IQ samples acquired at 100 MHz.

1672 Each time-series record is accompanied by an associated frequency spectrum consisting  
1673 of 4096 frequency bins approximately 24.4 kHz wide, which is represented as a power  
1674 spectral density. The individual frequency spectra can be organized temporally to create  
1675 a time-frequency spectrogram that represents the evolution of the cyclotron frequency  
spectrum over the course of the CRES event (see Figure 3.10). The time-frequency

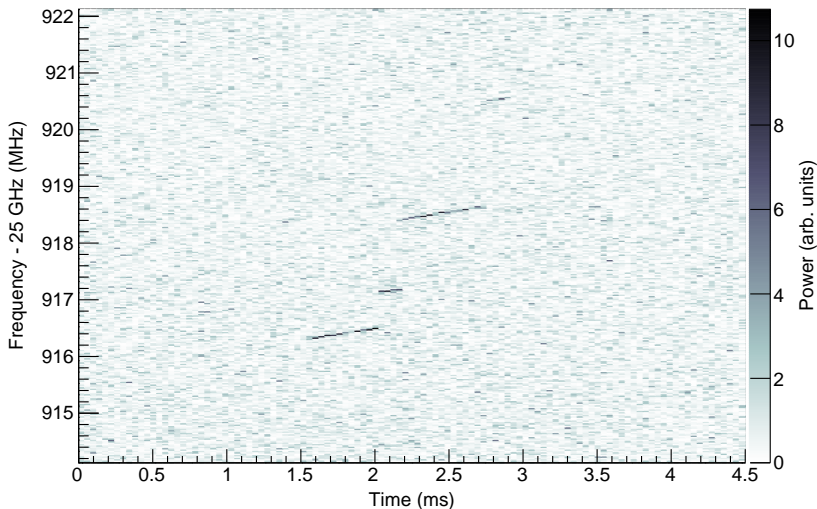


**Figure 3.10.** The time-frequency spectrogram of a tritium CRES event in the Phase II apparatus.

1676  
1677 spectrogram is represented as a two-dimensional image where the color of each pixel is  
1678 proportional to the power spectral density. Each vertical slice of pixels in the image  
1679 represents a frequency spectrum; therefore, each horizontal bin represents the data  
1680 obtained over a duration of  $4096 \times 0.01 \text{ MHz}^{-1} = 40.96 \mu\text{sec}$ .

1681    **CRES Event Data Features**

1682    Phenomenologically, a CRES signal appears as a sinusoidal signal whose frequency slowly  
1683    increases over time in what is called a frequency "chirp". Axial motion of the electron in  
1684    the trap leads to the formation of frequency sidebands that surround the more powerful  
1685    carrier frequency. The critical piece of information that must be extracted from the track  
1686    and event reconstruction procedure is the carrier frequency, since it is this frequency that  
1687    gives the cyclotron frequency and thus the kinetic energy. Axial motion from non-90°  
1688    pitch angles changes the average magnetic field experienced by an electron, because  
1689    the electron effectively samples the magnetic field along its trajectory. The change in  
1690    the average magnetic field with pitch angle leads to different cyclotron frequencies that  
1691    correspond to the same kinetic energy. However, because of the low-SNR in Phase  
1692    II, sidebands were unable to be observed, so no attempt to correct for this effect was  
1693    attempted. The effect of different pitch angles is to broaden the peak of a monoenergetic  
1694    electron line, which can be quantified by measuring the instrumental resolution of the  
1695    Phase II apparatus.

1696    In the time-frequency spectrogram representation, the chirping carrier frequency  
1697    appears as a linear track of high-power frequency bins (see Figure 3.10). The vertical  
1698    slope of the tracks is caused by the emission of energy from the electron in the form of  
1699    cyclotron radiation; therefore, the size of the slope parameter is directly proportional  
1700    to the Larmour power. The continuous track is periodically interrupted by random  
1701    jumps to higher frequency (lower energy) caused by random inelastic collisions with  
1702    background gas molecules. The length of a track is an exponentially distributed variable  
1703    whose mean value is inversely proportional to the gas density. The size of the frequency  
1704    discontinuities is directly proportional to the energies of the rotational and vibrational  
1705    states of background gas molecules.

1706    A CRES event refers to the collection of tracks produced by a trapped electron until  
1707    it inevitably scatters into a pitch angle that can no longer be trapped. The goal of track  
1708    and event reconstruction is to identify the set of tracks in a time-frequency spectrogram  
1709    that represents a segment of data acquired in the Phase II apparatus. These tracks must  
1710    be clustered into events, from which one can determine the first track produced by the  
1711    electron and thus estimate its starting cyclotron frequency and kinetic energy.

1712 **Track Reconstruction**

1713 The first step in CRES event reconstruction is the identification of tracks in the time-  
1714 frequency spectrogram, which is essentially an image processing task. Track finding  
1715 starts by normalizing the power spectral density based on the average noise power. Next  
1716 a power threshold is applied to the normalized spectrogram where only bins that have a  
1717 SNR ratio greater than five are selected to build tracks. In this case SNR is defined as the  
1718 ratio between the normalized, unitless power of a bin divided by the average normalized  
1719 power across the full frequency spectrum.

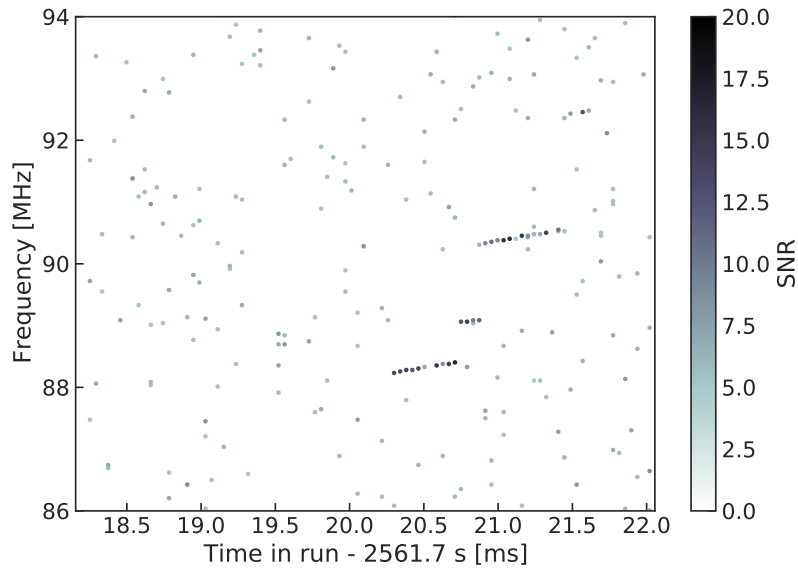


**Figure 3.11.** The sparse spectrogram obtained by placing a power cut on the raw spectrogram shown in Figure 3.10.

1720 The sparse spectrogram produced by this power cut consists only of a sparse collection  
1721 of high-power frequency bins that could be part of a CRES signal track (see Figure  
1722 3.11). In this form is it much easier to identify tracks "by eye"; however, for the Phase II  
1723 analysis Project 8 developed its own custom-made track finding algorithm, called the  
1724 sequential track finder (STF).

1725 The STF algorithm processes the sparse spectrogram in sequential fashion, processing  
1726 each time-slice one-by-one until the end of the spectrogram is reached. Tracks are found  
1727 by searching for points in the sparse spectrogram that appear to fall on a straight line.  
1728 Multiple configurable parameters are built into the STF algorithm that allow the user to  
1729 tune the criteria for adding a point to an existing track or creating a new track. These  
1730 include parameters such as maximum time and frequency differences between subsequent

1731 points in a track as well as minimum SNR values for the start and endpoints of the track.  
1732 Additionally, tracks are required to have a minimum length and slope to be considered  
1733 potential CRES tracks rather than random noise fluctuations.

1734 The resulting output of the STF is a collection of track objects that consist of the track  
1735 point objects and their properties. The final step is to calculate track-level properties and  
1736 apply cuts to reject false tracks found by the STF. This involves the fitting of a line to  
1737 the collection of track points as well as the total and average power of the track obtained  
1738 by computing the sum and mean of the points powers. The starting frequency of the  
1739 track is determined by calculating the time coordinate that intersects with the linear fit.  
1740 A cut is then performed to remove all tracks that do not have a specified average power  
1741 over their duration, which helps to remove the majority of noise fluctuations that have  
1742 passed all previous cuts up to this point.

### 1743 Event Reconstruction

1744 After track reconstruction comes event reconstruction, where the identified tracks are  
1745 grouped into events that correspond to the trajectory of a single electron in the trap.  
1746 This procedure attempts to match tracks head to tail by checking if the start and end  
1747 times of a pair of tracks falls within a certain tolerance. This tolerance is a configurable  
1748 parameter that can be tuned to an optimal value using Monte Carlo simulations of events  
1749 in the Phase II apparatus.

1750 After the event building procedure has completed, there remains a small likelihood  
1751 that false tracks have made it through to the event reconstruction stage. Typically, cuts  
1752 at the track level are able to remove 95% of the false tracks identified by the STF, which  
1753 leads to a significant number of false tracks at the event building stage. However, the  
1754 additional event-level information makes it possible to reject events that contain these  
1755 false tracks with a high degree of confidence.

1756 Two event level features are associated with events caused by real electrons — the  
1757 duration of the first track as well as the number of tracks in the event. Real electrons  
1758 tend to have event structures with longer first tracks and a higher number of total tracks.  
1759 Based on the values of these two criteria, a minimum threshold on the average power in  
1760 the first track was configured to reject false events. The average power in the first track  
1761 was chosen due to the critical nature of the starting frequency of the first track in an  
1762 event to the krypton and tritium spectrum analyses.

1763 **3.3.3 Results from Phase II**

1764 The main result from Phase II was the measurement of the tritium beta-decay spectrum  
1765 using CRES, which lead to the first neutrino mass limit with CRES. However, Phase  
1766 II also included a significant  $^{83m}\text{Kr}$  measurement campaign to understand important  
1767 systematics relevant to the tritium spectrum measurement and the fundamentals of  
1768 the CRES technique itself. This required high-resolution measurements of the  $^{83m}\text{Kr}$   
1769 internal-conversion spectrum [57], which is an interesting science result in its own right.

1770 The results from Phase II represents a significant effort from entire Project 8 over  
1771 several years. Because the focus of my contributions to Project 8 is directed towards the  
1772 research and development efforts for the Phase III experiments, the goal in this section  
1773 is not to provide a detailed description of the analyses that lead to the Phase II results.  
1774 Rather, I will provide brief descriptions of a few plots representative of the main results  
1775 from Phase II as reported in [42, 43].

1776 **Measurements with Krypton**

1777 Measurements with krypton were a key calibration tool for Phase II of the experiment and  
1778 will continue to be useful in Phase III. Krypton measurements are CRES measurements of  
1779 the internal-conversion spectrum of the metastable state of krypton-83,  $^{83m}\text{Kr}$ , produced  
1780 by electron capture decays of  $^{83}\text{Rb}$ . A supply of  $^{83}\text{Rb}$  was built into the Phase II apparatus  
1781 gas system that supplied the CRES cell with  $^{83m}\text{Kr}$  via emanation.

1782 The  $^{83m}\text{Kr}$  internal-conversion spectrum consists of several lines based on the orbital  
1783 of the electron ejected during the decay. The conversion lines useful to Project 8 are  
1784 those that emit electrons with kinetic energies that fall inside the detectable frequency  
1785 bandwidth of the Phase II apparatus. These are the K; L2 and L3; M2 and M3; and N2  
1786 and N3 lines; with kinetic energies of 17.8 keV,  $\approx$  30.4 keV,  $\approx$  31.9 keV, and  $\approx$  32.1 keV,  
1787 respectively. The different energies of the lines allows one to test the linearity of the  
1788 relationship between kinetic energy and frequency across the range of frequencies covered  
1789 by the continuous tritium spectrum.

1790 Numerous detector-related effects relevant to the tritium analysis can be characterized  
1791 by measuring the shape of the krypton spectrum. Specific examples include variations  
1792 in the magnetic field as a function of the radial position of the electron, variation in  
1793 the magnetic field caused by the trap shape, variation in the average magnetic field for  
1794 electrons with different pitch angles, and the effect of missing tracks due to scattering.  
1795 These spectrum shape measurements focused on the 17.8-keV krypton line and utilized

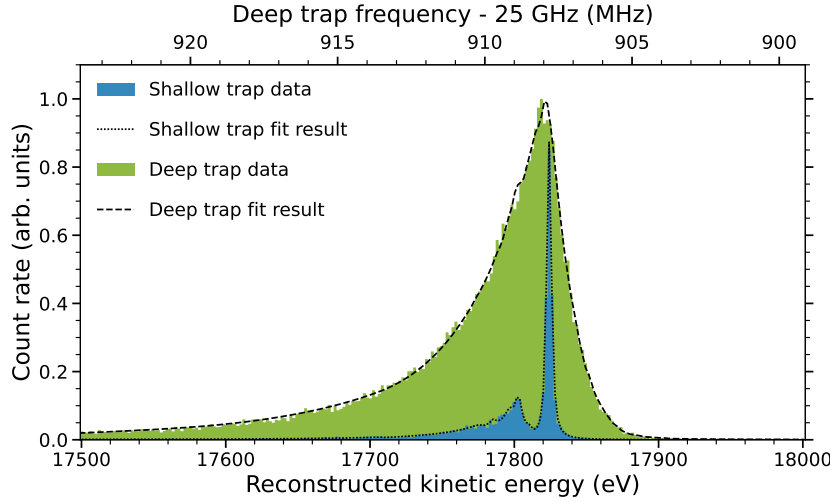


**Figure 3.12.** Fits to the measured 17.8-keV  $^{83m}\text{Kr}$  conversion line using the deep and shallow trap configurations.

1796 different trap geometries based on the particular goal of the dataset (see Figure 3.12).

1797 Krypton measurements with a shallow trap allow for high energy resolution, since  
 1798 variation in frequency due to pitch angle differences is sharply reduced in the shallow  
 1799 trap configuration. With this trap the main 17.8-keV peak of the conversion spectrum is  
 1800 clearly visible along with additional satellite peaks at lower energy, which correspond to  
 1801 the shakeup/shakeoff spectrum of the decay. The high accuracy of the fit demonstrates a  
 1802 high degree of understanding of the CRES systematics.

1803 The broadening of the krypton spectrum seen for the deeper track is due to the large  
 1804 range of electron pitch angles that can be trapped. Furthermore, with a deeper trap  
 1805 there is a larger parameter space of electron that could be produced with pitch angles  
 1806 that are trappable but not visible in the time-frequency spectrogram. These electrons  
 1807 remain in the trap and can scatter multiple times before randomly scattering to a visible  
 1808 pitch angle. This leads to one or more missing tracks earlier in the event, which leads to  
 1809 a misreconstruction of the true starting frequency. By measuring the krypton spectrum  
 1810 shape in the same trap used to detect tritium events, the effect this has on the spectrum  
 1811 shape can be characterized to mitigate its impact on the tritium measurements.

1812 Changes in the Krypton spectrum shape as a function of CRES frequency were  
 1813 used to study the detection efficiency of the Phase II apparatus. Variations in the  
 1814 detection efficiency as a function of frequency directly influences the measured shape of  
 1815 the continuous tritium spectrum, which can lead to errors in the neutrino mass estimate if  
 1816 not modeled appropriately. Using the field-shifting solenoid (FSS) the cyclotron frequency  
 1817 of the krypton 17.83 keV line was shifted across the full frequency range of the tritium

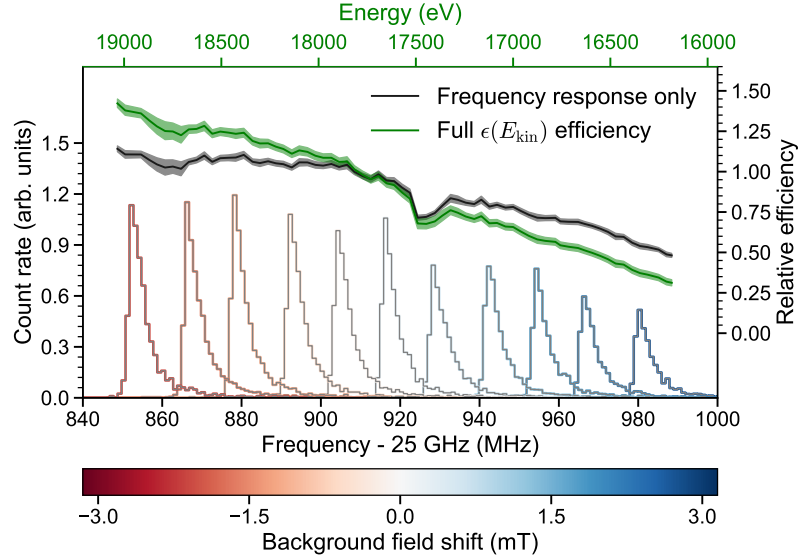


**Figure 3.13.** Measurements of the 17.8-keV  $^{83m}\text{Kr}$  line using the deep trap configuration for different values of the magnetic field from the field shifting solenoid.

1818 spectrum data (see Figure 3.13). The FSS is a wound copper solenoid magnet that  
 1819 surrounds the CRES cell. Controlling the current through this magnet allows one change  
 1820 the value of the background magnetic field and the frequency of the krypton conversion  
 1821 lines. Variations in the deep trap krypton spectrum shape can be used to infer the  
 1822 detection efficiency as a function of frequency and correct for this affect in the tritium  
 1823 measurements.

#### 1824 Tritium Spectrum and Neutrino Mass Results

1825 The tritium measurement campaign resulted in the collection of 82 days of detector  
 1826 live time during which 3770 total tritium events were detected. The track and event  
 1827 reconstruction analysis extracted the starting frequencies of these tritium events, which  
 1828 were used to build a frequency spectrum of tritium beta-decays. The resulting frequency  
 1829 spectrum was then converted to an energy spectrum using the information gleaned from  
 1830 the krypton measurement campaign to obtain the tritium beta-decay spectrum (see  
 1831 Figure 3.14).

1832 CRES is inherently a very low background technique with the dominant source of noise  
 1833 being random RF fluctuations. Monte Carlo simulations, validated using measurements  
 1834 of the RF noise background, were used to set track and event cuts to guarantee that  
 1835 zero false events would occur over the duration of the experiment with 90% confidence.

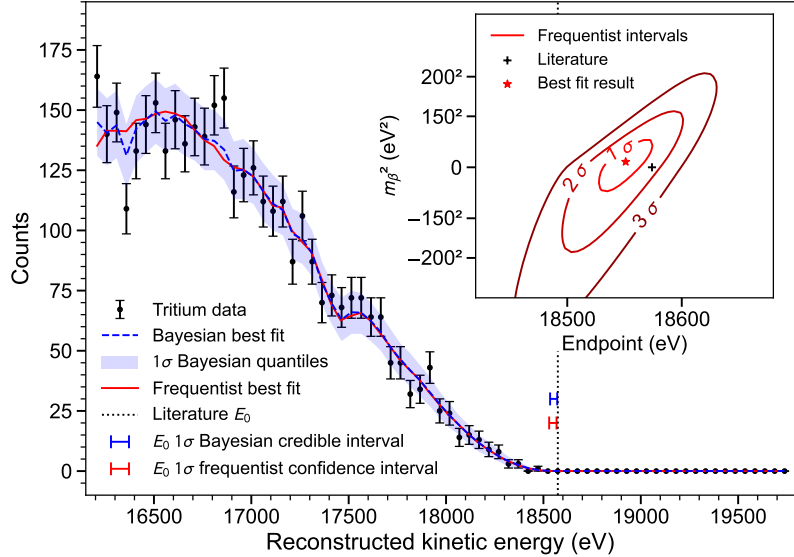


**Figure 3.14.** The measured tritium spectrum from Phase II with Bayesian and frequentist fits.

Notably, the measured spectrum has zero events beyond the tritium spectrum endpoint, which allows one to constrain the background rate in the Phase II apparatus to less than  $3 \times 10^{-10}$  counts/ev/s. Achieving a low background is critical for future neutrino mass experiments that seek to measure the neutrino mass with less than 100 meV sensitivity.

Bayesian and frequentist based fits to the measured tritium spectrum, incorporating information gained about CRES systematics from the krypton measurements, were performed to extract upper limits on the tritium beta-decay spectrum endpoint as well as the neutrino mass. The estimated spectrum endpoints are  $18553^{+18}_{-19}$  eV for the Bayesian analysis and  $18548^{+19}_{-19}$  eV for the frequentist analysis. The quoted uncertainties are  $1-\sigma$ , and both results are within  $2-\sigma$  of the literature endpoint value of 18574 eV. The estimated neutrino mass for both results is consistent with  $m_\beta^2 = 0$ . The 90% confidence upper limits for the Bayesian analysis is  $m_\beta < 155$  eV/c $^2$  and  $m_\beta < 152$  eV/c for the frequentist analysis.

Though the neutrino mass results from Phase II are not competitive with KATRIN, the experiment was a promising first step towards the development of more precise neutrino mass measurements using CRES. The low-background and high-resolution achievable with krypton measurements are promising features of the technique that were demonstrated with the Phase II apparatus. As new technologies are developed to enable CRES measurements in larger volume, many of the lessons learned from Phase II will continue to influence the operation and design of future experiments.

## 1856 3.4 Phase III R&D: Antenna Array CRES

1857 The goal of Phase III in the Project 8 experimental program is to develop the technologies  
1858 and expertise required to build an experiment that uses CRES to measure the neutrino  
1859 mass with a target sensitivity of 40 meV. One of the key technologies is a method for  
1860 performing high resolution CRES measurements in a large volume, which allows one to  
1861 observe a sufficient quantity of tritium to measure the low-activity endpoint region of  
1862 the tritium spectrum.

### 1863 3.4.1 The Basic Approach

1864 One possible approach, suggested in the original CRES publication [40], is to use many  
1865 antennas to surround a volume of tritium gas in a magnetic field (see Figure 3.15). When  
1866 a decay occurs the electron will emit cyclotron radiation that can be collected by the array  
and used to perform CRES. Each antenna in the array collects only a small fraction of

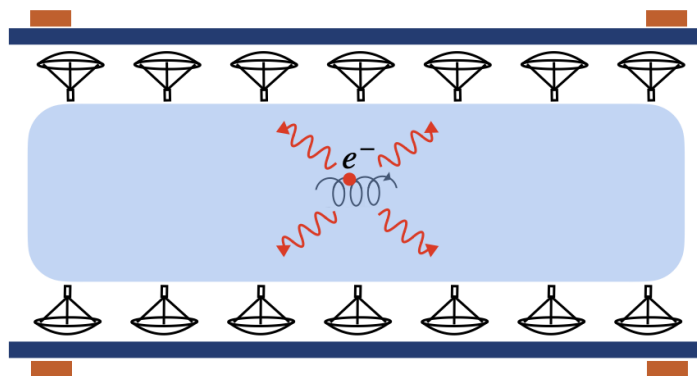


Figure 3.15. A cartoon illustration of the basics of the antenna array CRES technique.

1867  
1868 the electron's signal power, which is less than 1 fW for a 18.6 keV kinetic energy electron  
1869 in a 1 T magnetic field. Scaling to large volumes with the antenna array approach is  
1870 accomplished by increasing the number of antennas in the array, which increases the  
1871 volume available for CRES measurements.

1872 Several features of the antenna array approach make it an attractive candidate technol-  
1873 ogy for a large volume experiment. One example is the accurate position reconstruction  
1874 possible with a multichannel antenna array. Using techniques like digital beamforming,  
1875 it is possible to estimate the radial and azimuthal positions of the electron in the mag-  
1876 netic trap with a precision significantly less than the size of the cyclotron wavelength.  
1877 This capability allows one to perform event-by-event estimations of the magnetic fields

1878 experienced by an electron, which helps achieve high energy resolution with the CRES  
1879 technique.

1880 The easy availability of position information with the antennas array approach  
1881 is potentially a unique advantage that provides significant flexibility in the magnetic  
1882 field uniformity requirements compared to other proposed approaches to large volume  
1883 CRES (see Chapter 6). Spatial discrimination using digital beamforming leads to pileup  
1884 reduction, which helps to reduce the potential of background events caused by missing  
1885 tracks or by incorrectly clustering a group of tracks into an event. Limits on the  
1886 background rate for a neutrino mass measurement with 40 meV sensitivity are stringent  
1887 and the total activity of the tritium source is gigantic relative to the activity near the  
1888 endpoint. Thus, pileup discrimination could be an important tool for a large scale CRES  
1889 experiment.

1890 Another beneficial quality of antenna arrays is that the volume of the experiment can  
1891 be scaled independent of frequency by simply adding more antennas to the array (see  
1892 Figure 3.19). Resonant cavities, the proposed alternative large volume CRES technology,  
1893 are ideally operated in magnetic fields that cause electrons to move with cyclotron  
1894 frequencies near the fundamental cavity resonance, to avoid complex coupling of the  
1895 electron to multiple cavity modes simultaneously. This leads to a coupling between the  
1896 cavity volume and the magnetic field magnitude, which forces one to lower the magnetic  
1897 field in order to increase the experiment scale. Whereas, for antenna arrays, in principle  
1898 there is no physical limitation on the size of the antenna array that can be used at a  
1899 particular magnetic field. However, this approach to scaling an antenna array experiment  
1900 leads to rapidly increasing cost and complexity due to the large number of antennas,  
1901 amplifiers, and data streams, which require substantial computer processing power to  
1902 effectively utilize. The link between array size and computational cost will be explored  
1903 in Section 4.3.

### 1904 **3.4.2 The FSCD: Free-space CRES Demonstrator**

1905 The complexity of the antenna array CRES technique requires the construction of a  
1906 small scale demonstration experiment to develop an understanding of technique itself and  
1907 relevant systematics. Without a demonstrator experiment it is not possible to sufficiently  
1908 retire the technical risks associated with the full-scale experiment. Therefore, Phase  
1909 III of the Project 8 experimental program is primarily focused on the development and  
1910 operation of demonstrator experiments to inform the design of the Phase IV experiment.

1911 The Phase III demonstrator experiment for antenna array CRES is called the Free-

space CRES Demonstrator or FSCD. The FSCD is also a capable neutrino mass measurement experiment in its own right, with a target neutrino mass sensitivity of a few eV using a molecular tritium source. The higher-costs associated with antenna-based CRES, which were identified over the course of the development of the FSCD, have lead to the adoption of resonant cavities as the technology of choice for Phase III. Therefore, all future development of the FSCD and antenna-based CRES in Project 8 has been suspended.

## Magnetic Field

The background magnetic field for the FSCD is provided by a hospital-grade MRI magnet (see Figure 3.16). The magnet produces a magnetic field of approximately 0.958 T, which corresponds to a tritium spectrum endpoint frequency of approximately 25.86 GHz. The



**Figure 3.16.** An image of the MRI magnet installed in the Project 8 laboratory at the University of Washington, Seattle.

magnet is installed in the Project 8 laboratory located at the University of Washington, Seattle, and is shimmed to produce a uniform magnetic field with variations on the ppm-level. Measurements of the magnetic field non-uniformities are performed using a NMR probe and rotational gantry to capture measurements of the magnetic field around an elliptical surface in the center of the MRI magnet. During the operation of the FSCD an array of Hall or NMR magnetometers would be used to periodically measure the magnetic field to monitor its time stability.

Inside the field of the MRI additional electromagnets would be installed that provide the capability to shift the value of the background magnetic field and produce a magnetic

trap. Shifting the background magnetic field by a few  $\mu$  T lets one control the cyclotron frequencies of electrons with a fixed kinetic energy, which is key to an effective calibration of the FSCD. The preferred calibration method for the FSCD is a mono-energetic electron gun that can inject electrons into the magnetic trap with a known kinetic energy. In combination with the field shifting magnet, one can vary the cyclotron frequencies of the electrons to measure the response of the antenna array as a function of the radiation frequency and electron position. This procedure characterizes the response of the antenna array and provides further information on magnetic field uniformity, which is important to achieving good energy resolution.

The design of the magnetic trap is absolutely critical to the success of a CRES experiment. The ideal shape is the perfect magnetic box, which has a flat bottom and step function walls. Any variation in the average magnetic field experienced by an electron leads to changes in the cyclotron frequency that can make determining the true starting kinetic energy more difficult. This includes changes in the magnetic field caused by the walls of the magnetic trap as well as radial magnetic field variations.

The ideal box trap is completely uniform and has infinitely steep walls that cause no change in the electron's cyclotron frequency as it is reflected from the trap wall. However, such a trap cannot be made from any combination of magnetic coils since it violates Maxwell's equations. One of the goals of magnetic trap design is to identify the configuration of coils that produces a trap that approximates the perfect box trap as closely as possible.

## Antenna Array

The canonical antenna array design for CRES is a uniform cylindrical array of antennas that surrounds the magnetic trap volume. Since the FSCD is a demonstrator experiment, the simplest and lowest cost version of a uniform cylindrical array is used, which is a single circular ring of antennas. The FSCD array design has a diameter of 20 cm (see Figure 3.17). Along this circle are sixty slotted waveguide antennas that fully populate the available space around the array circumference. It is optimal to cover as large a fraction of the solid angle around the magnetic trap as possible in order to maximize the power collected from each electron .

The distance between antennas around the circumference of the array is proportional to the wavelength of the cyclotron radiation. Therefore, maximizing the solid angle coverage of the array, while minimizing channel count to keep the hardware and data acquisition costs manageable, biases one towards smaller array diameters. Antenna

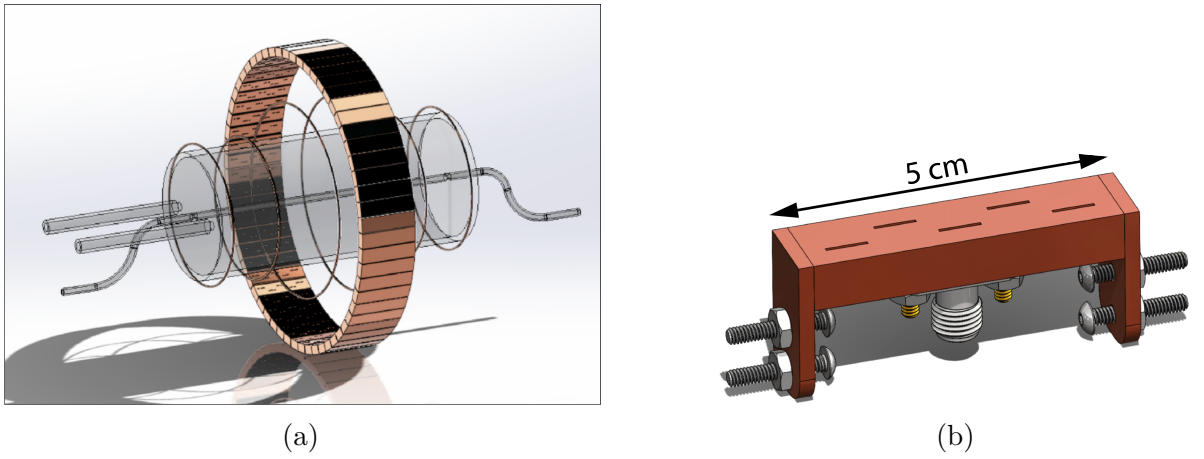


**Figure 3.17.** (a) A model of the FSCD antenna array, magnetic trap, and tritium containment vessel design.(b) A more detailed model of a prototype design for the 5-slot waveguide antenna design.

1966 near-field effects limit the minimum diameter of the array for a given antenna design,  
 1967 since the radiation from electrons that are too close to the array cannot be detected due  
 1968 to destructive interference.

1969 Slotted waveguide antennas are used in the FSCD antenna array due to their high  
 1970 efficiency and low loss, which comes from the lack of dielectric materials in the antenna  
 1971 structure. Coupling to the waveguide is performed with a coaxial cable connected at the  
 1972 center of the antenna. One of the drawbacks of waveguide antennas is the large amount  
 1973 of space required to fit them inside the limited MRI magnet volume. Alternative antenna  
 1974 designs, constructed from microstrip printed circuit boards require significantly less space  
 1975 at the cost of slightly higher energy losses in the antenna structure.

1976 The FSCD antenna design is a 5 cm long segment of WR-34 waveguide with 5 vertical  
 1977 slots cut into the side. The distance between slots along the length of the waveguide is  
 1978 a half wavelength for optimal power combination between the individual antenna slots.  
 1979 Each slot is offset from the center of the antenna face a small distance in order to most  
 1980 effectively couple the slot to waveguide modes inside the antenna.

1981 The passive power combination achieved by placing 5 slots in a single waveguide is a  
 1982 compromise intended to reduce the cost and complexity of the antenna array system.  
 1983 Each additional channel in the array requires its own cryogenic amplifier and also increase  
 1984 the required computer power to process the raw data collected by digitizing each channel.  
 1985 Passive summation, achieved by combining antennas into arrays axially, reduces the  
 1986 array channel count at the cost of losses from imperfect passive combination.

1987 Interference and re-radiation eventually limit the axial extent of passive power combi-

1988 nation. The 5-slot designed developed for the FSCD is optimized to minimize the impact  
1989 of these losses while achieving the maximum amount of axial coverage with a single ring  
1990 of antennas. Scaling beyond the volume covered by a single ring of antennas is achieved  
1991 by stacking additional rings of antennas together to cover a larger trap volume. A likely  
1992 scenario for the FSCD experiment involves a staged experiment approach, where first  
1993 a series of measurements is performed using only a single ring of antennas followed by  
1994 experiments that add additional rings to the FSCD. The goal would be to first understand  
1995 the principles of antenna array CRES using the simplest possible experiment, before  
1996 attempting to scale the technique by expanding the antenna array size.

### 1997 **Tritium Source**

1998 While the primary purpose of the FSCD is as a technology demonstrator, it is impossible  
1999 to retire all risks relevant to the Phase IV experiment without an intermediate scale  
2000 measurement of the neutrino mass. Therefore, the FSCD has the scientific goal of  
2001 measuring the neutrino mass with a rough sensitivity goal in the range of a few eV.  
2002 This level of precision is achievable using a molecular tritium source with a volume of  
2003 approximately 1 L at a density comparable to potential Phase IV scenarios.

2004 Unlike previous CRES experiments, where the tritium source could be colocated  
2005 with the receiving antenna inside a waveguide transmission line, the tritium source  
2006 in the FSCD is thermally isolated from the antenna array to avoid freeze-out of the  
2007 tritium molecules. The tiny radiation power emitted by electrons requires a system noise  
2008 temperature of  $\approx 10$  K or less, in order to detect events at a high enough efficiency to  
2009 reach the neutrino mass sensitivity goals of the experiment. Achieving a system noise of  
2010 10 K requires that the antenna array and amplifiers operate at liquid helium temperatures  
2011 of  $\approx 4$  K, which significantly lowers the vapor pressure of molecular tritium. By keeping  
2012 the molecular tritium isolated in an RF-transparent vessel the tritium gas can be kept  
2013 at a relatively warmer temperature in the range of 30 K to avoid the accumulation of  
2014 tritium on the experiment surfaces.

### 2015 **Data Acquisition and Reconstruction**

2016 A fundamental change in the data acquisition system for the FSCD is the shift from  
2017 single to multichannel reconstruction. This transition results in a significant increase in  
2018 the data-generation rate, which is linearly related to the number of independent channels  
2019 in the array. The larger data volume coincides with an increased demand for computer  
2020 processing power based on the need for more precise signal reconstruction algorithms

2021 driven by the FSCD and Phase IV sensitivity goals. Therefore, the data acquisition  
2022 system for the FSCD is likely to represent a significantly larger fraction of the experiment  
2023 cost and complexity than in Phase II.

2024 Each antenna is connected to a cryogenic amplifier and down-converted from the  
2025 26 GHz CRES frequency using an IQ-mixer to reduce the size of the analysis window.  
2026 Using an LO with a frequency of approximately 25.80 GHz the antenna array signals can  
2027 be digitized at a rate of 200 MHz, which is sufficient bandwidth to resolve the complete  
2028 sideband spectrum produced by axial oscillations of electrons in the FSCD magnetic  
2029 trap.

2030 Direct storage of the raw FSCD antenna array data is undesirable, since the estimated  
2031 amount of raw data generated is  $O(1)$  exabyte per year. The storage of such a large  
2032 dataset is infeasible for a demonstrator experiment like the FSCD, since it would represent  
2033 a disproportionate fraction of the total experiment budget in Phase III and Phase IV.  
2034 Therefore, a goal of the FSCD experiment is the development of real-time reconstruction  
2035 methods that could reduce the raw data volume by detecting and reconstructing CRES  
2036 events in real-time. Ultimately, a real-time CRES reconstruction pipeline is desired, which  
2037 takes raw voltages samples from the antenna array and converts them into measured  
2038 starting kinetic energy values for electrons.

2039 The feasibility of a real-time reconstruction pipeline rests on the development of  
2040 computationally efficient algorithms that can be implemented without the need for  
2041 enormous computing resources. One challenge with the antenna array approach is that  
2042 the small radiation power of a single electron is distributed among all channels in the array,  
2043 such that reconstruction using only the information in a single channel is not possible.  
2044 Therefore, simply performing the initial step in reconstruction — signal detection —  
2045 requires orders of magnitude more computational power than previous CRES experiments.  
2046 This operation will then be followed by other, potentially more expensive, reconstruction  
2047 steps that are required in order to determine the kinetic energy of the electron.

## 2048 **3.5 Pilot-scale Experiments**

2049 The Project 8 pilot-scale experiment represents the experiment that retires all technical  
2050 and engineering risks with Project 8’s neutrino mass measurement approach, by combining  
2051 all the required components of Phase IV in a multi-cubic-meter experiment. The larger  
2052 scope and complexity of the pilot-scale experiment requires a careful choice of magnetic  
2053 field and cyclotron frequency since this directly affects the design of nearly all parts of

2054 the experiment. Currently, designs for the pilot-scale experiment are in the conceptual  
2055 stage, but a goal of Phase III is to translate these design concepts into detailed technical  
2056 designs and specifications.

### 2057 **3.5.1 Choice of Frequency**

2058 The optimal CRES frequency for Project 8 is that which reaches the target sensitivity of  
2059 40 meV, while minimizing the cost and complexity of the overall experiment. The CRES  
2060 frequency is directly linked to the magnetic field, which is coupled to nearly all aspects  
2061 of the experiment design; therefore, an optimization of CRES frequency is effectively an  
2062 optimization of the sensitivity of the overall experiment.

### 2063 **Frequency Scaling Laws**

2064 The Phase I and II experiments utilized a background magnetic field of 0.959 T provided  
2065 by an NMR magnet. Since this magnet was already available, the 0.959 T background  
2066 field was selected for convenience. However, one additional reason to use this background  
2067 field is that the cyclotron frequencies for electrons near the tritium endpoint in a 0.959 T  
2068 field are approximately 26 GHz, which is within the standard RF Ka-band. Therefore,  
2069 microwave electronics specialized for these frequencies are obtainable for relatively low  
2070 cost. The operating frequency for the large-scale experiments must be selected in a more  
2071 rigorous manner due to the increased scale and complexity of the systems as well as the  
2072 requirements of the 40 meV neutrino mass science goal.

2073 There is a bias towards lower frequencies in a large-volume experiment, due to the  
2074 direct relationship between wavelength and the physical size of the compatible RF  
2075 components like antennas and cavities. With a longer wavelength more volume can  
2076 be surrounded by an array with fewer antennas, which reduces hardware and data-  
2077 processing costs. Additionally, the size of a cavity experiment is directly proportional to  
2078 the wavelength, since this sets the physical dimensions of the cavity. It is also simpler to  
2079 engineer a magnet that provides a uniform magnetic field across several cubic-meters of  
2080 space at lower magnetic fields, which provides advantages in terms of cost-reduction.

2081 A concern with lower magnetic fields and frequencies is the power scaling as described  
2082 by the Larmour equation, in which power is proportional to the square of the frequency.  
2083 Naively, one would predict that the SNR would decrease with lower fields; however, two  
2084 additional scaling laws that affect the noise power also come into play. Noise power  
2085 is directly proportional to the required bandwidth, which decreases linearly with the

2086 magnetic field. Furthermore, at lower frequencies it is possible to purchase amplifiers with  
 2087 lower noise temperatures until approximately 300 MHz, at which point this relationship  
 2088 tends to flatten. Therefore, it is expected that the SNR remains approximately constant  
 2089 as the frequency decreases.

2090 The facts that large-volume experiments are simpler to achieve at lower frequencies  
 2091 and SNR is expected to be approximately the same together motivate the usage of lower  
 2092 magnetic fields in the large-scale experiments. This is simply because a low-frequency  
 2093 experiment is less costly than a high-frequency experiment and there is little to no penalty  
 2094 in SNR or detection efficiency at these fields.

2095 One drawback of lower magnetic fields is the increased influence of external magnetic  
 2096 fields on the experiment. This includes magnetic fields from the building materials as well  
 2097 as variations in the earth's magnetic field. A suitable magnetic field correction system  
 2098 will need to be devised to deal with these effects, which includes constant monitoring of  
 2099 external fields.

## 2100 Atomic Tritium Considerations

2101 The pilot-scale experiments will be the first Project 8 experiments to combine CRES  
 2102 with atomic tritium; therefore, the optimal frequency should take into account the  
 affect of the background magnetic field on the atom trap. The primary influence of the

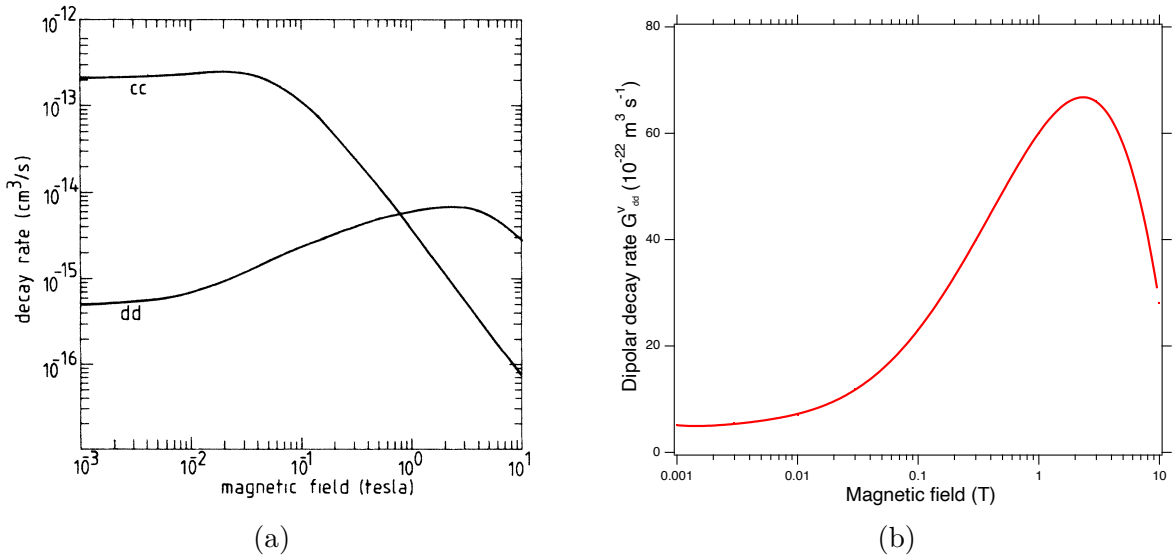


**Figure 3.18.** (a) A plot of the decay rate for the two-body dipolar spin exchange interaction for cc and dd state. (b) A plot of the decay rate of the dipolar spin exchange interaction for d+d states as a function of magnetic field magnitude. Lowering the magnetic field is key for reducing the losses from this interaction.

2103 background field magnitude is through the rate of dipolar spin-flips caused by a spin  
2104 exchange interaction between trapped atoms [58].

2105 Atomic tritium is a simple quantum system with a hyperfine structure given by the  
2106 addition of the nuclear and atomic spins. The addition of two spins leads to a hyperfine  
2107 structure with four states in the  $(m_s, m_I)$  basis [59]. The states with atomic spins directed  
2108 antiparallel to the magnetic field have  $m_s = -1/2$  and are labeled as the a and b states.  
2109 The a and b states are colloquially known as high-field seeking states, since their energy is  
2110 minimized when in regions of higher magnetic field. This leads to losses in the magnetic  
2111 trap as these atoms are drawn to higher fields away from the trap center. Alternatively,  
2112 the c and d states, with atomic spin  $m_s = +1/2$ , minimize their energy in low magnetic  
2113 fields because of the parallel alignment between spin and the magnetic field. Therefore,  
2114 these low-field seeking states tend to stay trapped significantly longer than the high-field  
2115 seeking states.

2116 It would be advantageous to prepare tritium atoms in purely c and d states before  
2117 trapping; however, even in this case losses still occur due to dipolar interactions between  
2118 pairs of c and d states leading to flipped atomic spins and subsequent losses from high-  
2119 field seeking atoms. The rate of these interactions depends on the magnitude of the  
2120 background magnetic field and is maximal for dd interactions around 1 T (see Figure  
2121 3.18). The rate of losses from these interactions at 1 T requires atomic tritium production  
2122 at a rate two orders of magnitude larger than at 0.1 T, thus, requirements on the whole  
2123 atomic tritium system are significantly relaxed at lower magnetic fields, which provides  
2124 powerful argument for moving to lower frequencies with the pilot-scale experiments and  
2125 Phase IV.

### 2126 **3.5.2 Pilot-scale Experiment Concepts**

2127 While the pilot-scale experiments are still in the early stages, enough is known to sketch  
2128 the general features of these experiments at the conceptual level. Development of the  
2129 antenna-based experiment has been suspended in favor of the cavity-based experiment.

#### 2130 **Pilot-scale Antenna Array CRES Experiment Concept**

2131 A conceptual design for an antenna-based CRES experiment is shown in Figure 3.19. A  
2132 large solenoid magnet provides a uniform background magnetic field less than 0.1 T in  
2133 magnitude. Inside this region is the atom trapping magnet that generates a high magnetic  
2134 field at the walls, which decays exponentially towards the central region. Known magnet

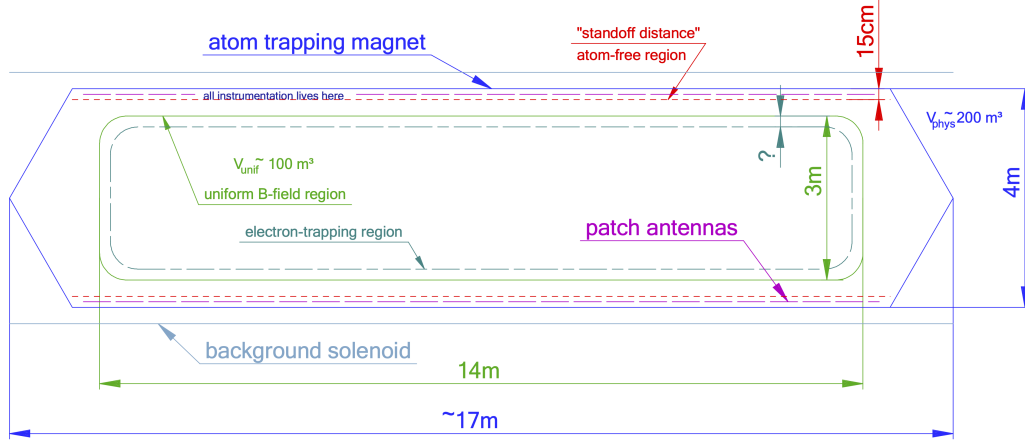


**Figure 3.19.** A conceptual sketch of a large-volume antenna array based CRES experiment to measure the neutrino mass.

designs that produce suitable atom trapping fields include Ioffe-Pritchard traps [60], which use conducting coils, as well as a Halbach array [61] made from permanent magnets. Either magnet choice produces a region of high magnetic fields, which excludes atoms and allows for the placement of antennas inside the experiment.

Inside this region an array of microstrip patch antennas is inserted to collect the cyclotron radiation without providing a surface for atomic tritium recombination. Due to the lower frequency of cyclotron radiation antennas of a larger size can be used, which lowers the total number of antennas required to observe the experiment volume. Because of this scaling, the lower frequency experiment uses a similar number of antennas compared to a much smaller demonstrator experiment with a 1 T magnetic field.

The atomic tritium beamline that supplies fresh tritium atoms to the experiment is not shown in the figure. The general configuration matches the one shown for the pilot-scale cavity experiment (see Figure 3.20).

### 2148 Pilot-scale Cavity CRES Experiment Concept

2149 The pilot-scale cavity experiment includes both an atomic tritium system and cavity  
 2150 CRES system. The atomic system consists of a thermal atom cracker located at the start  
 2151 of an evaporatively cooled atomic beamline. The atomic tritium system provides a supply  
 2152 of tritium atoms to the trap with temperatures on the order of a few mK. Atoms at this  
 2153 temperature can be trapped magneto-gravitationally, which is the reason for the vertical  
 2154 orientation of the cavity. At these low magnetic fields the trapping requirements for  
 2155 electrons and atoms differ enough such that it is advantageous to decouple the trapping

2156 potentials to avoid radioactive heating of the tritium atoms from excess trapped electrons.  
2157 Electron trapping is provided by a set of magnetic pinch coils at the top and bottom of  
2158 the cavity and a multipole Ioffe or Halbach magnet serves to contain the atoms.

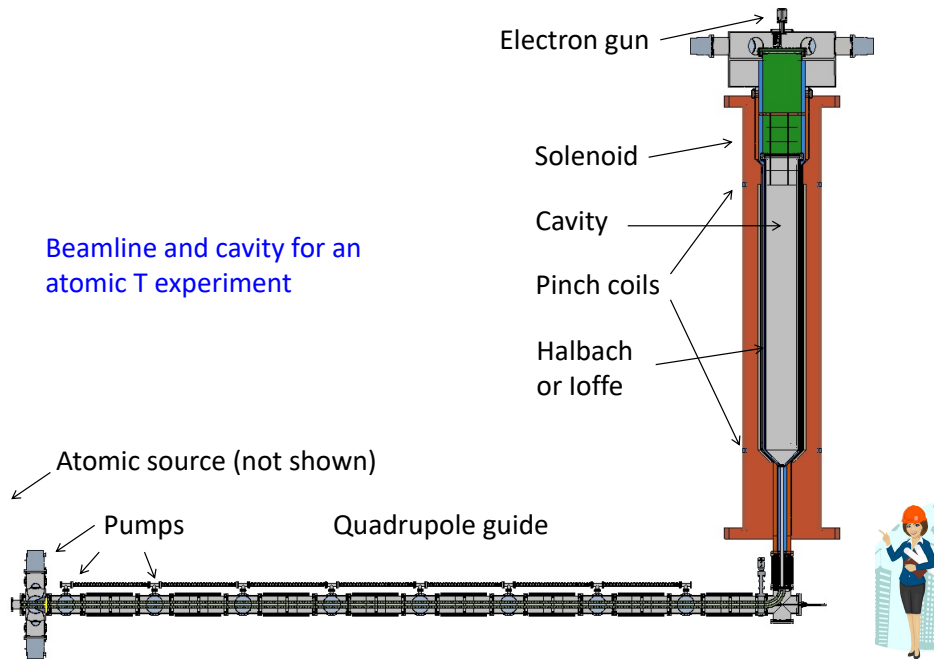


**Figure 3.20.** A conceptual sketch of a pilot-scale cavity CRES experiment with an atomic tritium beamline.

2159 The cavity design for the pilot-scale experiment consists of a large cylindrical cavity  
2160 with a TE011 resonance of 325 MHz. Such a cavity is truly enormous, with a diameter of  
2161 approximately 1.2 m and a height of 11 m. When an electron is produced inside the cavity  
2162 with a cyclotron frequency that matches the TE011 resonant frequency, its cyclotron  
2163 orbit couples the electron to the TE011 mode, which drives a resonance in the cavity.  
2164 These resonant fields can be read-out using an appropriate cavity coupling mechanism  
2165 located at the center of the cavity. For more information on the cavity approach to  
2166 CRES see Chapter 6.

2167 The bottom of the cavity has a cone termination to match the contour of the atom  
2168 trapping magnet. This shape still allows for TE011 resonances with high internal Qs,  
2169 which are required for good SNR in the cavity experiment. A small opening in the bottom  
2170 of the cone serves as an entry point for the tritium atoms. To allow for calibration of  
2171 the magnetic field inhomogeneities with an electron gun, the top of the cavity is left  
2172 nearly completely open. Normally, this would drastically lower the Q-factor of the TE011  
2173 mode, but a specially configured coaxial partition is inserted at the top. This termination

2174 scheme is designed to act as a perfect short for the TE011 mode since the circular shape  
2175 of the partition matches the electric field boundary conditions for the TE011 mode.  
2176 Simulations with HFSS have confirmed that this design results in a high quality TE011  
2177 resonance despite the nearly completely open end.

## 2178 3.6 Phase IV

2179 The baseline CRES technology being pursued by Project 8 are resonant cavities, which,  
2180 due to their geometric properties, simple CRES signal structure, and low channel  
2181 count, appear to be the better option for Phase IV. The current knowledge of the  
2182 antenna array CRES approach reveals no technical obstacles that would preclude it  
2183 as a baseline technology for Phase IV, though it would certainly be significantly more  
2184 expensive. Therefore, antenna arrays represent a fallback approach if resonant cavities  
2185 prove infeasible.

2186 The sensitivity of the pilot-scale atomic tritium experiment is estimated to be on  
2187 the order of 0.1 eV, which means that increasing the sensitivity to reach the Phase IV  
2188 goal will require an even larger experiment. Because of the direct coupling between the  
2189 RF characteristics of a cavity and its geometry, the baseline plan is to build multiple  
2190 copies of the pilot-scale experiment (see Figure 3.21) to obtain the required amount of  
2191 volume rather than increase the size of the cavity beyond the pilot-scale. The built-in  
2192 redundancy of this approach is useful in the sense that the experiment has no single  
2193 point of failure, additionally, building several copies of the pilot-scale experiment will  
2194 minimize new engineering and design effort.

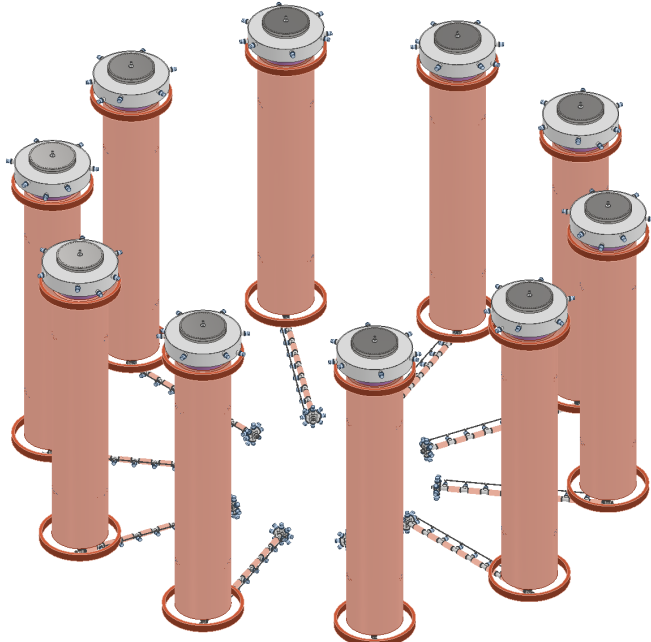


**Figure 3.21.** An illustration of a possible arrangement of ten pilot-scale cavity experiments for Phase IV. The experiments are arranged in a circle with an approximate diameter of 50 meters. Each atomic beamline connected to the bottom of each cavity is approximately 10 m in length. The cavities themselves are designed to operate at 325 MHz and are approximately 11 m tall. The circular arrangement of cavities has some advantages when it comes to cancellation of fringe fields from neighboring magnets, which is important due to the small magnetic field magnitudes consistent with these CRES frequencies. The advantage of ten independent atomic sources and cavities is that there is no single point of failure for the experiment. If an experiment goes down for repairs the other nine may continue running. Figure courtesy of Michael Huehn at UW-Seattle.

## **Chapter 4**

# **Signal Reconstruction Techniques for Antenna Array CRES and the FSCD**

### **4.1 Introduction**

An antenna array CRES (Cyclotron Radiation Emission Spectroscopy) experiment introduces new challenges related to data acquisition, signal detection, and signal reconstruction caused by the multi-channel nature of the data. The development of signal reconstruction algorithms [62] is crucial for the design of antenna array based experiments like the FSCD (Free Space CRES Demonstrator, described in Section 3.4.2), because these algorithms directly influence the detection efficiency and energy resolution of the CRES experiment. In this Chapter I summarize my contributions to the development and analysis of signal reconstruction and detection algorithms for the FSCD experiment.

In Section 4.2 I discuss the primary tool for this work, which is the Locust simulations package developed by the Project 8 experiment. Locust is used to simulate CRES events in the detector, which begins with calling a second software package — Kassiopeia — to calculate particle trajectory solutions for electrons in the magnetic trap. The trajectories are subsequently used to calculate the response of the antenna array to the cyclotron radiation produced by the electron, which results in signals that can be used to analyze the performance of different signal reconstruction algorithms. More recently, Project 8 has developed CREsana, which is a new simulations package that takes an analytical approach to CRES signal simulations. Although CREsana signals were not used for the signal reconstruction algorithm development, I introduce the software as it is the simulation software used to model the antenna array measurements presented in Section 5.4 in the next chapter.

In Section 4.3 I discuss the signal reconstruction and detection approaches analyzed for the FSCD experiment. In general there are two steps to signal reconstruction — detection

and parameter estimation. With signal detection one is concerned with distinguishing between data that contains a signal versus data that contains only noise; whereas, with parameter estimation one extracts the kinematic parameters of the electron encoded in the cyclotron radiation signal shape. Due to the low signal power of electrons near the spectrum endpoint in the FSCD experiment, signal detection is a non-trivial problem. This is magnified by the need to maximize the detection efficiency of the experiment in order to achieve the neutrino mass sensitivity goals. My contributions to signal reconstruction analyses for the FSCD are focused on the signal detection component of reconstruction.

After discussing various signal detection approaches, in Section 4.4 I present a detailed analysis of the detection performance of three algorithms, which could be used to signal detection in the FSCD. This section was prepared for publication in JINST as a separate paper. The algorithms include a digital beamforming algorithm, a matched filter algorithm, and a neural network algorithm, which I analyze in terms of classification accuracy and estimated computational cost.

## 4.2 FSCD Simulations

Antenna array CRES and the FSCD require a combination of different capabilities not often found in a single simulation tool. In particular, accurate calculations of the magneto-static fields produced by current-carrying coils are needed to accurately model the magnetic trap and background magnets. The resulting magnetic fields must then be used to calculate the exact relativistic trajectory of electrons. The electron trajectories are required to calculate the electro-magnetic (EM) fields produced by the acceleration of the electron. Finally, the simulation must model the interaction of the antenna and RF (radio-frequency) receiver chain with the EM-fields in order to yield the simulated voltage signals from the antenna array. No available simulation tools adequately perform these combined functions; therefore, Project 8 developed a custom simulation framework to simulate the FSCD and CRES. This simulation framework includes custom simulation tools developed by Project 8, as well as open-source and proprietary software developed by third-parties.

2250 **4.2.1 Kassiopeia**

2251 Kassiopeia<sup>1</sup> is a particle tracking and static EM-field solver developed by the KATRIN  
2252 collaboration for simulations of their spectrometer based on the MAC-E (magnetic  
2253 adiabatic collimation with electrostatic) filter technique [63]. Unfortunately, Kassiopeia is  
2254 not designed to solve for the EM-fields radiated by electrons in magnetic fields. However,  
2255 it does provide efficient solvers for static electric and magnetic fields and charged particle  
2256 trajectory solvers. Because of this, Project 8 has incorporated parts of Kassiopeia into  
2257 the Locust simulation framework.

2258 **Magnetostatic Field Solutions**

2259 The solutions to the electric and magnetic fields generated by a static configuration of  
2260 charges and currents is given by Maxwell's equations in the limit where the time-dependent  
2261 terms go to zero. In their static form Maxwell's equations [49] are

$$\nabla \cdot \mathbf{E} = \frac{\rho}{\epsilon_0} \quad (4.1)$$

$$\nabla \times \mathbf{E} = 0 \quad (4.2)$$

$$\nabla \cdot \mathbf{B} = 0 \quad (4.3)$$

$$\nabla \times \mathbf{B} = \mu_0 \mathbf{J}, \quad (4.4)$$

2262 where it can be seen that the electric and magnetic fields are completely decoupled from  
2263 one another. The solution for the magnetic field in this boundary value problem is given  
2264 by the Biot-Savart law

$$\mathbf{B}(\mathbf{r}) = \frac{\mu_0}{4\pi} \int dr' \frac{r'^3 \mathbf{J}(\mathbf{r}') \times (\mathbf{r} - \mathbf{r}')}{|\mathbf{r}' - \mathbf{r}|^3}, \quad (4.5)$$

2265 which Kassiopeia can use a variety of numeric integration techniques to solve for a  
2266 particular current distribution.

2267 **Kassiopeia Simulation of the FSCD Magnetic Trap**

2268 The trap developed for the FSCD experiment utilizes six current carrying coils, which  
2269 surround a cylindrical tritium containment vessel (see Figure 4.1). Some important  
2270 aspects of the trap design include the total trapping volume, the maximum trap depth,

---

<sup>1</sup><https://github.com/KATRIN-Experiment/Kassiopeia>

the steepness of the trap walls, as well as the radial and azimuthal uniformity of the magnetic fields.

The volume of the FSCD trap is a cylindrically shaped region with a radius of 5 cm and a length of 15 cm resulting in a roughly 1 L total trap volume. The trap volume is an important design feature, because it sets the volume of the experiment that is potentially usable for CRES measurements. Trapping a larger volume allows one to observe a larger number of tritium atoms, which increases the statistical power and sensitivity of the neutrino mass measurement. Due to the cost of constructing magnets with large and uniform magnetic fields it is important that the trap use as much of the available volume as possible to limit the overall cost of the experiment.

Coil	Radius (mm)	Z Pos. (mm)	Current (Amp. $\times$ Turns)
1	50.0	-92.3	750.0
2	50.1	-56.9	-220.3
3	68.5	-19.5	-250.0
4	68.5	19.5	-250.0
5	50.1	56.9	-220.3
6	50.0	92.3	750.0

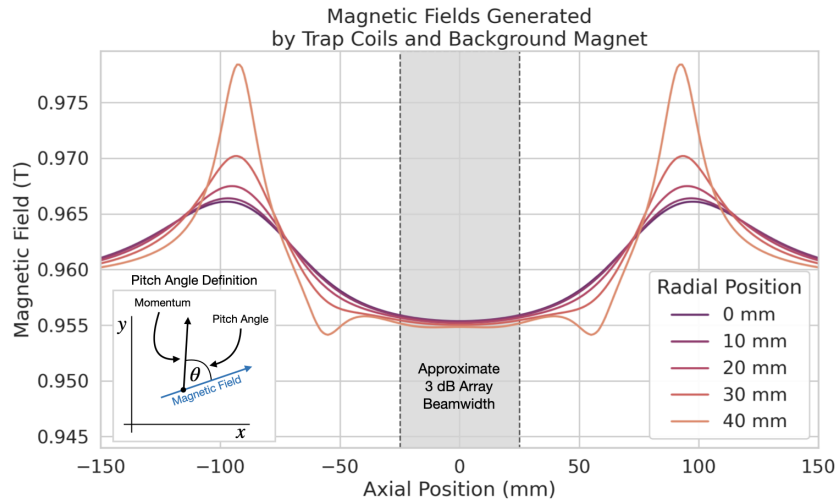
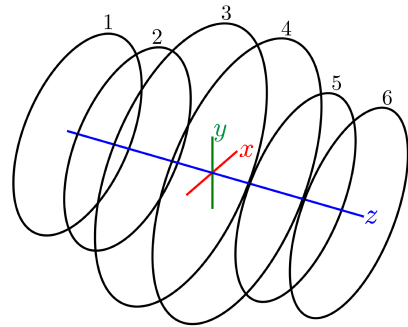


**Figure 4.1.** The geometry and parameters of the coils used to simulate the FSCD magnetic trap in Kassiopeia. Some axial profiles of the magnetic trap at different radial positions are shown to demonstrate the shape of the magnetic field and trap depth as a function of position. Calculation of the magnetic field profiles was graciously done by René Reimann.

The depth of the FSCD trap is approximately 10 mT when measured along the central axis, which is sufficient to trap electrons with pitch angles as small as 84°. The trap depth influences the efficiency of the experiment by directly controlling the range of

2284 electron pitch angles that can be trapped. If a higher fraction of pitch angles are trapped,  
2285 in principle, more decay events can be observed. However, the signals from electrons  
2286 with small pitch angles are significantly harder to detect in the FSCD than large pitch  
2287 angles, which increases the likelihood of not detecting the first track of the CRES event  
2288 and harms the energy resolution of the experiment.

2289 The steepness of the trap walls as well as non-uniformities in the magnetic field  
2290 contribute to the total energy resolution of the CRES measurement by causing uncertainty  
2291 in the relationship between an electron's kinetic energy and its cyclotron frequency. When  
2292 an electron is trapped, it oscillates back and forth along the trap z-axis (see Figure 4.1)  
2293 unless it has a pitch angle of exactly 90° [64]. As the electron is reflected from the trap  
2294 walls it experiences a change in the total magnetic field, which causes a modulation in the  
2295 cyclotron frequency. This change in magnetic field from the trap introduces a correlation  
2296 between the pitch angle and kinetic energy parameters of the electron that can reduce  
2297 energy resolution. In order to mitigate this effect it is important to make the trap walls  
2298 as steep as possible.

## 2299 Particle Trajectory Solutions

2300 The magnetic fields solved by direct integration of the coil current densities are used to  
2301 calculate the trajectories of electrons based on user specified initial conditions. Various  
2302 statistical distributions are available, which can be sampled to replicate realistic event  
2303 statistics. These include uniform, Gaussian, and Lorentzian distributions among others.  
2304 In general, an electron has six kinematic parameters that define its trajectory, which are  
2305 the three-dimensional coordinates of the initial position and the three components of the  
2306 electron's momentum vector. However, when simulating CRES events it is common to  
2307 parameterize the electron's trajectory in terms of the initial position, kinetic energy, pitch  
2308 angle, and initial direction of the component of the electron's momentum perpendicular  
2309 to the magnetic field. This parameterization is completely equivalent to specifying the  
2310 starting position and momentum vectors.

2311 From the initial parameters of the electron and the magnetic field, Kassiopeia solves  
2312 for the trajectory of the electron. The direct approach proceeds by solving the motion of  
2313 the electron using the Lorentz force equation, which takes the form of a set of differential  
2314 equations

$$\frac{d\mathbf{r}}{dt} = \frac{\mathbf{p}}{\gamma m} \quad (4.6)$$

$$\frac{d\mathbf{p}}{dt} = e(\mathbf{E} + \frac{\mathbf{p} \times \mathbf{B}}{\gamma m}), \quad (4.7)$$

where  $\mathbf{r}$  is the position of the electron,  $\mathbf{p}$  is the electron's momentum,  $e$  is the charge of the electron,  $m$  is the electron's mass, and  $\gamma$  is the relativistic Lorentz term. Kassiopeia solves this pair of differential equations using numerical integration, however, the exact trajectory can be computationally intensive to solve. If the adiabatic approximation can be applied, then Kassiopeia can make use of a simpler set of equations that can be more readily solved numerically.

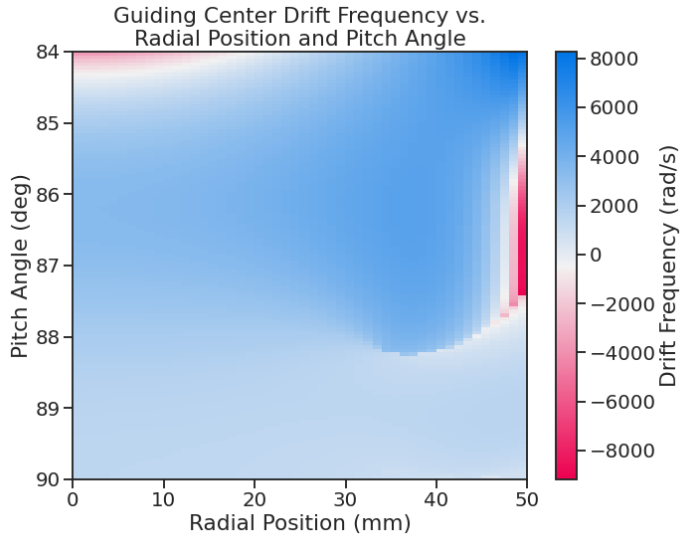


**Figure 4.2.** A map of the average  $\nabla B$ -drift frequency for electrons trapped in the prototype FSCD trap shown in Figure 4.1. Negative drift frequencies indicate electrons that are drifting opposite to the standard direction, which means that they are close to escaping the magnetic trap.

Though Kassiopeia is not directly capable of simulating the cyclotron radiation, it is an invaluable CRES simulation tool. With Kassiopeia it is possible to test the efficiency of a particular trap design, and analyze features of the electron trajectories that are important to the position, track, and event reconstruction (see Section 4.3). An example is the analysis of the average  $\nabla B$ -drift frequency as a function of the electrons radial position and pitch angle in the FSCD trap (see Figure 4.2). Radial gradients in the trap cause the guiding center of the electron to drift around the center of the magnetic trap with an average frequency on the order of  $10^3$  rad/s. This frequency, while slow compared to the length of a typical CRES time-slice, is large enough to cause a significant loss in efficiency of certain signal reconstruction algorithms. Therefore, it is important to model

2331 the drift of the electron in the reconstruction algorithm in order to mitigate the effects  
2332 of this motion on the reconstruction.

### 2333 4.2.2 Locust

2334 The Locust<sup>2</sup> software package [65] is the primary simulation tool developed and used  
2335 by the Project 8 collaboration for CRES experiments. Locust simulates the responses  
2336 of antennas and receiver electronics chain to rapidly time-varying electric fields using  
2337 a flexible approach that allows one to choose from a variety of electric field sources  
2338 and antennas. Similarly, one can simulate the receiver chain using a series of modular  
2339 generators that include standard signal processing operations such as down-mixing and  
2340 fast Fourier transforms (FFT). Since the primary focus of this chapter is the application  
2341 of Locust to analyses of the FSCD, I shall describe only the most relevant aspects of the  
2342 software rather than provide a comprehensive description.

### 2343 Cyclotron Radiation Field Solutions

2344 Simulating CRES events in the FSCD requires one to calculate the electric fields produced  
2345 by the acceleration of the electron. In the general case, this can be a complicated  
2346 computation, due to back-reaction forces on the electron. However, in the case of the  
2347 FSCD it is possible to ignore such effects and approximate the electron as radiating into  
2348 a free-space environment.

2349 The equations that describe the EM fields from a relativistic moving point particle  
2350 are the Liénard-Wiechert equations [66, 67], which are obtained by differentiating the  
2351 Liénard-Wiechert potentials. In their full form, the Liénard-Wiechert field equations are

$$\mathbf{E} = e \left[ \frac{\hat{n} - \boldsymbol{\beta}}{\gamma^2(1 - \boldsymbol{\beta} \cdot \hat{n})^3 |\mathbf{R}|^2} \right]_{t_r} + \frac{e}{c} \left[ \frac{\hat{n} \times [(\hat{n} - \boldsymbol{\beta}) \times \dot{\boldsymbol{\beta}}]}{(1 - \boldsymbol{\beta} \cdot \hat{n})^3 |\mathbf{R}|} \right]_{t_r} \quad (4.8)$$

$$\mathbf{B} = [\hat{n} \times \mathbf{E}]_{t_r}, \quad (4.9)$$

2352 where  $e$  is the charge of the particle,  $\hat{n}$  is the unit vector pointing from the particle to  
2353 the position where the fields are calculated,  $\boldsymbol{\beta}$  and  $\dot{\boldsymbol{\beta}}$  are the velocity and acceleration  
2354 of the particle divided by the speed of light ( $c$ ),  $\mathbf{R}$  is the distance from the particle to  
2355 the field calculation position, and  $\gamma$  is the relativistic Lorentz term. The subscript  $t_r$   
2356 indicates that the equations are evaluated at the retarded time so that the time-delay  
2357 from the travel time of the electromagnetic radiation is taken into account.

---

<sup>2</sup>[https://github.com/project8/locust\\_mc/tree/master](https://github.com/project8/locust_mc/tree/master)

2358        The only required input to calculate the electric field at the position of an FSCD  
 2359        antenna is the velocity and acceleration of the electron, which can be obtained from  
 2360        Kassiopeia simulations. Therefore, when simulating a CRES event Locust first runs  
 2361        a Kassiopeia simulation of the electron and subsequently calculates the electric field  
 2362        incident on the antenna. This requires one to calculate the retarded time. The retarded  
 2363        time corresponds to the time that a photon, which has just arrived at an antenna at  
 2364        the space-time position  $(t, \mathbf{r})$ , was actually emitted by the electron at the space-time  
 2365        position of  $(t_r, \mathbf{r}_e(t_r))$ . To calculate the retarded time one solves

$$c(t - t_r) = |\mathbf{r} - \mathbf{r}_e(t_r)|, \quad (4.10)$$

2366        where the distance traveled by the photon between the measurement and retarded times  
 2367        is equal to the distance between the antenna and the electron at the retarded time.  
 2368        Locust solves Equation 4.10 using root finding algorithm to calculate the retarded time,  
 2369        which yields the electric field emitted by the electron, at the position of each antenna in  
 2370        the FSCD array.

### 2371        Antenna Response Modeling

2372        The electric field solutions are used to calculate the resulting voltages produced in the  
 2373        antenna. However, direct simulation of the antenna itself is computationally expensive,  
 2374        since it requires modeling the complex interactions of the electron's electric fields with  
 2375        charge carriers in the antenna. Direct simulation of the antenna in Locust is avoided by  
 2376        modeling the antenna response using the antenna factor, or antenna transfer function.  
 2377        The antenna factor defines the voltage produced in the antenna terminal for an incident  
 2378        electric field [68],

$$A_F = \frac{V}{|\mathbf{E}|}, \quad (4.11)$$

2379        where  $V$  is the voltage and  $|\mathbf{E}|$  is the magnitude of the incident electric field. To obtain the  
 2380        antenna factor for the antennas developed for the FSCD Project 8 employs Ansys HFSS.  
 2381        HFSS is a commercially available finite element method electromagnetic solver widely  
 2382        used throughout the antenna engineering industry [69]. HFSS is capable of calculating  
 2383        the antenna factor and gain patterns for complex antenna designs and outputting the  
 2384        resulting quantities in the form of a text file that can be used as a configuration input to  
 2385        Locust.

2386        The antenna factor defines the steady-state response of the antenna to electromagnetic

2387 plane waves in the frequency-domain. Since the antenna response is calculated in the  
 2388 time-domain Locust models the antenna as a linear time-invariant system [70]. In this  
 2389 formalism the response of the system to the driving force is given by

$$y[n] = h * x = \sum_k h[k]x[n - k], \quad (4.12)$$

2390 where  $y[n]$  is the discretely sampled response,  $x$  is the driving force stimulus, and  $h$  is  
 2391 the finite impulse response (FIR) filter. When applied to the FSCD array, this formalism  
 2392 calculates the voltage time-series produced in each antenna by convolving the electric  
 2393 field time-series with the antenna FIR filter, which is obtained by performing an inverse  
 2394 Fourier transform on the transfer function from HFSS.

## 2395 Radio-frequency Receiver and Signal Processing

2396 After obtaining the voltage time-series by computing the electron trajectory and antenna  
 2397 response, Locust simulates the signal processing performed by the RF receiver chain.  
 2398 The simulated Locust receiver chain includes all operations that would be performed by  
 2399 the RF hardware (see Figure 4.3).

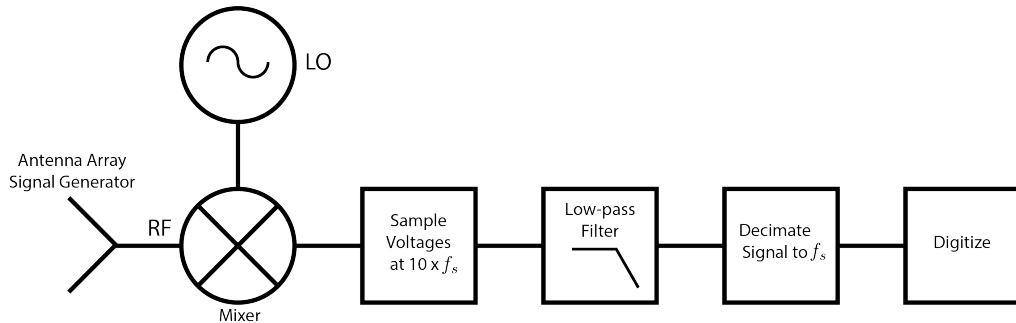


**Figure 4.3.** The receiver chain used by Locust when simulating CRES events in the FSCD.

2400 Frequency down-conversion reduces the digitization bandwidth required to read-out  
 2401 CRES data. According to the Nyquist sampling theorem [71], the minimal sampling rate  
 2402 that guarantees no information loss for a signal with a bandwidth  $\Delta f$  is given by

$$f_{\text{Nyq}} = 2\Delta f. \quad (4.13)$$

2403 The total bandwidth for CRES events ranges from 0 to 26 GHz in a 0.95 T magnetic field;  
 2404 therefore, direct digitization of CRES signals from the FSCD would require sampling  
 2405 frequencies greater than 50 GHz, which is infeasible for a real experiment. However, one

2406 need only measure the shape of the spectrum in the last 100 eV, which corresponds to a  
2407 frequency bandwidth of 5 MHz, to effectively measure the neutrino mass.

2408 Down-conversion is a technique for reducing the base frequencies of signals in a  
2409 bandwidth given by  $[f_{\text{LO}}, f_{\text{LO}} + \Delta f]$  to the bandwidth  $[0, \Delta f]$ , by performing the following  
2410 multiplication

$$x(t) \rightarrow x(t)e^{-2\pi f_{\text{LO}} t}. \quad (4.14)$$

2411 The signal,  $x(t)$ , is multiplied by a sinusoidal signal with frequency  $f_{\text{LO}}$  to reduce the  
2412 absolute frequencies of the signals in the bandwidth. In the FSCD, this allows one to  
2413 detect events in the last 100 eV of the tritium spectrum, while sampling the data far  
2414 below 50 GHz. The standard bandwidth used in the FSCD is 200 MHz, which allows for  
2415 higher frequency resolution than the minimum sampling frequency for 100 eV of energy  
2416 bandwidth.

2417 Directly simulating down-conversion with a frequency multiplication in Locust requires  
2418 sampling the electric fields at each antenna in the FSCD array with a period of  $\approx 20$  ps,  
2419 which is extremely slow computationally. To avoid this, Locust performs the down-  
2420 conversion by intentionally under-sampling the electric fields with a frequency of 2 GHz.  
2421 Sampling below the Nyquist limit causes the higher frequency components of the CRES  
2422 signal to alias, however, Locust can remove these aliased frequency peaks using a  
2423 combination of low-pass filtering and decimation to recreate frequency down-conversion.  
2424 After filtering and decimation, Locust simulates digitization by an 8-bit digitizer at a  
2425 sampling frequency of 200 MHz to recreate the conditions of the FSCD. The voltage  
2426 offset and digitizer range must be configured by the user based on the characteristics of  
2427 the simulation.

## 2428 Data

2429 The output of Locust simulations for the FSCD primarily consists of two data files. The  
2430 first is the electron trajectory information calculated by Kassiopiea, which is output in  
2431 the form of a `.root` file [72]. This file contains important kinematic information about  
2432 the electron such as its position and pitch angle as a function of time. The other file  
2433 is produced by Locust and contains the digitized signals acquired from each antenna  
2434 in the array. The Locust output files conform to the Monarch specification<sup>3</sup> developed  
2435 by Project 8, which is based on the commonly used HDF5 file format, and matches the  
2436 format of the files produced by the Project 8 data acquisition software. This makes it

---

<sup>3</sup><https://github.com/project8/monarch>

2437 possible to use the same data analysis code to analyze both simulated and real data.

### 2438 4.2.3 CRESana

2439 Locust is the primary simulation tool used by Project 8 in the development and simulation  
2440 of the FSCD. However, simulations of CRES events in larger antenna arrays ( $\geq 100$   
2441 antennas) can take several hours to complete, which is prohibitively long when one is  
2442 performing a sensitivity analysis and optimization. One reason for Locust's slow operation  
2443 is that the electric fields from the electron must be solved numerically for each time-step  
2444 for all antennas in the array. These numerical solutions allow Locust to accurately  
2445 simulate the electric fields from arbitrarily complicated electron trajectories at the cost  
2446 of more computations and slower simulations. Therefore, an additional simulation tool  
2447 that sacrifices the accuracy of numerical approaches for computational efficiency is a  
2448 useful tool for studying large antenna array experiments.

2449 Recently, Project 8 has developed a new simulations package called CRESana<sup>4</sup>, specif-  
2450 ically designed to perform analytical simulations of antenna-based CRES experiments.  
2451 CRESana provides a significant increase in simulation speed by using well-justified an-  
2452 alytical approximations of the electrons motion and electric fields in a magnetic trap.  
2453 The electric fields and signals generated by CRESana are consistent with theoretical  
2454 calculations of the electron's radiation, and are tested for accuracy using well-known  
2455 test-case simulations and consistency checks.

## 2456 4.3 Signal Detection and Reconstruction Techniques for 2457 Antenna Array CRES

### 2458 Antenna Array CRES Signal Reconstruction

2459 Antenna array CRES requires one to use the multichannel time-series obtained by  
2460 digitizing the array to estimate the starting kinetic energies of electrons produced in  
2461 the magnetic trap using CRES signal reconstruction algorithm. This procedure consists  
2462 of a multi-stage process of detecting a CRES signal followed by an estimation of the  
2463 electron's parameters.

2464 Antenna array CRES requires a significantly different approach to signal reconstruction  
2465 than previous Project 8 experiments. In Phases I and II, CRES was performed using a

---

<sup>4</sup><https://github.com/MCflowMace/CRESana>

2466 waveguide gas cell directly integrated into a waveguide transmission line. The transmission  
2467 line efficiently propagates the cyclotron radiation along its length to an antenna at the  
2468 ends of the waveguide. However, with an antenna array the electron is radiating into  
2469 free-space; therefore, the cyclotron radiation power collected by the array is directly  
2470 proportional to the solid angle surrounding the electron that is covered with antennas.  
2471 Because it is not practical to fully surround the magnetic trap with antennas, some of the  
2472 cyclotron radiation power that would have been collected by the waveguide escapes into  
2473 free-space. Furthermore, the power that is collected by the antenna array is split between  
2474 every channel in the antenna array, which significantly lowers the signal-to-noise ratio  
2475 (SNR) of CRES signals in a single antenna channel compared to a waveguide apparatus.  
2476 Therefore, a suite of completely new signal reconstruction techniques are needed in order  
2477 to perform CRES in the FSCD.

2478 Changes to the approach to CRES signal reconstruction are also motivated by the  
2479 scientific goals of Project 8. A measurement of the tritium beta-decay spectrum that is  
2480 sensitive to neutrino masses as small as 40 meV requires that we measure the kinetic  
2481 energies of individual electrons with a total energy broadening of 115 meV [73]. This  
2482 resolution includes all sources of uncertainty in the electron's kinetic energy such as  
2483 magnetic field inhomogeneities. This precise energy resolution is only achieved by an  
2484 event-by-event signal reconstruction approach where the kinetic energies, pitch angles,  
2485 and other parameters of the CRES events are estimated for individual electrons before  
2486 constructing the beta-decay spectrum.

2487 The event-by-event approach is distinct from the analysis done for the Phase I  
2488 and Phase II experiments, where the starting cyclotron frequency of the event was  
2489 measured by analyzing the tracks formed by the electron's carrier in a time-frequency  
2490 spectrogram. These frequencies were then combined into a frequency beta-spectrum,  
2491 which was converted to the beta-decay energy spectrum using an ensemble approach that  
2492 averaged over all other event parameters. The ensemble approach to signal reconstruction  
2493 results in poor energy resolution because other kinematic parameters such as pitch angle  
2494 change the cyclotron carrier frequency due to changes in the average magnetic field  
2495 experience by the electron.

## 2496 Components of Reconstruction: Signal Detection and Parameter Estimation

2497 CRES signal reconstruction is a two-step procedure consisting of signal detection followed  
2498 by parameter estimation. In the former, one is concerned with identifying CRES signals  
2499 in the data regardless of the signal parameters; whereas, in the latter one operates under

2500 the assumption that a signal is present and then estimates it's parameters.

2501 More formally, signal detection can be posed as a binary hypothesis test between  
2502 the signal and noise data classes, and parameter estimation is a process of fitting a  
2503 signal model to the observed data. While both of these are required for a complete  
2504 reconstruction (see Figure 4.4), the focus of my work and this chapter is on the signal  
2505 detection aspect of antenna array CRES signal reconstruction.

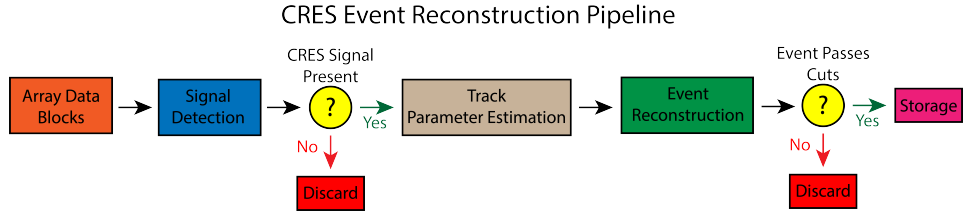


**Figure 4.4.** A high-level diagram depicting the process of CRES event reconstruction. The first step consists of identifying the presence of a signal in the data. This step is necessary to avoid the danger of performing a reconstruction of a false event, which would constitute a background contribution to the tritium spectrum measured by CRES.

## 2506 Detection Theory

2507 Signal detection is the process of deciding whether noisy data contains signal or noise,  
2508 which can be posed as a statistical hypothesis test [74]. For CRES signals, which are  
2509 represented by signal vectors with added white Gaussian noise (WGN), one needs to  
2510 choose between

$$\mathcal{H}_0 : \mathbf{y} = \boldsymbol{\nu} \quad (4.15)$$

$$\mathcal{H}_1 : \mathbf{y} = \mathbf{x} + \boldsymbol{\nu}, \quad (4.16)$$

2511 where  $\mathbf{y}$  is the CRES data vector,  $\boldsymbol{\nu}$  is a sample of WGN, and  $\mathbf{x}$  represents the CRES  
2512 signal. The hypothesis that the data contains only noise is labeled  $\mathcal{H}_0$  and the hypothesis  
2513 that the data contains a signal is labeled  $\mathcal{H}_1$ .

2514 For illustrative purposes, it is useful to study the case where only the first sample of  
2515 data is used to distinguish between  $\mathcal{H}_0$  and  $\mathcal{H}_1$ . The value of the first data sample is  
2516 distributed according to two possible Gaussian distributions(see Figure 4.5). By setting a  
2517 decision threshold on the value of this sample, one can choose the correct hypothesis with  
2518 a probability given by the area underneath the probability distribution curves. A true  
2519 positive corresponds to correctly identifying that the data contains signal; whereas, a true  
2520 negative means that one has correctly identified the data as noise. The rate at which the

2521 detector performs a true positive classification is given by the green region underneath  
 2522  $p(\mathbf{y}[0]; \mathcal{H}_0)$ , and the rate at which the detector performs a true negative classification is  
 given by the orange region underneath  $p(\mathbf{y}[0]; \mathcal{H}_1)$ . Two types of misclassifications are

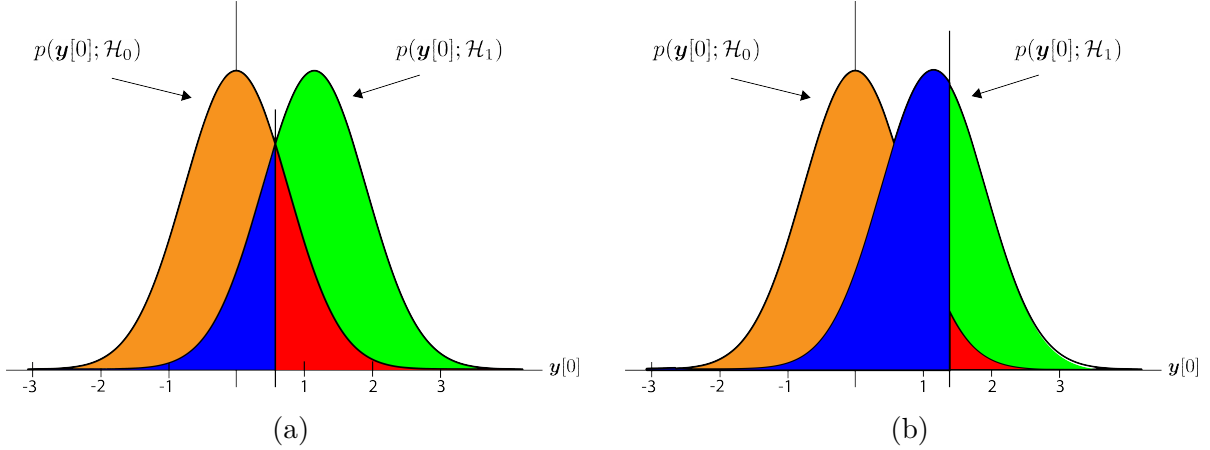


**Figure 4.5.** An illustration of two PDFs associated with a binary hypothesis test. The decision threshold is represented by the vertical line that partitions both distributions. The orange and red areas correspond to the true negative and false positive probabilities and the blue and green areas correspond to the false negative and true positive probabilities respectively. To decide between the two hypotheses the likelihood ratio test specified by the Neyman-Pearson theorem is applied. This approach achieves the highest true positive probability for a given false positive probability.

2523  
 2524 possible. Either one declares noise data as signal, which is called a false positive, or one  
 2525 declares signal data as noise, which is a false negative. Note that it is only possible to  
 2526 trade off these two types of errors by tuning the detection threshold. One cannot reduce  
 2527 the rate of false positives without also increasing the rate of false negatives.

2528 The approach taken with CRES signals is to fix the rate of false positives by setting  
 2529 a minimum decision threshold value. The rate of false positives that is acceptable at the  
 2530 detection stage depends upon the total rate of background events compatible with the  
 2531 sensitivity goals of the experiment. The ultimate goal of a neutrino mass measurement  
 2532 with 40 meV sensitivity in general has strict requirements on the number of background  
 2533 events, which requires a relatively high detection threshold to achieve. Consequently,  
 2534 the ideal signal detection algorithm is the one that achieves the maximum rate of true  
 2535 positives for a fixed rate of false positives, so that the detection efficiency of the experiment  
 2536 is maximized and potential sources of background are kept to a minimum.

2537 According to the Neyman-Pearson theorem [75], the statistical hypothesis test that  
 2538 maximizes the probability of detection for a fixed rate of false positives is the likelihood  
 2539 ratio test, which is formed by computing the ratio of the signal likelihood to the noise

2540 likelihood,

$$L(x) = \frac{P(\mathbf{y}; \mathcal{H}_1)}{P(\mathbf{y}; \mathcal{H}_0)} > \gamma. \quad (4.17)$$

2541 Here, the likelihood of the hypotheses  $\mathcal{H}_0$  and  $\mathcal{H}_1$  are described by the probability

2542 distributions  $P(\mathbf{y}; \mathcal{H}_0)$  and  $P(\mathbf{y}; \mathcal{H}_1)$  respectively, and  $\gamma$  is the threshold for deciding  $\mathcal{H}_1$ .

2543 The decision threshold is determined by integrating  $P(\mathbf{y}; \mathcal{H}_0)$  such that

$$P_{FP} = \int_{\gamma}^{\infty} P(\tilde{\mathbf{y}}; \mathcal{H}_0) d\tilde{\mathbf{y}} = \alpha, \quad (4.18)$$

2544 where  $\alpha$  is the desired false positive detection rate given by the red colored areas shown

2545 in Figure 4.5. The true positive detection rate is given by the similar integral

$$P_{TP} = \int_{\gamma}^{\infty} P(\tilde{\mathbf{y}}; \mathcal{H}_1) d\tilde{\mathbf{y}}, \quad (4.19)$$

2546 which corresponds to the green areas in Figure 4.5.

2547 Changing the decision threshold allows one to trade-off between  $P_{TP}$  and  $P_{FP}$  as  
2548 appropriate for the given situation. It is standard to summarize the relationship between  
2549  $P_{TP}$  and  $P_{FP}$  using the receiver operating characteristic (ROC) curve, which is obtained  
2550 by evaluating the true positive and false positive probabilities as a function of the decision  
threshold value (see Figure 4.6). The ROC curve provides a convenient way to compare

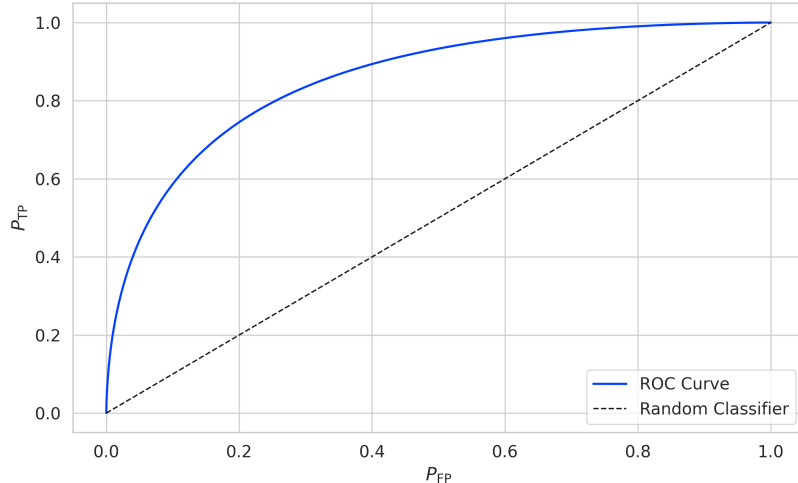


**Figure 4.6.** An example ROC curve formed by computing the  $P_{FP}$  and the  $P_{TP}$  for a given likelihood ratio test. As the decision threshold is increased  $P_{FP}$  decreases at the expense of a lower  $P_{TP}$ . The black dashed line indicates the lower bound ROC curve obtained by randomly deciding between  $\mathcal{H}_0$  and  $\mathcal{H}_1$ .

2551

2552 the performance of different signal detection algorithms. In general, a classifier with  
2553 a higher the  $P_{\text{TP}}$  as a function of  $P_{\text{FP}}$  is desirable, which corresponds to a larger area  
2554 underneath the respective ROC curve. A perfect classifier has an area underneath the  
2555 curve of 1.0, however, such a classifier is never achieved in practice.

### 2556 4.3.1 Digital Beamforming

#### 2557 Introduction to Beamforming

2558 Beamforming is an antenna array signal processing technique designed to enhance the  
2559 radiation of the array in a particular direction and suppress it in other directions [68].  
2560 Beamforming is of interest to Project 8 as a first level of signal reconstruction for the  
2561 FSCD and other antenna array CRES experiments, which operates at the signal detection  
2562 stage of reconstruction.

2563 Beamforming is performed using a phased summation of the signals received by the  
2564 antenna array. The beamforming phases are selected such that the signals emitted by  
2565 the array will constructively interfere at the point of interest (see Figure 4.7). As a  
2566 consequence of the principle of reciprocity [76], when the array is operating in receive  
2567 mode, the signals emitted from a source at the same point will constructively interfere  
2568 when summed. The origin of the phase delays in beamforming is the path-length difference  
2569 to the beamforming point between different antennas in the array. The relationship  
2570 between the phase delay and the path-length difference is given by the familiar equation

$$\phi = \frac{2\pi d}{\lambda}, \quad (4.20)$$

2571 where  $\phi$  is the phase delay,  $d$  is the path-length difference, and  $\lambda$  is the wavelength of  
2572 the radiation. In practice, one chooses the values of  $d$  by specifying the beamforming  
2573 positions of interest and then calculates the beamforming phases using Equation 4.20,  
2574 which is guaranteed to follow the constructive interference condition shown in Figure 4.7.

2575 Beamforming can be neatly expressed mathematically using the vector equation

$$y[n] = \Phi^T[n] \mathbf{x}[n], \quad (4.21)$$

2576 where  $\mathbf{x}[n]$  is the array snapshot vector,  $\Phi[n]$  is a vector of beamforming shifts, and  
2577  $y[n]$  is the resulting summed signal. The beamforming shifts consist of a set of complex

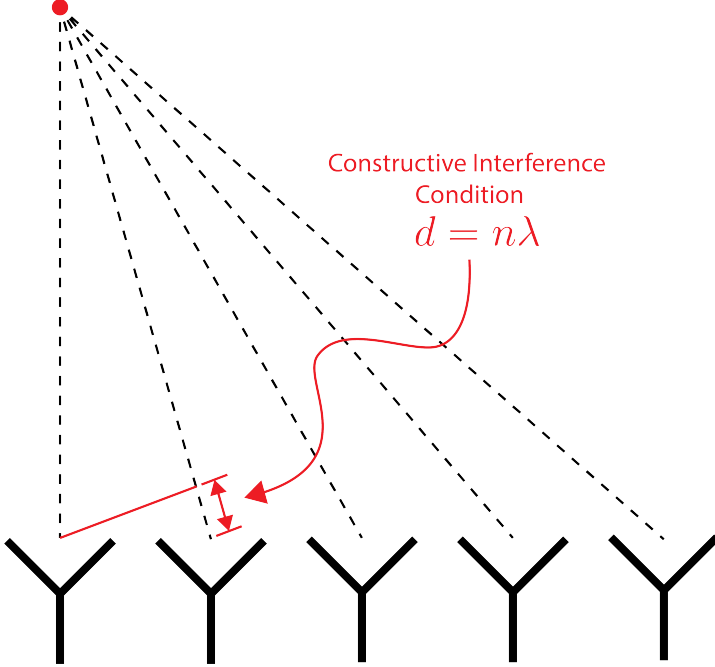


**Figure 4.7.** An illustration of the constructive interference condition which is the operating principle of digital beamforming using a uniform linear array as an example.

2578 numbers that contain the beamforming phase shift and an amplitude weighting factor,

$$\Phi[n] = [A_0[n]e^{-2\pi i \phi_0[n]}, A_1[n]e^{-2\pi i \phi_1[n]}, \dots, A_{N-1}[n]e^{-2\pi i \phi_{N-1}[n]}], \quad (4.22)$$

2579 where the set of magnitudes  $A_i[n]$  are amplitude weighting factors and  $\phi_i[n]$  are the  
 2580 phase shifts from the path-length differences. The index  $i$  is used to denote the antenna  
 2581 channel number. The amplitude weighting factor is the relative magnitude of the signal  
 2582 received by a particular antenna in the array. This factor properly accounts for antennas  
 2583 that are closer to the radiating source. In general, the beamforming phases can also be  
 2584 functions of time to track the motion of a non-stationary source.

2585 Digital beamforming specifically is the type of beamforming algorithm of interest to  
 2586 Project 8 for CRES. With digital beamforming, the phase shifts are applied to the array  
 2587 signals in software rather than employing fixed beamforming phase shifts in the receiver  
 2588 chain hardware. The advantage of digital beamforming is that for any given series of  
 2589 array data one can specify an arbitrarily large number of beamforming positions and  
 2590 search for electrons using a flexible and easily configurable beamforming grid.

2591 Digital beamforming can be viewed as the spatial filtering, which is a direct conse-  
 2592 quence of the constructive interference condition used to define the beamforming phases.

2593 Digital beamforming causes signals from multiple electrons at different positions in the  
2594 trap to be separated, because the interference condition will cause the signals from  
2595 electrons at other position to cancel out. This spatial filtering effect reduces pile-up that  
2596 could become an issue for large scale CRES experiments using a dense tritium source.

2597 Beamforming positions can be specified with arbitrary densities limited only by  
2598 the available computational resources. This provides a very straight-forward way to  
2599 estimate the position of the electron in the trap by using a dense grid of beamforming  
2600 positions and maximizing the output power of the beamforming summation over this  
2601 grid. This approach to position reconstruction is attractive due the requirements of an  
2602 event-by-event signal reconstruction, which needs an accurate estimation of the exact  
2603 magnetic field experienced by the electron in order to correctly estimate its kinetic  
2604 energy. Combined with an accurate map of the magnetic field inhomogeneities of the  
2605 trap obtained from calibrations, beamforming allows one to apply this magnetic field  
2606 correction with a spatial resolution that is a fraction of the cyclotron wavelength.

2607 **Laboratory Beamforming Demonstrations**

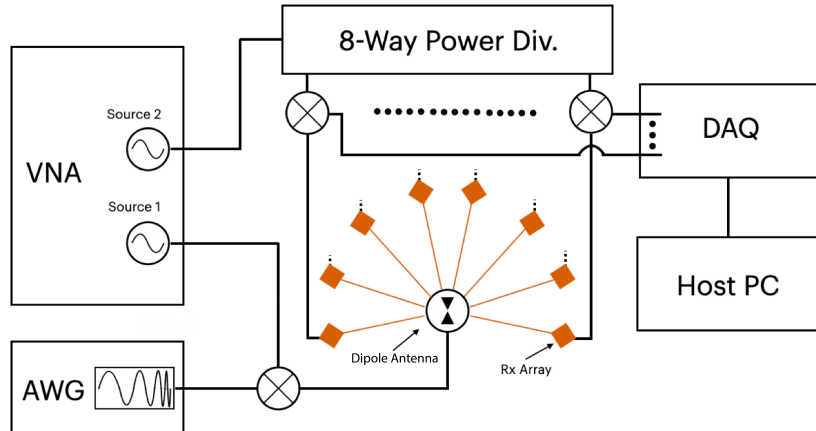


**Figure 4.8.** A system level diagram of the laboratory setup used for beamforming demonstrations at Penn State. For more information on this system see Chapter 5. Signals near 26 GHz are fed to a dipole antenna using an arbitrary waveform generator (AWG) and vector network analyzer (VNA), which drive a mixer. The dipole radiation is collected by an array of antennas connected to the digitizer data acquisition (DAQ) system.

2608 An antenna measurement setup was constructed at Penn State to serve as a testbed  
2609 for antenna prototypes and to perform laboratory validations of array simulations for  
2610 the FSCD. This system is discussed in more detail in Chapter 5. Early versions of

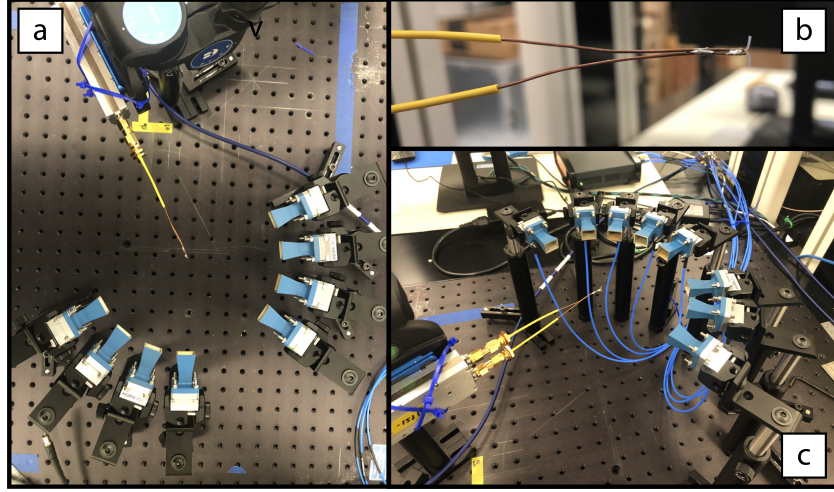


**Figure 4.9.** Photographs of the beamforming demonstration setup. In (a) I show a top-down view of the dipole antenna and the array of eight horn antennas. Manual repositioning of the horn antennas allows one to synthesize a full-circular antenna array. The dipole antenna is mounted on a camera tripod mount that allows for manual position tuning. (b) is a close up image of the dipole, which is manufactured from two segments of semi-rigid coaxial cable. (c) is another image of the dipole and array.

the antenna measurement system (see Figure 4.8 and Figure 4.9) were used to perform beamforming reconstruction studies of a simple probe antenna.

Signals from an arbitrary waveform generator were up-converted to 26 GHz using a mixer and a high-frequency source from a vector network analyzer and fed to a dipole antenna through a balun. The radiation from the dipole antenna was received by an array of horn antennas. The signals from the horn antennas were down-converted to baseband using a collection of mixers and an 8-way power divider. The signals were then digitized and saved to a host computer for analysis.

The data collected using the dipole and horn antenna array is reconstructed using the beamforming reconstruction approach specified in Section 4.3.1. A two-dimensional grid of xy-positions is defined and the beamforming phase shifts for each of these positions is calculated. The phased summation can be visualized by plotting the time-averaged power for each of the summations as a pixel in the resulting beamforming image (see Figure 4.10). White Gaussian noise (WGN) can be added to the data at this stage to simulate more realistic SNR if desired. The beamforming peak maxima is expected to have a Bessel function shape due to the circular symmetry of the array, and by analyzing the size of the beamforming maxima one can confirm that the beamforming reconstruction measurement has similar position resolution as expected from Locust simulations. Additionally, signal detection rates can be estimated from the data by

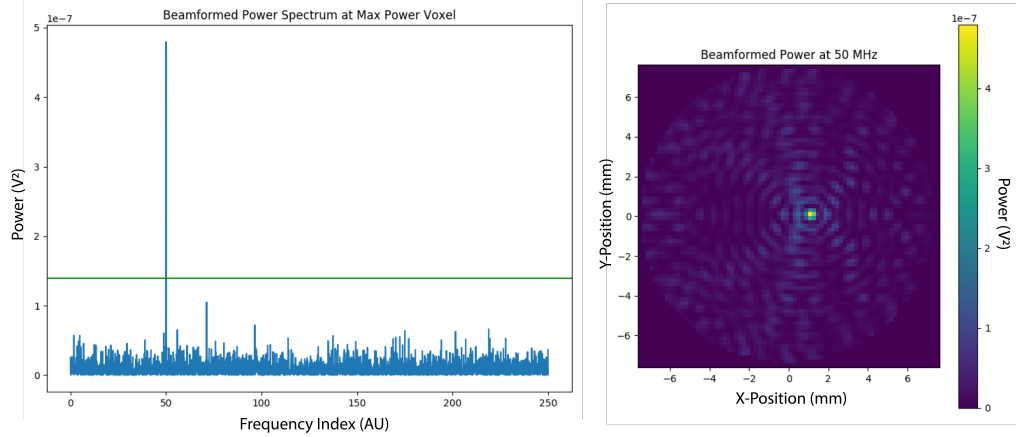


**Figure 4.10.** An example of digital beamforming reconstruction of a dipole antenna using a synthetic array of horn antennas. The beamforming image on the right is constructed by computing the time-averaged power of the summed signals for a two-dimensional grid of beamforming positions. In the image, one can see a clear maximum that corresponds to the position of the dipole antenna. On the left I show the frequency spectrum of the time-series at the maximum power pixel. White Gaussian noise is added to the signal to mimic a more realistic signal-to-noise-ratio. The signal emitted by the dipole is clearly visible as the high power peak in the frequency spectrum.

2630 comparing the magnitude of the beamforming signal peak in the frequency spectra to  
2631 simulation.

## 2632 FSCD Beamforming Simulations

2633 Locust simulations of the FSCD are used to generate simulated CRES signal data to  
2634 perform beamforming reconstruction studies. As mentioned in the previous section,  
2635 the beamforming procedure beings by specifying a set of beamforming positions and  
2636 corresponding beamforming shifts. The beamforming positions form a grid that covers  
2637 the region of interest. There are effectively an infinite number of ways to specify the  
2638 grid positions, however, uniform square grids are the most commonly used due to their  
2639 simplicity. In the actual experiment the number and pattern of beamforming positions  
2640 would be optimized to cover the most important regions of the trap volume, which  
2641 maximizes detection efficiency and minimizes superfluous calculations.

2642 The beamforming grids used for signal reconstruction with the FSCD consist of a set  
2643 of points that cover the two-dimensional plane formed by the perimeter of the antenna  
2644 array. The axial dimension is left out because electrons are treated as if they occupy only  
2645 their average axial position, which corresponds to the center of the magnetic trap. This  
2646 treatment is valid since it is impossible to resolve the axial position of the electron as a

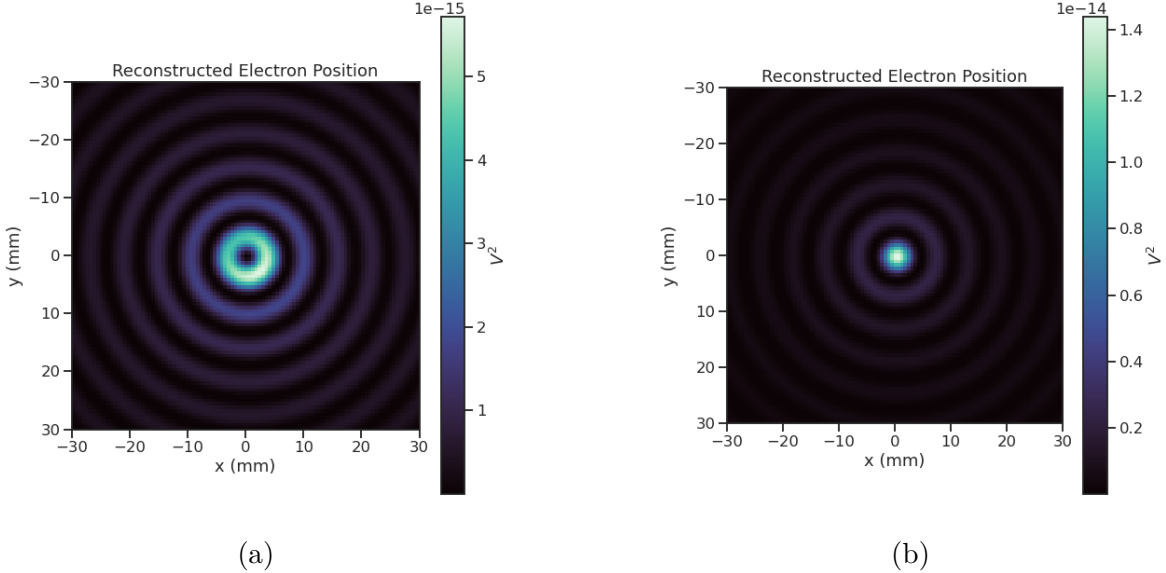


**Figure 4.11.** Beamforming images visualizing the reconstruction of an electron without (a) and with (b) the cyclotron phase correction. The images were generated using data from Locust simulations. The cyclotron phase refers to a phase offset equal to the relative azimuthal position of an antenna in the array. This phase offset is caused by the circular electron orbit and must be corrected for during reconstruction.

function of time due to the rapid oscillation frequencies of trapped electrons.

After beamforming, a summed time-series is obtained for each beamforming position that can be checked for a signal using a detection algorithm. A beamforming image is a visualization method that is equivalent to arranging the beamforming grid points according to their physical locations. Each pixel in the image corresponds to a summed time-series obtained for a digital beamforming position, and the image is obtained taking the time-averaged power at every pixel(see Figure 4.11).

If only the spatial beamforming phase component from Equation 4.20 is used, then the resulting image contains a ring-shaped feature centered on the position of the electron (see Figure 4.11a). The origin of this shape is an additional phase offset particular to a cyclotron radiation source. The circular cyclotron orbit introduces a relative phase offset to the electric fields equal to the azimuthal position of the field measurement point [77, 78]. Therefore, two antennas, one located at an azimuthal position of  $0^\circ$  and another located at an azimuthal position of  $90^\circ$ , will receive CRES signals out of phase by  $90^\circ$ , which is the difference in their azimuthal positions. This phase offset can be corrected by adding an additional term to the beamforming phase equation that is equal

2663 to the azimuthal position of the antenna relative to the electron,

$$\phi_i[n] = \frac{2\pi d_i[n]}{\lambda} + \Delta\varphi_i[n], \quad (4.23)$$

2664 where  $\Delta\varphi_i$  is difference between the azimuthal position of the electron and the  $i$ -th  
 2665 antenna channel. Using the updated beamforming phases changes the ring feature into  
 2666 the expected Bessel peak whose maximum corresponds to the position of the electron.  
 2667 Including this cyclotron phase correction significantly improves the signal detection and  
 2668 reconstruction capabilities of beamforming by more than doubling the summed signal  
 2669 power and shrinking the beamforming maxima feature size.

2670 The beamforming image examples in Figure 4.11 were produced using an electron  
 2671 located on the central axis of the magnetic trap, which do not experience  $\nabla B$ -drifts.  
 2672 However, electrons produced at non-zero radial position the beamforming phases must  
 2673 be made time-dependent to track the position of the electron's guiding center over  
 2674 time. Without this correction the  $\nabla B$ -drift causes the electron to move away from the  
 2675 beamforming position, which effectively spreads the cyclotron radiation power over a  
 wider area in the beamforming image (see Figure 4.12). This effect significantly reduces

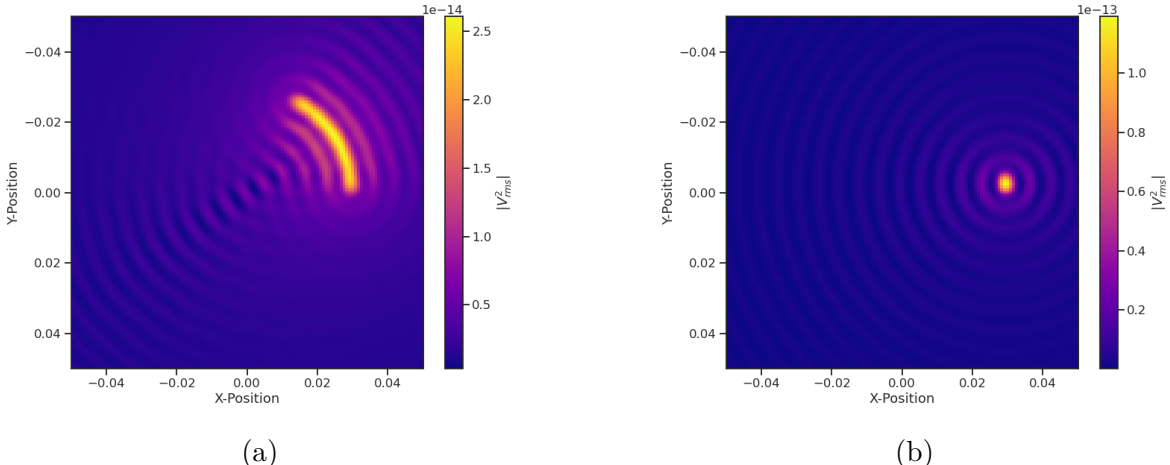


**Figure 4.12.** Beamforming images visualizing the reconstruction of an electron located off the central axis of the FSCD trap. In (a) beamforming is being performed without the  $\nabla B$ -drift correction, and in (b) it is included.

2676  
 2677 the power of the beamforming maxima and increases the size of the beamforming features,  
 2678 simultaneously harming detection efficiency and position reconstruction.

2679 The  $\nabla B$ -drift correction simply adds a circular time-dependence to the beamforming

2680 positions as a function of time,

$$r[n] = r_0 \quad (4.24)$$

$$\varphi[n] = \varphi_0 + \omega_{\nabla B} t[n], \quad (4.25)$$

2681 where  $\omega_{\nabla B}$  is the drift frequency and  $t[n]$  is the time vector. In the ideal case the  $\nabla B$ -drift  
2682 frequencies from Figure 4.2 for the correct pitch angle and radial position would be used,  
2683 however, it is not possible to know the electron's pitch angle a priori. In principle, one  
2684 could perform multiple beamforming summations for a given beamforming position using  
2685 different drift frequencies and choose the one that maximizes the summed power, but  
2686 this approach leads to a huge computational burden that would be impractical for a  
2687 real FSCD experiment. A compromise is to use an average value of  $\omega_{\nabla B}$  obtained by  
2688 averaging over the drift frequencies for electrons of different pitch angle at a particular  
2689 radius. This approach keeps the computational cost of time-dependent beamforming to a  
2690 minimum while still providing a significant increase in the detection efficiency of digital  
2691 beamforming.

## 2692 Signal Detection with Beamforming and a Power Threshold

2693 Up to this point I have neglected a specific discussion of how digital beamforming is used  
2694 for signal detection and reconstruction. Because, strictly speaking, digital beamforming  
2695 consists only of the phased summation of the array signals and cannot be used alone for  
2696 signal detection. The example beamforming images shown in Figure 4.11 and Figure 4.12  
2697 were produced using simulated data that contained no noise, which significantly degrades  
2698 the utility of analyzing the beamforming images for signal detection and reconstruction.

2699 In Project 8, digital beamforming as a detection algorithm is understood to mean  
2700 digital beamforming plus a power or amplitude threshold placed on the frequency  
2701 spectrum obtained by applying a fast Fourier transform (FFT) to the summed time-series  
2702 (see Figure 4.13). This approach is similar to the time-frequency spectrogram analysis  
2703 employed in Phase I and II. However, it is possible to use any signal detection algorithm  
2704 after beamforming. In Section 4.4 I analyze the signal detection performance of the  
2705 power threshold approach in detail.

2706 Without a reconstruction technique that coherently combines the signals from the  
2707 full antenna, the ability to detect CRES signals is drastically reduced (see Figure 4.13).  
2708 Because the CRES signals are in-phase at the correct beamforming position, the summed  
2709 power increases as a function of  $N^2$  compared to a single antenna channel, where  $N$  is

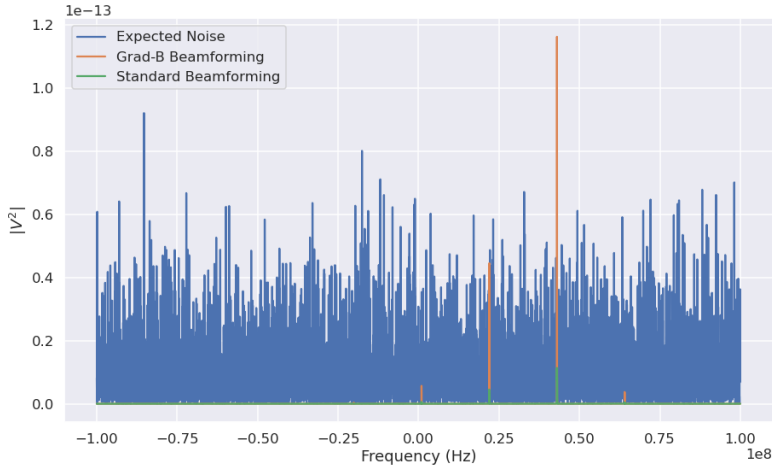


**Figure 4.13.** A plot of a typical frequency spectrum obtained by applying a Fourier transform to the time-series obtained from beamforming. The frequency spectra are plotted without noise on top of an example of a typical noise spectrum to visualize a realistic signal-to-noise ratio. In the example, without beamforming it would not be possible to detect anything since the signal amplitudes would be reduced by a factor of sixty relative to the noise. Additionally, it is clear the  $\nabla B$ -drift correction is needed to detect this electron in the presence of noise.

2710 the number of antennas. It is true that the noise power is also increased by beamforming,  
 2711 but, because the noise is incoherent, its power only increases linearly. Consequently, the  
 2712 SNR of the CRES signal increases linearly with the number of antennas, which greatly  
 2713 improves detection efficiency compared to using only the information in a single antenna.

2714 The power threshold detection algorithm searches for high-power frequency bins that  
 2715 should correspond to a frequency component of the CRES signal. In order to prevent  
 2716 random noise fluctuations from being mistaken as CRES signals the power threshold  
 2717 must be set high enough so that it is unlikely that random noise could be responsible. A  
 2718 consequence of this is that many electrons that can be trapped will go undetected because  
 2719 the modulation caused by axial oscillations leads to the cyclotron carrier power to falling  
 2720 below the decision threshold. The time-dependent beamforming used to correct for the  
 2721  $\nabla B$ -drift increases the volume of the magnetic trap where electrons can be detected,  
 2722 but it is ineffective at increasing the range of detectable pitch angles (see Figure 4.14).  
 2723 Fundamentally, this is because the power threshold only uses a fraction of the signal  
 2724 power to detect electrons and ignores the power present in the frequency sidebands. In  
 2725 the subsequent sections I examine two other signal detection algorithms that seek to  
 2726 improve the detection efficiency of the FSCD by utilizing the more of the signal shape to  
 2727 compute the detection test statistics.

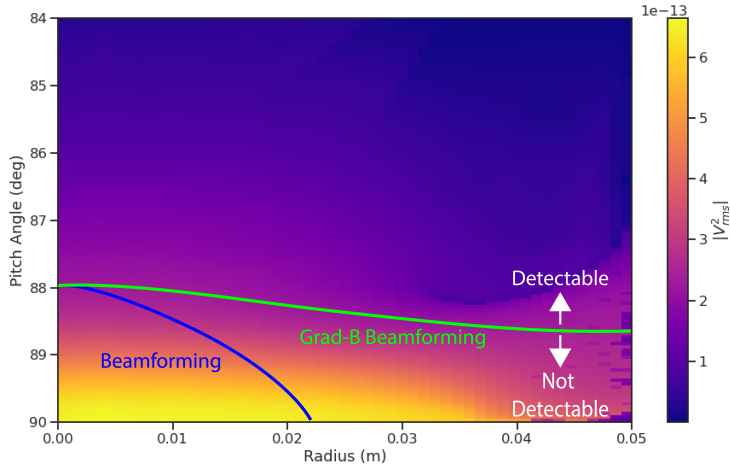


**Figure 4.14.** A plot of the total signal power received by the FSCD array from trapped electrons with different radial positions and pitch angles generated using Locust simulations. The lines on the plot indicate a 10 dB detection threshold above the mean value of the noise in the frequency spectrum. With static beamforming electrons with radial positions larger than about two centimeters are undetectable due to the change in the electron's position over time causing losses from beamforming phase mismatch. This is corrected by including  $\nabla B$ -drift frequencies in the beamforming phases. Both beamforming techniques fail to detect electrons below  $\approx 88.0^\circ$ , since these signal are composed of several relatively weak sidebands that are comparable to the noise.

### 2728 4.3.2 Matched Filtering

#### 2729 Introduction to Matched Filtering

2730 The problem of CRES signal detection is the problem of detecting a signal buried in  
 2731 WGN, which has been examined at great depth in the signal processing literature [74].  
 2732 For a fully known signal in WGN the optimal detector is the matched filter, which means  
 2733 that it achieves the highest true positive rate for a fixed rate of false positives.

2734 The matched filter test statistic is calculated by taking the inner product of the data  
 2735 with the matched filter template

$$\mathcal{T} = \left| \sum_n h^\dagger[n]y[n] \right|, \quad (4.26)$$

2736 where  $h[n]$  is the matched filter template and  $y[n]$  is the data. The matched filter test  
 2737 statistic defines a binary hypothesis test in which the data vector is assumed to be an  
 2738 instance of two possible data classes. By setting a decision threshold on the value of  $\mathcal{T}$ ,  
 2739 one can classify a given data vector as belonging to two distinct hypotheses. Under the

2740 first hypothesis the data is composed of pure WGN, and under the second hypothesis  
 2741 the data is composed of the known signal with additive WGN.

2742 The matched filter template is obtained by rescaling the known signal in the following  
 2743 way

$$h[n] = \frac{x[n]}{\sqrt{\tau \sum_n x^\dagger[n]x[n]}}, \quad (4.27)$$

2744 where  $\tau$  is the variance of the WGN and  $x[n]$  is the known signal. Strictly speaking,  
 2745 Equation 4.27 is only true for noise with a diagonal covariance matrix, which is assumed  
 2746 to be true for the FSCD. Defining the matched filter templates in this way guarantees  
 2747 that the expectation value of  $\mathcal{T}$  is equal to one when the data contains only noise, which  
 2748 is the standard matched filter normalization.

2749 Although matched filters are canonically formulated in terms of a perfectly known  
 2750 signal, it is possible to apply the matched filter technique with imperfect information  
 2751 provided the signal is deterministic. From the discussion of CRES simulation tools (see  
 2752 Section 4.2) it was shown that the shape of CRES signals are completely determined  
 2753 by the initial parameters of the electron. The random collisions with background gas  
 2754 molecules, which cause the formation of signal tracks, are the only stochastic component  
 2755 of the CRES event after the initial beta-decay. Therefore, a matched filter can be used  
 2756 for the detection of deterministic CRES signal tracks between scattering events.

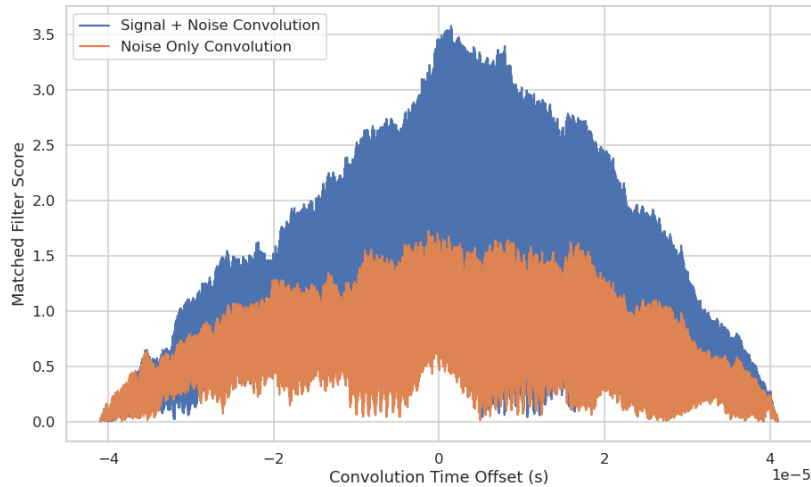


**Figure 4.15.** Example of a convolution of a CRES signal template with a segment of noisy data. A simulated CRES signal was simulated using Locust and normalized to create a matched filter template. When this template is convolved with noisy data the contains the matching signal the convolution output increases dramatically compared to data with only noise. The decreasing convolution output as the time offset of the convolution increases is caused by zero-padding of the data and template.

2757        The matched filter test statistic for CRES signals is a modified version of Equation  
2758        4.26

$$\mathcal{T} = \max_{h,m} |\mathbf{h} * \mathbf{y}| = \max_{h,m} \left| \sum_k h^\dagger[k] x[m-k] \right|, \quad (4.28)$$

2759        where the matched filter inner product has been replaced with a convolution operation  
2760        and a maximization over the template and convolution delay ( $m$ ). Replacing the inner  
2761        product with a convolution accounts for the fact that the start time of the CRES signal is  
2762        now an unknown parameter. In addition, a maximization of the matched filter convolution  
2763        is performed over a number of different templates. Because the shape of the signal is  
2764        unknown, a range of different signal shapes, called a template bank, must be checked  
2765        using an exhaustive search.

## 2766        Matched Filtering in the Frequency Domain

2767        The template bank approach, while powerful, can become computationally intractable.  
2768        Specifically, the time-domain convolution specified by Equation 4.28 is particularly  
2769        computationally intensive and is a major barrier towards the implementation of a  
2770        matched filter for signal detection in an experiment like the FSCD. This can be avoided  
2771        by using the convolution theorem to replace the time-domain convolution with an inner  
2772        product in the frequency domain.

2773        The convolution theorem states that

$$\mathbf{f} * \mathbf{g} = \mathcal{F}^{-1}(\mathbf{F} \cdot \mathbf{G}) \quad (4.29)$$

2774        where  $\mathbf{f}$  and  $\mathbf{g}$  are discretely sampled time-series,  $\mathbf{F}$  and  $\mathbf{G}$  are the respective discrete  
2775        Fourier transforms, and  $\mathcal{F}^{-1}$  is the inverse discrete Fourier transform operator. The  
2776        convolution theorem allows us to perform the matched filter convolution by first com-  
2777        puting the Fourier transform of the template and data, then performing a point-wise  
2778        multiplication of the two frequency series, and finally performing the inverse Fourier  
2779        transform to obtain the convolution output. Because discrete Fourier transforms can be  
2780        performed extremely efficiently, the convolution theorem is almost always used in lieu of  
2781        directly computing the convolution.

2782        One thing to note here is that the convolution theorem for discrete sequences shown  
2783        here, is technically valid only for circular convolutions, which is not directly specified  
2784        in Equation 4.28. However, because typical CRES track lengths are much longer than  
2785        the Fourier analysis window and the frequency chirp rates are small compared to the

2786 time-slice duration, it is safe to use circular convolutions to evaluate matched filter scores  
2787 for CRES signals, which allows one to apply the convolution theorem to compute matched  
2788 filter scores for the FSCD.

2789 **Matched Filter Analysis of the FSCD**

2790 Since the matched filter is the optimal signal detection approach, it provides the ultimate  
2791 upper bounds on signal detection. This makes it a useful algorithm for assessing the  
2792 upper bounds on neutrino mass sensitivity for the FSCD, since it indicates the best  
2793 possible detection efficiency achievable for that experiment configuration. The standard  
2794 approach to performing these studies involves generating numerous simulated electron  
2795 signals that span the kinematic parameter space of electrons.

2796 To limit the number of simulations required to evaluate the detection efficiency,  
2797 the standard approach is to fix the starting axial position, starting azimuthal position,  
2798 starting direction of the perpendicular component of the electron’s momentum, and event  
2799 start time. This reduces the dimensionality of the simulated parameter space to three  
2800 parameters — the starting radial position, starting kinetic energy, and starting pitch  
2801 angle. The fixed variables are nuisance parameters, which do not affect the detection  
2802 efficiency estimates for the FSCD design, because they simply introduce overall phase  
2803 offsets that can be marginalized during the calculation of the matched filter score. Across  
2804 radial position, kinetic energy, and pitch angle one defines a regular grid of parameters  
2805 and uses Locust to simulate the corresponding signals (see Figure 4.16). This grid of  
2806 simulated signals is used to estimate detection efficiency by calculating the detection  
2807 probability of a randomly parameterized signal using the grid as a set of matched filter  
2808 templates (see Section 4.4).

2809 The matched filter approach can also be used to estimate the achievable energy  
2810 resolution of the experiment by using a dense grid of templates generated with parameters  
2811 close to the unknown signal (see figure 4.17). Because matched filter templates with similar  
2812 parameters have closely matching signal shapes, templates with incorrect parameters can  
2813 have nearly identical matched filter scores as the correct template. Since only one sample  
2814 of noise is included in a sample of real data, one cannot guarantee that the template  
2815 with the maximum score corresponds to the ground truth parameters of the signal. This  
2816 introduces uncertainty into the signal parameter estimation that manifests as an energy  
2817 broadening. Dense grids of matched filter templates allow one to quantify this broadening  
2818 by analyzing the parameter space of templates with matched filter scores close to the  
2819 ground truth. This approach is analogous to maximum likelihood estimation and is one

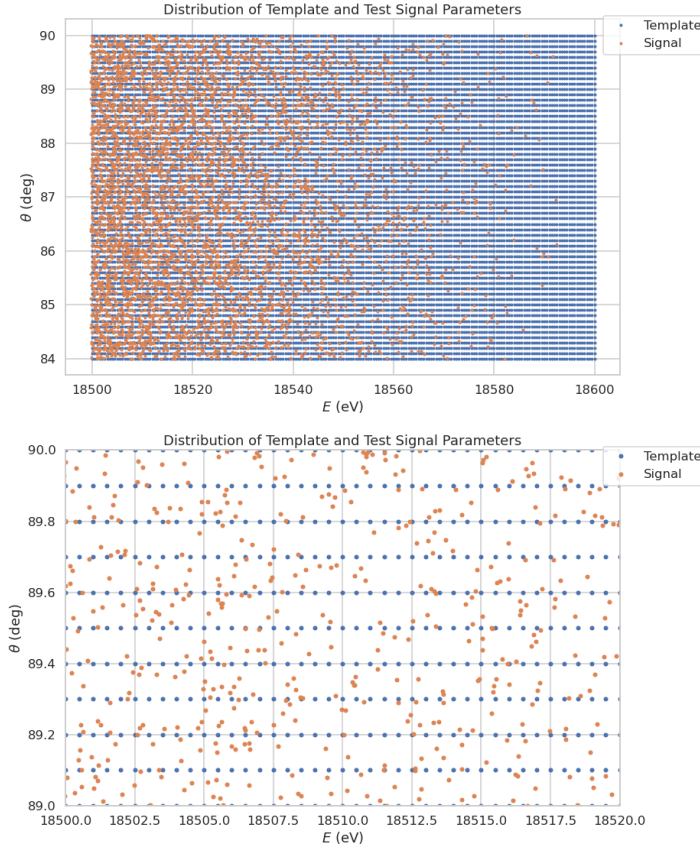


**Figure 4.16.** An example two-dimensional parameter distribution of a matched filter template bank and random test signals.  $\theta$  refers to the pitch angle of the electron and  $E$  is the kinetic energy. The template bank forms a regular grid of in pitch angle and energy; whereas, the test signals are uniformly distributed in pitch angle and follow the tritium beta-decay kinetic energy distribution. This is why there are fewer test signals at higher energies. The need for high match across the full parameter space prevents one from reducing the density of templates in this low activity region. A zoomed in version of the template bank illustrates the relative density of templates and signals needed for match  $> 90\%$ .

2820 key component of a complete sensitivity analysis for an antenna array CRES experiment.

2821 A figure of merit that summarizes the performance of a matched filter template  
 2822 bank at signal detection is "mean match", which is defined as the average ratio of the  
 2823 highest matched filter score for a random signal to the matched filter score for a perfectly  
 2824 matching template. In equation form the match ratio for a single template is given by

$$\text{Match} \equiv \Gamma = \frac{\mathcal{T}_{\text{best}}}{\mathcal{T}_{\text{ideal}}}, \quad (4.30)$$

2825 where  $\mathcal{T}_{\text{best}}$  is the matched filter score of the best fitting template in the bank and  $\mathcal{T}_{\text{ideal}}$

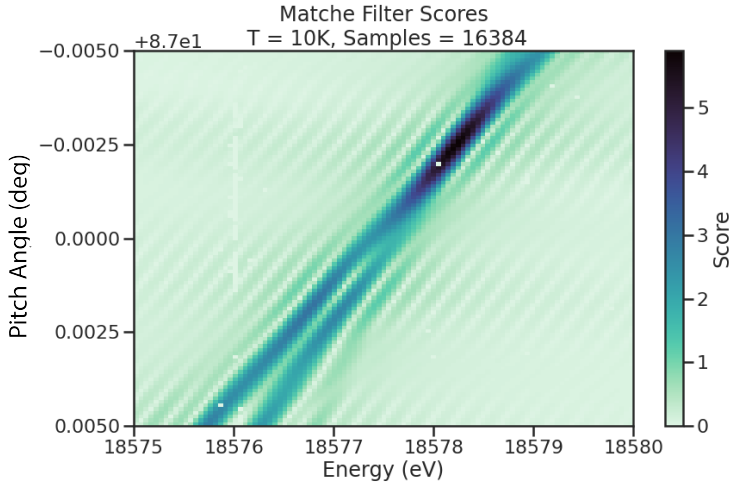


**Figure 4.17.** The matched filter scores of a dense grid of templates in pitch angle energy space. Dense template grids allow one to estimate the kinetic energy of the electron by identifying the best matching template. The uncertainty on this value is proportional to the space of templates that also match the test signal well. In the worst case matched filter templates can be completely degenerate where templates with different parameters match a signal with equal likelihood.

is the hypothetical score one would measure if the signal perfectly matched the template. The mean match is the average value of match for a typical signal inside the parameter range covered by the matched filter template bank. Generally, one desires a mean match as close to unity as possible, which is typically an exponential function of the number of templates in the template bank (see Figure 4.18).

The exponential relationship between match and template bank size manifests for dense and sparse template grids. Sparse template grids are used for signal detection when no prior information on the signal is available; whereas, dense templates grids are more useful for parameter estimation. The mean match value directly influences the detection efficiency of the template bank, but due to the exponential scaling, achieving a high average match at the detection stage can easily overwhelm the available computational resources.

The effect of match on the detection efficiency of the matched filter template bank can be summarized using the ROC curve (see Figure 4.19). The average performance of the template bank can be described by a single ROC curve obtained by averaging over the PDFs that describe the detection probabilities of each template in the bank.

The distribution that describes the matched filter score under the signal hypothesis is a Rician distribution, which has a mean value equal to the matched filter score multiplied by the match ratio (see Section 4.4). Alternatively, the distribution of the matched

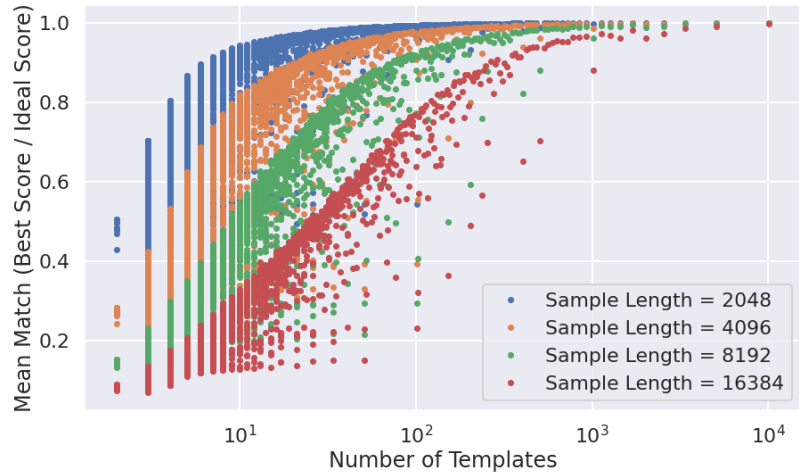


**Figure 4.18.** The mean match of the dense template grid shown in Figure 4.17 for different numbers of templates. Grids of different sizes were obtained by decimating a dense grid of templates and the average match for each grid was computed using the same set of randomly distributed test signals. Plotting the mean match against the size of the grid allows one to visualize the exponential relationship between match and template bank size. The noise in each curve is caused by sampling effects from the decimation algorithm. In general, longer templates are harder to match than shorter templates.

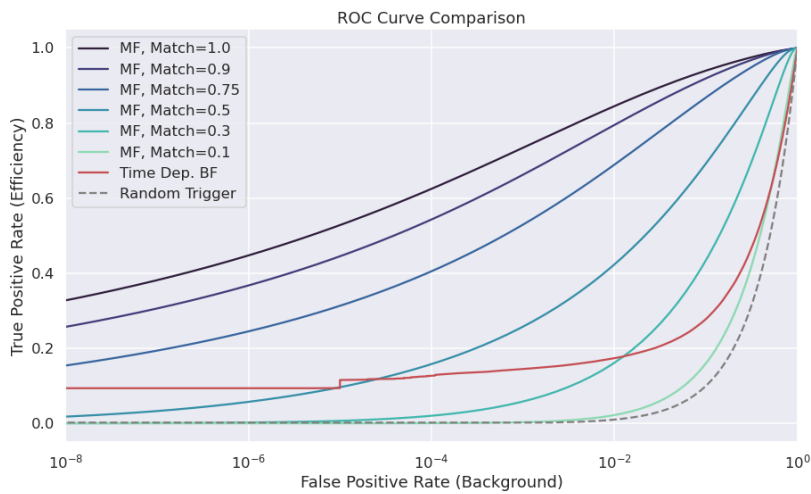


**Figure 4.19.** Matched filter template bank ROC curves as a function of mean match. One can see that for low match a matched filter is on average worse than the more straight forward beamforming detection approach.

filter score when there is no signal in the data follows a Rayleigh distribution, which is equivalent to a Rician distribution with zero mean. The matched filter score for each template in the template bank is described by a separate Rician distribution. Therefore, one way to model detection probability for a given signal is to average across all matched filter distributions in the template bank to obtain a single distribution that describes the statistical behavior of the matched filter score.

A different way to visualize the detection performance for each algorithm is to specify a minimum acceptable false positive rate at the trigger level. This is equivalent to specifying a minimum threshold on the value of the matched filter score or the size of a frequency peak for a beamforming power threshold trigger. One can then draw regions of detectable signals as a function of the electron's pitch angle and radial position (see Figure 4.20). A kinetic energy shift is equivalent to an overall frequency shift of the

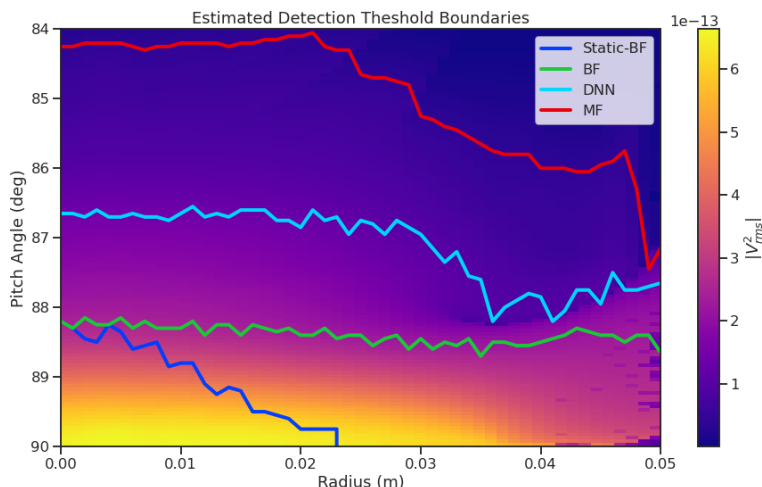


**Figure 4.20.** Boundaries of detectable electrons in pitch angle kinetic energy space for a series of different signal detection algorithms. A detectable signal is defined as a signal that is above a consistent decision with at least 50% probability. This non-rigorous treatment of detection probability is primarily useful for the visualization the relative increases in detection performance provided by the different algorithms. The static beamforming (Static-BF) algorithm is the digital beamforming algorithm introduced above without the  $\nabla B$ -drift correction. The DNN algorithm refers to a convolutional neural network classifier trained to detect CRES signals (see Section 4.3.3).

signal and should have no effect on the detection probability assuming sufficient density of matched filter templates in the energy dimension. A electron is declared "detectable" for the regions in Figure 4.20 if the signal has at least 50% probability of falling above the decision threshold of the respective classifier. One can see that the parameter space of detectable signals is greatly expanded beyond the beamforming power threshold trigger

2862 with a matched filter (MF) or deep neural network (DNN) (see Section 4.3.3). Plots such  
2863 as Figure 4.20 are useful for visualization, but, since the handling of detection likelihood  
2864 is not sufficiently rigorous, the detection probability boundaries are not well-suited to  
2865 sensitivity estimates.

## 2866 Optimized Matched Filtering Implementation for the FSCD

2867 The biggest practical obstacle to the implementation of a matched filter template bank is  
2868 the computational cost associated with exhaustively calculating the matched filter scores;  
2869 therefore, one must employ several optimizations in a practical setting.

2870 Computing a matched filter score requires the convolution of two vectors, which can  
2871 be performed very efficiently by computers if the convolution theorem and fast Fourier  
2872 transforms (FFT) are utilized. Furthermore, one can apply digital beamforming as a  
2873 pre-processing step to reduce the dimensionality of the data before the matched filter.  
2874 In order to understand the relative gain in computational efficiency offered by these  
2875 optimizations I analyze the total number of floating-point operations (FLOP) of several  
2876 matched filter implementations in big  $O$  notation that utilize different combinations of  
2877 optimizations.

2878 A direct implementation of a matched filter as specified by Equation 4.28 involves  
2879 the convolution of  $N_{\text{ch}}$  signals of length  $N_s$  with template signals of length  $N_t$ . The  
2880 FLOPs of the various matched filter implementations on a per-template basis will be  
2881 used as a consistent metric, since each implementation scales linearly with the number of  
2882 templates. The direct convolution approach to matched filtering costs

$$O(N_{\text{ch}}) \times O(N_s \times N_t) \quad (4.31)$$

2883 FLOP per-template, whose cost is dominated by the  $O(M \times N)$  convolution operation.

2884 The computational cost of the direct matched filter approach can be significantly  
2885 reduced by exploiting the convolution theorem and FFT algorithms. By restricting oneself  
2886 to signals and templates that contain equal numbers of samples, the convolution can be  
2887 calculated by Fourier transforming both vectors, performing the point-wise multiplication,  
2888 and taking the inverse Fourier transform to obtain the convolution result. The FFT  
2889 algorithm is able to compute the Fourier transform utilizing only  $O(N \log N)$  operations.  
2890 This optimization results in a computational cost per-template of

$$O(N_{\text{ch}}) \times O(N_s \log N_s) \quad (4.32)$$

2891 A typical signal vector in the FSCD contains  $O(10^4)$  samples in which case the FFT  
 2892 reduces the computational cost of the matched filter by a factor of  $O(10^3)$ . In practice,  
 2893 due to the large reduction in computational cost with a frequency-domain matched filter,  
 2894 direct implementations of the matched filter using a time-domain convolution are almost  
 2895 never attempted in practice. Particularly, a time-domain matched filter is completely  
 2896 computationally infeasible for the the FSCD due to resource constraints.

2897 Rather than relying solely on the matched filter it is tempting to consider using  
 2898 digital beamforming as an initial step in the signal reconstruction for the purposes of  
 2899 data reduction. The primary motivation is to reduce the dimensionality of the data by  
 2900 a factor of  $N_{\text{ch}}$  by combining the array outputs coherently into a single channel. One  
 2901 can view the beamforming operation as a partial matched filter, in the sense that the  
 2902 matched filter convolution contains the beamforming phased summation along with a  
 2903 prediction of the signal shape. By separating beamforming from the signal shape one  
 2904 hopes to reduce the overall computational cost by effectively shrinking the number of  
 2905 templates and reducing the number of operations required to check each one.

2906 The nature of this optimization requires that one account for the number of templates  
 2907 used for pure matched filtering versus the hybrid approach. To first order, the total  
 2908 number of templates at the trigger stage is a product of the number of guesses for each  
 2909 of the electron's parameters

$$N_T = N_E \times N_\theta \times N_r \times N_\varphi, \quad (4.33)$$

2910 where  $N_E$  is the number of kinetic energies,  $N_\theta$  is the number of pitch angles,  $N_r$  is the  
 2911 number of starting radial positions, and  $N_\varphi$  is the number of starting azimuthal positions.  
 2912 The starting axial position and cyclotron motion phase are not necessary to include in  
 2913 the template bank, since these parameters manifest themselves as the starting phase of  
 2914 the signal, which is effectively marginalized when using a FFT to compute the matched  
 2915 filter convolution. Therefore, the total number of operations required by a matched filter  
 2916 to detect a signal in a segment of array data is on the order of

$$O(N_T) \times O(N_{\text{ch}}) \times O(N_s \log N_s) \quad (4.34)$$

2917 With the hybrid approach one removes spatial parameters from the template bank  
 2918 by using beamforming to combine the array signals into a single channel. Beamforming  
 2919 explicitly assumes a starting position, which allows one to use matched filter templates  
 2920 that span the two-dimensional space of kinetic energy and pitch angle. The total

2921 computational cost of the hybrid method is directly proportional to the number of  
 2922 beamforming positions. For the time-dependent beamforming defined in Section 4.3.1,  
 2923 the number of beamforming positions is given by

$$N_{\text{BF}} = N_r \times N_\varphi \times N_{\omega_{\nabla B}}, \quad (4.35)$$

2924 where  $N_r$  and  $N_\varphi$  are the same spatial parameters encountered in the pure matched  
 2925 filter template bank and  $N_{\omega_{\nabla B}}$  is the number of  $\nabla B$ -drift frequency assumptions. If a  
 2926 unique drift frequency is used for each pitch angle then the hybrid approach is effectively  
 2927 equivalent to a pure matched filter in the number of operations. The key efficiency gain  
 2928 of the hybrid approach is to exploit the relatively small differences in  $\omega_{\nabla B}$  for electrons  
 2929 of different pitch angles by using only a few average drift frequencies.

2930 The total number of operations for the hybrid approach can be expressed as a sum of  
 2931 the operations required by the beamforming and matched filtering steps,

$$O(N_{\text{BF}}) \times O(N_{\text{ch}}N_s) + O(N_{\text{BF}}) \times O(N_E N_\theta) \times O(N_s \log N_s). \quad (4.36)$$

2932 The first product in the sum is the number of operations required by beamforming,  
 2933 which is simply the number of beamforming points times the computational cost of the  
 2934 beamforming matrix multiplication, and the second product is the computational cost  
 2935 of matched filtering the summed signal generated by each beamforming position. To  
 2936 compare this to pure matched filtering, one takes the ratio of Equations 4.34 and 4.36 to  
 2937 obtain

$$\Gamma_{\text{BFMF}} = \frac{O(N_{\omega_{\nabla B}})}{O(N_E N_\theta) \times O(\log N_s)} + \frac{O(N_{\omega_{\nabla B}})}{O(N_{\text{ch}})}. \quad (4.37)$$

2938 This expression can be simplified by observing that  $O(N_E N_\theta) \times O(\log N_s) \gg O(N_{\text{ch}})$ ,  
 2939 which means that the ratio of computational cost for the two methods can be reduced to

$$\Gamma_{\text{BFMF}} \approx \frac{O(N_{\omega_{\nabla B}})}{O(N_{\text{ch}})}. \quad (4.38)$$

2940 Limiting oneself to a number of estimated drift frequencies of  $O(1)$ , then it can be seen  
 2941 that the estimated computational cost reduction of the hybrid approach is of  $O(N_{\text{ch}})$ .  
 2942 This is a large reduction considering that the FSCD antenna array contains sixty antennas  
 2943 in the baseline design.

2944 The main drawback of the hybrid approach is that the limited number of allowed  
 2945 drift frequency guesses can lead to detection efficiency loss due to phase mismatch. The

2946 degree of phase error from an incorrect drift frequency is proportional to the length of  
 2947 the array data vector used by the signal detection algorithm. For signals with lengths  
 2948 equal to the baseline FSCD Fourier analysis window of 8192 samples, typical phase errors  
 2949 from using an average versus the exact  $\nabla B$ -drift frequency are on the order of a few  
 2950 percent in terms of the signal energy. This has a relatively small impact on the overall  
 2951 detection efficiency, however, future experiments with antenna array CRES will want to  
 2952 balance optimizations such as these during the design phase to keep experiment costs to  
 2953 a minimum while still achieving scientific goals.

## 2954 Kinetic Energy and Pitch Angle Degeneracy

2955 Accurate modeling of a matched filter requires one to consider the effects of mismatched  
 2956 signals and template, since this more accurately reflects the real-world usage of a matched  
 2957 filter. One way to study this is to use a signal grid to compute the matched filter scores  
 2958 between mismatched signals and templates and evaluate the matched filter scores under  
 2959 this scenario. What one finds when performing this analysis is that templates for signals  
 2960 with incorrect parameters can have matched filter scores that are indistinguishable from  
 the matched filter score of the correct template (see Figure 4.21 and Figure 4.21).

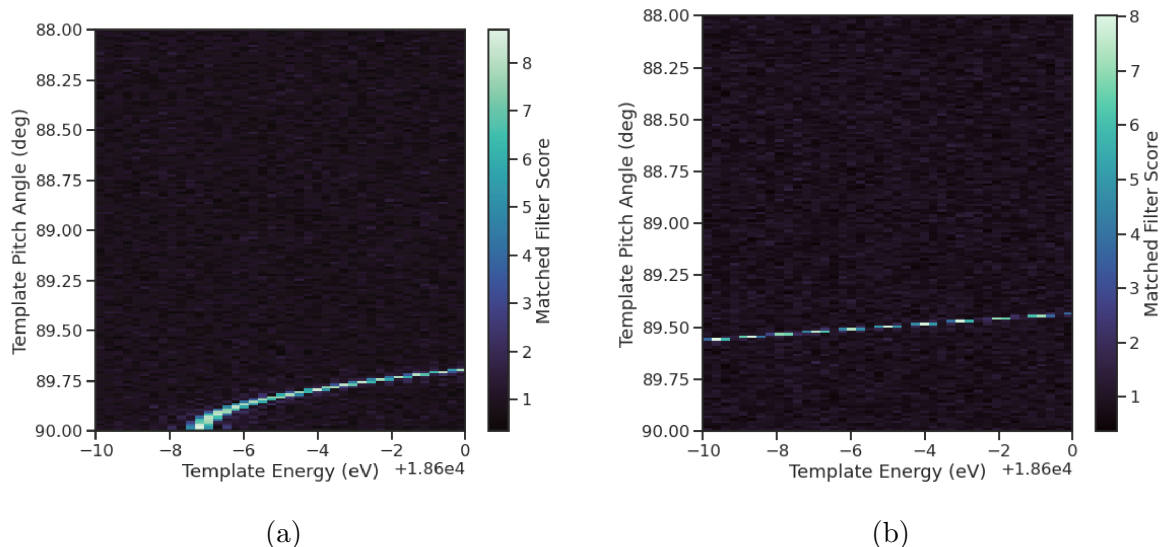


**Figure 4.21.** Two example illustrations of the correlation between kinetic energy and pitch angle imparted by the shape of the FSCD magnetic trap. The correlations manifest themselves as degeneracies in the matched filter score where multiple matched filter templates have the same matched filter for a particular signal. These degeneracies are a sign that the magnetic trap must be redesigned in order to break the correlation between pitch angle and kinetic energy.

2961

2962 This degeneracy in matched filter score is the result of correlations between the kinetic  
 2963 energy and pitch angle of the electron caused by the magnetic trap. These correlations  
 2964 are unacceptable since they greatly reduce the energy resolution of the experiment by  
 2965 causing electrons with specific kinetic energy to match templates across a wide range of  
 energies.

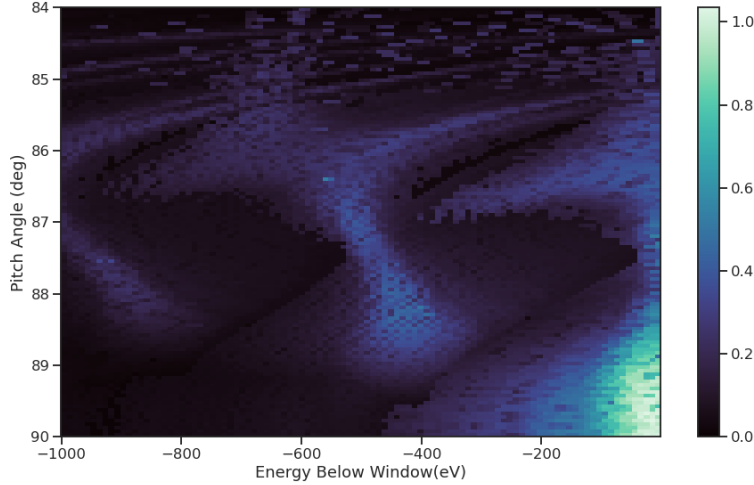


**Figure 4.22.** A visualization of the correlation between energy and pitch angle in the FSCD magnetic trap. The image is formed by computing the match of the best template from a grid consisting of pitch angles from 84 to 90 degrees in steps of 0.05 degrees, kinetic energies from 17574 to 18574 eV, located at 2 cm from the central axis, and simulated for a length of three FSCD time-slices. The signals used to compute the best matching template consisted of a grid from 84 to 90 degrees in steps of 0.05 degrees, kinetic energies from 18550 to 18575 eV in steps of 0.25 eV, located 2 cm from the central axis, and simulated for three FSCD time-slices. The colored regions of the plot show how well signals with lower energy can match those of higher energy for the FSCD magnetic trap, which is proportional to the achievable energy resolution of the FSCD design.

2966  
 2967 This degeneracy cannot be fixed by implementing a different signal reconstruction  
 2968 algorithm. As revealed by the matched filter scores the shapes of the signals for different  
 2969 parameters are identical. Resolving this degeneracy between pitch angle and energy  
 2970 requires the design of a new magnetic trap with steeper walls so that the average magnetic  
 2971 field experienced by an electron is less dependent on pitch angle.

### 2972 4.3.3 Machine Learning

2973 Machine learning is a broad field of research [79] that has been particularly transformative  
 2974 in the recent past. In this Section I provide a brief introduction to some concepts and

2975 techniques of machine learning that were applied to CRES signal detection in my  
2976 dissertation.

## 2977 **Introduction to Machine Learning**

2978 Digitization of the FSCD antenna array generates large amounts of data that must  
2979 be rapidly processed for real-time signal detection and reconstruction. While digital  
2980 beamforming combined with a power threshold is relatively computationally inexpensive,  
2981 it is ineffective at detecting CRES signal with small pitch angles, since it relies on a  
2982 visible frequency peak above the noise. On the other hand, a matched filter is able to  
2983 detect signals with a significantly larger range of parameters, however, the exhaustive  
2984 search of matched filter templates can be computationally expensive. Machine learning  
2985 based triggering algorithms have been used successfully in many high-energy physics  
2986 experiments [80], and recently have shown success in the detection of gravitational wave  
2987 signals [81, 82] in place of more traditional matched filtering methods. The success of  
2988 machine learning in these domains motivates the exploration of machine learning as a  
2989 potential CRES signal detection algorithm.

2990 Various approaches to machine learning are possible, but the one most important  
2991 to the discussion here is the supervised learning approach. In supervised learning, one  
2992 uses a differentiable model or function that is designed to map the input data to the  
2993 appropriate label [79]. The data is represented as a multidimensional matrix of floating  
2994 point values such as an image or a time-series, and the label is typically a class name such  
2995 as signal or noise for classification problems, or a continuous value like kinetic energy for  
2996 regression problems.

2997 In supervised learning the model is trained to map from the data to the correct label  
2998 by evaluating the output of the model using a training dataset consisting of a set of  
2999 paired data and labels. To evaluate the difference between the model output and the  
3000 correct label a loss function is used to quantify the error between the model prediction  
3001 and the ground truth. For example, a common loss function in regression problems is the  
3002 squared error loss function, which quantifies error using the squared difference between  
3003 the model output and label.

3004 Using the outputs of the loss function the next step in supervised learning is to  
3005 compute the gradient of error with respect to the model parameters in a process called  
3006 backpropagation. The gradients are used to update the model parameter values in  
3007 order to minimize errors in the model predictions across the whole dataset. This loop is  
3008 performed many times while randomly shuffling the dataset until the error converges to a

3009 minimum value at which point the training procedure has finished. It is standard practice  
3010 to monitor the training procedure by evaluating the performance of the model using a  
3011 separate validation dataset that matches the statistical distribution of the training data  
3012 and to check the performance of the model after training using yet another dataset called  
3013 the test dataset. These practices help to guard against overtraining which is a concern  
3014 for models with many parameters.

3015 **Convolutional Neural Networks**

3016 A popular class of machine learning models are neural networks. A neural network is  
3017 a function composed of a series of linear operations called layers, which take a piece of  
3018 data typically represented as a matrix, multiply the elements of the data by a weight,  
3019 and then sums these products to produce an output matrix. Neural networks composed  
3020 of purely linear operations are unable to model complex non-linear behavior. Therefore,  
3021 non-linear activation functions are applied to the outputs of each of the layers to increase  
3022 the ability of the neural network to model complex relationships between the data.

3023 Neural networks are typically composed of at least three layers, but with the present  
3024 capabilities of computer hardware they typically contain much more than this. The first  
3025 layer in a neural network is called the input layer, because it takes the data objects  
3026 as input, and the last layer in a neural network is known as the output layer. The  
3027 output layer is trained by machine learning to map the data to an output label using  
3028 the supervised learning procedure described in Section 4.3.3. Between the input and the  
3029 output layers are typically several hidden layers that receive inputs from and transmit  
3030 outputs to other layers in the neural network model. The term deep neural network  
3031 (DNN) refers to those neural networks that have at least one hidden layer, which have  
3032 proven to be extremely powerful tools for pattern recognition and function approximation.

3033 An important type of DNN are convolutional neural networks (CNN) that typically  
3034 contain several layers which perform a convolution of the input with a set of filters. These  
3035 convolution operations are typically accompanied by layers that attempt to down-sample  
3036 the data along with the standard neural network activation functions. A standard CNN  
3037 is composed of several convolutional layers at the beginning of the network and ends  
3038 with a series of fully-connected neural network layers at the output. Intuitively, one  
3039 can imagine that the convolutional layers are extracting features from the data that  
3040 fully-connected layers use to perform the classification or regression task.

3041 Deep Filtering for Signal Detection in the FSCD

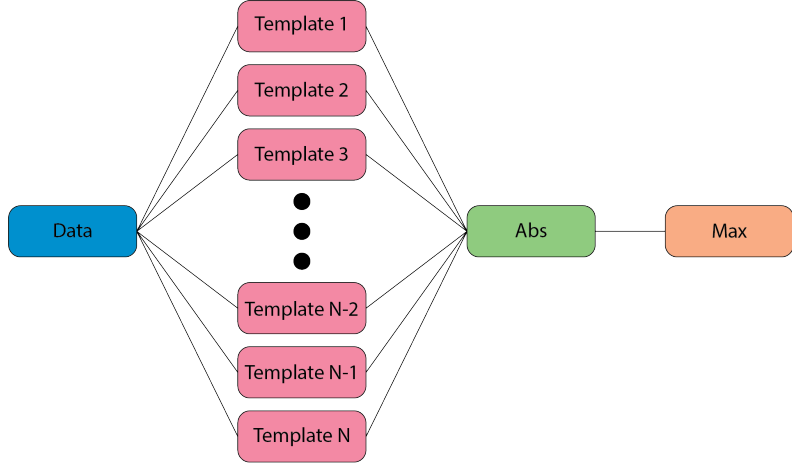


**Figure 4.23.** A representation of a matched filter template bank as a convolutional neural network. The network has a single layer composed of the templates, which act as convolutional filters. The activation of the neural network is an absolute value followed by a max operator.

3042 CNNs have been extremely influential in the field of computer vision, particularly tasks  
3043 such as image segmentation and classification, but have also been applied in numerous  
3044 experimental physics contexts. Given the particular challenge posed by signal detection  
3045 and reconstruction in the FSCD, CNNs are an interesting choice for real-time signal  
3046 detection, since this application requires both high efficiency and fast evaluation.

3047 In the machine learning paradigm, signal detection is a binary classification problem  
3048 between the signal and noise data classes. My investigation focuses specifically on the  
3049 application of CNNs to signal detection in the FSCD, which is motivated by relatively  
3050 recent demonstrations of CNNs achieving classification accuracies for gravitational wave  
3051 time-series signals comparable to a matched filter template bank. In this framework  
3052 it is possible to interpret the matched filter as a type of CNN composed of a single  
3053 convolutional layer with the templates making up the layer filters (see Figure 4.23).  
3054 Since this neural network has no hidden layers, it is not a DNN, but one can attempt to  
3055 construct a proper CNN that attempts to reproduce the classification performance of the  
3056 matched filter network, which can be referred to as "deep filtering".

3057 The reason why deep filtering can be effective is that it may be possible to exploit  
3058 redundancies and correlations between templates, which allows one to perform signal  
3059 detection with similar accuracy but with fewer computations. This is relevant to real-time  
3060 detection scenarios like the FSCD experiment. In Section 4.4 I perform a detailed  
3061 comparison of the signal detection performance of a CNN to beamforming and a matched

3062 filter template bank.

3063 Deep filtering is conceptually a simple technique. Similar to a matched filter template  
3064 bank, many simulated CRES signals are generated and used to train a model to distinguish  
3065 between signal and noise data (see Figure 4.24). To reduce the dimensionality of the  
3066 input FSCD data, a digital beamforming summation is applied to the raw time-series  
3067 data generated by Locust to compress the 60-channel data to a single time-series. CRES  
3068 signals have a sparse frequency representation and experiments training CNN's on time-  
3069 series and frequency-series data found that models trained on frequency spectrum data  
3070 performed significantly better. Therefore, an FFT is applied to the summed time-series  
3071 before being normalized and fed to the classification model.

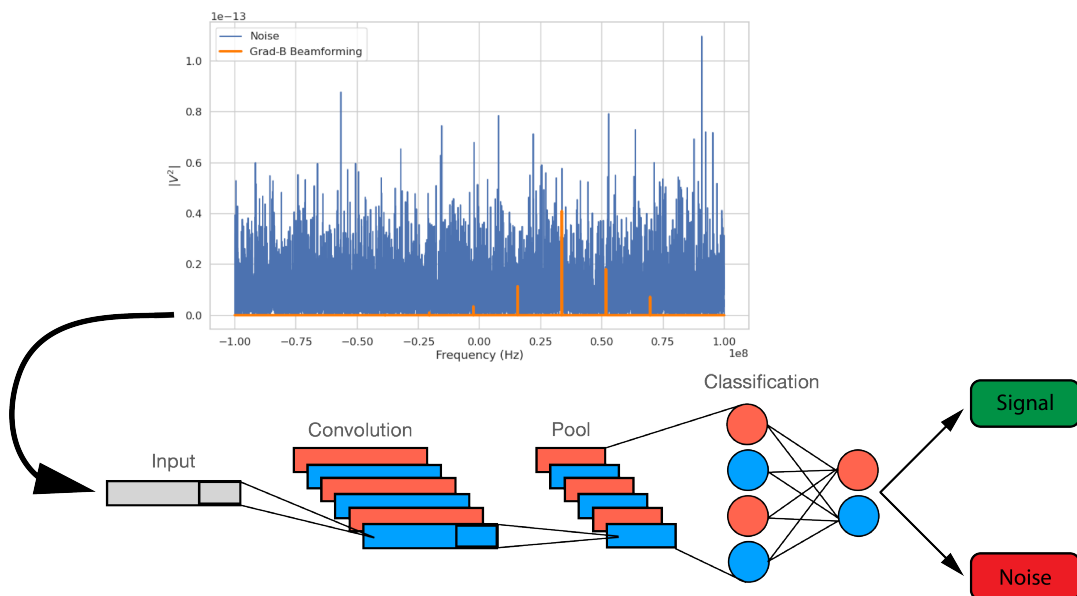


**Figure 4.24.** A graphical depiction of CRES signal detection using a CNN. A noisy segment of data is converted to a frequency series using digital beamforming and a FFT. The complex-valued frequency series is input into a trained CNN model that classifies the data as signal or noise using a decision threshold on the CNN output.

3072 The data used to train the model consists of an equal proportion of signal and noise  
3073 frequency spectra. Unique samples of WGN are generated and added to the signals during  
3074 training time to avoid having to pre-generate and store large samples of noise data. The  
3075 binary cross-entropy loss function combined with the ADAM optimizer proved effective  
3076 at training the models to classify CRES data. A simple hyperparameter optimization  
3077 was performed by manually tuning model, loss function, and optimizer parameters. The  
3078 model and training loops was implemented in python using the PyTorch deep learning  
3079 framework. Standard machine learning practices were followed when training the models,

such as overtraining monitoring using a validation dataset. Models were trained until the training loss and accuracy converged and then evaluated using a separate test data set.

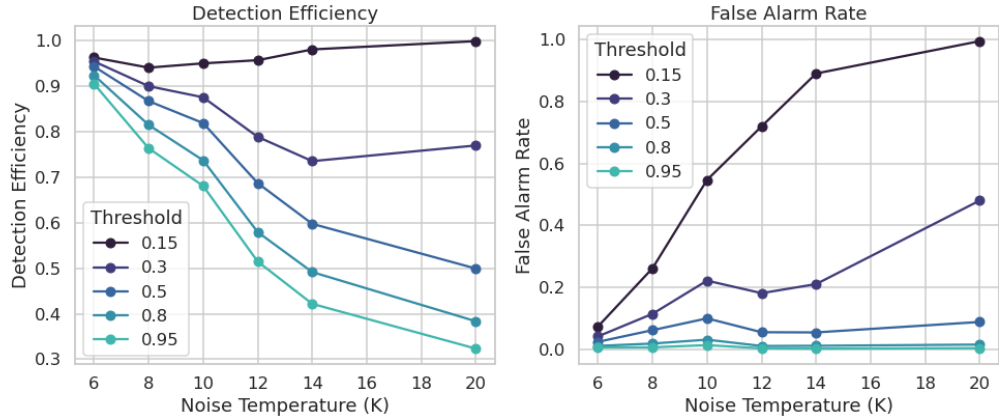


**Figure 4.25.** The detection efficiency and false alarm rate (false positive rate) as a function of the decision threshold for different values of the noise temperature. The model is trained to output a value close to one for data that contains a signal and outputs a value near zero when the data contains only noise. One sees that a lower decision threshold will have a high detection efficiency at the cost of a high rate of false alarms.

The classification results of the test dataset are used to quantify the relationship between the true positive rate and the false positive rate for the model. The true positive rate is analogous to detection efficiency and the false positive rate is a potential source of background in the detector. One can limit the rate of false positives using a sufficiently high threshold on the model output at the cost of a lower detection efficiency (see Figure 4.25 and Figure 4.26). As expected, the performance of the model at signal classification is negatively effected by the noise power, which is quantified by the noise temperature.

## 4.4 Analysis of Signal Detection Algorithms for the FSCD

This section consists of a modified manuscript for an antenna-based CRES signal detection paper prepared for publication in JINST. The contents of this paper were still undergoing collaboration review at the time of writing. In it I present a detailed analysis of the signal detection performance of the three signal detection approaches discussed so far using a population of simulated CRES signals generated with Locust. The focus of the paper is on the performance of the signal detection algorithms for pitch angles below  $88.5^\circ$  where the beamforming power threshold is least effective.

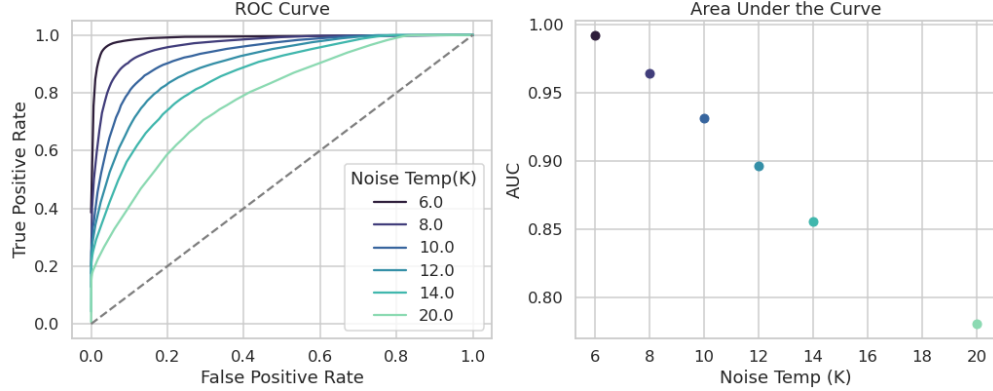


**Figure 4.26.** ROC curves for a CNN model classifying CRES signals. One can see that the area under the curve, which is a figure of merit that describes the performance of the classifier, is roughly linearly dependent with the noise temperature.

### 3097 4.4.1 Introduction

3098 One approach to large volume CRES is to surround a large volume with an array of  
 3099 antennas that together collect a portion of the cyclotron radiation emitted by trapped  
 3100 electrons [41, 83]. A promising design is an inward-facing uniform cylindrical array that  
 3101 surrounds the tritium containment volume. Increasing the size of the antenna array,  
 3102 by adding additional rings of antennas along the vertical axis, allows one to grow the  
 3103 experiment volume until a sufficient amount of tritium gas can be observed by the array.  
 3104 A challenging aspect of this approach is that the total radiated power emitted by an  
 3105 electron near the tritium spectrum endpoint is on the order of 1 fW or less in a 1 T  
 3106 magnetic field, which is then distributed among all antennas in the array. Because the  
 3107 CRES signal information is spread across the antenna array, detecting the presence of  
 3108 a CRES signal and determining the electron's kinetic energy requires reconstructing  
 3109 the entire array output over the course of the CRES event, posing a significant data  
 3110 acquisition and signal reconstruction challenge.

3111 Previous measurements with the CRES technique (see Section 3.3) have utilized  
 3112 a threshold on the frequency spectrum formed from a segment of CRES time-series  
 3113 data. This algorithm relies on the detection of a frequency peak above the thermal  
 3114 noise background, which limits the kinematic parameter space of detectable electrons  
 3115 (see Section 4.4.2.2). Although a power threshold based classification was adequate for  
 3116 smaller detectors, improvements in detection efficiency are needed for better sensitivity  
 3117 to the neutrino mass. Better detection efficiency is possible by taking advantage of the  
 3118 deterministic CRES signal structure with a matched filter or machine learning based

3119 classifier [84]. In order to evaluate the relative gains in detection efficiency that come  
3120 from utilizing these algorithms for antennas, analytical models that describe the detection  
3121 performance a power threshold and matched filter classifier are developed. In addition,  
3122 a basic convolutional neural network (CNN) is implemented and tested as a first step  
3123 towards the development of neural-network based classifiers for antenna array based  
3124 CRES measurements. These results allow for a comparison between the estimated  
3125 detection efficiencies of each of these methods, which are weighed against the associated  
3126 computational costs for real-time applications.

3127 The outline of the remainder of this chapter is as follows. Section 4.4.2 is an overview  
3128 of a prototypical antenna array CRES experiment, and describes the approach to real-time  
3129 signal identification. Section 4.4.3 develops models for the power threshold and matched  
3130 filter algorithms and introduces the machine learning approach and CNN architecture.  
3131 Section 4.4.4 describes the process for generating simulated CRES signal data and the  
3132 details of training the CNN. Finally, Section 4.4.5 compares the signal classification  
3133 accuracy for the three approaches and discusses the relevant trade-offs in terms of  
3134 detection efficiency and computational cost.

## 3135 **4.4.2 Signal Detection with Antenna Array CRES**

### 3136 **4.4.2.1 Antenna Array and Data Rate Estimates**

3137 In order to explore the potential of antenna array CRES for neutrino mass measurement,  
3138 the Project 8 Collaboration has developed a conceptual design for a prototype antenna  
3139 array CRES experiment [41,83], called the Free-space CRES Demonstrator or FSCD (see  
3140 Figure 4.27). The FSCD utilizes a single ring of antennas, which is the simplest form of a  
3141 uniform cylindrical array configuration, to surround a radio-frequency (RF) transparent  
3142 tritium gas vessel. A prototype version of this antenna array has been built and tested  
3143 by the Project 8 collaboration [44] to validate simulations of the array radiation pattern  
3144 and beamforming algorithms [85]. In the FSCD the antenna array is positioned at the  
3145 center of the magnetic trap formed by a set of electromagnetic coils, which create a local  
3146 minimum in the magnetic field with flat central region and steep walls in the radial and  
3147 axial directions.

3148 When an electron is trapped its motion consists of three primary components. The  
3149 component with the highest frequency is the cyclotron orbit whose frequency is determined  
3150 by the size of the background magnetic field. The FSCD design assumes a background  
3151 magnetic field value of approximately 0.96 T, which results in cyclotron frequencies

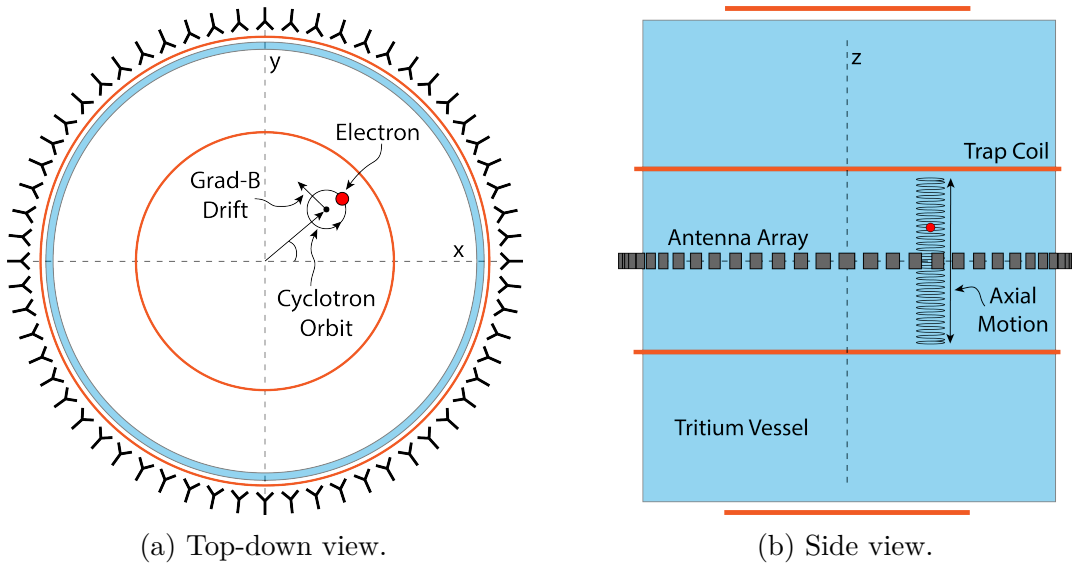


**Figure 4.27.** An illustration of the conceptual design for an antenna array CRES tritium beta-decay spectrum measurement. The antenna array geometry consists of a 20 cm interior diameter with 60 independent antenna channels arranged evenly around the circumference. The nominal antenna design is sensitive to radiation in the frequency range of 25-26 GHz, which corresponds to the cyclotron frequency of electrons emitted near the tritium beta-spectrum endpoint in a 0.96 T magnetic field. The array is located at the center of the magnetic trap produced by a set of current-carrying coils. The nominal magnetic trap design is capable of trapping electrons up to 5 cm away from the central axis of the array and traps electrons within an approximately 6 cm long axial region centered on the antenna array.

for electrons with kinetic energies near the tritium beta-spectrum endpoint of 26 GHz.  
 The component with the next highest frequency is the axial oscillation experienced by electrons with pitch angles<sup>5</sup> of less than 90° [64]. The flat region of the FSCD magnetic trap extends approximately 3 cm above and below the antenna array plane causing electrons to move back and forth as they are reflected from the trap walls. Typical oscillation frequencies are on the order of 10's of MHz, which results in an oscillation period that is  $O(10^3)$  smaller than the duration of a typical CRES event. Therefore, the axial extent of the electron's motion is generally ignored for the purposes of reconstruction, since the electron can be treated as if it is located in the average axial position at the bottom of the magnetic trap. The component of motion with the smallest frequency is the  $\nabla B$ -drift caused by radial field gradients in the trap, producing an orbit of the electron around the central axis of the trap with a frequency on the order of a few kHz, dependent on the pitch angle and the radial position of the electron.

<sup>5</sup>Pitch angle is defined as the angle of the particle's total momentum with respect to the local magnetic field.

3165        Each component of motion influences the shape of the cyclotron radiation signals  
 3166        received by the antenna array; therefore, the data acquisition (DAQ) system must be  
 3167        properly designed in order to resolve the effects of the cyclotron motion, pitch angle, and  
 3168         $\nabla$ -B drift on the signal shape. Frequency down-conversion allows for intentional under-  
 3169        sampling of the CRES signals at a nominal bandwidth of 200 MHz. The bandwidth is  
 3170        required to be large enough to contain all sidebands produced by pitch angle modulation,  
 3171        but must be limited to reduce the Nyquist-Johnson noise power for adequate signal-to-  
 3172        noise ratio. The estimated noise temperature for the FSCD is  $\approx 10$  K, achievable with  
 3173        low-noise HEMT amplifiers and cryogenic temperatures.

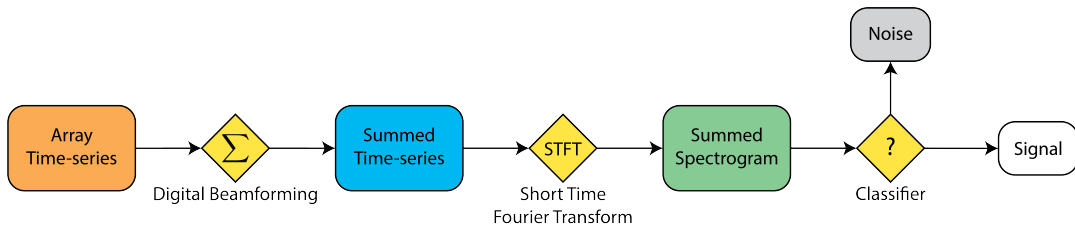


**Figure 4.28.** A block diagram illustration of the real-time triggering algorithm proposed for antenna array CRES reconstruction.

3174        A design goal for the FSCD DAQ system is to enable a significant portion of the  
 3175        CRES event reconstruction to occur in real-time. The estimated data volume generated  
 3176        by the FSCD is 1 exabyte of raw data per year of operation, with the nominal array size  
 3177        of 60 antennas sampled at 200 MHz, which would be too expensive to store for offline  
 3178        processing. Therefore, it is ideal to perform some CRES event reconstruction in real-time  
 3179        so that it is possible to save a reduced form of the data for offline analysis. The first step  
 3180        of the real-time reconstruction would be a real-time signal detection algorithm, which is  
 3181        the focus of this paper. The basic approach consists of three operations performed on the  
 3182        time-series data blocks including digital beamforming, a short time Fourier transform  
 3183        (STFT), and a binary classification algorithm to distinguish between signal and noise  
 3184        data (see Figure 4.28).

#### 3185        4.4.2.2 Real-time Signal Detection

3186        The first step in the real-time detection algorithm is digital beamforming, which is a  
 3187        phased summation of the signals received by the array (see Figure 4.29). The phase shifts  
 3188        correspond to the path length differences between a spatial position and the antennas  
 3189        such that, when there is an electron located at the beamforming position, all the signals  
 3190        received by the array constructively interfere. Since one does not know a priori where an

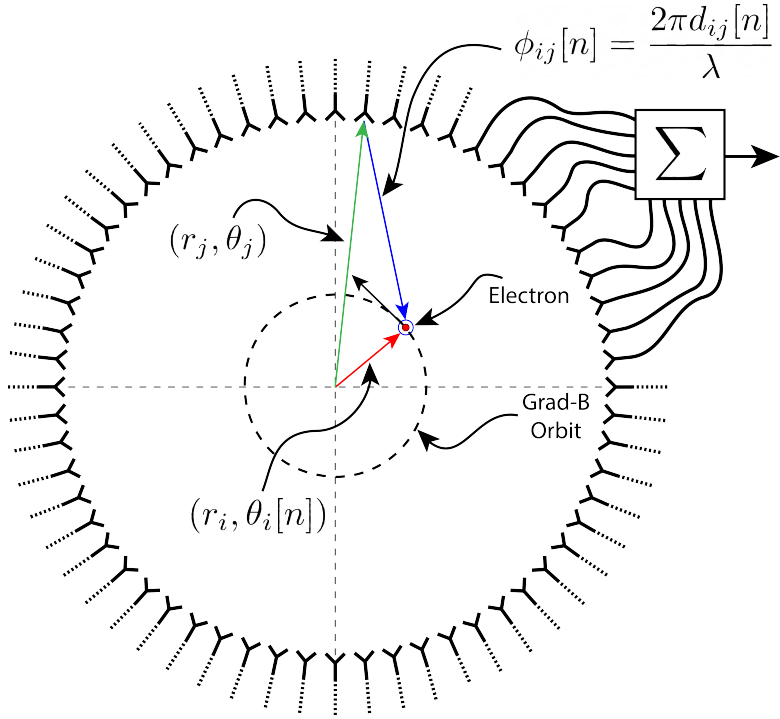


**Figure 4.29.** An illustration of the digital beamforming procedure. The blue lines indicate the distances from the beamforming position to each antenna. In the situation depicted the actual position of the electron matches the beamforming position; therefore, one expects constructive interference when the phase shifted signals are summed. To prevent the electron's  $\nabla B$ -motion from moving the electron off of the beamforming position, the beamforming phases include time-dependence to follow the trajectory of the electron in the magnetic trap.

3191 electron will be produced in the detector, a grid of beamforming positions is designed to  
 3192 cover the entire azimuthal plane where electrons can be trapped. A beamforming phased  
 3193 summation is performed for all points in the grid at each time-step. As shown in Section  
 3194 4.4.2.1, the axial oscillation of the electrons prevents one from resolving its position along  
 3195 the z-axis; therefore, the beamforming grid need only cover the possible positions of the  
 3196 electron in the two-dimensional plane defined by the antenna array.

3197 Digital beamforming can be expressed as

$$\mathbf{y}[n] = \Phi^T[n]\mathbf{x}[n], \quad (4.39)$$

3198 where  $\mathbf{x}[n]$  is the array snapshot vector at the sampled time  $n$ ,  $\Phi[n]$  is the matrix of  
 3199 beamforming phase shifts, and  $\mathbf{y}[n]$  is the summed output vector that contains the  
 3200 voltages for each of the summed channels corresponding to a particular beamforming  
 3201 position. The elements of the beamforming phase shift matrix can be expressed as a

3202 weighted complex exponential

$$\Phi_{ij}[n] = A_{ij}[n] \exp(2\pi i \phi_{ij}[n]), \quad (4.40)$$

3203 where the indices  $i$  and  $j$  label the beamforming and antenna positions respectively. The  
3204 weight  $A_{ij}$  accounts for the relative power increase for antennas that are closer to the  
3205 position of the electron, and  $\phi_{ij}$  is the total beamforming phase shift for the  $j$ -th antenna  
3206 at the  $i$ -th beamforming position.

3207 The beamforming phase shift is a sum of two terms described by Equation 4.23, which  
3208 in the notation of Figure 4.29 is

$$\phi_{ij}[n] = \frac{2\pi d_{ij}[n]}{\lambda} + \theta_{ij}[n]. \quad (4.41)$$

3209 The  $\nabla B$ -drift in the trap is accounted for using time-dependent beamforming phases as  
3210 in Equation 4.25. In the coordinate system of Figure 4.29 the time-dependent azimuthal  
3211 position of the electron is

$$\theta_i[n] = \omega_{\nabla B} t[n] + \theta_{i,0}. \quad (4.42)$$

3212 Predicting accurate values of  $\omega_{\nabla B}$  for a specific trap and set of kinematic parameters can  
3213 be done with simulations, which are performed using the Locust software package [65]  
3214 developed by Project 8.

3215 After digital beamforming, a short-time Fourier transform (STFT) is applied to the  
3216 summed time-series to obtain the signal frequency spectrum (see Figure 4.30). From the  
3217 detection perspective, the frequency representation of the CRES data is advantageous  
3218 compared to the time domain, due to the sparseness of CRES signals in the frequency  
3219 domain. The frequency spectra of CRES signals are well-approximated by a frequency and  
3220 amplitude modulated sinusoidal whose carrier frequency increases as a linear chirp [64].  
3221 The modulation is caused by the axial oscillation of the electron in the magnetic trap,  
3222 and the linear chirp is caused by the energy loss due to cyclotron radiation, which results  
3223 in a relatively slow increase in the frequency components of the CRES signal over time.  
3224 A typical CRES signal increases in frequency by approximately 15 kHz during the  
3225 standard Fourier analysis window of 40.96  $\mu$ sec, which is smaller than the frequency  
3226 bin width for a 200 MHz sample rate. Therefore, when considering a single frequency  
3227 spectrum it is justifiable to neglect the effects of the linear frequency chirp.

3228 The majority of the CRES signal power for electrons in the FSCD trap is contained in  
3229 a single frequency component when the electron has a pitch angle  $\gtrsim 88.5^\circ$ . The remain-

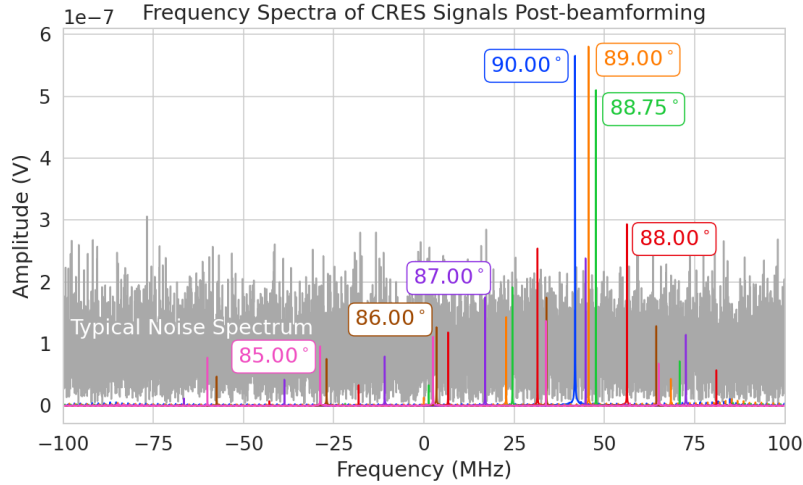


**Figure 4.30.** Frequency spectra of simulated CRES events in the FSCD magnetic trap after beamforming. The signal of a  $90^\circ$  electron consists of a single frequency component that is clearly detectable using a power threshold on the frequency spectrum. This power threshold remains effective for signals with relatively large pitch angles such as  $89.0^\circ$  and  $88.75^\circ$ , which are composed of a main carrier and a few small sidebands. Signals with smaller pitch angles, below about  $88.5^\circ$ , are dominated by sidebands such that no single frequency component can be reliably distinguished from the noise with a power threshold.

ing signal power is distributed between a small number of sidebands with amplitudes proportional to the electron's axial modulation (see Figure 4.30). Signal detection for these pitch angles is straightforward using a simple power threshold on the STFT, since the amplitude of the main signal peak is well above the thermal noise spectrum. However, as the pitch angle of the electron is decreased below  $88.5^\circ$ , the maximum amplitude of the frequency spectrum becomes comparable to typical noise fluctuations. At this point, the power threshold trigger is no longer able to distinguish between signal and noise leading to a reduction in detection efficiency, which is directly linked to the neutrino mass sensitivity of the FSCD. Because the distribution of electron pitch angles is effectively uniform, utilizing a signal detection algorithm that can improve efficiency for pitch angles less than  $88.5^\circ$  will lead to improvements in the neutrino mass sensitivity of the FSCD.

#### 4.4.3 Signal Detection Algorithms

Modeling detection performance requires one to pose the signal detection problem in a consistent manner. The approach studied here uses the frequency spectra obtained from a STFT applied to the beamformed time-series from the FSCD to perform a binary hypothesis test. The basic mathematics of this hypothesis test approach was described

3246 above (Section 4.3), where the noise and signal hypotheses represent the following samples  
 3247 of data,

$$\mathcal{H}_0 : y[n] = \nu[n] \quad (4.43)$$

$$\mathcal{H}_1 : y[n] = x[n] + \nu[n]. \quad (4.44)$$

3248 Under hypothesis  $\mathcal{H}_0$  the vector representing the frequency spectrum ( $y[n]$ ) is composed of  
 3249 complex white Gaussian noise (cWGN,  $\nu[n]$ ) with total variance  $\tau$ , and under hypothesis  
 3250  $\mathcal{H}_1$  the frequency spectrum is composed of a CRES signal ( $x[n]$ ) with added cWGN.  
 3251 The dominant noise source for the FSCD is expected to be thermal Nyquist-Johnson  
 3252 noise, which is well approximated by a cWGN distribution. The hypothesis test is  
 3253 performed by calculating the ratio between the log-likelihood probability distributions  
 3254 for the classifier under  $\mathcal{H}_1$  and  $\mathcal{H}_0$ , which is the standard Neyman-Pearson approach  
 3255 to hypothesis testing [74]. The output of the log-likelihood ratio test is called the test  
 3256 statistic, which is used to assign the data as belonging to the noise or signal classes using  
 3257 a decision threshold.

3258 In practice, the decision threshold is selected by finding the value of the test statistic  
 3259 that guarantees a tolerable rate of false positives. Given this false positive rate (FPR),  
 3260 one attempts to find a classifier that maximizes the true positive rate (TPR), which is  
 3261 the probability of correctly identifying if a piece of data contains signal or noise. Because  
 3262 FSCD signal classifiers will be used to evaluate the spectra of  $O(10^2)$  beamforming  
 3263 positions every  $40.96 \mu\text{sec}$ , there is a requirement that the signal classifiers with FPR  
 3264 significantly smaller than 1% to reduce the burden placed on later stages of the CRES  
 3265 reconstruction chain.

#### 3266 4.4.3.1 Power Threshold

3267 The power threshold detection algorithm uses the maximum amplitude of the frequency  
 3268 spectrum as the detection test statistic. Consider the  $\mathcal{H}_0$  hypothesis where the signal is  
 3269 pure cWGN. The performance of the power threshold can be modeled by first analyzing  
 3270 a single bin in the frequency spectrum. The probability that the amplitude of a single  
 3271 frequency bin falls below the decision threshold is given by the Rayleigh cumulative  
 3272 distribution function (CDF),

$$\text{Ray}(x; \tau) = 1 - \exp(-|x|^2/\tau), \quad (4.45)$$

3273 where the complex value of the frequency bin is  $x$ , and  $\tau$  is the cWGN variance. Because  
 3274 the noise samples are independent and identically distributed (IID), the probability that  
 3275 all bins in the frequency spectrum fall below the threshold is the joint CDF formed by  
 3276 the product of each individual frequency bin CDF,

$$F_0(x; \tau, N_{\text{bin}}) = \text{Ray}(x; \tau)^{N_{\text{bin}}}. \quad (4.46)$$

3277 Finally, the PDF for the power threshold classifier can be obtained by differentiating  
 3278 Equation 4.46.

3279 The noise variance of a beamformed frequency spectrum can be obtained directly  
 3280 from the estimated noise power in a single antenna channel. The Nyquist-Johnson noise  
 3281 power is given by  $k_B T \Delta f$ , where  $k_B$  is Boltzmann's constant,  $T$  is the system noise  
 3282 temperature, and  $\Delta f$  is the sample rate. The beamformed noise variance is increased  
 3283 by a factor of  $N_{\text{ch}}$ , where  $N_{\text{ch}}$  is the number of antennas, caused by the summation of  
 3284 incoherent noise samples, however, the noise variance per frequency bin is decreased by a  
 3285 factor equal to the number of samples in the STFT ( $N_{\text{FFT}}$ ). The final expression for the  
 3286 noise variance of the beamformed frequency spectrum is given by

$$\tau = k_B T \Delta f N_{\text{ch}} R / N_{\text{FFT}}, \quad (4.47)$$

3287 where the system impedance ( $R$ ) has been used to convert from power to voltage-squared.

3288 The probability distribution for the power threshold classifier under  $\mathcal{H}_1$  is calculated  
 3289 in a similar way, but the frequency bins that contain signal must be treated separately.  
 3290 The probability that the amplitude of a frequency bin containing both signal and noise  
 3291 bin falls below the decision threshold is described by a Rician CDF,

$$\text{Rice}(x; \tau, \alpha) = 1 - \int_x^\infty d|\tilde{x}| \frac{2|\tilde{x}|}{\tau} \exp\left(-\frac{|\tilde{x}|^2 + |\alpha|^2}{\tau}\right) \mathcal{I}_0\left(\frac{2|\tilde{x}||\alpha|}{\tau}\right), \quad (4.48)$$

3292 where the parameter  $|\alpha|$  defines the noise-free amplitude of the signal. The CDF that  
 3293 describes the probability that the entire spectrum falls below the decision threshold is  
 3294 the product of both signal and noise CDFs,

$$F_1(x; \tau, \alpha, N_{\text{bin}}, N_s) = \text{Ray}(x; \tau)^{N_{\text{bin}} - N_s} \prod_{k=0}^{N_s} \text{Rice}(x; \tau, \alpha_k). \quad (4.49)$$

3295 The first half of Equation 4.49 is the contribution from the bins in the frequency spectrum

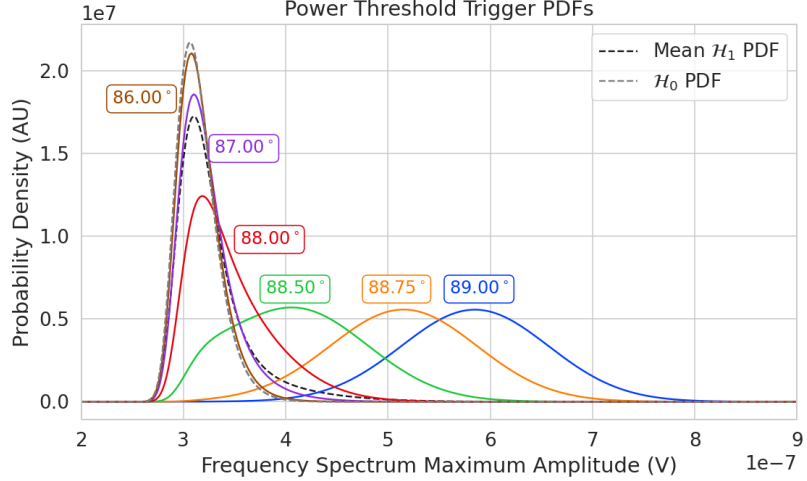


**Figure 4.31.** PDFs of the power threshold test statistic for CRES signals with various pitch angles as well as the PDF for the noise-only signal case. The average PDF computed for pitch angles ranging from 85.5 to 88.5° is also shown. As the pitch angle is decreased the signal PDF converges towards the noise PDF which indicates that the power threshold trigger is unable to distinguish between small pitch angle signals and noise.

3296 that contain only noise, and the second half is the product of the Rician CDFs for the  
 3297 frequency bins that contain signal peaks with a noise-free amplitude of  $|\alpha_k|$ . Figure 4.31  
 3298 shows plots of example PDFs under  $\mathcal{H}_1$  and  $\mathcal{H}_0$ .

#### 3299 4.4.3.2 Matched Filtering

3300 The shape of a CRES signal in-between random scattering events with the background  
 3301 gas is completely determined by the initial conditions of the electron, which implies that  
 3302 it is possible to apply matched filtering as a signal detection algorithm. A matched filter  
 3303 uses the shape of the known signal, which is called a template, to filter the incoming  
 3304 data by computing the convolution between the signal and the data [74]. The matched  
 3305 filter is the optimal detector, which means it achieves the maximum TPR for a particular  
 3306 FPR, under the assumption that the signal is perfectly known and the noise is Gaussian  
 3307 distributed. Since CRES signals have an unknown shape but are deterministic, the  
 3308 matched filter can be applied by using simulations to generate a large number of signal  
 3309 templates, called a "template bank", which spans the parameter space of possible signals.  
 3310 Then at detection time, the template bank is used to identify signals by performing the  
 3311 matched filter convolution for each template in an exhaustive search.

3312 CRES signals are highly periodic in nature. In such cases, it is advantageous to utilize  
 3313 the convolution theorem to replace the matched filter convolution with an inner product

3314 in the frequency-domain. Utilizing the matched filter formalism described above (Section  
 3315 4.3.2) the matched filter test statistic can be written as

$$\mathcal{T} = \max_h \left| \sum_{n=0}^{N_{\text{bin}}} h^\dagger[n] y[n] \right|, \quad (4.50)$$

3316 where  $h^\dagger[n]$  is the complex conjugate of the signal template.

3317 The approach to deriving PDFs that describe the matched filter template bank will  
 3318 be to first derive PDFs for  $\mathcal{H}_0$  and  $\mathcal{H}_1$  in the case of a single template and use these  
 3319 solutions to create PDFs that describe the multi-template case. In the case when the  
 3320 template bank consists of only a single template it is possible to derive an exact analytical  
 3321 form for the PDF. Consider the  $\mathcal{H}_1$  case, where the equation describing the matched  
 3322 filter test statistic, also known as the matched filter score, becomes

$$\mathcal{T} = \left| \sum_{n=0}^{N_{\text{bin}}} h^\dagger[n] y[n] \right|. \quad (4.51)$$

3323 Each noisy frequency bin is a sum of signal and cWGN, which means  $y[n]$  is also a  
 3324 Gaussian distributed variable. Therefore, the value of the inner product between the  
 3325 template and the data is also a complex Gaussian variable; and, since the matched filter  
 3326 score is the magnitude of this inner product, it must follow a Rician distribution.

3327 The distribution that describes the matched filter score under  $\mathcal{H}_1$  can be derived  
 3328 starting with the matched filter template equation. The matched filter template  $\mathbf{h}$  is a  
 3329 simulated signal ( $\mathbf{x}_h$ ) with a normalization factor

$$\mathbf{h} = \frac{\mathbf{x}_h}{\sqrt{\tau |\mathbf{x}_h|^2}}, \quad (4.52)$$

3330 where  $\tau$  is the noise variance. Inserting this into Equation 4.50 and expressing the data  
 3331 as a sum between a signal and a WGN vector yields,

$$\mathcal{T} = \frac{1}{\sqrt{\tau |\mathbf{x}_h|^2}} \left| \sum_{n=1}^{N_{\text{bin}}} x_h^\dagger[n] x[n] + \sum_{n=1}^{N_{\text{bin}}} x_h^\dagger[n] \nu[n] \right|. \quad (4.53)$$

3332 The first term is a scalar product between the signal and template vectors and the  
 3333 second term is a complex Gaussian distributed variable with variance one. For the  
 3334 purposes of identifying the statistical distribution, it is useful to rewrite the summation

3335 describing an inner product

$$\sum_{n=1}^{N_{\text{bin}}} x_h^\dagger[n] x[n] = \mathbf{x}_h \cdot \mathbf{x} = |\mathbf{x}_h \cdot \mathbf{x}| e^{i\vartheta} \leq |\mathbf{x}_h| |\mathbf{x}| e^{i\vartheta}, \quad (4.54)$$

3336 the last step utilizes the Cauchy-Schawrz inequality, where equality is guaranteed when  
3337  $\mathbf{x} = \mathbf{x}_h$ . Instead of the inequality it is useful to define a quantity called "match" such that

$$|\mathbf{x}_h \cdot \mathbf{x}| e^{i\vartheta} = |\mathbf{x}_h| |\mathbf{x}| \Gamma e^{i\vartheta}, \quad (4.55)$$

3338 where the match factor  $\Gamma \in [0, 1]$ . The match factor quantifies how well the template  
3339 matches the signal.

3340 The fact that the second term is a random complex Gaussian variable with unity  
3341 variance can be seen by noting that each of the noise samples are drawn from the complex  
3342 Gaussian distribution,  $\mathcal{N}(0, \tau)$ . Therefore,

$$\frac{x_h^\dagger[n]}{\sqrt{\tau |\mathbf{x}_h|^2}} \nu[n] \sim \mathcal{N}\left(0, \frac{x_h^\dagger[n] x_h[n]}{|\mathbf{x}_h|^2}\right), \quad (4.56)$$

$$n = \sum_{n=1}^{N_{\text{bin}}} \frac{x_h[n]}{\sqrt{\tau |\mathbf{x}_h|^2}} \nu[n] \sim \mathcal{N}\left(0, \frac{\sum_{n=1}^{N_{\text{bin}}} x_h^\dagger[n] x_h[n]}{|\mathbf{x}_h|^2}\right) = \mathcal{N}(0, 1). \quad (4.57)$$

3343 Equation 4.53 can now be simplified

$$\mathcal{T} = ||\mathbf{h}||\mathbf{x}| \Gamma e^{i\vartheta} + n |, \quad (4.58)$$

3344 where Equation 4.52 has been used to redefine the inner product term. The quantity  
3345  $||\mathbf{h}||\mathbf{x}| \Gamma$  is a real number, which is the matched filter score that one would expect if the  
3346 data contained no noise. The final simplification is to define  $\mathcal{T}_{\text{ideal}} = ||\mathbf{h}||\mathbf{x}| \Gamma$ , from which  
3347 one obtains

$$\mathcal{T} = |\mathcal{T}_{\text{ideal}} e^{i\vartheta} + n|. \quad (4.59)$$

3348 From Equation 4.59 on can see that  $\mathcal{T}$  is simply the magnitude of a complex number  
3349 with added cWGN of variance 1, which follows the Rician distribution; therefore the  
3350 distribution that describes the matched filter score for a single template under  $\mathcal{H}_1$  is

$$P_1(x; \mathcal{T}_{\text{ideal}}) = 2x \exp(- (x^2 + \mathcal{T}_{\text{ideal}}^2)) I_0(2x\mathcal{T}_{\text{ideal}}). \quad (4.60)$$

3351 The shape of the matched filter score distribution is controlled by the parameter  $\mathcal{T}_{\text{ideal}}$ ,

3352 which is effectively the value of the matched filter score if the data contained no noise.  
 3353 Without noise, the data vector reduces to the signal,  $\mathbf{x}$ , in which case Equation 4.51  
 3354 becomes the magnitude of an inner product between two vectors. The magnitude of an  
 3355 inner product can be expressed in terms of the magnitudes of the vectors and a constant  
 3356 that describes the degree of orthogonality between them. Applying this to Equation 4.51,  
 3357 one obtains

$$\mathcal{T}_{\text{ideal}} = |\mathbf{h}^\dagger \cdot \mathbf{x}| = |\mathbf{h}| |\mathbf{x}| \Gamma \quad (4.61)$$

3358 where  $\Gamma$  describes the orthogonality between  $\mathbf{h}$  and  $\mathbf{x}$ .  $\Gamma$  effectively quantifies how well  
 3359 the template matches the unknown signal in the data.

3360 The matched filter score PDF under  $\mathcal{H}_0$  is readily obtained from Equation 4.60 by  
 3361 setting the value of  $\mathcal{T}_{\text{ideal}}$  to zero, since the data contains no signal in the noise case.  
 3362 Doing this, one obtains a Rayleigh distribution,

$$P_0(x) = 2x \exp(-x^2). \quad (4.62)$$

3363 Equations 4.60 and 4.62 describe the behavior of the matched filter test statistic  
 3364 under  $\mathcal{H}_0$  and  $\mathcal{H}_1$  for a single template. However, defining a PDF that describes the  
 3365 matched filter test statistic in the case of multiple templates is in general a mathematically  
 3366 intractable problem, since there is no guarantee of orthogonality between matched filter  
 3367 templates. This leads to correlations between the matched filter scores of different  
 3368 templates, because only one sample of noise is used to compute the matched filter scores  
 3369 of the template bank. In order to proceed, it is assumed that the matched filter scores for  
 3370 all templates are IID variables, which allows one to ignore correlations between templates.  
 3371 The overall effect of this will be an underestimate of the performance of the matched  
 3372 filter by over-estimating the required number of templates and; therefore, the magnitude  
 3373 of the statistical trials penalty.

3374 The probability that the matched filter score falls below the decision threshold under  
 3375  $\mathcal{H}_0$  is again given by the CDF. Because of the assumption that matched filter scores from  
 3376 different templates are independent, the probability that the matched filter score for all  
 3377 templates falls below the threshold value is simply the joint CDF, which is

$$F_0(x) = \left(1 - e^{-x^2}\right)^{N_t}, \quad (4.63)$$

3378 where  $x$  is the matched filter score threshold and  $N_t$  is the number of templates. One  
 3379 should expect that the distribution describing the maximum score of the matched filter

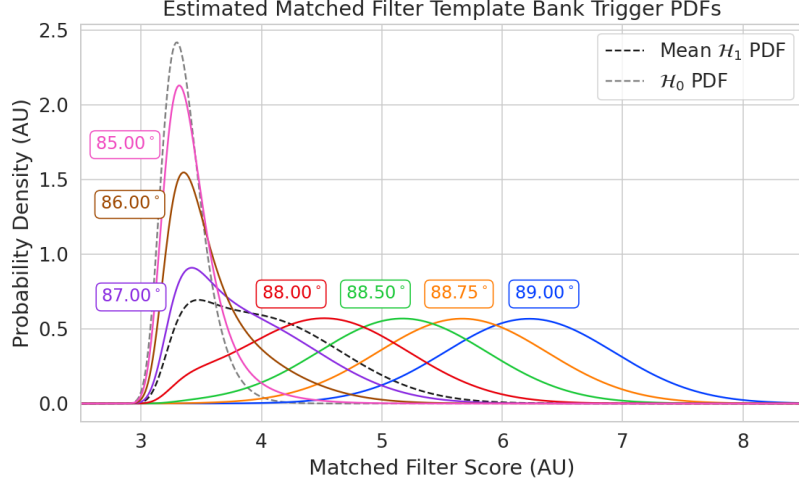


**Figure 4.32.** Plots of PDFs that describe the matched filter template bank test statistic for CRES signals with various pitch angles, as well as the estimated PDF for the noise only case.  $10^5$  matched filter templates are used and perfect match between signal and template i.e.  $\Gamma_{\text{best}} = 1$  is assumed. The mean PDF includes signals ranging from  $85.5 - 88.5^\circ$  in pitch angle. There is a larger distinction between the signal PDFs at small pitch angles compared to the power threshold, which indicates a higher detection efficiency for these signals.

3380 template bank depends on  $N_t$ , because with more templates there is a greater chance of  
 3381 a random match between the template and data.

3382 The CDF that describes  $\mathcal{H}_1$  is derived by starting with the CDF of the best matching  
 3383 template,  $F_{\text{best}}(x; \mathcal{T}_{\text{best}})$ . Because of the orthogonality assumption, the matched filter  
 3384 scores for all other templates are negligible ( $\mathcal{T}_{\text{ideal}} \approx 0$ ). The joint CDF that describes  
 3385 the total template bank is obtained by combining the distributions for all templates used  
 3386 during detection. Therefore, the estimated CDF under  $\mathcal{H}_1$  is

$$F_1(x; \mathcal{T}_{\text{best}}) = F_{\text{best}}(x; \mathcal{T}_{\text{best}}) \left(1 - e^{-x^2}\right)^{N_t}. \quad (4.64)$$

3387 Figure 4.32 shows plots of the matched filter template bank PDFs under  $\mathcal{H}_0$  and  $\mathcal{H}_1$ .

#### 3388 4.4.3.3 Machine Learning

3389 The focus in this paper is on the potential of Convolutional Neural Networks (CNN)  
 3390 as a machine learning based signal classifier at the trigger level. CNNs are constructed  
 3391 using a series of convolutional layers, each composed of a set of filters that are convolved  
 3392 with the input data. The individual convolutional filters can be viewed heuristically  
 3393 as matched filter templates [86] that are learned from a set of simulated data rather

3394 than being directly generated. This opens the possibility of finding a more efficient  
 3395 representation of the matched filter templates during the training process that can  
 3396 potentially reduce computational cost at inference time while retaining good classification  
 3397 performance.

3398 The machine learning approach is distinct from the power threshold and matched  
 3399 filtering in that there is no attempt to manually engineer a test statistic that can be  
 3400 computed from the input data. Instead, a test statistic is calculated by constructing a  
 3401 differentiable function that maps the complex frequency series to a binary classification  
 3402 as signal or noise. The differentiable function is trained using supervised learning to  
 3403 correctly perform this mapping. The test statistic for the machine learning classifier is  
 3404 expressed mathematically as

$$\mathcal{T} = G(\mathbf{y}; \boldsymbol{\Omega}) \quad (4.65)$$

3405 where  $\mathbf{y}$  is the noisy data vector and  $G(\mathbf{y}; \boldsymbol{\Omega})$  is the machine learning model parameterized  
 3406 by the weights  $\boldsymbol{\Omega}$ .

**Table 4.1.** A summary of the CNN model layers and parameters. The output of each 1D-Convolution and Fully Connected layer is passed through a LeakyReLU activation function and re-normalized using batch normalization before being passed to the next layer in the model. The output of the final Fully Connected layer in the model is left without activation so that the model outputs can be directly passed to the Binary Cross-entropy loss function used during training. The first layer in the network has two input channels for the real and imaginary components of the spectrum.

Layer	Type	Input Channels	Output Channels	Parameters
1	1D-Convolution	2	15	( $N_{\text{kernel}} = 4$ , $N_{\text{stride}} = 1$ )
2	Maximum Pooling	15	15	( $N_{\text{kernel}} = 4$ , $N_{\text{stride}} = 4$ )
3	1D-Convolution	15	20	( $N_{\text{kernel}} = 4$ , $N_{\text{stride}} = 1$ )
4	Maximum Pooling	20	20	( $N_{\text{kernel}} = 4$ , $N_{\text{stride}} = 4$ )
5	1D-Convolution	20	25	( $N_{\text{kernel}} = 4$ , $N_{\text{stride}} = 1$ )
6	Maximum Pooling	25	25	( $N_{\text{kernel}} = 4$ , $N_{\text{stride}} = 4$ )
7	Fully Connected	3200	512	NA
8	Fully Connected	512	64	NA
9	Fully Connected	64	2	NA

3407 The CNN architecture used for this work is summarized by Table 4.1. No strategic  
 3408 hyper-parameter optimization approach was implemented beyond the manual testing  
 3409 of different CNN architecture variations, so this particular model is best viewed as a  
 3410 proof-of-concept rather than a rigorously optimized design. Numerous model variations  
 3411 were tested, some with significantly more layers and convolutions filters per layer, as  
 3412 well as others that were even smaller than the architecture in Table 4.1. Ultimately, the

3413 model architecture choice was driven by the motivation to find the minimal model whose  
3414 classification performance was still comparable to the larger CNN's tested, because of  
3415 the importance of minimizing computational cost in real-time applications. It is possible  
3416 that more sophisticated machine learning models could improve upon the classification  
3417 results achieved here, but this investigation is left for future work.

3418 **4.4.4 Methods**

3419 **4.4.4.1 Data Generation**

3420 Simulated CRES signals were generated using the Locust simulations package [65, 77].  
3421 Locust uses the separately developed Kassiopeia package [63] to calculate the magnetic  
3422 fields produced by a user defined set of current carrying coils along with any specified  
3423 background magnetic fields, resulting in a magnetic trap. Next, Kassiopeia calculates the  
3424 trajectory of an electron in this magnetic field starting from a set of user specified initial  
3425 conditions. The Locust software then uses the electron trajectories from Kassiopeia  
3426 to calculate the resulting electromagnetic fields using the Liénard-Wiechert equations,  
3427 and determines the voltages generated in the antenna array with the antenna transfer  
3428 function. Locust then simulates the down-conversion, filtering, and digitization steps  
3429 resulting in the simulated CRES signals for an electron.

3430 The shape of the received CRES signal is determined by the initial kinematic param-  
3431 eters, including the starting position of the electron, the starting kinetic energy of the  
3432 electron, and the pitch angle. The studies performed here are constrained to a single  
3433 initial electron position located at  $(x, y, z) = (5, 0, 0)$  mm. Two datasets are generated  
3434 using this starting position by varying the initial kinetic energy and pitch angle. The  
3435 first dataset consists of a two-dimensional square grid spanning an energy range from  
3436 18575-18580 eV with a spacing of 0.1 eV, and pitch angles from 85.5-88.5° with a spacing  
3437 of 0.001°, resulting in 153051 signals with a unique energy-pitch angle combination. This  
3438 dataset is intended to represent a matched filter template bank. The upper range of pitch  
3439 angles is limited because of the greater relative detection efficiency of the matched filter  
3440 and neural network classifiers in this pitch angle range. The second dataset was generated  
3441 by randomly sampling uniform probability distributions covering the same parameter  
3442 space to produce approximately 50000 signals randomly parameterized in energy and  
3443 pitch angle. This dataset provides the training and test data for the machine learning  
3444 approach, and acts as a representative sample of signals to evaluate the performance of  
3445 the matched filter template bank.

3446     Each signal was simulated for a duration of  $40.96 \mu\text{s}$  or 8192 samples starting at  
 3447     time  $t = 0$  s for all simulations. This duration represents a single frequency spectrum  
 3448     generated by the STFT. The FSCD antenna array has sixty channels, and the output of  
 3449     the Locust simulations are a matrix of array snapshots with a size given by the number  
 3450     of channels times the event length ( $N_{\text{ch}} \times N_{\text{sample}}$ ). The raw data from Locust is first  
 3451     summed using digital beamforming and converted to frequency spectra using a Fourier  
 3452     transform. The beamforming procedure uses the exact position and  $\nabla B$ -drift correction  
 3453     to simplify the comparison between trigger algorithms. Many beamforming positions  
 3454     would be used in practice and potentially several estimates of a typical  $\omega_{\nabla B}$  depending  
 3455     on the variation of the  $\nabla B$ -drift frequency with pitch angle.

#### 3456     **4.4.4.2 Template Number and Match Estimation**

3457     The estimated PDF for the matched filter template bank on the number of templates and  
 3458     the mean match ( $\Gamma_{\text{best}}$ ). A given signal with random parameters will have a template in  
 3459     the filter bank that gives the highest matched filter score; therefore, the mean match  
 3460     ratio is obtained by averaging over the best matching templates for a representative  
 3461     population of test signals.  $\Gamma_{\text{best}}$  is a figure of merit that characterizes the performance of  
 3462     a template bank at signal detection. One expects that with more templates the value  
 3463     of  $\Gamma_{\text{best}}$  will increase, however, there is a point of diminishing returns at which more  
 3464     templates will not significantly increase match, but will still increase the likelihood of  
 3465     false positives. Therefore, it is desirable to use the minimum number of templates that  
 provide an acceptable mean value of  $\Gamma_{\text{best}}$ .

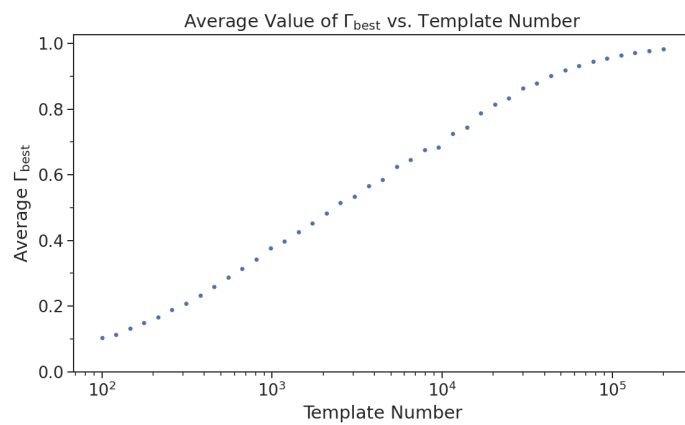


**Figure 4.33.** The mean match of the matched filter template bank to a test set of randomly parameterized signals as a function of the number or density of templates. The parameter space includes pitch angles from  $85.5 - 88.5^\circ$  and energies from 18575 – 18580 eV.

3466 To quantify the relationship between match and template number, the mean match  
3467 of the random dataset to a selection of templates from the regularly spaced dataset was  
3468 calculated using a subset of the mean match values from Figure 4.18 with a sample  
3469 length of 8192. Again, one sees that the average value of  $\Gamma_{\text{best}}$  is an exponential function  
3470 of the number of templates (see Figure 4.33). Using this plot one can infer the required  
3471 number of templates for the desired value of mean match.

#### 3472 4.4.4.3 CNN Training and Data Augmentation

3473 The random dataset is split in half to create distinct training and test datasets for  
3474 training the model. A randomly selected 20% of the training data is isolated for use as  
3475 a validation set during the training loop. The size of the training, validation, and test  
3476 datasets are tripled by appending two additional copies of the data to increase the sample  
3477 size of the dataset after data augmentation. A different sample of noise is added to the  
3478 simulation data during the training loop, which prevents the model from overtraining on  
3479 noise features. The training and test datasets contain an equal split between signal and  
3480 noise data, which are randomly shuffled after each training epoch.

3481 The Locust simulation data was augmented to make the datasets more representative  
3482 of actual experiment data. As the signals are loaded for training a unique random phase  
3483 shift is applied. Since the simulations are generated using the same initial axial position  
3484 and cyclotron orbit phase, the randomization is an attempt to prevent overtraining on  
3485 these features. During each training epoch the data is randomly shuffled and split into  
3486 batches of 2500 signals. Each batch of signals is then circularly shifted by a random  
3487 number of frequency bins to simulate a kinetic energy shift from  $-75$  to  $20$  eV, which  
3488 imitates a dataset with a larger energy range. Next, a sample of cWGN, consistent  
3489 with  $10$  K Nyquist-Johnson noise, is generated and added to the signal, which prevents  
3490 overtraining on noise features. As a final step, the data is renormalized by the standard  
3491 deviation of the noise so that the range of values in the data is close to  $[-1, 1]$ , which  
3492 ensures well-behaved back-propagation.

3493 The Binary Cross-entropy loss function is used to compute the loss for each batch of  
3494 data, and the model weights are updated using the ADAM optimizer with a learning  
3495 rate of  $5 \times 10^{-3}$ . After each training epoch, the loss and classification accuracy of the  
3496 validation dataset are computed to monitor for overtraining. It was noticed that because  
3497 of the relatively high noise power and the fact that a new sample of noise was used for  
3498 each batch, it was nearly impossible to over-train the model. Typically, the loss and

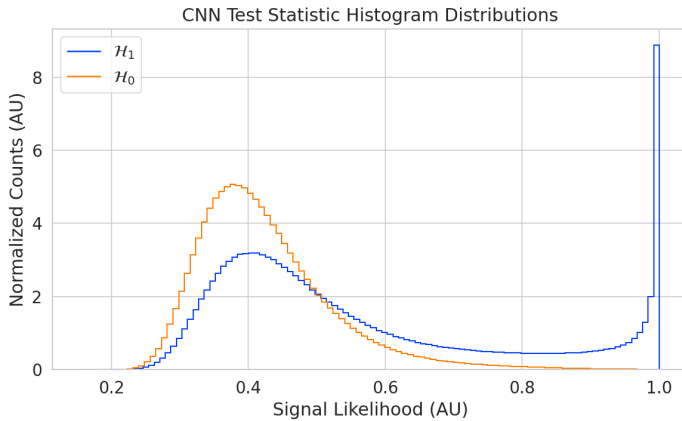


**Figure 4.34.** Histograms of the trained CNN model output from the test dataset. The blue histogram shows the model outputs for signal data. The oddly shaped peak near the end is the result of the softmax function mapping the long tail of the raw output distribution to the range [0, 1].

classification accuracy of the model converged after a few hundred training epochs, but the training loop was extended to 3000 epochs to attempt to achieve the best possible performance. The training procedure generally took about 24 hrs using a single NVIDIA V100 GPU [87].

After training the model, it was used to classify the test dataset and generate histograms of the model outputs for both classes of data. The data augmentation procedure for the evaluation of the test data mirrors the training procedure without the validation split. Since a random circular shift and a new sample of WGN is added to each batch, the testing evaluation loop is run for 100 epochs to get a representative sample of noise and circular shifts. The model outputs are passed through a softmax activation and then combined into histograms (see Figure 4.34).

## 4.4.5 Results and Discussion

### 4.4.5.1 Trigger Classification Performance

The detection performance of the signal classifiers can be compared by computing the receiver operating characteristic (ROC) curves (see Figure 4.35). A single ROC curve is obtained for the matched filter and power threshold classifiers by averaging over analytical ROC curves obtained from the distributions in Section 4.4.3. Two ROC curves are calculated for the matched filter with different numbers of templates and mean match. The ROC curve describing the CNN is obtained numerically from the histograms of the

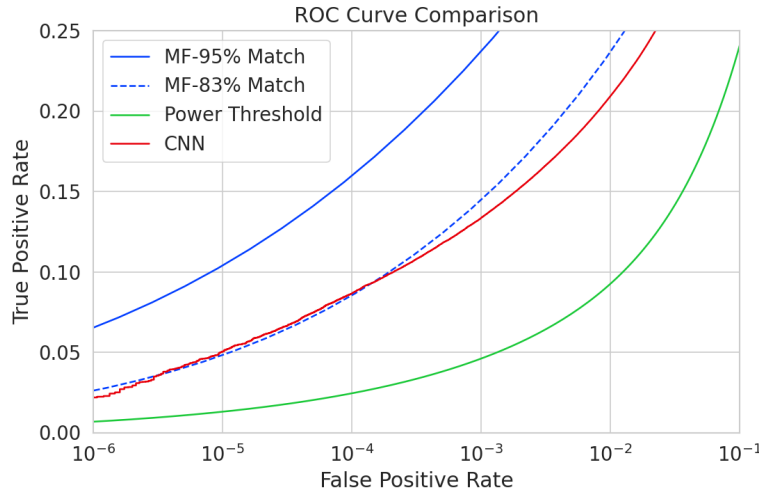


**Figure 4.35.** ROC curves describing the detection efficiency or true positive rates for the three signal classification algorithms examined in this paper. The matched filter (MF) and Power Threshold curves are computed analytically using the distribution functions introduced in Section 4.4.3, and the CNN curve is computed numerically using the classification results on the test dataset. The percent match indicated in the legend refers to the mean match of the classifier.

3518 model outputs for each signal class.

3519 The TPR of a signal classifier is equivalent to its detection efficiency, and one sees  
 3520 that for the population of signals with pitch angles  $< 88.5^\circ$  the power threshold has  
 3521 a consistently lower detection efficiency than the CNN and the matched filter. This  
 3522 result might have been predicted from the visualization of signal spectra in Figure 4.30,  
 3523 where it can be seen that a noise peak and a signal peak cannot be distinguished with  
 3524 high-confidence at small pitch angles. The CNN offers a significant and consistent increase  
 3525 in detection efficiency over the power threshold approach, with the relative improvement  
 3526 in detection efficiency increasing as the false positive rate decreases.

3527 If one compares the CNN to the matched filter, it can be seen that the performance of  
 3528 the tested network is roughly equivalent to a matched filter detector with a mean match  
 3529 of about 83%, which uses approximately  $2 \times 10^4$  matched filter templates. The overall  
 3530 best detection efficiency is achieved by the matched filter classifier if a large enough  
 3531 template bank is used. The plot displays the ROC curve for a matched filter template  
 3532 bank with 95% mean match, which is achieved with approximately  $10^5$  templates. Since  
 3533 the matched filter is known to be statistically optimal for detecting a known signal in  
 3534 WGN, it is unsurprising that this algorithm has the highest detection efficiency.

3535 An important difference between the matched filter and CNN algorithms is that the

3536 CNN relies upon convolutions as its fundamental calculation mechanism; whereas our  
3537 implementation of a matched filter utilizes an inner product. Since convolution is a  
3538 translation invariant operation, the detection performance of CNN can be extended to  
3539 a wider range of CRES event kinetic energies with less cost than the matched filter, a  
3540 feature that is exploited during the CNN training by including circular translations of  
3541 the CRES frequency spectra in the training loop. Increasing the range of detectable  
3542 kinetic energies with a matched filter requires a proportional increase in the number of  
3543 templates, which directly translates into increased computational and hardware costs.  
3544 From a practical perspective, the detection algorithm is always limited by the available  
3545 computational hardware, so estimating the relative costs is a key factor in determining  
3546 their feasibility. A more detailed analysis of the relative costs of each of the detection  
3547 algorithms is performed below.

#### 3548 4.4.5.2 Computational Cost and Hardware Requirements

3549 The trade-off between better detection efficiency and computational cost is common  
3550 to many signal detection problems and the FSCD is no exception. Computational  
3551 costs can be related to actual hardware costs by calculating the theoretical amount of  
3552 computer hardware required to implement the signal classifiers for real-time detection.  
3553 The approach taken here utilizes order of magnitude estimates of the theoretical peak  
3554 performance values for currently available Graphics Processing Units (GPUs) as a metric.  
3555 This approach underestimates the amount of required hardware, since it is unlikely that  
3556 any CRES detection algorithm could reach the theoretical peak performance of the  
3557 hardware.

3558 Since the signal detection algorithms are designed to work using beamformed frequency  
3559 spectra, the computational cost of beamforming combined with a fast Fourier transform  
3560 (FFT) is constant for all classifiers. The beamforming grid is assumed to contain  $N_{\text{bf}}$   
3561 beamforming positions, each of which will produce a frequency spectrum containing  $N_{\text{bin}}$   
3562 after the FFT.

3563 Considering the power threshold classifier, this results in  $N_{\text{bin}}N_{\text{b}}$  frequency bins  
3564 that must be checked every  $N_{\text{bin}}/f_s$  seconds. The 20 cm diameter FSCD array requires  
3565  $N_{\text{bf}} \approx O(10^2)$  for sufficient coverage and has a sampling frequency  $f_s = 200$  MHz with a  
3566 Fourier analysis window of  $N_{\text{bin}} = 8192$  samples. Therefore the power threshold requires  
3567 approximately  $O(10^{10})$  FLOPS to check in real-time with these parameters

3568 Current generations of GPUs have peak theoretical performances in the range of  
3569  $O(10^{13}) - O(10^{14})$  FLOPS [88], dependent on the required floating-point precision of

3570 the computation. Therefore, the entire computational needs of a real-time triggering  
3571 system using a power threshold classifier, including digital beamforming and generation  
3572 of the STFT, could be met by a single high-end GPU or a small number of less powerful  
3573 GPUs. Since triggering is only one step of the full real-time signal reconstruction  
3574 approach, limiting the computational cost of this stage is ideal. However, the power  
3575 threshold classifier does not provided sufficient detection efficiency across the entire  
3576 range of possible signals, which is the primary motivation for exploring more complicated  
3577 triggering solutions.

3578 As discussed, the computational cost of the matched filter approach requires counting  
3579 the number of templates that must be checked for each frequency spectra produced by  
3580 the STFT. Computing the matched filter scores requires  $O(N_{\text{bf}}N_t N_{\text{bin}})$  operations, since  
3581 for each of the beamforming positions one must multiply  $N_t$  templates with a data vector  
3582 that has length  $N_{\text{bin}}$ . The computation must be performed in a time less-than or equal  
3583 to  $N_{\text{bin}}/f_s$  to keep up with the data generation rate. A 5 eV range of kinetic energies  
3584 required  $10^4$  to  $10^5$  templates in order for the matched filter to exceed the performance  
3585 of the CNN. The number of templates is expected to scale linearly with the total kinetic  
3586 energy range of interest; therefore,  $10^5$  to  $10^6$  matched filter templates would be expected  
3587 for the nominal 50 eV analysis window of the FSCD. Considering this, the estimated  
3588 computational cost of the matched filter is between  $O(10^{15})$  to  $O(10^{16})$  FLOPS, which is  
3589  $O(10^2)$  to  $O(10^3)$  high-end GPUs.

3590 The computational cost of the CNN can be estimated by simply summing the compu-  
3591 tational costs of the convolutions and matrix multiplications specified by the network  
3592 architecture shown in Table 4.1. Each convolutional layer consists of  $N_{\text{in}}N_{\text{out}}N_{\text{kernel}}L_{\text{input}}$   
3593 floating-point operations, where  $N_{\text{in}}$  is the number of input channels,  $N_{\text{out}}$  is the number  
3594 of output channels,  $N_{\text{kernel}}$  is the size of the convolutional kernel, and  $L_{\text{input}}$  is the length  
3595 of the input vector, and the fully connected layers each contribute  $N_{\text{in}}N_{\text{out}}$  operations.  
3596 Summing all the neural network layers it is estimated that the CNN requires  $O(10^6)$   
3597 floating point operations to evaluate each frequency spectra; therefore, the total com-  
3598 putational cost of the CNN trigger is value multiplied by the number of beamforming  
3599 positions per the data acquisition time, which is  $O(10^{13})$  FLOPS or  $O(10^0)$  GPUs.

3600 Compared with the matched filter approach the CNN requires  $O(100)$  to  $O(1000)$   
3601 fewer GPUs to implement, dependent on the exact number of templates used in the  
3602 template bank. The 50 eV kinetic energy range is motivated by the application of these  
3603 detection algorithms to an FSCD-like neutrino mass measurement experiment. However,  
3604 if a significantly larger range of kinetic energies is required, a CNN may be the preferred

3605 detection approach despite the lower mean detection efficiency due to computational cost  
3606 considerations.

3607 Additional experiments with larger CNNs, generated by increasing the depth and  
3608 width of the neural network, were performed. It was observed that these changes  
3609 provided minimal ( $\lesssim 1\%$ ) improvement in the classification accuracy of the model. A  
3610 potential reason for this could be the sparse nature of the signals in the frequency  
3611 domain and the low SNR, which makes for a challenging dataset to learn from. Future  
3612 work might investigate modifications to the neural network architecture such as sparse  
3613 convolutions, which may improve the classification accuracy of the model or further  
3614 reduce the computational costs of this approach. Alternatively, more complicated CNN  
3615 architectures such as a ResNet [89] or VGG model [90] may provide improved classification  
3616 performance over a basic CNN. An additional promising area of investigation are recurrent  
3617 neural networks, which may be able to exploit the time-ordered features of the STFT for  
3618 more accurate signal detection if the electron signals last for multiple Fourier transform  
3619 windows.

3620 The estimate of the computational costs of the matched filter is somewhat naive if one  
3621 notices that the majority of the values that make up a CRES frequency spectrum are zero  
3622 (see Figure 4.30). Therefore, the majority of operations in the matched filter inner product  
3623 are unnecessary, and one could instead evaluate the matched filter inner product using  
3624 only the  $\lesssim 10$  frequency peaks that make up the CRES signal. This optimization reduces  
3625 the number of operations required to check each template by a factor of  $O(100)$  to  $O(1000)$ ,  
3626 which brings the estimated computational cost of the matched filter in line with the  
3627 CNN. Although this level of sparsity results in a multiplication with very low arithmetic  
3628 complexity, the resulting sparse matched filter algorithm is still likely to be constrained  
3629 by memory access speed rather than compute speed. Ultimately, the comparison of  
3630 the relative computational and hardware costs between the matched filter and CNN  
3631 will depend on the efficiency of the software implementation and hardware support for  
3632 neural network and sparse matrix calculations, which will need to be determined using  
3633 real-world benchmarks.

#### 3634 **4.4.6 Conclusion**

3635 Increasing the detection efficiency and overall event rate of the CRES technique represents  
3636 a key developmental path towards new scientific results and broader applications of the  
3637 CRES technique. It is what motivates both the antenna array detection approach and  
3638 the development of real-time signal reconstruction algorithms. The work presented here

3639 demonstrates that significant gains in the detection efficiency of the CRES technique  
3640 are achievable by utilizing triggering algorithms that account for the specific shape of  
3641 CRES signals in the detector. These algorithms emphasize the need for accurate and fast  
3642 methods for CRES simulation, since they directly contribute to the success of matched  
3643 filter methods by providing a way to generate expected signal templates and also serve  
3644 as a source of training data for machine learning approaches.

3645 The down-side of these more advanced approaches to signal detection is the increase  
3646 in computational resources required to implement them. However, it was shown that a  
3647 CNN of minimal size was able to significantly improve detection performance above the  
3648 baseline power threshold trigger algorithm with a theoretical computational cost of only  
3649  $O(1)$  high-end GPU. This algorithm improves on detection performance while requiring  
3650 at least a factor  $O(10^2)$  less in computer relative to a matched filter template bank,  
3651 which would be the classical approach to signal detection in Gaussian noise. Future work  
3652 obtaining real-life benchmarks of the CNN and matched filter algorithms are required to  
3653 support these conclusions, but this study has indicated that a real-time signal detection  
3654 algorithm for an antenna array CRES experiment is computationally feasible without  
3655 extraordinary compute power.

3656 While this work has focused on the real-time detection of CRES signals from antenna  
3657 arrays, these same signal classifiers could be used in CRES experiments utilizing different  
3658 detector technologies, since the same principles of signal detection will apply. For example,  
3659 previous CRES measurements by the Project 8 collaboration that utilized a waveguide  
3660 gas cell, could have improved their detection efficiency by employing a matched filter  
3661 or neural network classifier to identify trapped electrons with pitch angles that are too  
3662 small to be detected by the power threshold approach. Furthermore, alternative CRES  
3663 detector technologies such as resonant cavities [41] could also see similar improvements  
3664 in detection efficiency, which is of crucial importance to future efforts by the Project 8  
3665 collaboration to utilize CRES to measure the neutrino mass.

# **Chapter 5**

## **Antenna and Antenna Measurement System Development for the Project 8 Experiment**

### **5.1 Introduction**

The FSCD (free space CRES demonstrator) and antenna array CRES (cyclotron radiation emission spectroscopy) represent an innovative approach to beta-decay spectroscopy. While much can be learned from simulations about the systematics of CRES with antenna arrays, laboratory measurements and demonstrations provide critical inputs to sensitivity and simulation models, and provide a means for calibration and commissioning of the experiment. Therefore, a robust program of antenna and antenna measurement hardware development is key to the success of the FSCD and the development of antenna array CRES more broadly.

In this chapter I summarize the development of an antenna measurement system at Penn State to implement and test the techniques of antenna array CRES on the bench-top. In Section 5.2 I provide an introduction to some fundamental parameters and concepts related to antenna measurements as well as an overview of the Penn State antenna measurement system hardware. In Section 5.3 I include the manuscript of a paper [78] which details the design and characterization of a specialized antenna developed to mimic the electric fields emitted by an electron in a CRES experiment. This antenna, called the Synthetic Cyclotron Antenna (SYNCA), is intended as a calibration tool for antenna arrays developed for CRES measurements. Lastly, in Section 5.4 I summarize a set of prototype FSCD antenna array measurements with the SYNCA [44], which I use to validate the simulated performance of the antenna array and estimate systematic errors associated with the antenna array.

## 3691 5.2 Antenna Measurements for CRES experiments

### 3692 5.2.1 Antenna Parameters

3693 Antenna characterization measurements are intended to validate simulations of the  
3694 antenna array performance, which ultimately informs the neutrino mass sensitivity of  
3695 the experiment. In this section, I shall summarize a few fundamental concepts relating  
3696 to antennas and antenna measurement, before introducing how Project 8 uses antenna  
3697 measurements for the development of antenna array CRES.

#### 3698 5.2.1.1 Radiation Patterns

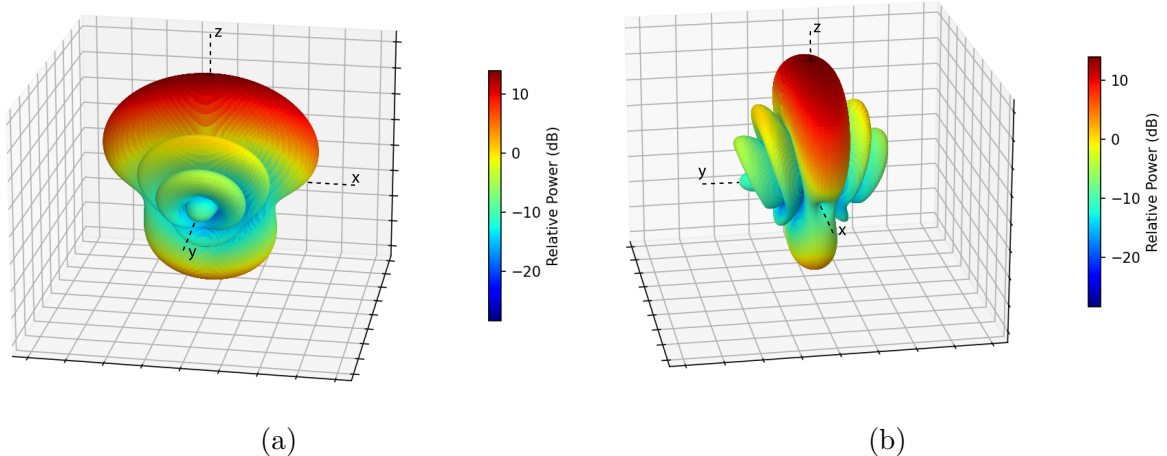


**Figure 5.1.** An example radiation pattern generated using HFSS simulations. The color and radial distance of the surface from the origin indicate the relative magnitude of radiation power emitted by the antenna in that direction. The primary goal of most antenna measurements is typically to measure the antenna pattern, which is used to derive many useful antenna performance parameters.

3699 Antennas are conductive structures designed to carry alternating electric currents  
3700 to transmit energy in the form of EM (electro-magnetic) waves [68]. Perhaps the most  
3701 fundamental way to characterize an antenna, is to map out the radiated power density  
3702 as a function of position, which is called the radiation pattern (see Figure 5.1). The  
3703 radiation power density is obtained by calculating the time-averaged Poynting vector for  
3704 all positions surrounding the antenna, which in equation form is

$$\mathbf{W}(x, y, z) = \langle \mathbf{E}(x, y, z, t) \times \mathbf{H}^*(x, y, z, t) \rangle_t, \quad (5.1)$$

3705 where  $\mathbf{E}(x, y, z, t)$  and  $\mathbf{H}(x, y, z, t)$  are the time-dependent electric and magnetic fields  
 3706 produced by the antenna [49]. The radiation power density has units of  $\text{W/m}^2$  and is  
 3707 more typically called the energy flux density in physics applications, since it is a measure  
 3708 of the amount of energy passing through a unit area over time.

3709 Because the radiation power density is a measure of power per unit area, its value  
 3710 in a particular direction will depend on the distance from the antenna at which one is  
 3711 measuring. This is undesirable for practical applications. A related quantity, which is  
 3712 distance independent, is the energy flux per unit solid angle or radiation intensity. This  
 3713 is computed directly from the radiation power density by multiplying by the squared  
 3714 distance from the antenna. Specifically,

$$U = r^2 W(x, y, z), \quad (5.2)$$

3715 where  $r$  is the distance from the antenna to the field measurement point. The radiation  
 3716 intensity is typically defined in regions where the Poynting vector consists only of a radial  
 3717 component where it is safe to treat as a scalar quantity.

### 3718 5.2.1.2 Directivity and Gain

3719 Since the radiation intensity is a measure of average power per unit solid angle, it is  
 3720 independent of distance and a more useful quantity for antenna measurements. The  
 3721 radiation intensity is directly related to antenna directivity and gain, which are common  
 3722 antenna engineering figures-of-merit. Directivity is defined as the ratio between the  
 3723 radiation intensity at particular point on the radiation pattern to the average radiation  
 3724 intensity computed over all solid angles [68]. The equation that relates the radiation  
 3725 intensity to directivity is

$$D = \frac{U}{U_0} = \frac{4\pi U}{P_{\text{rad}}}, \quad (5.3)$$

3726 where  $U_0$  is the average radiation intensity over all solid angles, which simply the total  
 3727 radiated power ( $P_{\text{rad}}$ ) divided by  $4\pi$ . Closely related to directivity is antenna gain, which  
 3728 accounts for energy losses that occur inside then antenna when attempting to transmit  
 3729 or receive a signal. The antenna gain is given by

$$G = \frac{4\pi U}{P_{\text{in}}}, \quad (5.4)$$

3730 where  $P_{\text{in}}$  is the total power delivered to the antenna. Gain can be thought of as the ratio  
 3731 of the antenna's radiation intensity to that of a hypothetical isotropic, lossless radiator.

3732 The maximum values of gain and directivity exhibited by the main lobe of the antenna  
 3733 pattern as well as the ratio between the gain of the main lobe and any side-lobes are  
 3734 important figures-of-merit to evaluate antenna design performance.

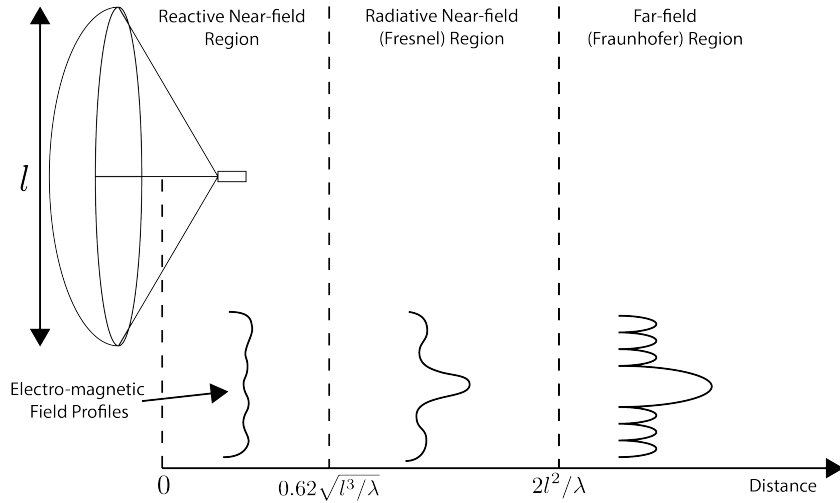


**Figure 5.2.** An illustration of the three field regions important for the analysis of an antenna system. Very close to the antenna the electric fields are primarily reactive so there is no radiation. If a receiving antenna were placed in this region most of the energy would be reflected back to the transmitter. Outside of the reactive near-field is the radiative near field. At these distances the antenna does radiate, but the radiation pattern is not well-defined since it changes based on the distance of the receiving antenna. It is only in the far-field region where the radiation pattern becomes constant as a function of distance, which is where the majority of antenna engineering is assumed to take place. The antenna arrays developed by Project 8 for CRES measurements operate in the radiative near-field due to the importance of limiting power loss from free-space propagation, which complicates the design of the antenna system.

### 3735 5.2.1.3 Far-field and Near-field

3736 Radiation patterns are well-defined only in regions where the shape of the radiation  
 3737 pattern is independent of distance. The region where this approximation is valid is called  
 3738 the "far-field", and in this region the EM fields from the antenna can be approximated as  
 3739 spherical plane waves. A rule of thumb for antennas is that the far-field approximation  
 3740 applies when the condition

$$R > \frac{2l^2}{\lambda} \quad (5.5)$$

3741 is true. In this expression,  $R$  is the distance from the antenna,  $l$  is the largest characteristic  
 3742 dimension of the antenna, and  $\lambda$  is the wavelength of the radiation (see Figure 5.2).

3743 The region very close to the antenna is called the reactive near-field, because in this  
 3744 region the reactive component of the EM field is dominant. Unlike radiative electric

fields, the reactive electric and magnetic fields are out of phase from each other by  $90^\circ$ , since they are caused by electrostatic and magnetostatic effects from the self-capacitance and self-inductance of the antenna. The reactive fields are unable to transfer energy a significant distance from the antenna and are thus completely negligible for most antenna applications. The limit of the reactive near-field for an electrically-large antenna is typically taken to be

$$R < 0.62\sqrt{l^3/\lambda}. \quad (5.6)$$

The unique application of antennas by Project 8 is limited by reactive near-field effects, since it defines an absolute minimum distance for detectable electrons inside the uniform cylindrical antenna array. If electrons are too close to the edge of the array than reactive near-field effects leads to a large reduction in the received power and detection efficiency. This leads to a significant volume inside the antenna array that is unsuitable for CRES lowering the volumetric efficiency of the antenna array CRES technique.

Between the reactive near-field and the far-field is the radiative near-field region. In this region the fields are primarily radiative, however, it is too close to the antenna for the spherical plane wave approximation to apply. Therefore, interference effects between EM waves emitted from different points on the antenna occur causing the shape of the radiation pattern to change as a function of distance from the antenna. Evaluating the far-field distance limit for the FSCD antennas one finds an estimated far-field distance of 43 cm, which is a factor of four larger than the radius of the antenna array designed for the experiment. Consequently, it is expected that near-field effects will influence the performance of the antenna array highlighting the importance of calibration and characterization measurements to mitigate these effects.

#### 5.2.1.4 Polarization

The polarization of an EM wave defines the spatial orientation of the electric field oscillations. Conventionally, polarization vectors  $\mathbf{a}$  defined in the plane perpendicular to the direction of propagation for the EM wave. For radiation moving in the radial ( $\hat{r}$ ) direction the electric field can be decomposed into the orthogonal basis

$$\mathbf{E}_{\text{tot}} = E_\theta \hat{\theta} + E_\phi \hat{\phi}, \quad (5.7)$$

assuming a spherical coordinate system.

In general, one defines partial radiation patterns, directivities, and gains so that the performance of the antenna can be analyzed for the desired polarization. The radiation

3775 pattern defined in terms of partial patterns is

$$U_{\text{tot}} = U_\phi + U_\theta, \quad (5.8)$$

3776 where  $U_\phi$  and  $U_\theta$  are the radiation intensities in a particular direction for the respective  
3777 polarization components. Similarly, a quantity such as gain can be written in terms of  
3778 partial gains,

$$G_{\text{tot}} = G_\phi + G_\theta = \frac{2\pi U_\phi}{P_{\text{in}}} + \frac{2\pi U_\theta}{P_{\text{in}}}. \quad (5.9)$$

3779 An electron performing a circular orbit in the XY-plane from the side, viewed along  
3780 the X or Y axes, would be seen as performing a linear oscillation perpendicular to the  
3781 viewing axis. From this picture, one would predict that the primary polarization of  
3782 electric fields from CRES events is linear polarization in the  $\hat{\phi}$  direction in the XY-plane.

### 3783 5.2.1.5 Antenna Factor and Effective Aperture

3784 A useful way to characterize the performance of an antenna is to measure the electric  
3785 field magnitude required to produce a signal with an amplitude of one volt in the antenna  
3786 terminals. This ratio between the magnitude of the incoming electric field and the  
3787 magnitude of the signal produced by the antenna is called the antenna factor, which is  
3788 written as

$$A_F = \frac{|\mathbf{E}_{\text{in}}|}{V_{\text{ant}}}, \quad (5.10)$$

3789 where  $A_F$  is the antenna factor,  $E_{\text{in}}$  is the incoming electric field, and  $V_{\text{ant}}$  is the magnitude  
3790 of the voltage produced by the antenna.

3791 The antenna factor can be expressed in terms of the antenna's gain through a related  
3792 quantity called the effective aperture. The effective aperture defines for a given incident  
3793 radiation power density ( $\text{W/m}^2$ ) the power that is received by the antenna. Therefore,  
3794 the effective aperture gives the equivalent area of the antenna,

$$A_{\text{eff}} = \frac{P_{\text{rec}}}{P_{\text{in}}} = \frac{\lambda^2}{4\pi} G, \quad (5.11)$$

3795 where the received power is  $P_r$  and the total incoming power is  $P_{\text{in}}$ .

3796 The magnitude of the Poynting vector can be written as

$$|\mathbf{S}_{\text{in}}| = |\mathbf{E}_{\text{in}}|^2 / \eta_0, \quad (5.12)$$

<sup>3797</sup> where  $\eta_0$  is the impedance of free-space, which relates the magnitudes of the electric and  
<sup>3798</sup> magnetic fields in a vacuum, and is defined by

$$\eta_0 = \frac{|\mathbf{E}|}{|\mathbf{H}|} = \sqrt{\frac{\epsilon_0}{\mu_0}}. \quad (5.13)$$

<sup>3799</sup> Therefore, the total received power by the antenna is

$$P_{\text{rec}} = |\mathbf{S}_{\text{in}}| A_{\text{eff}} = |\mathbf{S}_{\text{in}}| \frac{\lambda^2}{4\pi} G = \frac{|\mathbf{E}_{\text{in}}|^2 \lambda^2 G}{4\pi \eta_0}. \quad (5.14)$$

<sup>3800</sup> To relate this to the antenna factor recall that the voltage produced by the antenna  
<sup>3801</sup> is related to the received power by

$$P_{\text{rec}} = \frac{V_{\text{ant}}^2}{Z} = \frac{|\mathbf{E}_{\text{in}}|^2}{A_F^2 Z}, \quad (5.15)$$

<sup>3802</sup> where  $Z$  is the system impedance. Setting Equations 5.14 and 5.15 equal to each other,  
<sup>3803</sup> one obtains the following expression for antenna factor in terms of gain

$$A_F = \sqrt{\frac{4\pi\eta_0}{ZG\lambda^2}} = \frac{9.73}{\lambda\sqrt{G}}. \quad (5.16)$$

<sup>3804</sup> The second expression in Equation 5.16 is obtained by evaluating the constant terms  
<sup>3805</sup> assuming a system impedance of  $50 \Omega$ .

<sup>3806</sup> This exercise highlights that the majority of antenna parameters that one cares  
<sup>3807</sup> to measure about an antenna can be obtained from the radiation or gain pattern of  
<sup>3808</sup> the antenna. The antenna factor is a particularly important parameter for CRES  
<sup>3809</sup> measurements due to it's relevance to antenna array simulations with the Locust software  
<sup>3810</sup> [65, 77].

<sup>3811</sup> To compute the response of the antenna to the electric field, Locust relies upon  
<sup>3812</sup> linear time-invariant system theory, which computes the response of the antenna (i.e. the  
<sup>3813</sup> voltage time series generated by the antenna) using a convolution between the electric field  
<sup>3814</sup> time-series and the antenna impulse response. This approach is necessary for correctly  
<sup>3815</sup> modeling the antenna response to the electric field due to the broadband and non-  
<sup>3816</sup> stationary nature of the electric fields from CRES events. Since antenna measurements  
<sup>3817</sup> take place under steady-state conditions, parameters such as the radiation pattern, gain,  
<sup>3818</sup> and antenna factor are defined in the frequency domain. However, by performing an  
<sup>3819</sup> inverse Fourier transform on the antenna factor one obtains the antenna impulse response,

3820 which is used to calculate CRES signal voltages in Locust.

## 3821 5.2.2 Antenna Measurement Fundamentals

### 3822 5.2.2.1 Friis Transmission Equation

3823 The antenna factor or antenna transfer function is used to model how the antenna  
3824 responds to electric fields emitted from a CRES event. Therefore, directly measuring the  
3825 antenna transfer functions of the array is a key step in the commissioning and calibrating  
3826 the FSCD experiment. A common approach to antenna characterization is to perform a  
3827 two antenna transmit-receive measurement where an antenna with a known gain is used  
to characterize the unknown gain of the antenna under test (see Figure 5.3).

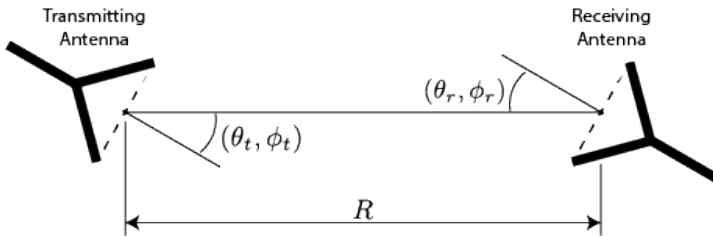


**Figure 5.3.** An illustration of the Friis measurement technique commonly used for antenna characterization measurements.

3828  
3829 Analyzing this two antenna setup involves calculating the power received from the  
3830 transmitting antenna. The received power density is expressed as a function of the  
3831 antenna gain in a direction  $(\theta_t, \phi_t)$  at frequency  $f$  and distance  $R$

$$w_t = \frac{P_t}{4\pi R^2} G_t(\theta_t, \phi_t, f), \quad (5.17)$$

3832 where the subscript  $t$  denotes the transmitting antenna, and  $P_t$  is the total power delivered  
3833 to the transmitting antenna. The power density is power per unit area, so the total  
3834 power delivered to the receiving antenna is the transmitted power density multiplied by  
3835 the effective area of the receiving antenna

$$P_r = w_t A_{\text{eff},r} = P_t \frac{G_t(\theta_t, \phi_t, f) G_r(\theta_r, \phi_r, f) c^2}{(4\pi R f)^2}, \quad (5.18)$$

3836 where  $G_r(\theta_r, \phi_r, f)$  is the gain of the receiving antenna. Equation 5.18 is called the Friis  
3837 transmission equation [91], which is of fundamental importance for antenna measurements,  
3838 since it allows one to measure the gain of an unknown antenna by measuring the power

3839 received from an antenna with a known gain pattern. Alternatively, if an antenna with a  
 3840 known gain pattern is unavailable, two identical antennas with unknown gain patterns  
 3841 can be used.

3842 **5.2.2.2 S-Parameters and Network Analyzers**

3843 It is more common to measure the ratio of the received power to the transmitted power  
 3844 instead of the absolute received power

$$\frac{P_r}{P_t} = \frac{G_t(\theta_t, \phi_t, f) G_r(\theta_r, \phi_r, f) c^2}{(4\pi R f)^2}. \quad (5.19)$$

3845 This power ratio can be easily measured using a vector network analyzer (VNA), which  
 3846 automates a significant fraction of the measurement process. Network analyzers are used  
 3847 to measure the scattering or S-parameters of a multi-port RF device [92], which describes  
 3848 how waves are scattered between the device ports. Friis antenna measurements can be  
 3849 modeled as a two-port microwave device that is characterized by measuring how incident  
 voltage waves are transmitted or reflected (see Figure 5.4). The scattered waves ( $V_1^-$

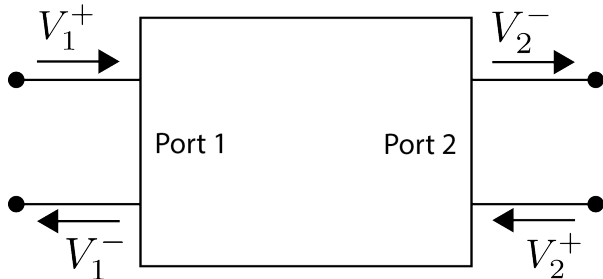


**Figure 5.4.** Illustration of a two-port S-parameter measurement setup. S-parameters characterize how incoming waves of voltage or power scatter off of the RF device under test. This allows you to measure important properties of the device. In particular, this framework can be used to model a two antenna radiation pattern measurement, which can be automated using a VNA.

3850  
 3851 and  $V_2^-$ ) can be written in terms of the incident ( $V_1^+$  and  $V_2^+$ ) waves using the scattering  
 3852 matrix

$$\begin{pmatrix} V_1^- \\ V_2^- \end{pmatrix} = \begin{pmatrix} S_{11} & S_{12} \\ S_{21} & S_{22} \end{pmatrix} \begin{pmatrix} V_1^+ \\ V_2^+ \end{pmatrix}, \quad (5.20)$$

3853 where the elements of the matrix are the device S-parameters. It is assumed that,  
 3854 when exciting the device from a particular port, that all other ports in the network are  
 3855 terminated at the system impedance. This ensures that the incident waves from other  
 3856 ports in the network are zero. Therefore, the S-parameters are the ratios between the

3857 scattered and incident waves,

$$S_{ij} = \frac{V_i^-}{V_j^+}. \quad (5.21)$$

3858 Alternatively, S-parameters can be defined as the ratio of the scattered and incident  
3859 power, which is proportional to the ratio of the squared voltage waves.

3860 Returning to the antenna measurement setup, it is clear that measuring the ratio of  
3861 the received to the transmitted power is equivalent to measuring the ratio of power being  
3862 scattered from port 1 to port 2 in a RF (radio-frequency) network. Therefore, measuring  
3863 an antenna's gain can be accomplished quite easily using a VNA to perform a two port  
3864  $S_{21}$  measurement.

3865 **5.2.2.3 Antenna Array Commissioning and Calibration Measurements**

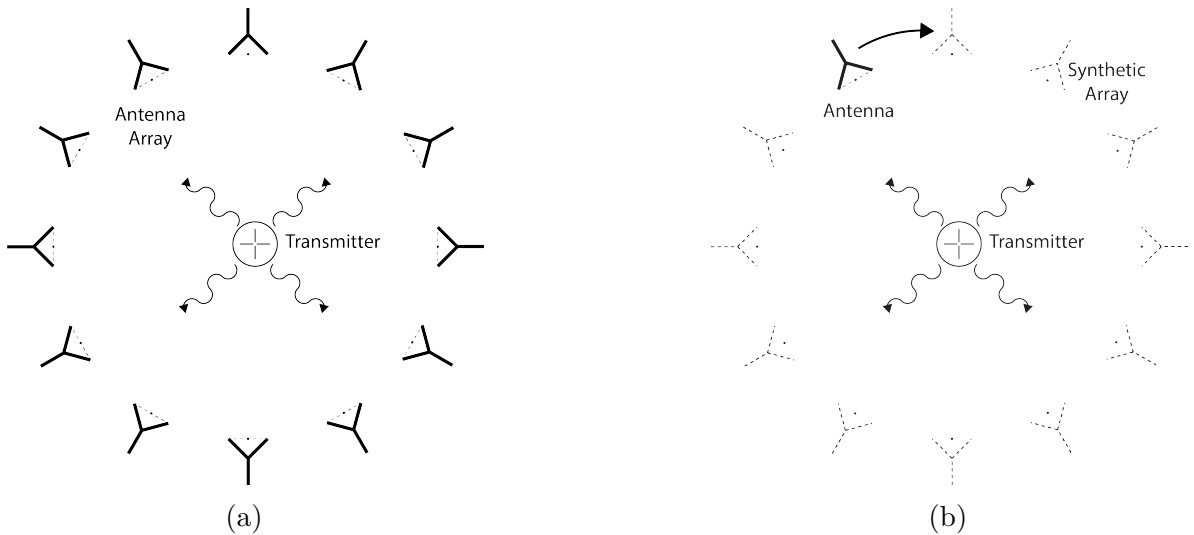


**Figure 5.5.** Two measurement approaches to characterizing an antenna array for CRES measurements. The full-array approach (a) requires a complete antenna array with all the associated hardware. The synthetic array approach (b) utilizes a single antenna and a set of rotation/translation stages to reposition the transmitter or the receiving antenna to synthesize the signals that would be received by the full-array. This approach reduces the cost and complexity of array measurements. A down-side of the synthetic array approach is that multi-channel effects such as reflections cannot be measured. Utilizing both the full-array and the synthetic array is a powerful way to quantify the impact of errors from the multi-channel array.

3866 Measuring the gain of each individual array element allows to predict the features of  
3867 the signals received during a CRES event (see Section 5.2.1.5). However, unpredictable  
3868 changes to the antenna performance can be introduced by the incorporation of the

3869 antennas into the circular array geometry, therefore, both individual antenna and full-  
3870 array characterization measurements are performed as part of the commissioning of the  
3871 FSCD.

3872 There are two main approaches to array measurements that could be used for  
3873 characterization and calibration (see Figure 5.5). One approach is to construct the  
3874 complete array and use a omni-directional transmitting antenna to measure the power  
3875 received by each channel in the antenna array. In Section 5.3 I describe the development  
3876 of an omni-directional transmitter that also mimics the radiation phase characteristics of a  
3877 CRES event, which is useful because the entire array can be tested without repositioning.  
3878 Alternatively, a full antenna array can be synthesized by repeatedly moving and measuring  
3879 a single array element. This approach is ideal for identifying if different channels in the  
3880 antenna array are affecting each other through multi-path interference by comparing the  
3881 measurement results of the synthetic array to the real array.

### 3882 **5.2.3 The Penn State Antenna Measurement System**

3883 The development of antenna array based CRES requires the capability to test and  
3884 calibrate different antenna array designs to validate the performance of the as-built  
3885 antenna array before and during the experiment. With these aims in mind an antenna  
3886 measurement system was developed at Penn State specifically designed to mimic the  
3887 characteristics of the FSCD experiment.

3888 The Penn State antenna measurement system utilizes a two antenna measurement  
3889 configuration with a stationary reference antenna and a test antenna mounted on a set  
3890 of motorized translation and rotation stages (see Figure 5.6). The antenna measurement  
3891 system can be operated in two distinct modes, one focused on the characterization of  
3892 the radiation patterns of prototype antennas, and the other focused on the validation of  
3893 data-acquisition (DAQ) and CRES signal reconstruction techniques to bridge the gap  
3894 between real measurements and simulation. In both measurement configurations, it is  
3895 critical to isolate the antennas from the environment so that multi-path reflections do not  
3896 negatively influence the measurement results. For this reason the measurement volume  
3897 is surrounded with microwave absorber foam (AEMI AEC-1.5) specifically designed to  
3898 attenuate microwave radiation near the 26 GHz measurement range of the system.

3899 In the first measurement configuration, the reference antenna is a well-characterized  
3900 horn antenna as pictured, since horn antennas have well-known and stable radiation  
3901 patterns making them ideal as standard references. For characterization measurements,  
3902 the test antenna represents the antenna-under-test whose pattern is being characterized.

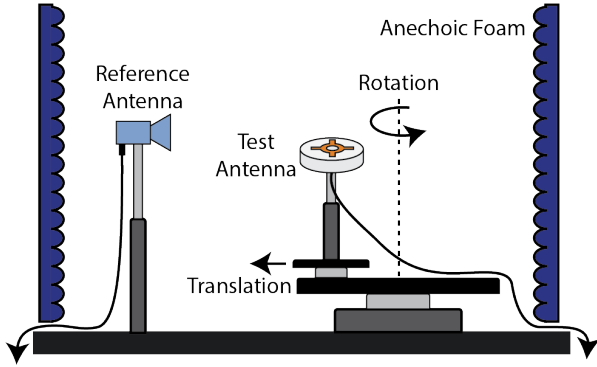


**Figure 5.6.** Illustration of the antenna measurement system developed for the Project 8 Collaboration. The reference and test antennas can be connected to different data acquisition configurations depending on the measurement goals. The reference antenna is typically a standard horn antenna and the test antenna is mounted on a set of translation stages for positioning. Automated translation stages allows for relatively painless data-taking enabling synthetic antenna array measurements using only a single receiving antenna. Anechoic form designed to mitigate RF reflections surrounds the setup.

3903 Mounting the test antenna on motorized rotation and translation stages allows for  
 3904 automation, which significantly speeds up the radiation pattern measurement process.

3905 The second measurement configuration mimics the conditions of the FSCD as it  
 3906 concerns the antenna array and DAQ system. In this configuration, the reference antenna  
 3907 is a prototype FSCD antenna, and the test antenna is a specially designed synthetic  
 3908 cyclotron antenna (SYNCA) as picture in Figure 5.6. The SYNCA is designed such that  
 3909 the radiation pattern mimics that of a CRES electron so that the signals received by the  
 3910 prototype CRES array antenna mimic what is expected for a real CRES experiment.

3911 Figure 5.7 shows two high-level system diagrams of the Penn State antenna measure-  
 3912 ment system that depict the important system components and the connections between  
 3913 them. The two configurations of the measurement system utilize different hardware. For  
 3914 characterization and radiation pattern measurements, the configuration shown in Figure  
 3915 5.7a is used. In this case a vector network analyzer (VNA) is used as the transmission  
 3916 source and data acquisition system, which is easy to calibrate over a wide range of  
 3917 frequencies. The configuration in 5.7b is used to mimic the FSCD experiment, since this  
 3918 system includes a more realistic receiver chain.

3919 The characterization configuration utilizes a network analyzer (Keysight N5222A)  
 3920 with two independent sources and four measurement ports as the primary measurement  
 3921 tool. A standard reference antenna is connected to one measurement port, and the test  
 3922 antenna is connected to a second port. The typical reference antenna used for these  
 3923 studies is a Pasternack PF9851 horn antenna. In the measurement shown, the test

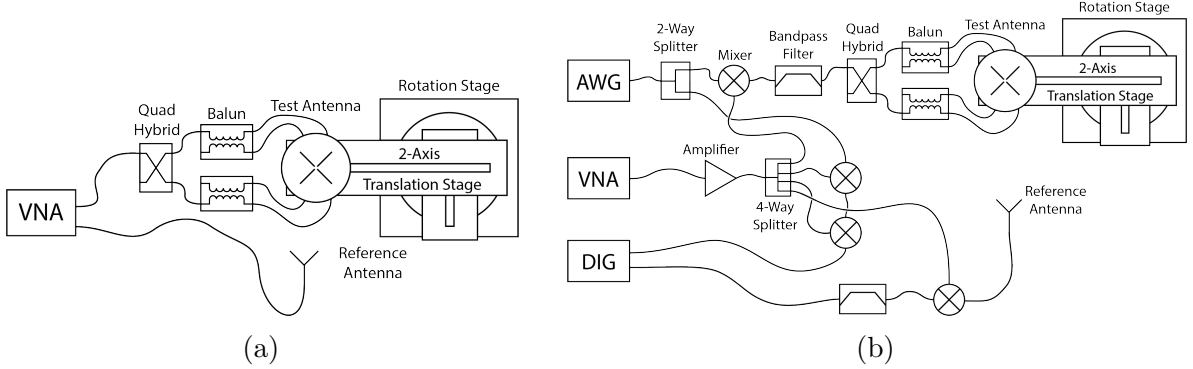


**Figure 5.7.** Diagrams of two measurement system configurations. Configuration (a) utilizes a VNA and is more suited to antenna characterization. Configuration (b) utilizes an AWG (arbitrary waveform generator) and VNA as a signal generation system and digitizer to collect measurement data, which is more suited to simulating CRES measurements. The transmission chain utilizes a quadrature hybrid and a pair of baluns to drive the cross-dipole variant test antenna developed for synthetic CRES measurements.

3924 antenna represents a SYNCA antenna, which requires a transmission chain consisting of  
 3925 quadrature hybrid coupler (Marki QH-0226) connected to two baluns (Marki BAL-0026)  
 3926 to generate feed signals with the appropriate phases. The VNA measures the radiation  
 3927 pattern by performing a transmission S-parameter measurement, which can be used with  
 3928 the knowledge of the reference antenna's radiation pattern to determine the radiation  
 3929 pattern of the test antenna (see Section 5.2.1).

3930 The second configuration incorporates more hardware components to mimic the DAQ  
 3931 system envisioned for the FSCD experiment. The basic approach is to produce CRES-like  
 3932 radiation and use an antenna combined with a realistic RF receiver chain to acquire the  
 3933 signals. On the transmit side, an arbitrary waveform generator (AWG, RIGOL DG5252)  
 3934 is used to generate a waveform that mimics a CRES signal at a baseband frequency up  
 3935 to 250 MHz. This frequency is then up-converted to the CRES signal frequency band  
 3936 of 25.8 to 26.0 GHz using a mixer (Marki MM1-0832L) and a bandpass filter (K&L  
 3937 Microwave 3C62-25900/T200-K/K) to reject unwanted mixing components outside out  
 3938 of the 200 MHz CRES signal band. The local oscillator signal for mixing is provided by  
 3939 one of the VNA sources configured to run in a continuous wave setting. On the receive  
 3940 side, a prototype antenna is used to detect the radiation emitted by the test antenna,  
 3941 which is down-converted and filtered using the same mixer and bandpass filter as the  
 3942 transmission chain. Lastly, data acquisition is performed using a 14-bit ADC sampling  
 3943 at 500 MSa/s (CAEN DT530) to digitize the down-converted signals.

3944 In order to distribute the LO to all mixers a 4-way power splitter (MiniCircuits

3945 ZC4PD-18263-S+) along with an amplifier (Marki APM-6848) is used to drive the four  
3946 mixers used in the measurement system. A limitation of using the VNA as an LO source  
3947 is that there is no control of the LO phase when a measurement is triggered by the  
3948 control script, which leads to a random phase offset between acquisitions. This makes it  
3949 impossible to perform synthetic array measurements, which require strict control over  
3950 the starting phase of the transmitted signal. In order to monitor the random phase of the  
3951 LO, a 2-way power splitter (MiniCircuits Z99SC-62-S+) is used to split the signal from  
3952 the AWG between the transmission path and a LO monitoring path. The LO monitoring  
3953 path consists of an up-conversion and down conversion using two mixers connected by a  
3954 coaxial cable, and monitors the relative phase of the LO using a channel on the digitizer  
3955 to sample this path. A phase shift in the LO will lead to a proportional phase shift in  
3956 the mixed signal, which is measured and removed from the received signals.

3957 The test antenna is mounted on a set of motorized stages, which are identical for  
3958 both measurement configurations. A rotational stage (ThorLabs PRMTZ8) is used as  
3959 the base layer with additional translation stages mounted on top. The rotational stage is  
3960 ideal for measuring a complete azimuthal scan of the test antenna's radiation pattern  
3961 as well as for moving a SYNCA antenna in circular motion to recreate the symmetry  
3962 of the FSCD antenna array. On top of the rotational stage, are mounted two linear  
3963 translation stages (ThorLabs MTS50-Z8 and MTS25-Z8) in a cross-wise manner so that  
3964 the test antenna can be moved along two perpendicular axes. Using the linear stages in  
3965 combination with the rotational stage allows one to fine-tune the positioning of the test  
3966 antenna so that it can be perfectly aligned with the central axis of the array. A LabView  
3967 script was developed to automate the measurement of a full 360° radiation pattern and  
3968 control the measurement electronics. Data from these acquisitions is stored on university  
3969 provided cloud storage.

### 3970 **5.3 Development of a Synthetic Cyclotron Antenna (SYNCA)** 3971 **for Antenna Array Calibration**

3972 This section is the manuscript of the publication [78] detailing the development of a  
3973 Synthetic Cyclotron Antenna (SYNCA) for antenna array characterization measurements  
3974 by the Project 8 collaboration.

### 3975 5.3.1 Introduction

3976 Neutrinos are the most abundant standard model fermions in our universe, but due to  
3977 weak interaction cross-sections with other particles, neutrinos are particularly difficult  
3978 to study. Consequently, many fundamental properties of neutrinos are still unknown  
3979 including the absolute scale of the neutrino mass [24]. Direct, kinematic measurements of  
3980 the neutrino mass are particularly valuable due to their model independent nature [37].  
3981 To date the most sensitive direct neutrino mass measurements have been performed by  
3982 the KATRIN collaboration [93], which measures the molecular tritium  $\beta$ -decay spectrum  
3983 to infer the neutrino mass. Current data from neutrino oscillation measurements [24]  
3984 allow for neutrino masses significantly smaller than the design sensitivity of the KATRIN  
3985 experiment; therefore, there is a need for new technologies for performing direct neutrino  
3986 mass measurements to probe lower neutrino masses.

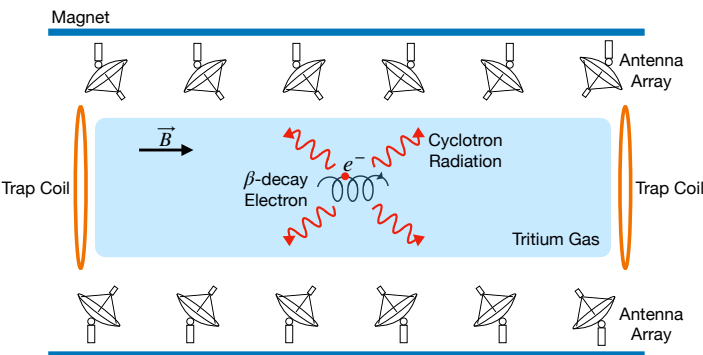


**Figure 5.8.** A sketch of an antenna array large-volume CRES experiment. Electrons from  $\beta$ -decays are confined in a magnetic field using a set of trap coils. The cyclotron radiation produced by the motion of the trapped electrons can be detected by a surrounding antenna array to determine the electron energies. Measuring the energies of many electrons produces a  $\beta$ -decay spectrum.

3987 The Project 8 collaboration is developing new methods for neutrino mass measurement  
3988 based on Cyclotron Radiation Emission Spectroscopy (CRES) [56, 94–96], with the goal  
3989 of measuring the absolute scale of the neutrino mass with a 40 meV/c<sup>2</sup> sensitivity [37, 73].  
3990 This sensitivity goal will require the development of two separate technical capabilities.  
3991 First is the development of an atomic tritium source, which avoids significant spectral  
3992 broadening due to molecular final states [55]. Second is the technology for performing  
3993 CRES in a multi-cubic-meter experimental volume with high combined detection and  
3994 reconstruction efficiency, which is required in order to obtain sufficient event statistics  
3995 near the tritium spectrum endpoint.

One approach for a large-volume CRES experiment is to use an array of antennas,  
 which surrounds a volume of tritium gas, to detect the cyclotron radiation produced  
 by the  $\beta$ -decay electrons when they are trapped in a background magnetic field using a  
 set of magnetic trapping coils (see Figure 5.8). Project 8 has developed a conceptual  
 experiment design to study the feasibility of this approach. The design consists of a  
 single circular array of antennas with a radius of 10 cm and 60 independent channels  
 positioned around the center of the magnetic trap. The motivation behind this antenna  
 array design is to first develop an understanding of the antenna array approach to CRES  
 with a small scale experiment before attempting to scale the technique to large volumes  
 by using multiple antenna rings to construct the full cylindrical array. The development  
 of the antenna array approach to CRES has largely proceeded through simulations using  
 the Locust software package [77, 97], which is used to model the fields emitted by CRES  
 events and predict the signals received by the surrounding antenna array. To validate  
 these simulations, a dedicated test stand is being constructed to perform characterization  
 measurements of the prototype antenna array developed by Project 8 (see Figure 5.9)  
 and benchmark signal reconstruction methods using a specially designed transmitting  
 calibration probe antenna.

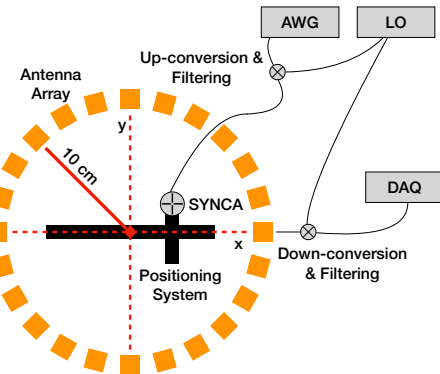


**Figure 5.9.** A schematic of the antenna array test stand. The circular antenna array has a radius of 10 cm with 60 independent channels (limited number shown for clarity). The test stand includes an arbitrary waveform generator (AWG), local oscillator (LO), and data acquisition (DAQ) hardware. Finally, a specialized Synthetic Cyclotron Antenna (SYNCA) is used to inject signals to test the antenna array.

We call this probe antenna the Synthetic Cyclotron Antenna or SYNCA. The SYNCA is a novel antenna design that mimics the cyclotron radiation generated by individual charged particles trapped in a magnetic field, which will be used in the antenna test stand to perform characterization measurements, simulation validation, and reconstruction benchmarking. This paper provides an overview of the design, construction, and

4018 characterization measurements of the SYNCA performed in preparation for its usage as  
 4019 a transmitting calibration probe.

4020 In Section 5.3.2 we provide a description of the cyclotron radiation field characteristics  
 4021 that we recreate with the SYNCA. In Section 5.3.3 we give an overview of the simulations  
 4022 performed to develop an antenna design that mimics the characteristics of cyclotron  
 4023 radiation. In Section 5.3.4 we outline characterization measurements to validate that  
 4024 the fields generated by the SYNCA match simulation, and finally in Section 5.3.5 we  
 4025 demonstrate an application of the SYNCA to test phased array reconstruction techniques  
 4026 on the bench-top.

### 4027 5.3.2 Cyclotron Radiation Phenomenology

4028 To understand the cyclotron radiation phenomenology that the SYNCA should mimic,  
 4029 we consider a charged particle moving at relativistic speed in the presence of an external  
 4030 magnetic field (see Figure 5.10). In the special case we shall examine, the entirety of  
 4031 the electron's momentum is directed perpendicular to the magnetic field; therefore, the  
 4032 trajectory of the electron is confined to the cyclotron orbit plane. Because the momentum  
 4033 vector is oriented perpendicular to the magnetic field, electrons with these trajectories  
 4034 are said to have pitch angles of 90°.

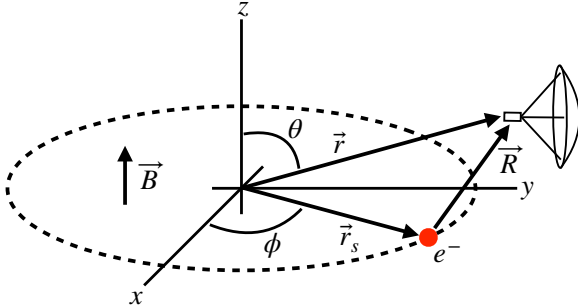


**Figure 5.10.** An electron (red dot) performing cyclotron motion in the x-y plane. The resulting cyclotron radiation is observed by an antenna located at the field point of interest.

4035 The cyclotron radiation fields generated by this circular trajectory are those which  
 4036 we aim to reproduce with the SYNCA. We can describe the electromagnetic (EM) fields  
 4037 using the Liénard-Wiechert equations [49, 77], which in non-covariant form express the  
 4038 electric field as

$$\vec{E} = e \left[ \frac{\hat{n} - \vec{\beta}}{\gamma^2(1 - \vec{\beta} \cdot \hat{n})^3 |\vec{R}|^2} \right]_{tr} + \frac{e}{c} \left[ \frac{\hat{n} \times [(\hat{n} - \vec{\beta}) \times \dot{\vec{\beta}}]}{(1 - \vec{\beta} \cdot \hat{n})^3 |\vec{R}|} \right]_{tr}, \quad (5.22)$$

4039 where  $e$  is the particle's charge,  $\hat{n} = (\vec{r} - \vec{r}_s)/|\vec{r} - \vec{r}_s|$  is the unit vector pointing from the  
 4040 electron to the field measurement point,  $\vec{\beta} = \dot{\vec{r}}_s/c$  is the velocity of the particle divided  
 4041 by the speed of light, and  $\gamma$  is the relativistic Lorentz factor. The equation is meant to  
 4042 be evaluated at the retarded time as indicated by  $t_r = t - |\vec{R}|/c$ , which accounts for the  
 4043 time delay due to the finite speed of light between the point where the field was emitted  
 4044 and the point where the field is detected.

4045 We would like to simplify Equation 5.22 it at all possible. As a first step we analyze  
 4046 the relative magnitudes of the electric field polarization components. Consider an electron  
 4047 following a circular cyclotron orbit in a uniform magnetic field whose guiding center  
 4048 is positioned at the origin of the coordinate system. The equation of motion can be  
 4049 expressed as

$$\vec{r}_s = (r_c \cos \omega_c t_r) \hat{x} + (r_c \sin \omega_c t_r) \hat{y}. \quad (5.23)$$

4050 For single antenna located along the  $y$ -axis at position  $\vec{r} = r_a \hat{y}$  we are interested in the  
 4051 incident electric fields from the electron. The electric field is given by Equation 5.22,  
 4052 which we evaluate in the regime where  $r_a \gg r_c$ . This limit can be justified by comparing  
 4053 the radius of the cyclotron orbit for an electron with the tritium beta-spectrum endpoint  
 4054 energy of 18.6 keV in a 1 T magnetic field to the typical ( $r_a \simeq 100$  mm) radial position  
 4055 of the receiving antenna. We find that the cyclotron orbit has a radius of 0.46 mm which  
 4056 is approximately a factor of 200 smaller than the typical antenna radial position. In this  
 4057 regime we can make the approximation  $\vec{R} \simeq r_a \hat{y}$  and the expression for the electric field  
 4058 at the antenna's position becomes

$$\vec{E} = \frac{e}{\gamma^2 r_a^2} \frac{\hat{x} \left( \frac{r_c \omega_c}{c} \sin \omega_c t_r \right) + \hat{y} \left( 1 - \frac{r_c \omega_c}{c} \cos \omega_c t_r \right)}{(1 - \frac{r_c \omega_c}{c} \cos \omega_c t_r)^3} - \frac{e}{c r_a} \frac{\hat{x} \left( \frac{r_c^2 \omega_c^3}{c^2} - \frac{r_c \omega_c^2}{c} \cos \omega_c t_r \right)}{(1 - \frac{r_c \omega_c}{c} \cos \omega_c t_r)^3}. \quad (5.24)$$

4059 Since the receiving antenna is part of a circular array of antennas, it is useful to rewrite  
 4060 Equation 5.24 in terms of the azimuthal ( $\hat{\phi}$ ) and radial ( $\hat{r}$ ) polarizations. Making use of  
 4061 the fact that for an antenna located at  $R = r_a \hat{y}$  that  $\hat{\phi} = -\hat{x}$  and  $\hat{r} = \hat{y}$  we find

$$\vec{E} = \hat{\phi} E_\phi + \hat{r} E_r \quad (5.25)$$

$$E_\phi = \frac{e}{(1 - \frac{r_c \omega_c}{c} \cos \omega_c t_r)^3} \left[ -\frac{\frac{r_c \omega_c}{c} \sin \omega_c t_r}{\gamma^2 r_a^2} + \frac{\omega_c \left( \frac{r_c^2 \omega_c^2}{c^2} - \frac{r_c \omega_c}{c} \cos \omega_c t_r \right)}{c r_a} \right] \quad (5.26)$$

$$E_r = \frac{e \left( 1 - \frac{r_c \omega_c}{c} \sin \omega_c t_r \right)}{\gamma^2 r_a^2 (1 - \frac{r_c \omega_c}{c} \cos \omega_c t_r)^3}. \quad (5.27)$$

4062 For the purposes of designing a synthetic cyclotron radiation antenna we are interested  
 4063 in the dominant electric field polarization emitted by the electron. The antenna is being  
 4064 designed to mimic the cyclotron radiation produced by electrons with kinetic energies of  
 4065 approximately 18.6 keV in a 1 T magnetic field [55]. Since the relativistic beta factor for  
 4066 an electron with this kinetic energy is  $|\vec{\beta}| \simeq \frac{1}{4}$ , the approximations  $\gamma \simeq 1$  and  $\frac{r_c \omega_c}{c} \simeq \frac{1}{4}$  are  
 4067 justified. Inserting these expressions into the equations for the electric field components  
 4068 above simplifies the comparison of the magnitudes of the two components. Additionally,  
 4069 we compare the time-averaged magnitudes to evaluate the root mean squared electric  
 4070 field ratio. The time-averaged ratio of the radial and azimuthally polarized electric fields  
 4071 with the above simplifications is given by

$$\frac{\langle |E_r| \rangle}{\langle |E_\phi| \rangle} = \frac{8 - \sqrt{2}}{\left| 1 - \frac{r_a}{r_c} \frac{1-2\sqrt{2}}{8} \right|} \simeq \frac{r_c}{r_a} \frac{8(8 - \sqrt{2})}{2\sqrt{2} - 1} = 0.13, \quad (5.28)$$

4072 where we have made use of the fact that for these magnetic fields and kinetic energies  
 4073 the cyclotron radius is much smaller than the radius of the antenna array.

4074 From Equation 5.28 we see that the time-averaged azimuthal polarization is larger than  
 4075 the radial polarization by about a factor of 8, which makes it the dominant contribution  
 4076 to the electric fields at the position of the antenna. We must also consider the directivity  
 4077 of the receiving antenna which can have a gain that is disproportionately large for a  
 4078 specific polarization component. Because the  $E_\phi$  component is dominant, the receiving  
 4079 antenna array is designed with an azimuthal polarization, which negates the voltages  
 4080 induced in the antenna from the radially polarized fields. Therefore, we conclude that  
 4081 for the purpose of designing the SYNCA antenna it is acceptable to approximate the  
 4082 electric fields from Equation 5.22 as purely azimuthally or  $\phi$ -polarized. The simplified  
 4083 expression for the electric field received by an antenna becomes

$$\vec{E} = E_\phi \hat{\phi} = \frac{e^{\frac{r_c \omega_c}{c}}}{4r_a r_c} \left[ \frac{\frac{r_c \omega_c}{c} - \cos \omega_c t - \frac{4r_c}{r_a} \sin \omega_c t}{(1 - \frac{r_c \omega_c}{c} \cos \omega_c t)^3} \right]_{t_r} \hat{\phi}, \quad (5.29)$$

4084 where the radius of the cyclotron orbit is called  $r_c$ , the cyclotron frequency is called  $\omega_c$ ,  
 4085 and the radial position of the receiving antenna is called  $r_a$ . Equation 5.29 has been  
 4086 evaluated in the non-relativistic limit where  $\gamma \simeq 1$ , which is justified by the fact that  
 4087  $|\vec{\beta}| \simeq \frac{c}{4}$  for an electron with an 18.6 keV kinetic energy in a 1 T magnetic field.

4088 This rather complicated expression can be simplified using Fourier analysis. Assuming  
 4089 a background magnetic field of 1 T and a kinetic energy of 18.6 keV we calculate

numerically the electric field using Equation 5.29 and apply a discrete Fourier Transform to visualize the frequency spectrum (see Figure 5.11).

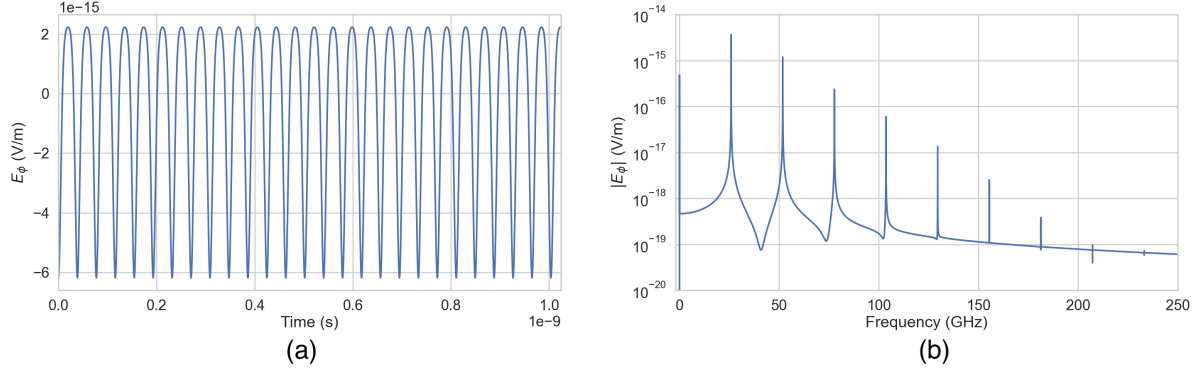


**Figure 5.11.** A plot of the numeric solution to Equation 5.30. The time-domain representation of the signal (a) is composed of a zero frequency term and a series of harmonics separated by the main cyclotron frequency as shown in the plot of the frequency spectrum (b). We can see that the relative amplitude of the harmonics beyond  $k = 7$  are smaller than the main carrier by a factor of about  $10^{-5}$  and are completely negligible.

We observe that the azimuthally polarized electric field is periodic with a base cyclotron frequency of 25.898 GHz corresponding to the highest power frequency component in Figure 5.11. The frequency spectrum reveals that the signal is composed of a constant term with zero frequency and a series of harmonics separated by 25.898 GHz. Therefore, we can represent the azimuthal electric fields from the electron as a linear combination of pure sinusoids with frequencies given by  $\omega_k = k\omega_c$  ( $k \in 0, 1, 2, \dots$ ) and amplitudes extracted from the Fourier representation. Using this representation we can transform the equation for the azimuthally polarized electric fields in Equation 5.29 into

$$E_\phi = \frac{e^{\frac{r_c \omega_c}{c}}}{4r_a r_c} \sum_{k=0}^7 A_k e^{i\omega_k t_r}, \quad (5.30)$$

where we have truncated the sum over harmonics at the 7th order for completeness. The amplitudes  $A_k$  are dimensionless complex numbers, which encode the relative powers of the harmonics as well as the starting overall phase of the cyclotron radiation. Because magnitude of the relative amplitudes exponentially decreases for higher harmonics, it is usually sufficient to consider only the terms up to  $k = 4$  where the relative amplitude of the harmonics has decreased from the main carrier by a factor of approximately 100. However, for completeness we include harmonics up to 7th order in Equation 5.30. The range of frequencies to which the receiving antenna array in the antenna test stand is sensitive is defined by the antenna's transfer function. The receptive bandwidth for

4109 the antennas used in the test stand is a range of frequencies with a bandwidth on the  
 4110 order of a few GHz centered around the main cyclotron carrier frequency of 25.898 GHz.  
 4111 Therefore, the higher order harmonics as well as the zero frequency term can be ignored  
 4112 when considering only the signals that will be received by the antenna array.

4113 Considering only the 1st order harmonic term from Equation 5.30, which represents  
 4114 the portion of the electric field that will be detected by the array, and evaluating this at  
 4115 the retarded time we obtain the following for the  $\phi$ -polarized electric fields

$$E_\phi \propto \cos \left( \omega_c \left( t - |\vec{R}|/c \right) - \Delta \right), \quad (5.31)$$

4116 where the arbitrary phase  $\Delta$  is defined by  $A_k = |A_k|e^{i\Delta}$ . We are interested in the  
 4117 characteristics of the amplitude of the electric field as a function of the radial distance  
 4118 component ( $|\vec{R}|$ ) of the retarded time. In particular, the maximum of  $E_\phi$  occurs when  
 4119 the argument of the cosine function is equal  $n\pi$  where  $n \in \{0, \pm 2, \pm 4, \dots\}$ ; however, the  
 4120 solutions where  $n$  is negative can be discarded since they represent unphysical negative  
 4121 overall phases. Applying this condition to Equation 5.31 gives a condition on the radial  
 4122 position of the maximum of  $E_\phi$

$$\omega_c(t - |\vec{R}|/c) - \Delta = n\pi, \quad (5.32a)$$

$$|\vec{R}| = \frac{c}{\omega_c} ((\omega_c t - \Delta) - n\pi), \quad (5.32b)$$

4123 which is a function of time in the frame of the moving electron ( $t$ ). Equation 5.32 can  
 4124 be further simplified by noticing that the azimuthal position of the electron ( $\phi_e(t)$ ) as a  
 4125 function of time is defined by  $\phi_e(t) = \omega_c t - \Delta$  which reduces Equation 5.32 to

$$|\vec{R}| = \frac{c}{\omega_c} (\phi_e(t) - n\pi). \quad (5.33)$$

4126 Equation 5.33 represents an archimedian spiral which is formed when plotting the  
 4127 amplitude of  $E_\phi$  in the x-y plane. The solution where  $n = 0$  represents the leading edge  
 4128 of the radiation spiral which propagates outward from the electron at the speed of light.  
 4129 The additional solutions for  $n > 0$  represent the persistent spiral at radii inside the  
 4130 leading edge of the radiated fields that have not yet been detected by the receiver at the  
 4131 current time. In Figure 5.12a we show the expected spiral pattern for the maxima of the  
 4132 cyclotron radiation.

4133 In particular, we note that for the circular array geometry of the test stand, depicted  
 4134 as the series of circles in Figure 5.12a, each antenna receives a linearly polarized wave

4135 with a phase offset that corresponds to the azimuthal angle for that antenna element.  
 4136 Therefore, as we show in Figure 5.12b, when the relative phase of the received signal is  
 4137 plotted as a function of the receiving antenna's azimuthal position the result is also an  
 4138 Archimedean spiral.

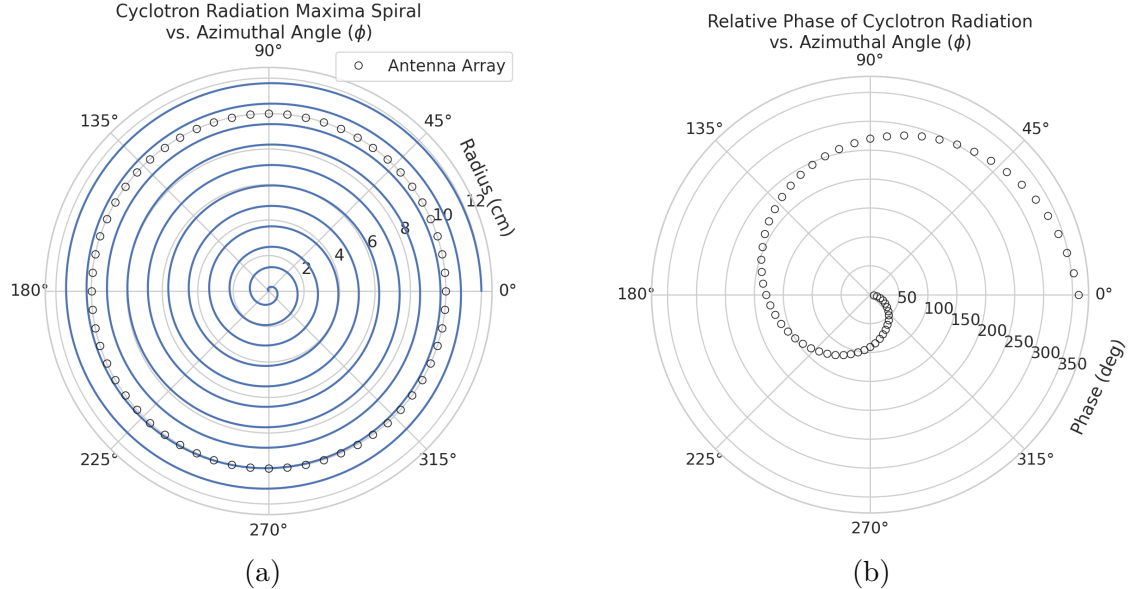


**Figure 5.12.** The amplitude maxima of the cyclotron radiation form an Archimedean spiral as the radiation propagates outward from the cyclotron orbit center (a). A circular antenna array located at a fixed radius from the orbit center will receive electric fields with equal magnitude in each of its channels, but the phase of the electric field incident on each array channel will be linearly out of phase from its neighbor antennas by an amount equal to the angular separation of the two channels (b).

4139 Based on these analytical calculations we can characterize the magnitude, polarization,  
 4140 and phase of the signals received by the antenna array using three criteria. These criteria  
 4141 are the basis of comparison for the radiation produced by the SYNCA and cyclotron  
 4142 radiation emitted by electrons and will be used to evaluate the performance of antenna  
 4143 designs. The criteria are:

- 4144 1. Electric fields that are  $\phi$ -polarized near  $\theta = 90^\circ$
- 4145 2. Uniform time-averaged electric field magnitudes around the circumference of a  
4146 circle centered on the antenna
- 4147 3. Electric fields whose phase is equal to the azimuthal angle at the point of measure-  
4148 ment plus a constant

4149        The Locust simulation package [97] can be used to directly simulate the EM fields  
4150    generated by electrons performing cyclotron motion to validate the analytical calculations.  
4151    Locust simulates the EM fields by first calculating the trajectory of the electrons in  
4152    the magnetic trap using the Kassiopeia software package [98]. The trajectory can then  
4153    be used to solve for the EM fields using the Liénard-Wiechert equations directly with  
4154    no approximations. The resulting electric field solutions drive a receiving antenna by  
4155    convolving the time-domain fields with the finite-impulse response filter of the antenna  
4156    or they can be examined directly to study the field characteristics that the SYNCA must  
4157    reproduce. In the next section we compare the radiation field patterns for electrons  
4158    simulated with Locust to patterns from a SYNCA antenna design.

### 4159    **5.3.3 SYNCA Simulations and Design**

#### 4160    **Early SYNCA Design Development**

4161    A crossed-dipole antenna [99] (see Figure 5.13) was identified early on as a candidate  
4162    SYNCA design. The crossed-dipole is a circularly polarized antenna, consequently, the  
4163    electric fields measured in the plane of the dipole antenna exhibit the same relative phase  
4164    offsets as a 90° electron in a magnetic trap. These phase offsets were measured with the  
4165    first rudimentary crossed-dipole prototype manufactured from coaxial cables with the  
4166    insulation and shield stripped away.

4167        Because the SYNCA is ultimately a calibration tool, it is desireable that the antenna  
4168    have a well-characterized and robust antenna pattern. Therefore, manufacturing a  
4169    SYNCA using the stripped wire method shown in Figure 5.13 is infeasible. Studies of  
4170    crossed-dipole antennas manufactured out of printed circuit boards were performed using  
4171    HFSS to identify an antenna design that imitated an electron, while being more robust  
4172    and simpler to manufacture (see Figure 5.14).

4173        Identifying a design that was robust, manufacturable, and matched the electric fields  
4174    of a trapped electron proved to be a non-trivial task. The primary factor driving the  
4175    difficulty was the high operating frequency of the antenna (26 GHz) combined with  
4176    the requirement that the antenna be electrically-small. An antenna that is electrically-  
4177    small at 26 GHz has a largest dimension on the order of 1 mm, which poses significant  
4178    manufacturability challenges given the limited available budget for SYCNA fabrication.

4179        One of the key limitations with the small size requirements is the diameter of the  
4180    coaxial cables needed to feed the crossed-dipole antenna. The smallest commonly available  
4181    rigid coaxial cables available on the market have diameters of approximately 0.5 mm,

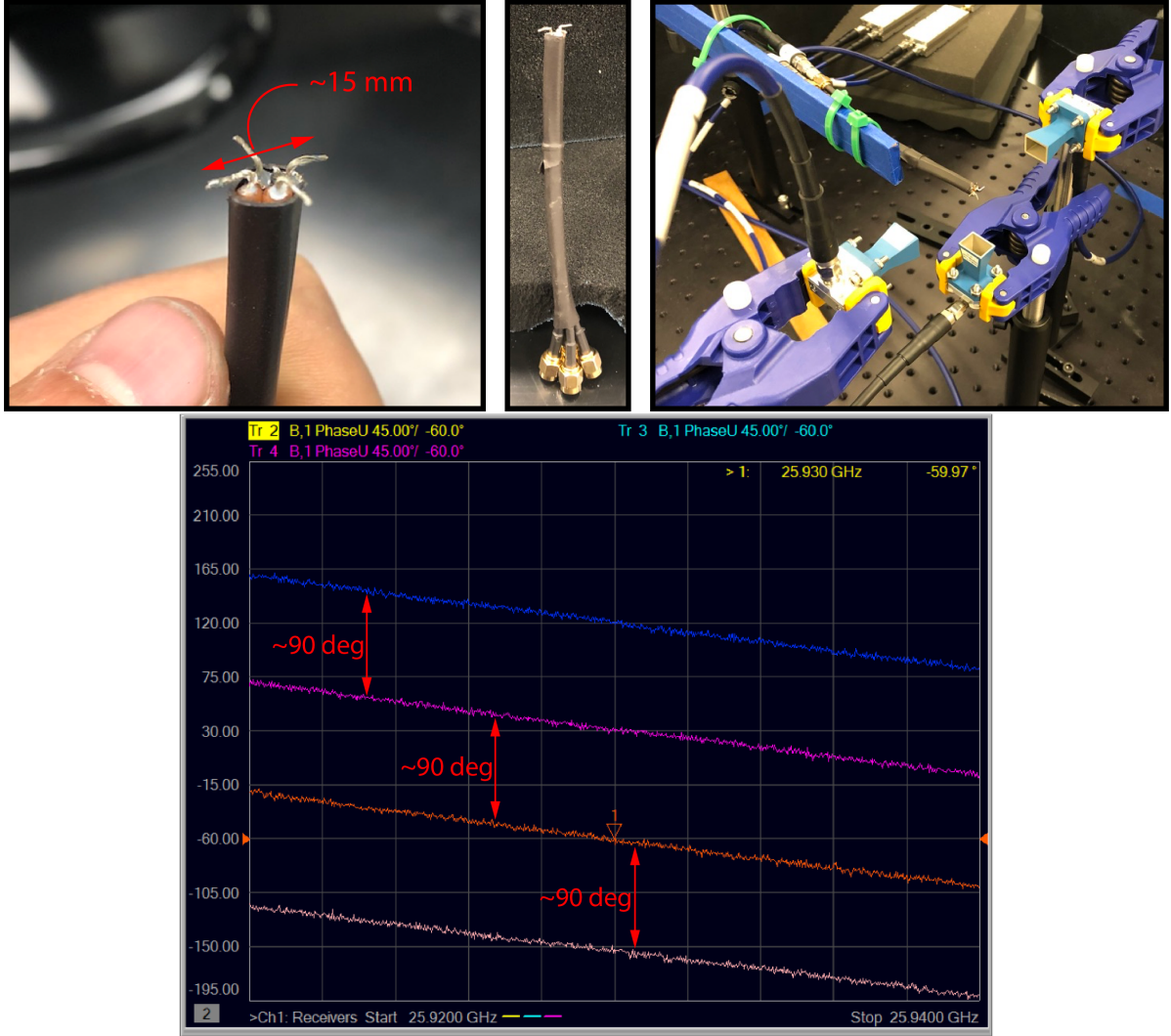


**Figure 5.13.** Images of an early prototype crossed-dipole antenna manufactured by hand and the first measurement setup. The antenna was constructed by hand using four stripped coaxial cables. The antenna was connected to one port of the VNA, and the remaining three ports on the VNA were connected to horn antenna arranged with 90 deg offsets around the crossed-dipole. The measured unwrapped S-parameter phases exhibit the desired relative phase behavior for a SYNCA. These early measurements were the first laboratory proof-of-principle for the crossed-dipole SYNCA.

which limited the spacing between dipole arms to a minimum of about 1 mm. The crossed-dipole antenna performs better as a SYNCA if the dipole arm separation is significantly less than the operating wavelength. Therefore, the high operating frequency ultimately limited how well the SYNCA could mimic an electron. If the desired cyclotron frequency was lowered by an order of magnitude to approximately 3 GHz a significantly higher quality SYNCA could be manufactured at lower cost.

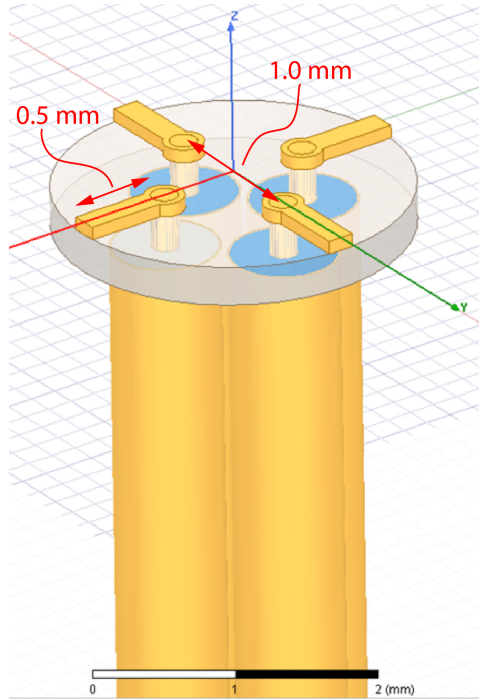


**Figure 5.14.** An early iteration of a crossed-dipole SYNCA antenna simulated in HFSS. The antenna is electrically small at 26 GHz, which requires dipole arms on the order of 1 mm long. This design is limited by the minimum achievable distance between the dipole arms caused by the available diameters of coaxial cables. The assumed termination scheme for the coaxial cables to the antenna is hand-soldering, which introduces random variation in the antenna pattern from the inevitable blobs of solder left on the surface of the PCB.

4188 The decision to use coaxial transmission lines terminated on the antenna PCB with a  
 4189 hand-soldered connection was driven primarily to limit the costs of SYNCA development  
 4190 and contributed to the observable variations in the SYNCA's gain and phase patterns.  
 4191 A second iteration of the SYNCA design that minimized hand-soldering by using surface-  
 4192 mount components could significantly reduce variations in the antenna pattern. The  
 4193 major drawback in the development of a surface-mount SYNCA is the cost, and given the  
 4194 transition to a cavity based design for Phase IV, such a design was never investigated.

#### 4195 **Finalized SYNCA Simulations and Design**

4196 One of the main drawbacks of a standard crossed-dipole design is that they do not radiate  
 4197 uniform electric fields near the  $\theta = \pi/2$  plane. Typical crossed-dipole antennas use dipole  
 4198 arm lengths equal to  $\lambda/4$  or larger [99], where  $\lambda$  is the wavelength at the desired operating  
 4199 frequency. Such large arm lengths cause the electric field magnitude to vary significantly  
 4200 around the circumference of the antenna. However, making the antenna electrically small

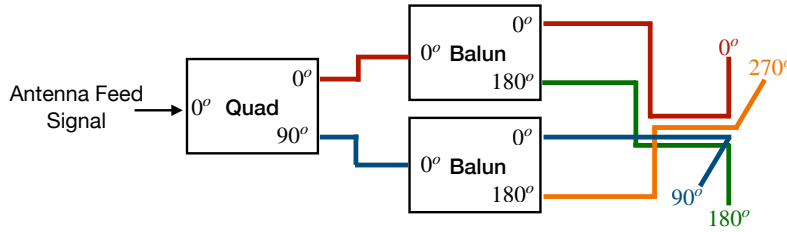


**Figure 5.15.** An idealized crossed-dipole antenna consists of two electric dipole antennas oriented perpendicular to each other and is fed with four signals with a quadrature phase relationship. An example antenna feed circuit is shown which is composed of a chained combination of a quadrature hybrid-coupler (Quad) and two baluns.

4201 by shrinking the arm length can improve the antenna pattern uniformity.

4202 In general, the criterion for an electrically small antenna is that the largest dimension  
 4203 of the antenna ( $D$ ) obey  $D \lesssim \lambda/10$  [68]. In our application, we are attempting to mimic  
 4204 the cyclotron radiation emitted by electrons produced from tritium  $\beta$ -decay with energies  
 4205 near the spectrum endpoint. For a background magnetic field of 1 T, the corresponding  
 4206 cyclotron frequency of tritium endpoint electrons is approximately 26 GHz. Therefore, the  
 4207 electrically small condition would require that the largest dimension of the crossed-dipole  
 4208 antenna be smaller than 1.2 mm.

4209 A crossed-dipole antenna with an overall size of 1.2 mm is challenging to fabricate due  
 4210 to the small dimensions of the dipole arms that, in practice, are fragile and unsuitable  
 4211 for use as a calibration probe. To mitigate some of the challenges with the fabrication  
 4212 of such a small antenna, a variant crossed-dipole antenna design using printed circuit  
 4213 board (PCB) technology (see Figure 5.16) was developed in partnership with an antenna  
 4214 prototyping company, Field Theory Consulting <sup>1</sup>.

4215 The PCB crossed-dipole design uses four rectangular pads to represent the dipole arms,  
 4216 which are connected by a thin circular trace. The circular trace both adds mechanical  
 4217 stability to the antenna and improves the azimuthal uniformity of the electric fields  
 4218 compared to a more standard crossed-dipole geometry. Furthermore, the circular trace  
 4219 allows for a greater separation between dipole arms than standard crossed-dipoles, which  
 4220 is required to accommodate the coaxial connections to each pad. The pads each contain  
 4221 a through-hole solder joint to connect coaxial transmission lines using hand soldering.  
 4222 The antenna PCB has no ground plane on the bottom layer as this was observed in

---

<sup>1</sup><https://fieldtheoryinc.com/>

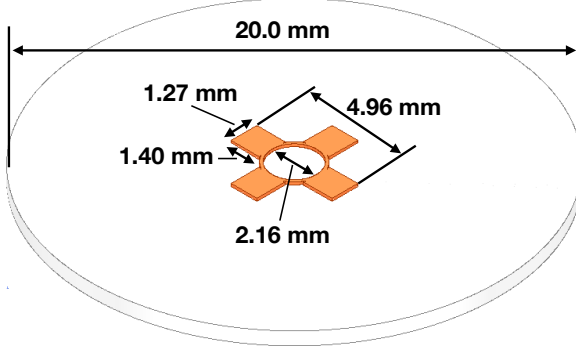


**Figure 5.16.** A model of the PCB crossed-dipole antenna with dimensions. The design has an inside diameter of 2.16 mm for the central circular trace, which is 0.13 mm wide. The dipole arms each have a width of 1.27 mm and protrude beyond the circular trace by 1.40 mm, which gives an overall width of 4.96 mm for the length of the antenna PCB trace from end-to-end. The overall size of the antenna is 20.0 mm the majority of which is the PCB dielectric material. This design was observed in simulation to maintain the field characteristics of the idealized crossed-dipole while being simpler to fabricate due to the increased size of the antenna.

4223 simulation to significantly distort the radiation pattern in the plane of the PCB. The  
 4224 only ground planes present in the model are the outer conductors of the four coaxial  
 4225 transmission lines which feed the antenna. These are left unterminated on the bottom of  
 4226 the PCB dielectric material.

4227 The antenna design development utilized a combination of Locust electron simula-  
 4228 tions and antenna simulations using ANSYS HFSS [69], a commercial finite-element  
 4229 electromagnetic simulation software. Two antenna designs were simulated: an idealized  
 4230 electrically small crossed-dipole antenna with an arm length of 0.40 mm and an arm  
 4231 separation of 0.05 mm, as well as a PCB crossed-dipole antenna with the dimensions  
 4232 shown in Figure 5.16. Plotting the magnitude of the electric fields generated by the  
 4233 antennas across a 10 cm square located in the same plane as the respective antennas  
 4234 reveals the expected cyclotron spiral pattern (see Figure 5.17) which closely matches  
 4235 the prediction for simulated electrons. The spiral pattern demonstrates that the electric  
 4236 fields have the appropriate phases to mimic cyclotron radiation, which fulfills SYNCA  
 4237 criterion 3 identified in Section 5.3.2.

4238 As we can see from Figure 5.18, the crossed-dipole antenna, which uses an idealized  
 4239 geometry, exhibits good agreement with simulation. The antenna has a maximum  
 4240 deviation from a simulated electron of approximately 0.5 dB in the total electric field, 1  
 4241 dB for the  $\phi$ -polarized electric field and 1 dB for the  $\theta$ -polarized electric field.

4242 In comparison, the pattern of the PCB crossed-dipole antenna, because the simulation  
 4243 incorporates the geometry of the coax transmission lines, exhibits some distortion from

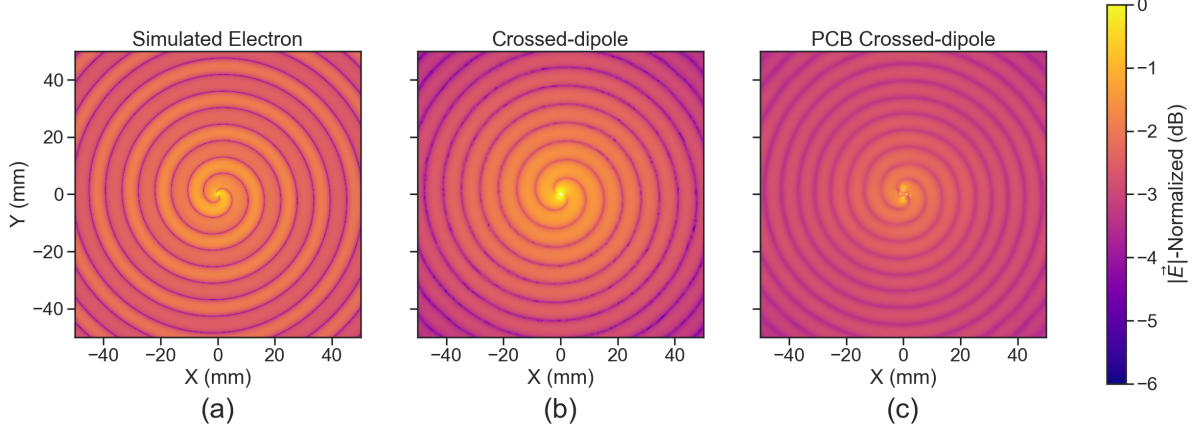


**Figure 5.17.** A comparison of the electric field magnitudes, normalized by the maximum value of the electric field in each simulation, plotted on a 10 cm square to visualize the Archimedean spirals formed by the electron (a), the crossed-dipole antenna (b), and a PCB crossed-dipole antenna (c). The matching patterns indicate that the electric fields have similar phase characteristics. These images were generated using Locust simulations for the electron and ANSYS HFSS for both antennas.

the idealized cross-dipole simulations. The vertically oriented ground planes of the coax lines introduce more  $\theta$ -polarized electric fields than are observed for simulated electrons near  $\theta = 90^\circ$ . The significant  $\theta$ -polarized field minimum is still present but shifted to approximately  $\theta = 65^\circ$ . The  $\theta$ -polarized field deviations of the PCB crossed-dipole antenna should not greatly impact the performance of the antenna because the receiving antenna array is primarily  $\phi$ -polarized. Therefore deviations in the  $\theta$ -polarized fields will be suppressed due to the polarization mismatch. More importantly, the  $\phi$ -polarized electric field pattern generated by the PCB crossed-dipole closely matches simulated electrons across the polar angle range of  $50^\circ < \theta < 150^\circ$ . In this region the PCB crossed-dipole differs by less than 0.5 dB from simulated electrons. This range greatly exceeds the beamwidth of the receiving antenna array which is designed to be most sensitive to fields produced near  $\theta = 90^\circ$ . Therefore, we conclude that the PCB crossed-dipole antenna generates a  $\phi$ -polarized radiation pattern that fulfills SYNCA criterion 1 from Section 5.3.2.

The final SYNCA criterion is related to the uniformity of the electric fields when measured azimuthally around the antenna. As we saw for real electrons in Section 5.3.2 it is expected that the magnitude of the electric field be completely uniform as a function of the azimuthal angle due to the symmetry of the cyclotron orbit. In Figure 5.19 we plot the total electric field as a function of azimuthal angle for an electron, the crossed-dipole antenna, and the PCB crossed-dipole antenna. The crossed-dipole antenna exhibits

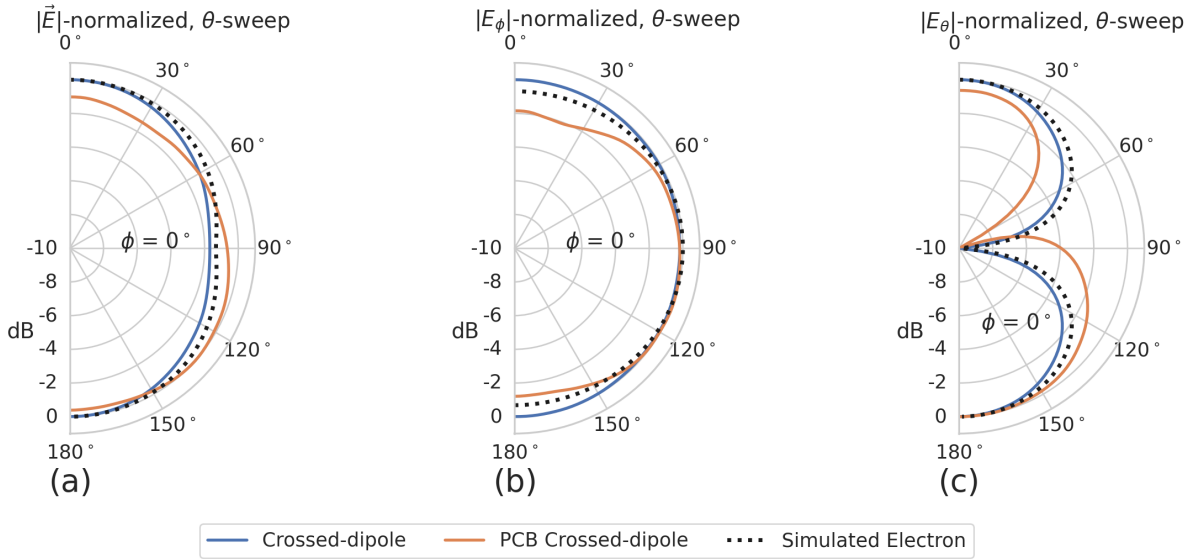


**Figure 5.18.** A comparison of the normalized electric field magnitudes for the ideal crossed-dipole, PCB crossed-dipole, and a simulated electron as a function of the polar angle ( $\theta$ ). (a) Shows the total electric field, (b) shows the  $\phi$ -polarized electric field component, and (c) shows the  $\theta$ -polarized electric field component. These images were generated using Locust simulations for the electron and ANSYS HFSS for both antennas.

perfect uniformity around the azimuthal angle, whereas the PCB crossed-dipole has a small periodic deviation with a maximum difference of 0.3 dB caused by the coaxial transmission lines below the PCB. Such a small deviation from uniformity is acceptable since it is smaller than the expected variation in uniformity caused by imperfections in the antenna fabrication process, which modifies the antenna shape in an uncontrolled manner by introducing solder blobs with a typical size of a few tenths of a millimeter on the dipole arms (see Figure 5.20). Additionally, the SYNCA will be separately calibrated to account for azimuthal differences in the electric field magnitude. Therefore we see from the simulated performance of the PCB crossed-dipole antenna that this antenna design meets all three of the SYNCA criteria.

#### 5.3.4 Characterization of the SYNCA

Two SYNCAs were manufactured using the PCB crossed-dipole design (see Figure 5.20). The antenna PCB (Matrix Circuit Board Materials, MEGTRON 6) is connected to four 2.92 mm coaxial connectors (Fairview Microwave, SC5843) using semi-rigid coax (Fairview Microwave, FMBC002), which also physically support the antenna PCB. The antenna PCB consists only of two layers which correspond to the copper antenna trace

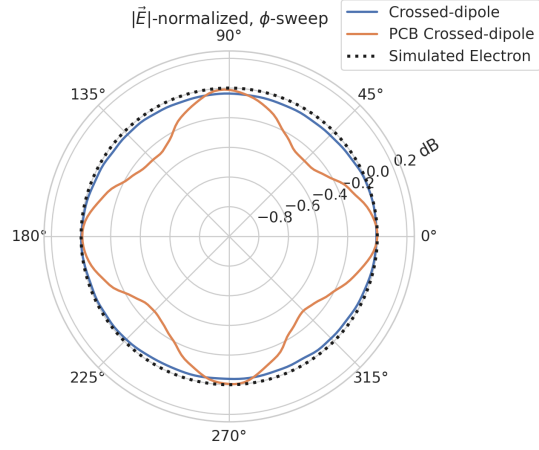


**Figure 5.19.** A comparison of the normalized electric field magnitudes for the crossed-dipole, PCB crossed-dipole, and a simulated electron as a function of the azimuthal angle ( $\phi$ ) evaluated at  $\theta = 90^\circ$ . This image was generated using Locust simulations for the electron and ANSYS HFSS for both antennas.

and the PCB dielectric. Each coax line is connected to the associated dipole arm using through-hole soldering and phase matched to ensure that the electrical length of each of the transmission lines is identical at the operating frequency. The antenna PCB is further reinforced using custom cut polystyrene foam blocks, which have an electrical permittivity nearly identical to air. A custom 3D printed mount is included at the base of the antenna to support the coax connectors and to provide a sturdy mounting base.

Characterization measurements were performed using a Vector Network Analyzer (VNA) to measure the electric field magnitude and phase radiated by the SYNCA to verify the radiation pattern (see Figure 5.21). The VNA is connected to the SYNCA at one port through a hybrid-coupler whose outputs are connected to two baluns to generate the signals with the appropriate phases to feed the SYNCA (see Figure 5.15). The other port of the VNA is connected to a single reference horn antenna that serves as a field probe. To position the SYNCA, a combination of translation and rotation stages are used to characterize the antenna's fields across the entire radiation pattern circumference. This measurement scheme is equivalent to measuring the fields generated by the SYNCA using a full circular array of probe antennas.

The antenna measurement space is surrounded by RF anti-reflective foam to isolate the measurements from the lab environment (see Figure 5.21b) and remaining reflections are removed using the VNA's time-gating feature. The SYNCA is affixed to the stages by a custom RF transparent mount made of polystyrene foam. The coaxial cables deliver the antenna feed signals generated by the VNA to the SYNCA while still allowing

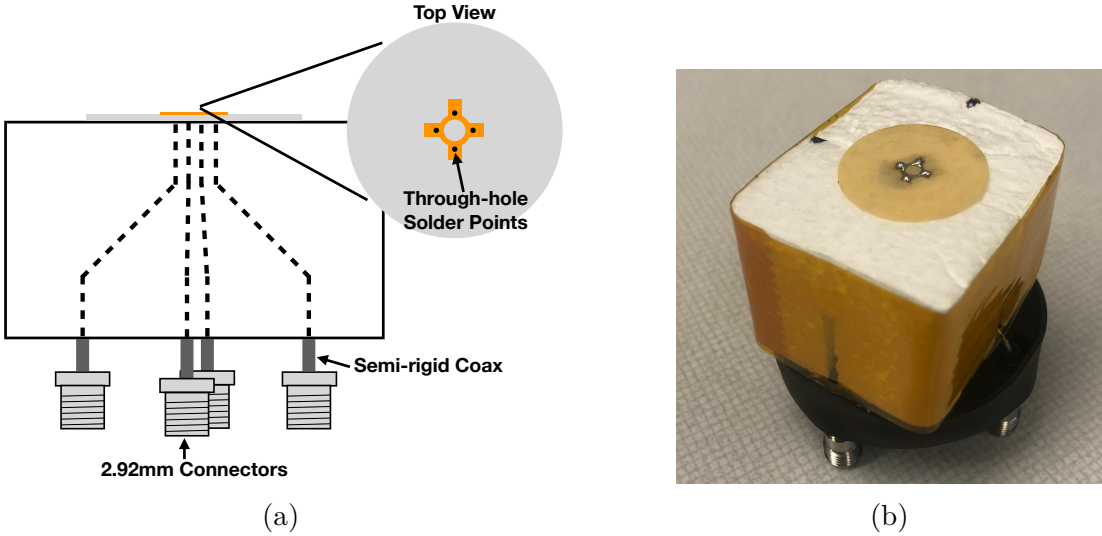


**Figure 5.20.** (a) A cartoon schematic which highlights the routing of the semi-rigid coax transmission lines. (b) A photograph of a SYNCA constructed using the modified crossed-dipole PCB antenna design. Visible in the photograph of the SYNCA are four blobs of solder which are an artifact of the SYNCA’s hand-soldered construction. These solder blobs are the most significant deviation from the SYNCA design shown in Figure 5.16 and are responsible for a significant fraction of the irregularities seen in the antenna pattern.

unrestricted rotation. The horn antenna probe is nominally positioned in the plane formed by the antenna PCB ( $\theta = 90^\circ$  or  $z = 0$  mm) at a distance of 10 cm from the SYNCA, to match the expected position of the antenna array relative to the SYNCA in the antenna array test stand. The horn antenna can be manually raised or lowered to different relative vertical positions to characterize the radiation pattern at different polar angles.

Several  $360^\circ$  scans were performed with probe vertical offsets of -10.0 mm, -5.0 mm, 0.0 mm, 5.0 mm, and 10.0 mm relative to the antenna PCB plane. These probe offsets cover a 2 cm wide vertical region centered on the SYNCA PCB, approximately equal to  $\pm 6$  degrees of polar angle. The measurements show that the SYNCA is generating fields with nearly isotropic magnitude across the probed region. The standard deviation of the electric field magnitude measured around the antenna circumference is approximately 2.9 dB for a typical rotational scan. The presence of a significant pattern null is noted near  $45^\circ$  (see Figure 5.22), which we attribute to small imperfections in the antenna PCB that could be introduced from the hand soldered terminations connecting the coax cables to the antenna. There is no significant difference in the radiation pattern when measured across the 2 cm vertical range. The measured relative phases closely follow



**Figure 5.21.** A schematic of the VNA characterization measurements (a). This setup allows for antenna gain and phase measurements across a full  $360^\circ$  of azimuthal angles using a motorized rotation stage and control of the radial position of the SYNCA using a translation stage. A photo of the setup in the lab is shown in (b).

4318 the expectation for an electron, being linear with the measurement rotation angle and  
 4319 forming the expected spiral pattern. Other than the small phase imperfections there is  
 4320 a slight sinusoidal bias to the phase data, which we determined is the result of a small  
 4321 ( $\lesssim 1$  mm) offset of the antenna's phase center from the rotation axis of the automated  
 4322 stages.

4323 The characterization measurements confirm the simulated performance of the SYNCA.  
 4324 As expected the fields generated by the antenna are nearly isotropic in magnitude,  $\phi$ -  
 4325 polarized, and are linearly out of phase around the circumference of the antenna as  
 4326 predicted for cyclotron radiation in Section 5.3.2. Small imperfections in the magnitude  
 4327 and phase of the antenna are expected, particularly at the antenna's high operating  
 4328 frequency of 26 GHz where small geometric changes can have significant impacts on  
 4329 electrical properties. However, calibration through careful characterization measurements  
 4330 can be used to remove the majority of these pattern imperfections, including the relatively  
 4331 large pattern null near  $45^\circ$ , which will allow for the usage of the SYNCA as a test source  
 4332 for free-space CRES experiments utilizing antenna arrays. In the next section we use the  
 4333 VNA measurements obtained here as a calibration for signal reconstruction using digital  
 4334 beamforming.

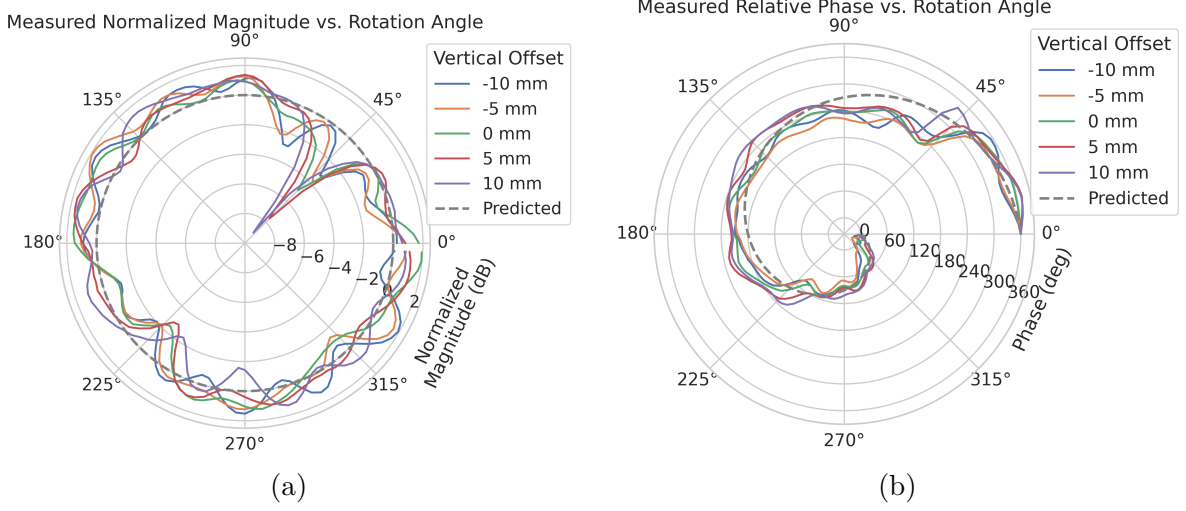


**Figure 5.22.** Linear interpolations of the measured electric field magnitude (a) and phase (b). The data was acquired using a VNA at 120 points spaced by 3 degrees from 0 to 357 degrees of azimuthal angle. The different color lines indicate the vertical offset of the horn antenna relative to the SYNCA PCB and the dashed line shows the expected shape from electron simulations. No significant difference in the antenna pattern is observed for the measured vertical offsets.

### 4335 5.3.5 Beamforming Measurements with the SYNCA

4336 Digital beamforming is a standard technique for signal reconstruction using a phased  
 4337 array [100]. The SYNCA, since it exhibits the same cyclotron phases as a trapped  
 4338 electron, can be used to perform simulated CRES digital beamforming reconstruction  
 4339 experiments on the bench-top without the need for the magnet, cryogenics, and vacuum  
 4340 systems required by a full CRES experiment. The fields received by the individual  
 4341 elements of the antenna array will have phases dependent on the spatial position of the  
 4342 source relative to the antennas. Therefore, a simple summation of the received signals  
 4343 will fail to reconstruct the signal due to destructive interference between the individual  
 4344 channels in the array. However, applying a phase shift associated with the source's  
 4345 spatial position removes phase differences and results in a constructive summation of the  
 4346 channel signals (see Figure 5.23). We can summarize the digital beamforming operation  
 4347 succinctly using the following equation

$$y[t_n] = \sum_{m=0}^{N-1} x_m[t_n] A_m e^{i\phi_m}, \quad (5.34)$$

4348 where  $y[t_n]$  represents the summed array signal at time  $t_n$ ,  $x_m[t_n]$  is the signal received  
 4349 by channel  $m$  at time  $t_n$ ,  $\phi_m$  is the phase shift applied to the signal received at channel  
 4350  $m$ , and  $A_m$  is an amplitude weighting factor that accounts for the different signal power  
 4351 received by individual channels. By changing the digital beamforming phases, the point  
 4352 of constructive interference can be scanned across the sensitive region of the array to  
 4353 search for the location of a radiating source, which is identified as the point of maximum  
 4354 summed signal power above a specified threshold. The digital beamforming phases consist  
 4355 of two components,

$$\phi_m = 2\pi d_m / \lambda + \theta_m, \quad (5.35)$$

4356 where  $d_m$  is the distance from the  $m$ -th array element to the source, and  $\theta_m$  is the  
 4357 relative angle between the source position and the  $m$ -th antenna. The first component is  
 4358 the standard digital beamforming phase that corresponds to the spatial position of the  
 4359 source, and the second component is the cyclotron phase that corresponds to the relative  
 4360 azimuthal phase offset.

4361 With a small modification to the hardware used to characterize the SYNCA (see  
 4362 Figure 5.21), we can perform a digital beamforming reconstruction of a synthetic CRES  
 4363 event. By replacing the VNA with an arbitrary waveform generator (AWG), the SYNCA  
 4364 can be used to generate cyclotron radiation with an arbitrary signal structure, which  
 4365 can then be detected by digitizing the signals received by the horn antenna. Rotational  
 4366 symmetry allows us to use the rotational stage of the positioning system to rotate the  
 4367 SYNCA to recreate the signals that would have been received by a complete circular

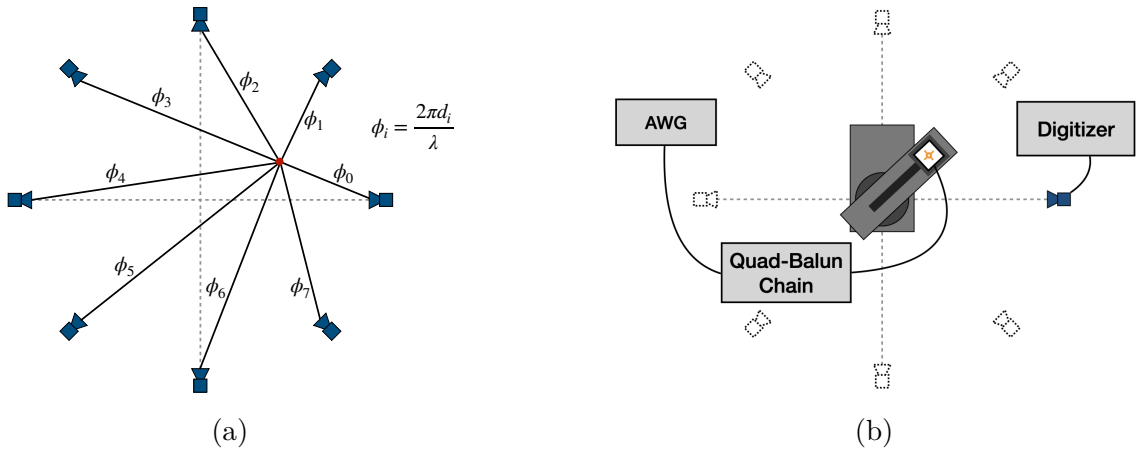


**Figure 5.23.** (a) A depiction of the relative phase differences for signals received by a circular antenna array from an isotropic source. The phases correspond to a unique spatial position.  
 (b) A schematic of the setup used to perform digital beamforming.

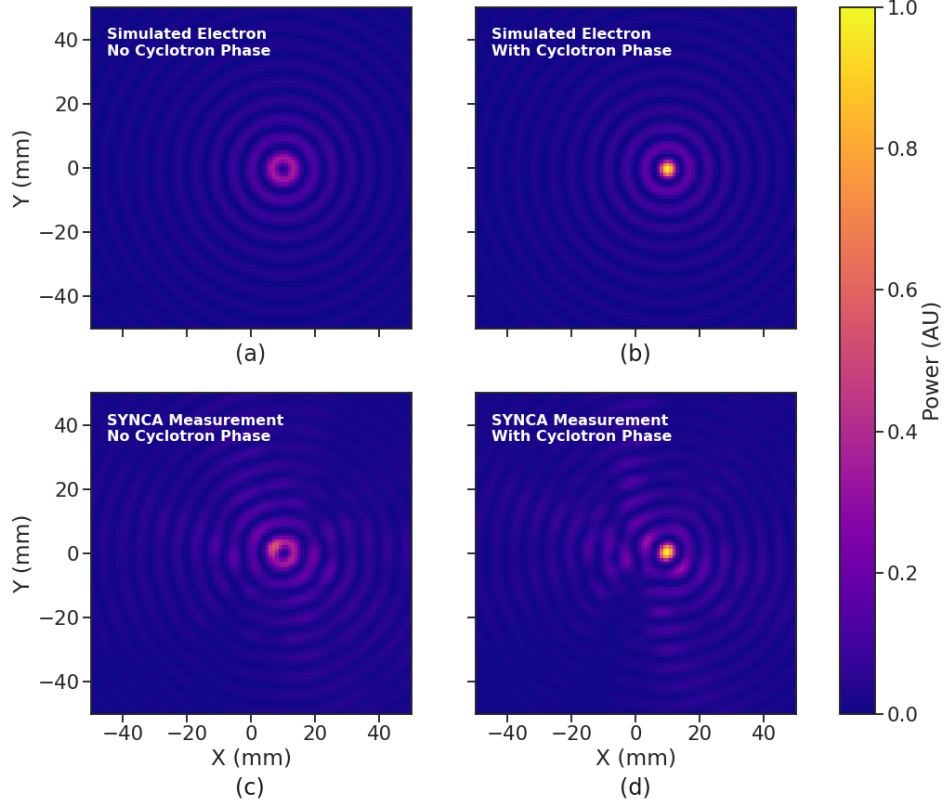


**Figure 5.24.** Digital beamforming maps generated using a simulated 60 channel array and electron simulated using the Locust package. (a) and (b) show the beamforming maps for simulated electrons without the cyclotron spiral phases and with the cyclotron spiral phases respectively. (c) and (d) show the beamforming maps produced from SYNCA measurements. We observe good agreement between simulated electrons and the SYNCA measurements.

4368 array of antennas.

4369 Using this setup, signals from a 60 channel circular array of equally spaced horn  
 4370 antennas were generated with the SYNCA positioned 10 mm off the central array axis,  
 4371 reconstructed using digital beamforming, and compared to Locust simulation (see Figure  
 4372 5.24). When the cyclotron spiral phases are not used, which is equivalent to setting  $\theta_m$   
 4373 in Equation 5.35 to zero, the SYNCA's position is reconstructed as a relatively faint ring  
 4374 as predicted by simulation. However, when the appropriate cyclotron phases are used  
 4375 during the beamforming procedure, both the simulated electron and the SYNCA appear  
 4376 as a single peak of high relative power corresponding to the source position. Therefore,  
 4377 we observe good agreement between the simulated and SYNCA reconstructions. While it  
 4378 may seem that for the case with no cyclotron phase corrections the ring reconstructs the  
 4379 position of the electron as effectively as beamforming with the cyclotron phase corrections,

4380 it is important to note that the simulations and measurements were generated without a  
 4381 realistic level of thermal noise. The larger maxima region and lower signal power, which  
 4382 occurs without the cyclotron phase corrections, significantly reduce the probability of  
 detecting an electron in a realistic noise background.

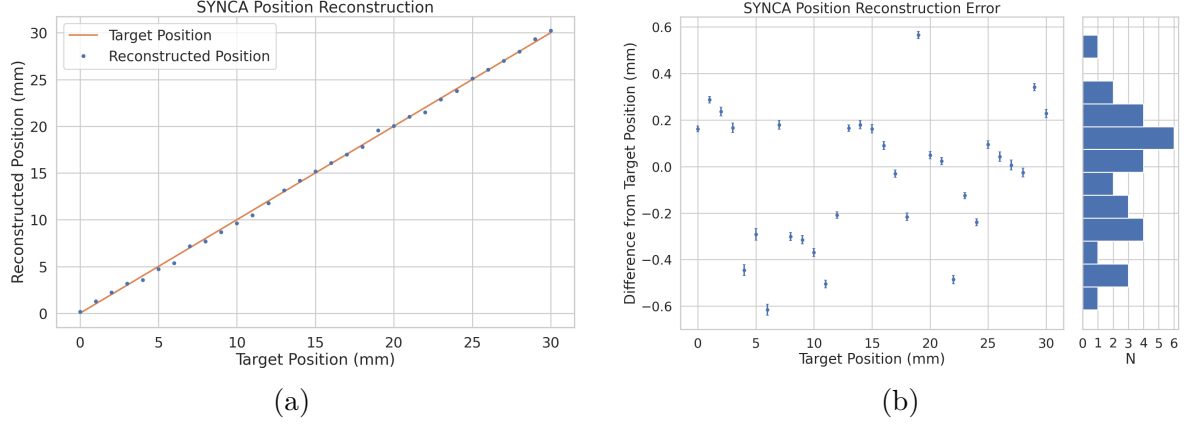


**Figure 5.25.** A plot of the SYNCA’s reconstructed position using the synthesized horn-antenna array and digital beamforming. (a) Shows the reconstructed position of the SYNCA compared with the target position indicated by the positioning system readout. (b) Shows the reconstruction error, which is the difference between the target and reconstructed positions. The error bars in (b) are the uncertainty in the mean position of the 2D Gaussian used to fit the digital beamforming reconstruction peak obtained from the fit covariance matrix. The mean fit position uncertainty of 0.02 mm is an order of magnitude smaller than the typical reconstruction error of 0.3 mm obtained by calculating the standard deviation of the difference between the reconstructed and target position.

4383  
 4384 To bound the beamforming capabilities of the synthetic array of horn antennas, we  
 4385 performed a series of beamforming reconstructions where the SYNCA was progressively  
 4386 moved off the central axis of the array (see Figure 5.25). To extract an estimate of the  
 4387 position of the SYNCA using the digital beamforming image we apply a 2-dimensional  
 4388 (2D) Gaussian fit to the image data and extract the estimated centroid value. We find  
 4389 that the synthetic horn antenna array reconstructs the position of the SYNCA with a  
 4390  $1\sigma$ -error of 0.3 mm with no apparent trend across the 30 mm measurement range. This  
 4391 reconstruction error is an order of magnitude larger than mean fit position uncertainty  
 4392 of 0.02 mm indicating that systematic effects related to the SYNCA positioning system  
 4393 could be contributing additional uncertainty to the measurements. Note that the current  
 4394 mean reconstruction error of 0.3 mm is a factor of 20 smaller than the full width at half  
 4395 maximum of the digital beamforming peak (6 mm), which could be interpreted as a naive  
 4396 estimate of the position reconstruction performance of this technique. Because these  
 4397 measurements are intended as a proof-of-principle demonstration, we do not investigate

4398 potential sources of systematic errors further; however, we expect that a similar and  
4399 more thorough investigation will be performed using the Project 8 antenna array test  
4400 stand, where typical reconstruction errors can be used to estimate the energy resolution  
4401 limits of antenna array designs.

### 4402 5.3.6 Conclusions

4403 In this paper we have introduced the SYNCA, which is a novel antenna design that  
4404 emits radiation that mimics the unique properties of the cyclotron radiation generated by  
4405 charged particles moving in a magnetic field. The characterization measurements of the  
4406 SYNCA validated the simulated performance of the PCB crossed-dipole antenna design.  
4407 Additionally, the SYNCA was used to estimate the position reconstruction capabilities  
4408 of a synthesized array of horn antennas and experimentally reproduced the simulated  
4409 digital beamforming reconstruction of electrons.

4410 While the SYNCA performs well, there exist discrepancies in the phase and magnitude  
4411 of the radiation pattern compared to the simulated SYNCA design that are related to  
4412 the small geometric differences in the soldered connections. Future design iterations that  
4413 replace the soldered connections with a fully surface mount design could improve the  
4414 radiation pattern at the cost of some complexity and expense. Furthermore, improving  
4415 the design of the antenna PCB and mounting system would allow the antenna to be  
4416 inserted into a cryogenic and vacuum environment where in-situ antenna measurement  
4417 calibrations could be performed.

4418 The discrepancies in the radiation pattern and phases exhibited by the as-built  
4419 SYNCA should not greatly impact its performance as a calibration probe. Both magni-  
4420 tude and phase variations can be accounted by applying the SYNCA characterization  
4421 measurements as a calibration to the data collected by the antenna array test stand. The  
4422 separate calibration of the SYNCA radiation does not impact the primary goals for the  
4423 antenna array test stand which are array calibration and signal reconstruction algorithm  
4424 performance characterization, because it can be performed with standard reference horn  
4425 antennas with well understood characteristics.

4426 The SYNCA antenna technology advances the CRES technique by providing a  
4427 mechanism to characterize free-space antenna arrays for CRES measurements without  
4428 the need for a magnet and cryogenics system, which would be required for calibration  
4429 using electron sources. Both the Project 8 collaboration as well as future collaborations  
4430 which are developing antenna array based CRES experiments can make use of SYNCA  
4431 antennas as an important component of their calibration and commissioning phases.

## 4432 5.4 FSCD Antenna Array Measurements with the SYNCA

### 4433 5.4.1 Introduction

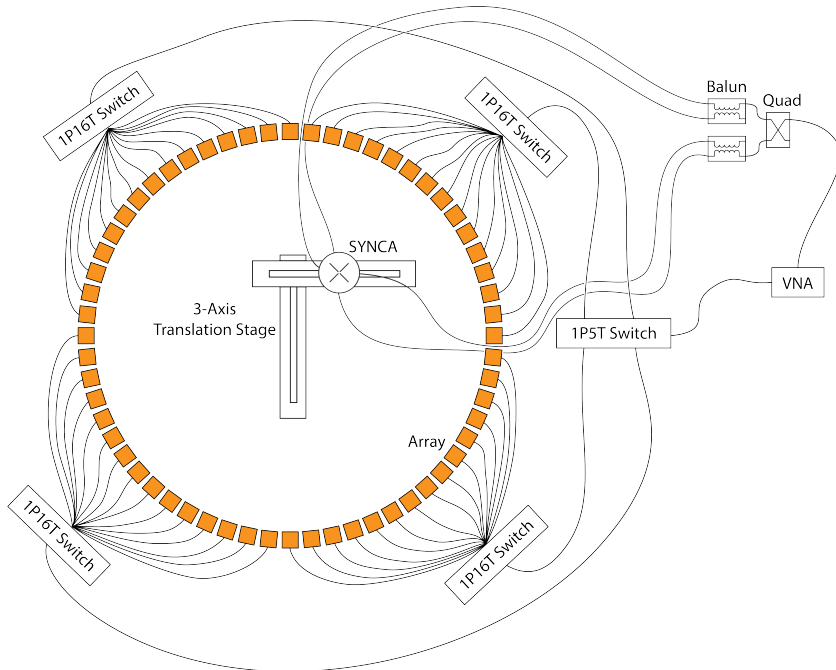


**Figure 5.26.** A diagram of the array measurement system used to test the prototype FSCD antenna array. A VNA is used as the primary measurement tool, which is connected to the array through a series of switches. The other port of the VNA connects to the SYNCA through the quad-balun chain used to provide the SYNCA feed signals. During measurements the SYNCA is positioned inside the center of the antenna array and translated to different radial and axial positions using a 3-axis manual translation stage setup.

4434 Using the SYNCA it is possible perform full-array measurements of prototype versions  
4435 of the FSCD antenna array with a realistic cyclotron radiation source (see Figure 5.26).  
4436 The goal is to compare the measured power received to FSCD simulations as a function  
4437 of the radial and axial position of the SYNCA source. These measurements are intended  
4438 to validate the antenna research and development by Project 8, which has been driven  
4439 primarily by simulations with Locust [65] and CRESana (see Section 4.2.3), and identify  
4440 any discrepancies with these simulations tools. This knowledge will provide confidence  
4441 in the simulations necessary for the analysis of the sensitivity of larger antenna array  
4442 based CRES experiment designs to the neutrino mass.

4443 As shown in Section 5.3, the SYNCA has some radiation pattern imperfections  
4444 that complicate the comparison between measurement and simulation data. One way

4445 to disentangle the effects of these imperfections is to perform an additional set of  
4446 measurements using a synthetic antenna array setup along with the SYNCA antenna.  
4447 Since the synthetic array setup uses only a single array antenna, the data should be  
4448 free of errors associated with individual antenna differences and multi-path interference,  
4449 which are two error sources being tested with the full-array setup. By comparing the  
4450 synthetic array data to the FSCD array data and to simulation data one can evaluate the  
4451 significance of these effects relative to the errors introduced by SYNCA imperfections.

## 4452 **5.4.2 Measurement Setups**

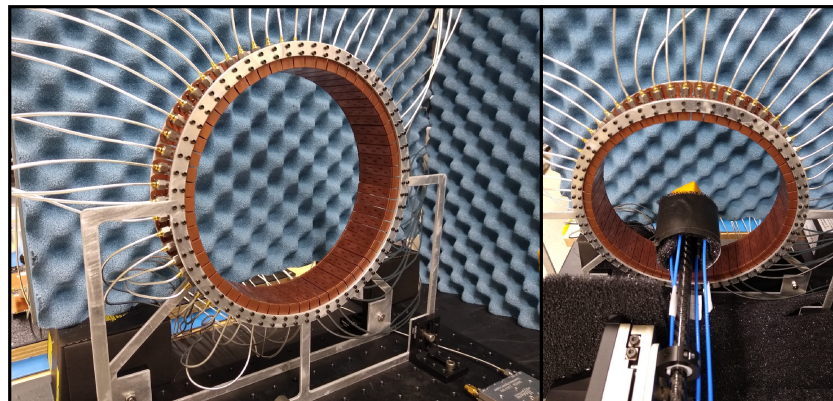
### 4453 **5.4.2.1 FSCD Array Setup**

4454 The antenna design that composes the array is the 5-slot waveguide antenna developed  
4455 for the FSCD experiment (see Figure 5.27a). The antenna is 5 cm long and is constructed  
4456 out of WR-34 waveguide with a 2.92 mm coax connector located at the center of the  
4457 antenna. Copper flanges located on both ends of the antenna are used to mount the  
4458 antenna in the array support structure. The antennas are supported by two circular steel  
4459 brackets that can be bolted to both ends of the waveguide to construct the circular array  
4460 (see Figure 5.27b). The antenna array consists of sixty identical waveguide antennas  
4461 with a radius of 10 cm. The array is mounted perpendicular to an optical breadboard  
4462 surface using a pair of the steel brackets, which provide sufficient space for the coaxial  
4463 cable connections and allows for easy positioning of the SYNCA antenna. The SYNCA is  
4464 mounted on the end of a carbon fiber rod attached to a set of manual translation stages,  
4465 which are used to move the SYNCA antenna to different positions inside the array (see  
4466 Figure 5.27c). The stages allow for independent motion in three different axes and can  
4467 position the SYNCA at radial distances up to 5 cm from the center.

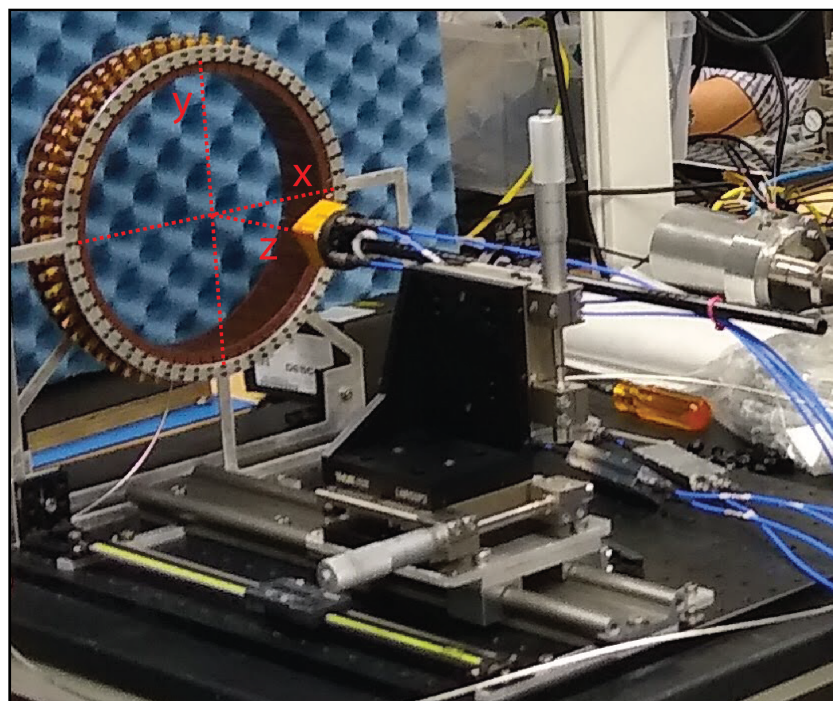
4468 Data acquisition is accomplished using a two-port VNA in combination with a series  
4469 of microwave switches that allow the VNA to connect to each channel in the array . The  
4470 first port of the VNA is connected to the quad-balun chain used to feed the SYNCA (see  
4471 Section 5.3), and the second port of the VNA connects to a 1P5T microwave switch. The  
4472 1P5T switch is connected to four separate 1P16T switch boards that connect directly  
4473 to the array. The data acquisition is controlled by a python script running on a lab  
4474 computer, which is connected to the VNA and an Arduino board programmed to control  
4475 the microwave switches. The script uses the switches to iteratively connect each of the  
4476 antennas in the array to the VNA. The VNA is configured to load a specific calibration  
4477 file for each antenna channel and performs the measurements of all available S-parameters.



(a)



(b)



(c)

**Figure 5.27.** Photos of the prototype FSCD antenna (a), the FSCD array and SYNCA (b), and the translation stages and coordinate system used to position the SYNCA (c).

4478 The separate calibration files is an attempt to remove phase and magnitude errors caused  
4479 by different propagation through the RF switches. Array measurements were performed  
4480 for the set of SYNCA positions consisting of radial (x-axis) positions from 0 to 50 mm  
4481 in 5 mm steps and axial (z-axis) positions from 0 to 50 mm in 5 mm steps resulting in  
4482 121 array measurements. At each SYNCA position the two-port S-parameter matrix  
4483 is measured using a linear frequency sweep from 25.1 to 26.1 GHz with 101 discrete  
4484 frequencies.

4485 **5.4.2.2 Synthetic Array Setup**

4486 A photograph of the setup used to perform the synthetic array measurements is shown  
4487 in Figure 5.28. A difference between this setup and the FSCD array setup is that the  
4488 synthetic array measurements were performed with a waveform generator and digitizer  
4489 instead of a VNA. The electronics configuration is identical to the diagram in Figure  
4490 5.7b. Despite the differences, one is still able to compare the measured phases of the  
4491 synthetic array and the relative magnitude of the power, since the digitized signal power  
4492 is directly proportional to S21.

4493 The arbitrary waveform generator in the setup is configured to produce a 64 MHz  
4494 sine wave signal that is up-converted to 25.864 GHz using a mixer and the VNA source.  
4495 This signal is passed through a bandpass filter and fed to the SYNCA quad-balun chain.  
4496 A single FSCD antenna is positioned 10 cm from the SYNCA and aligned vertically so  
4497 that the center of the 5-slot waveguide is in the plane of the SYNCA PCB (see Figure  
4498 5.28). This position corresponds to  $z = 0$  in Figure 5.27c. The SYNCA is rotated  
4499 in three degree steps to synthesize an antenna array with 120 channels. This channel  
4500 count is more than could physically fit in a 10 cm radius array, but there is no cost to  
4501 over-sampling. The signals from the FSCD antenna are down-converted using the second  
4502 mixer connected to the VNA source before being digitized at 250 MHz and saved to  
4503 disk. Several synthetic array measurement scans were performed by using the linear  
4504 translation stage to change the radial position of the SYNCA. In total eight scans were  
4505 taken from 0 to 35 mm using a radial position step size of 5 mm.

4506 **5.4.3 Simulations, Analysis, and Results**

4507 The Locust and CRESana simulation packages utilize the antenna transfer functions  
4508 to calculate the power that would be received by each antenna from a CRES electron.  
4509 The equivalent quantity in the measurement setup is the S21 matrix element, which

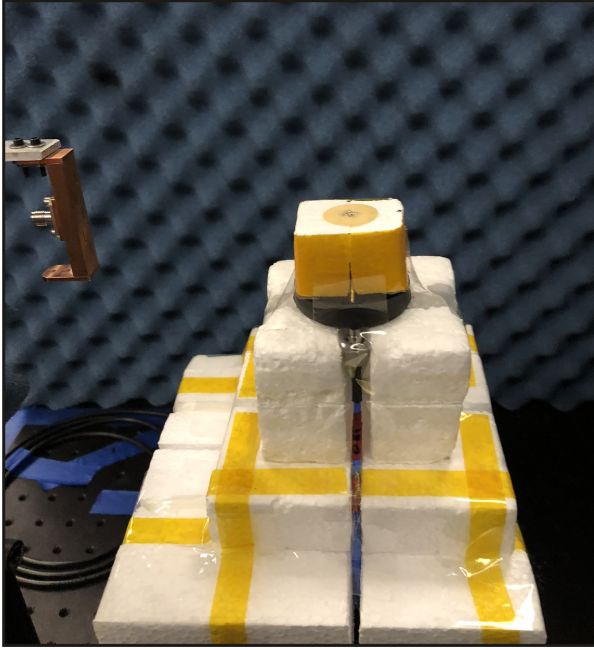


**Figure 5.28.** A photo of the FSCD antenna and the SYNCA in the synthetic array measurement setup at Penn State.

4510 indicates the ratio of the power received by an antenna in the array to the amount of  
4511 power delivered to the SYNCA. Therefore, the analysis focuses on comparing the relative  
4512 magnitudes and phase of the S21 parameters measured by the VNA as a function of the  
4513 array channel and the SYNCA position. Additionally, a beamforming reconstruction  
4514 using the S21 data is done to evaluate how the summed power and beamforming images  
4515 change as a function of the position of the SYNCA.

#### 4516 5.4.3.1 Simulations

4517 Simulations for the FSCD array measurements were performed using CREsana, which  
4518 performs analytical calculations of the EM-fields produced by an electron at the position  
4519 of the antennas. At each sampled time CREsana computes the electric field vector at the  
4520 antenna positions, which is projected onto the antenna polarization axis to obtain the  
4521 co-polar electric field. The magnitude of the co-polar electric field is then multiplied by  
4522 a flat antenna transfer function to calculate the corresponding voltage signal. CREsana  
4523 simulations exploit the flat transfer functions of the FSCD antennas, which allows the  
4524 electric field to be multiplied by the antenna transfer function rather than performing  
4525 the full FIR calculation. These calculations produce a voltage time-series for each of the  
4526 antennas in the array that can be compared to the laboratory measurements.

CRESana was configured to simulate a  $90^\circ$  electron in a constant background magnetic field of  $\approx 0.958$  T with a kinetic energy of 18.6 keV. These parameters were chosen in order to mimic a CRES event near the tritium beta-decay spectrum endpoint in the FSCD experiment. The constant background magnetic field guarantees that the guiding center of the electron is stationary across the duration of the simulation which is consistent with the SYNCA in the laboratory measurements. Simulations were performed with the electron's guiding center at radial positions from 0 to 45 mm in steps of 1 mm and axial positions from 0 to 30 mm in steps of 1 mm. The simulations generated time series consisting of 8192 samples at 200 MHz for the sixty channel FSCD antenna array geometry.

#### 5.4.3.2 Phase Analysis

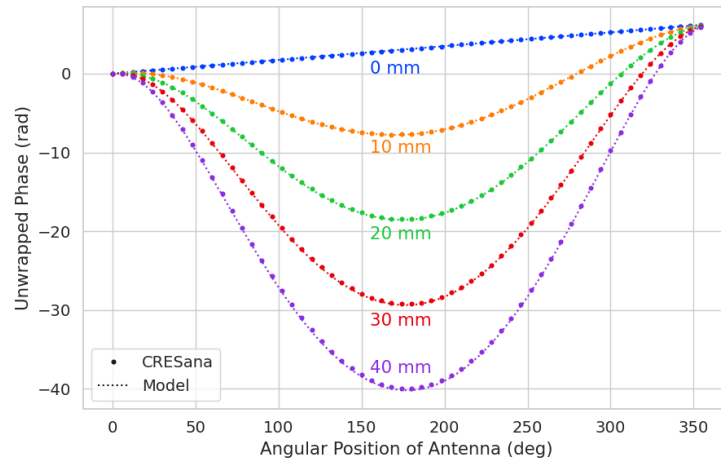


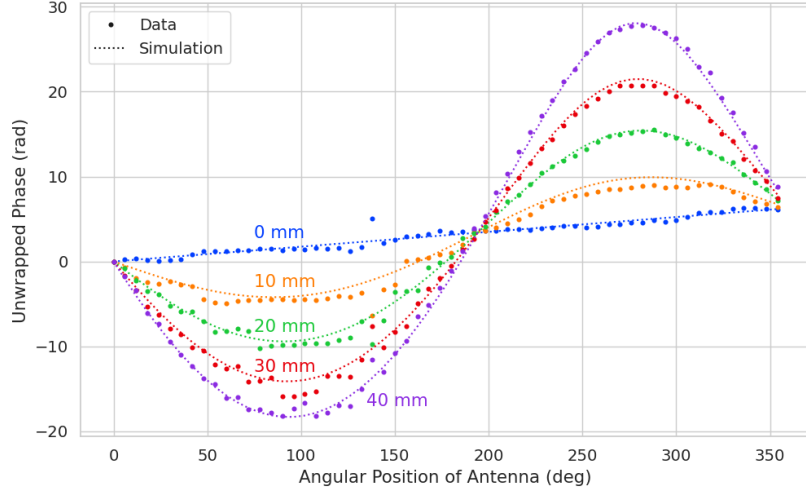
**Figure 5.29.** The unwrapped phases of signals received by the FSCD antenna array from an electron with a  $90^\circ$  pitch angle located in the plane of the antenna array. The data points indicated the phases extracted from simulation and the dashed lines show the model predictions.

Correct modeling of the signal phases is fundamental to reconstruction for both beamforming and matched filter approaches. The beamforming reconstruction relies on a signal phase model developed from Locust simulations, which allows one to predict the relative signal phases for a specific magnetic trap and electron position. The equation for the model is

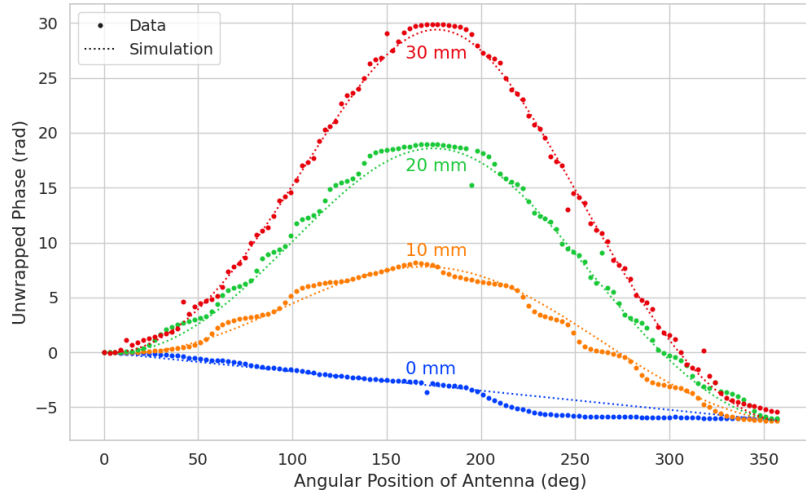
$$\phi_{ij}(t) = \frac{2\pi d_{ij}(t)}{\lambda} + \theta_{ij}(t), \quad (5.36)$$

where  $d_{ij}(t)$  is distance between the assumed electron position and the antenna position, and  $\theta_{ij}(t)$  is the angular separation between the electron and antenna positions. For

4545 details on the components of the phase model see Section 5.3.2. In Figure 5.29 I compare  
 4546 the phases predicted by Equation 5.36 to phases extracted from CRESana simulations of  
 4547 an electron located in the plane of the antenna array at a series of radial positions. One  
 4548 observes excellent agreement between the model and simulation.



(a)



(b)

**Figure 5.30.** Plots of the measured unwrapped phases from the FSCD array (a) and the synthetic array (b) compared to the model predictions for a series of radial positions. The different phases of the sinusoidal phase oscillations in the two plots reflects differences in the coordinate systems of the measurements.

4549 The measured signal phases from the FSCD array and synthetic array are shown  
 4550 in Figures 5.30a and 5.30b compared to the signal phase model. The axial position of

4551 the SYNCA in both plots is  $z = 0$  mm, such that the plane of the PCB is aligned with  
 4552 the center of the FSCD antenna. The data shown in Figure 5.30a corresponds to the  
 4553 S-parameters measured at 25.80 GHz which is the frequency closest to the one used in  
 4554 the synthetic array setup. The different slope and sinusoidal phases exhibited by Figure  
 4555 5.30a and 5.30b reflects differences in the coordinate system for each setup. In general,  
 4556 the phase model predicts the large scale features of the phases well, but there are some  
 4557 small scale deviations or errors from the phase model that do not appear to be present  
 4558 in simulation.

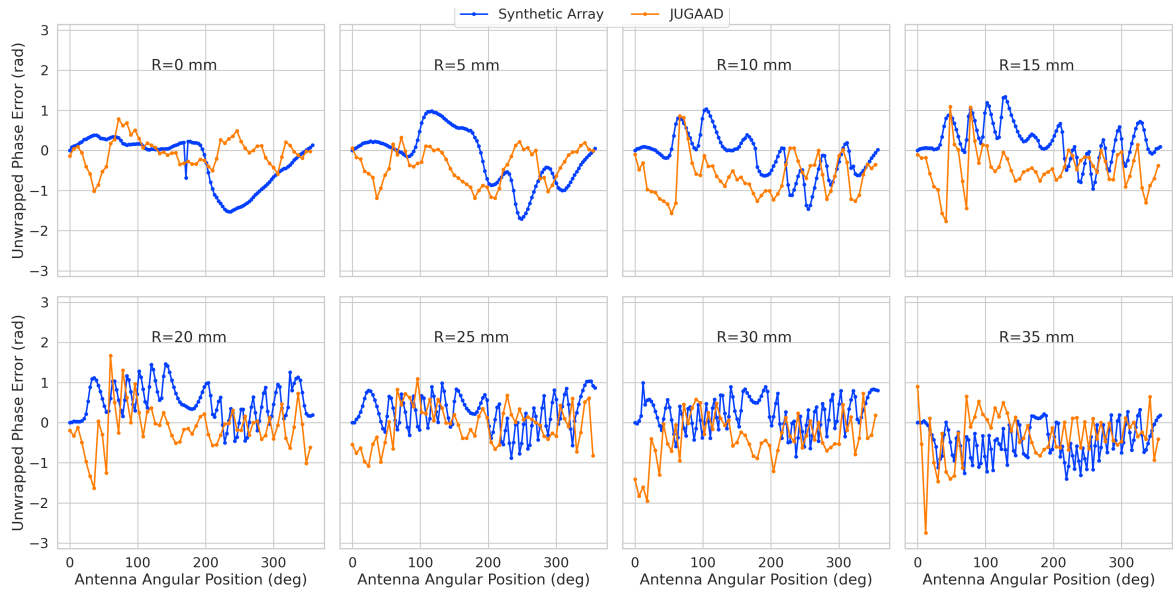


**Figure 5.31.** The phase errors between the measurement and model for the synthetic array (blue) and the FSCD array (orange) for a series of radial positions. The label JUGAAD refers to an alternative name for the FSCD array setup. As the SYNCA is translated off-axis phase errors with progressively higher oscillation frequency enter into the measurements.

4559 A comparison of the phase errors, which are the difference between measurement and  
 4560 model is shown in Figure 5.31. The FSCD array data is referred to as the JUGAAD  
 4561 data in the plot legend, which is an alternative name for the FSCD array setup.

4562 The phase error at  $R = 0$  in Figure 5.31 forms a smooth curve, with the exception of  
 4563 an outlier data point caused by a bug in the data acquisition script. One can attribute  
 4564 the observed phase error at this position to imperfections in the antenna pattern of the  
 4565 SYNCA. As the SYNCA is moved away from  $R = 0$  mm one observes that the phase  
 4566 error exhibits oscillations whose frequency increases as a function of the radial position  
 4567 of the SYNCA. These oscillations have the appearance of a diffraction pattern, which  
 4568 is particularly clear for the radii  $\geq 15$  mm, due to the bilateral symmetry of the phase

4569 error peaks around  $180^\circ$ .

4570 One can observe a higher average variance in the phase errors measured for the FSCD  
4571 array compared to the synthetic array. This is best seen by comparing the curves at  
4572  $R \leq 15$  mm where the smooth synthetic array curves are distinct from the relatively  
4573 noisy FSCD array errors. The extra noise in the FSCD array is most likely caused by  
4574 differences in the radiation patterns of the antennas that make up the array as well as  
4575 differences in the transmission lines through the switch network that introduce additional  
4576 phase errors into the measurement. Since the synthetic array measurements use only  
4577 a single antenna, these extra error terms are not present, which explains the relatively  
4578 smoother phase error curves. Despite the extra phase errors in the FSCD array, it is still  
4579 possible to observe a similar phase error oscillation effect as the SYNCA is moved away  
4580 from  $R = 0$  mm.

4581 The diffraction pattern exhibited by the phase error oscillations is more easily observed  
4582 by plotting the phase errors in a two-dimensional map, which is done in Figures 5.32a and  
4583 5.32b. For the synthetic array data ones observes a relatively clear diffraction pattern  
4584 that emerges as the SYNCA is moved radially. The bilateral symmetry of the diffraction  
4585 patterns is due to the bilateral symmetry of the circular synthetic array around the  
4586 translation axis of the SYNCA. A similar pattern is also visible in the FSCD array data,  
4587 although, it is obscured by the additional phase error that results from the multi-channel  
4588 array.

4589 The physical origin of the phase error diffraction pattern is attributed to interference  
4590 effects arising from path-length differences between the individual slots in the FSCD  
4591 antenna and the SYNCA transmitter. Since measurements are being performed in the  
4592 radiative near-field of the FSCD antenna, the path length differences between the slots  
4593 introduces a significant change in the summation of the signals that occurs inside the  
4594 waveguide, which causes the radiation pattern of the antenna to change as a function of  
4595 distance. Therefore, when the SYNCA is positioned off-axis the different path-lengths  
4596 from the SYNCA to each antenna results in different radiation patterns leading to the  
4597 observed diffraction pattern.

4598 This near-field effect is not present in simulations, because in order to simplify the  
4599 calculations it is assumed that the far-field approximation can be applied to the FSCD  
4600 antennas. This means that the radiation pattern and antenna transfer functions are  
4601 independent of the distance between the transmitter and the receiving antenna. In  
4602 principle, the near-field effects can be accounted for with a more detailed simulation of  
4603 the FSCD antennas either in CRESana or Locust, which would result in an additional

4604 term in the beamforming phase model. However, this would increase the computational  
4605 intensity of the simulation software. In the next section I briefly discuss the impact of  
4606 these near-field effects on the measured magnitude of the signals.

4607 **5.4.3.3 Magnitude Analysis**

4608 Exactly as for the signal phase, one can use simulations to construct a model that  
4609 describes the magnitude of the signals received by each channel in the antenna array.  
4610 By examining the results of simulations or by analyzing the Liénard-Wiechert equation  
4611 one can show that radiation pattern from a 90° pitch angle electron in a magnetic field  
4612 is omni-directional. Therefore the relative magnitudes of the signals received by each  
4613 channel will be determined by the free-space power loss, which is proportional to the  
4614 inverse distance between the assumed electron position and the antenna.

4615 A consequence of this is that the signals produced in the array for electrons off the  
4616 central axis will have larger amplitudes for the antennas closer to the electron compared  
4617 to those which are further away. The amplitudes of the signals received by the array  
4618 from an electron located at a series of radial positions are shown in Figure 5.33.

4619 One expects to see a similar trend in the signal magnitudes in both the FSCD and  
4620 synthetic arrays. The normalized signal magnitudes extracted from the full and synthetic  
4621 array setups for a series of radial SYNCA positions are shown in Figure 5.34. The data  
4622 corresponds to a SYNCA axial position of  $z = 0$  mm and at a frequency 25.86 GHz. One  
4623 complication is that the radiation pattern of the SYNCA is not perfectly omni-directional,  
4624 which causes the measured magnitudes at  $R = 0$  mm to diverge from the perfectly flat  
4625 behavior exhibited by electrons.

4626 As the SYNCA is moved off-axis one observes a similar increase in the number of  
4627 magnitude peaks in the synthetic array data that one would expect from a diffraction  
4628 pattern, although this trend is not as stark compared to the phase data. Noticeably,  
4629 there does not appear to be a set of channels with disproportionately larger amplitude at  
4630 large  $R$ , which would be expected based on the trends from CREsana.

4631 Comparing the magnitudes of the synthetic array to the FSCD array in Figure 5.34,  
4632 one observes a similar amount of variability in the magnitudes at  $R = 0$  mm, although  
4633 there is potentially more small scale error in the magnitude curve caused by channel  
4634 differences in the FSCD array. A similar trend is seen in the number of magnitude error  
4635 peaks in the FSCD array data to the synthetic array data, which mirrors the diffraction  
4636 effect observed in the phase data. The diffraction effect can be visualized more clearly  
4637 by plotting a similar two-dimensional map of the magnitudes (see Figure 5.35).

4638        The fact that one observes a similar diffraction pattern in the signal magnitudes  
4639        as a function the SYNCA position reinforces the conclusions from the phase analysis  
4640        that near-field effects are having a significant impact on the radiation pattern of the  
4641        FSCD array. These near-field effects lead to changes in the magnitude and phase of the  
4642        radiation pattern of the FSCD antenna as a function of distance. If left uncorrected these  
4643        errors reduce detection efficiency by causing power loss in the beamforming or matched  
4644        filter reconstruction due to phase mismatch. I explore the impact of these phase and  
4645        magnitude errors on beamforming in the next section.

4646        **5.4.3.4 Beamforming Characterization**

4647        Errors in the signal magnitudes and phases lead to errors in signal reconstruction. For  
4648        example, a matched filter reconstruction requires accurate knowledge of the signals in  
4649        each channel to achieve optimal performance. Uncorrected errors leads to mismatches  
4650        between the template and signal, which reduces detection efficiency and introduces  
4651        uncertainty in the parameter estimation. In this section, I analyze the beamformed signal  
4652        amplitude as a function of the position of the SYNCA to quantify the impact of the  
4653        phase and magnitude errors on signal reconstruction. Because of the imperfections in  
4654        the SYNCA source, it is inappropriate to directly compare the measured beamformed  
4655        signal amplitudes of the FSCD array or synthetic array to simulations. Because such a  
4656        comparison, would not allow one to disentangle losses that occur because of the antenna  
4657        array from those that occur because of the source. Therefore, I focus on comparing  
4658        the measured beamforming results of the FSCD array to the synthetic array, since the  
4659        SYNCA imperfections are common to both setups.

4660        The first method of comparison is to analyze the images generated by applying the  
4661        beamforming reconstruction specified in Section 4.3.1 to the FSCD and synthetic array  
4662        data (see Figure 5.36). The beamforming grid consisting of a square  $121 \times 121$  grid  
4663        spanning a range of -60-mm to 60 mm in the x and y dimensions. The beamforming  
4664        images formed from the synthetic array produces a three-dimensional matrix where each  
4665        grid position contains a summed time series. A single beamforming image is formed from  
4666        this data matrix by taking the mean over the time dimension. In the case of the FSCD  
4667        array, the VNA generates frequency domain data such that each grid position contains a  
4668        summed frequency series produced by the VNA sweep. For this data a single image is  
4669        formed by averaging in the frequency domain.

4670        There is a clear difference between the synthetic and FSCD array beamforming images,  
4671        which is the additional faint beamforming maxima located directly opposite the maxima

4672 corresponding to the SYNCA position. The images in Figure 5.36 were generated with  
4673 data collected at a SYNCA radial position of 15 mm, which agrees well with the observed  
4674 beamforming maximum in both images. The faint beamforming peak is located directly  
4675 opposite of the true beamforming maximum similar to a mirror image. Therefore, the  
4676 origin of this additional feature appears to be reflections between the two sides of the  
4677 circular antenna array that are not present for the synthetic array since only a single  
4678 physical antenna is used.

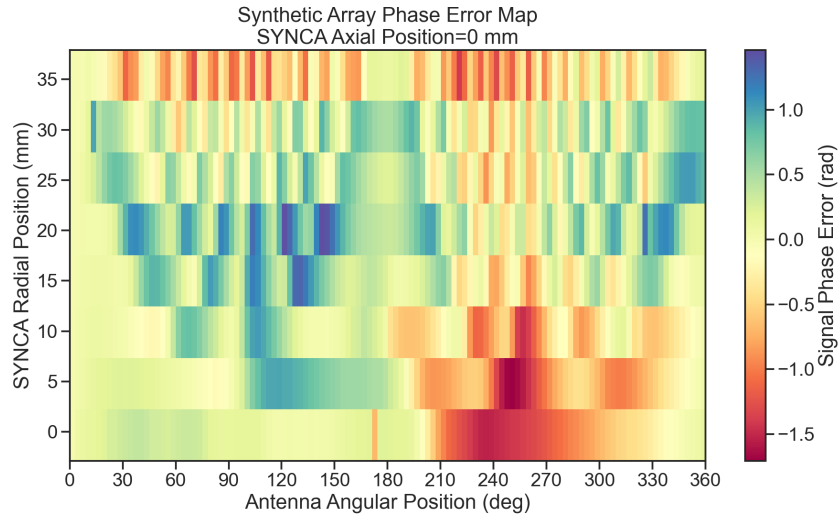
4679 From the beamforming images the maximum amplitude is extracted, which can be  
4680 plotted as a function of the radial position of the SYNCA (see Figure 5.37). The phase  
4681 errors observed in the FSCD and synthetic arrays leads to power loss at the beamforming  
4682 stage due to phase mismatches between the signals at different channels. This power loss  
4683 can be quantified by comparing the signal amplitude obtained from beamforming to the  
4684 amplitude which would be obtained from an ideal summation. The ideal summation is  
4685 performed by phase shifting each array channel to an identical phase and then summing.  
4686 The comparison between the beamforming and ideal sums is shown in Figure 5.37,  
4687 where it is seen that the synthetic and FSCD arrays experience power losses from the  
4688 beamforming summation.

4689 The beamforming power loss can be quantified using the ratio of the beamforming to  
4690 ideal signal amplitudes. Computing this ratio as a function of SYNCA radial position  
4691 radius for the FSCD and synthetic arrays, it is found that the FSCD array has a uniformly  
4692 smaller beamforming amplitude ratio, which means that the FSCD array has a larger  
4693 beamforming power loss (see Figure 5.38). The primary contributions to the beamforming  
4694 power loss in the synthetic array are phase errors from the SYNCA and phase errors  
4695 from the FSCD antenna near-field. Both of these phase errors contribute to beamforming  
4696 losses in the FSCD array, but there are clearly additional phase errors in the FSCD array  
4697 measurements contributing to the smaller ratio. Two potential error sources include phase  
4698 differences in the different antenna channels that could not be corrected by calibration as  
4699 well as reflections between antennas in the array. The total effect of these additional phase  
4700 errors is to reduce the beamforming amplitude ratio by about 5% from the beamforming  
4701 ratio of the synthetic array. Therefore, it is estimated that if no effort is made to correct  
4702 these phase errors in an FSCD-like experiment, then one would expect approximately a  
4703 10% total signal amplitude loss from a beamforming signal reconstruction.

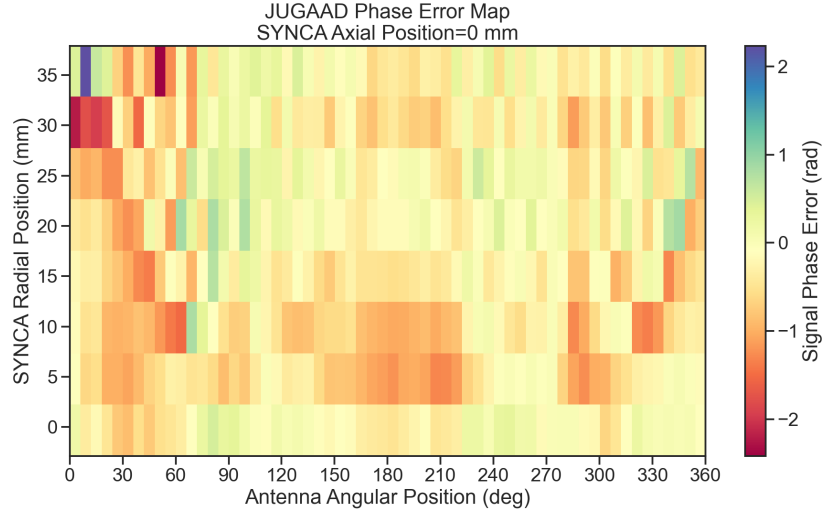
4704 **5.4.4 Conclusions**

4705 The estimated power loss of a beamforming reconstruction obtained from this analysis  
4706 provides valuable inputs to sensitivity calculations of a FSCD-like antenna array exper-  
4707 iment to measure the neutrino mass, since it helps to bound systematic uncertainties  
4708 from the antenna array and reconstruction pipeline. This power loss lowers the estimated  
4709 detection efficiency of the experiment since some of the signal power is lost due to  
4710 improper combining between channels and also increases the uncertainty in the electron's  
4711 kinetic energy by contributing to errors in the estimation of the electron's cyclotron  
4712 frequency.

4713 If these reconstruction losses prove unacceptable there are steps that can be taken  
4714 to mitigate their effects. Some examples include the development of a more accurate  
4715 antenna simulation approach that can reproduce the observed near-field interference  
4716 patterns of the FSCD antennas and the implementation of a calibration approach that  
4717 allows for the relative phase delays of the array to be measured without changing or  
4718 disconnecting the antenna array configuration.



(a)



(b)

**Figure 5.32.** Two dimensional plots of the phase errors for the synthetic array (a) and the FSCD (JUGAAD) array (b). In both plots there is evidence of a similar diffraction pattern with bilateral symmetry, but the FSCD array measurements have an additional phase error contribution from the different antennas and paths through the switch network.

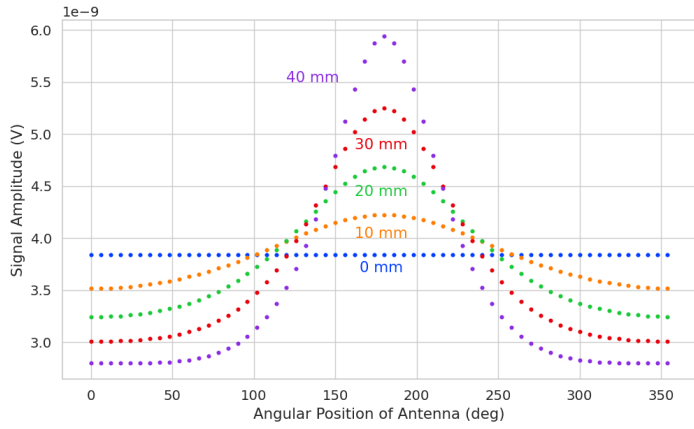


**Figure 5.33.** The amplitude of the signals from CREsana for the FSCD array from a 90° electron. As the electron is moved from  $R = 0$  the signals begin to have unequal amplitudes depending on the distance from the electron to the antenna.

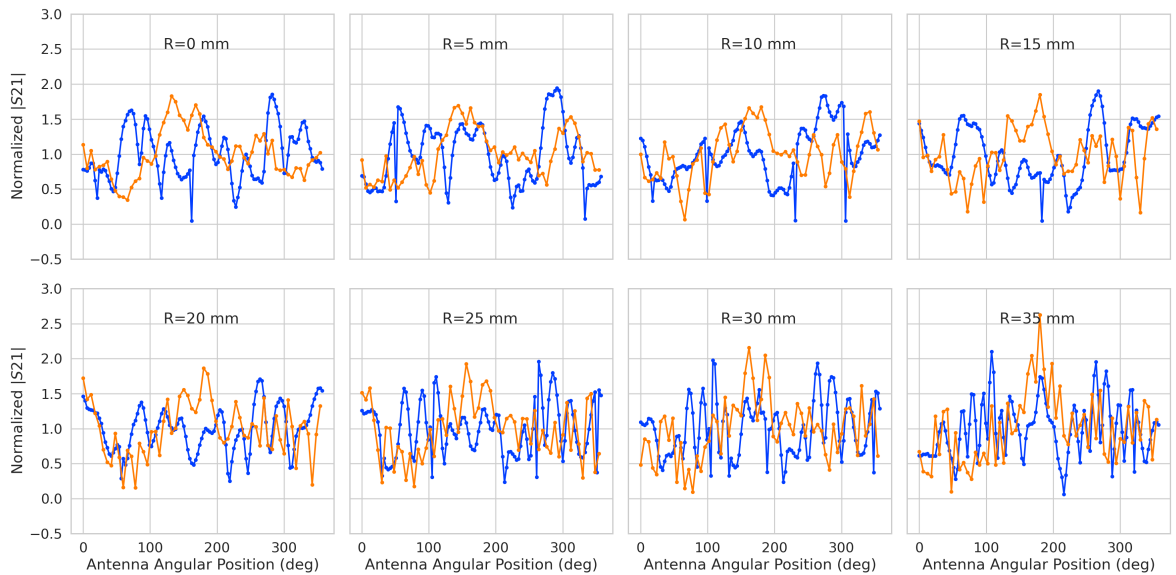
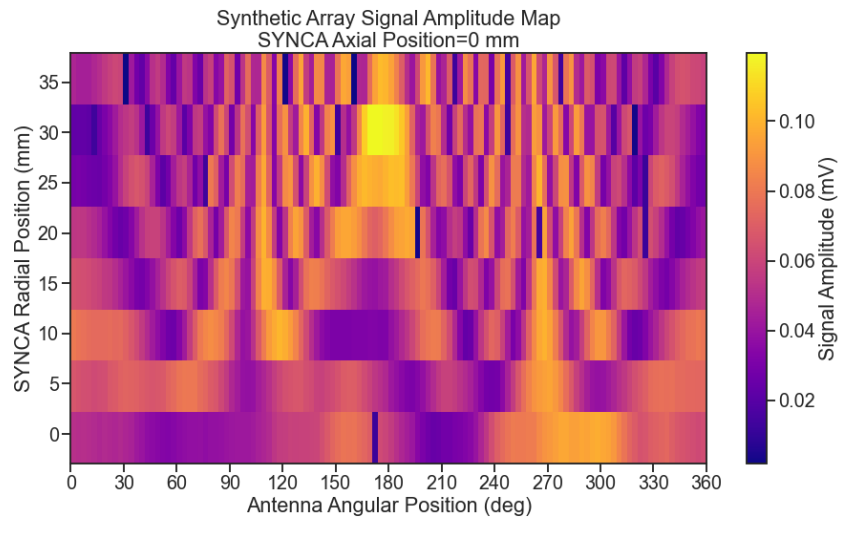
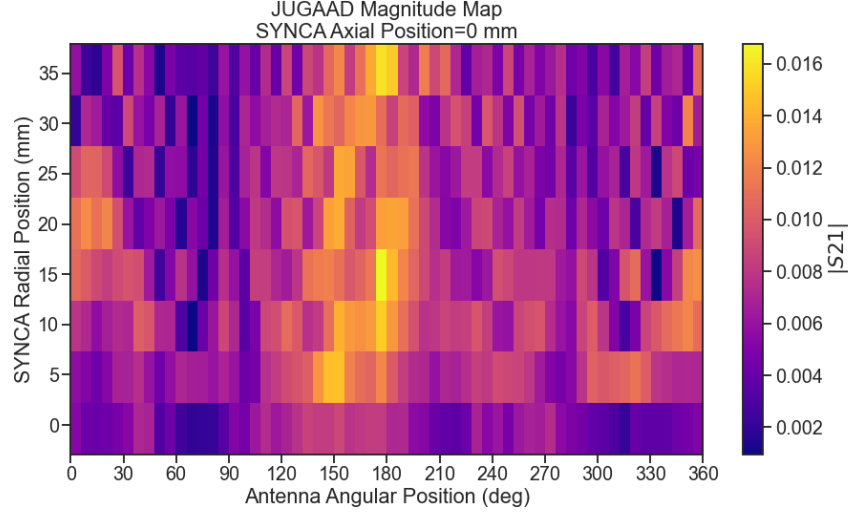


**Figure 5.34.** The normalized magnitudes of the S21 parameters measured in the FSCD (orange) and synthetic array (blue) setups. The dominant observed behavior as a function of radius is the increase in the number of magnitude peaks, which was noted in the phase error curves. There does not appear to be a strong change in the relative amplitude of a group of antennas as predicted by CREsana.



(a)



(b) The two-dimensional maps showing the diffractive pattern exhibited by the FSCD and synthetic array signal magnitudes.

**Figure 5.35.**

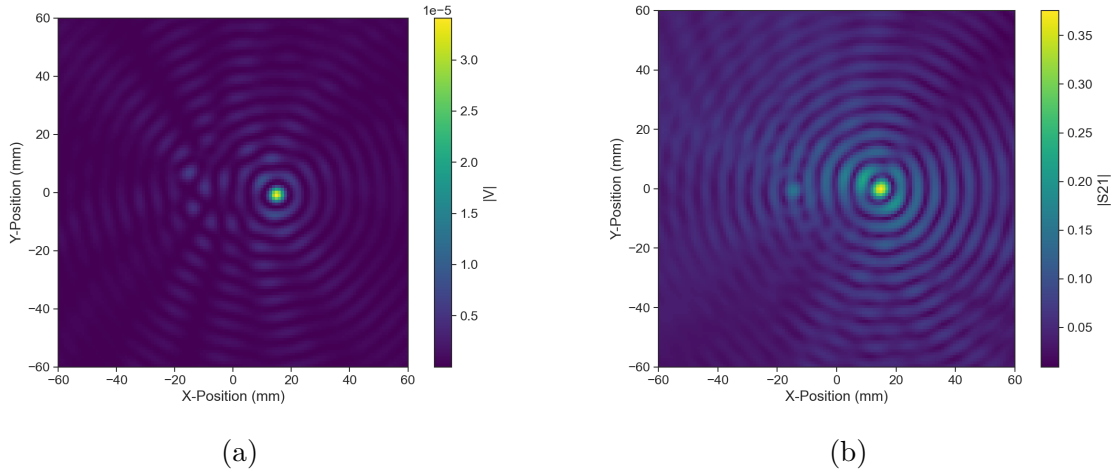


**Figure 5.36.** Beamforming images from the synthetic array (a) and FSCD array (b) setups with the SYNCA positioned 15 mm off the central axis. In both images, there is a clear maxima that corresponds to the true SYNCA position. However, in the FSCD array there is an additional faint peak located at the opposite position of the beamforming maximum. This additional peak is the mirror of the true peak and is the result of reflections between antennas in the FSCD array.

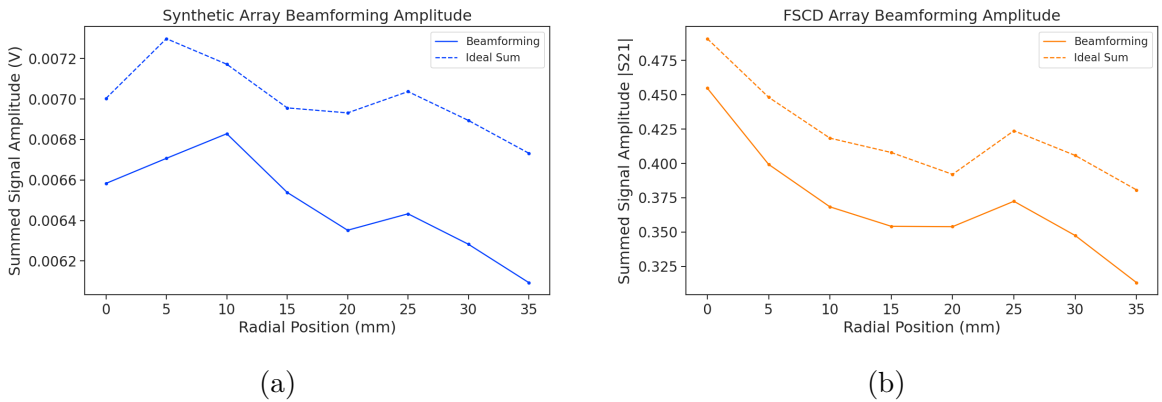


**Figure 5.37.** A comparison of the maximum signal amplitude obtained by beamforming to the signal amplitude obtained with an ideal summation as a function of the radial position of the SYNCA. The amplitudes for the synthetic array are shown in (a) and the FSCD array are shown in (b). In both setups, the signal amplitudes obtained from beamforming are smaller than the signal amplitude that could be attained with the ideal summation without phase mismatch.

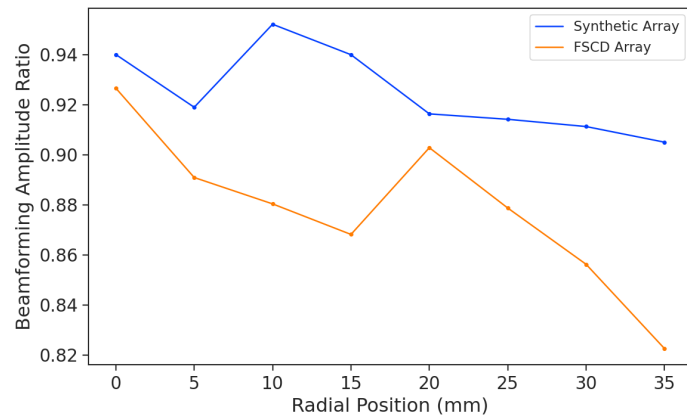


**Figure 5.38.** The ratio of the beamforming signal amplitude to the ideal signal amplitude for the FSCD and synthetic arrays. The FSCD array has a larger power loss from phase error compared to the synthetic array which indicates that calibration errors associated with the multiple channels as well as reflections are impacting the signal reconstruction.

# **Chapter 6**

## **Development of Resonant Cavities for Large Volume CRES Measurements**

### **6.1 Introduction**

The cavity approach was originally an alternative CRES measurement technology under consideration by the Project 8 collaboration for the Phase IV experiment. After pursuing an antenna array based CRES demonstrator design for several years, the increasing costs and complexity of the antenna arrays led to a reconsideration of the baseline technology for the ultimate CRES experiment planned by Project 8. Currently, a cavity based CRES experiment is the preferred technology choice for future experiments by the Project 8 collaboration including the Phase IV experiment.

In this chapter I provide a brief summary of resonant cavities and sketch out the key features of a cavity based CRES experiment. In Section 6.2 I provide a brief introduction to cylindrical resonant cavities and the solutions for the electromagnetic fields in the cavity volume.

In Section 6.3 I describe the main components of a cavity based CRES experiment, including the background and trap magnets, cavity geometry and design, and cavity coupling considerations. I also discuss some relevant trade-offs between an antenna array and cavity CRES experiment, and highlight some reasons for the transition of Project 8 to the development of a cavity based experiment.

Finally, in Sections 6.4 and 6.5, I present the design and development of an open mode-filtered cavity that could be used in a cavity based CRES experiment with atomic tritium. The results of the cavity simulations are confirmed by laboratory measurements of a proof-of-principle prototype that demonstrates key features of the design.

## 6.2 Cylindrical Resonant Cavities

Resonant cavities are sealed conductive containers, which allows one to describe the electromagnetic (EM) fields contained in the cavity volume as a superposition of resonant modes [92]. The field shapes of the resonant modes are determined by Maxwell's equations and the boundary conditions enforced by the cavity geometry. Of interest to Project 8 for CRES measurements are cylindrical cavities due to their ease of construction and integration with atom and electron trapping magnets.

### 6.2.1 General Field Solutions

Consider a long segment of conducting material with a cylindrical cross-section (see Figure 6.1). A geometry such as this can be used as a waveguide transmission line to transfer EM energy from point to point, or, if conducting shorts are inserted on both ends of the cylinder, the waveguide becomes a resonant cavity.

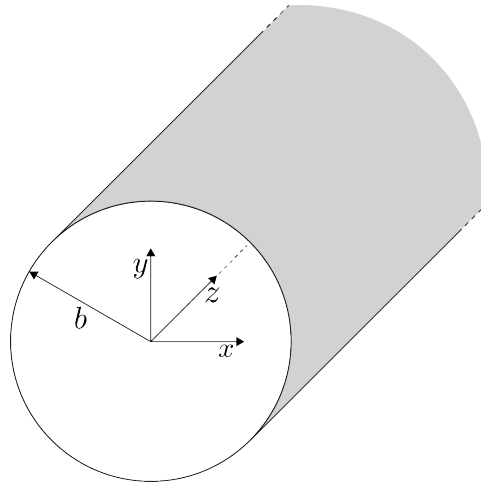


**Figure 6.1.** Geometry of a cylindrical waveguide with radius  $b$ .

The fields allowed inside a cylindrical cavity are determined by the boundary conditions of the cylindrical geometry. The general approach to solving the fields begins by assuming solutions to Maxwell's equations of the form

$$\mathbf{E}(x, y, z) = (\mathbf{e}(x, y) + \hat{z}e_z(x, y))e^{-i\beta z}, \quad (6.1)$$

$$\mathbf{H}(x, y, z) = (\mathbf{h}(x, y) + \hat{z}h_z(x, y))e^{-i\beta z}. \quad (6.2)$$

The solutions assume a harmonic time dependence of the form  $e^{i\omega t}$  and propagation

4759 along the positive z-axis. The functions  $\mathbf{e}(x, y)$  and  $\mathbf{h}(x, y)$  represent the transverse  
4760 ( $\hat{x}, \hat{y}$ ) components of the electric and magnetic fields respectively, and  $e_z(x, y)$ ,  $h_z(x, y)$   
4761 represent the longitudinal components. The version of Maxwell's equations in the case  
4762 where there are no source terms can be written as a pair of coupled differential equations,

$$\nabla \times \mathbf{E} = -i\omega\mu\mathbf{H}, \quad (6.3)$$

$$\nabla \times \mathbf{H} = i\omega\epsilon\mathbf{E}, \quad (6.4)$$

4763 where  $\epsilon$  and  $\mu$  are the permittivity and permeability of the material inside the waveguide  
4764 or cavity. Using the field solutions from Equations 6.1 and 6.2 one can solve for the  
4765 transverse components of the fields in terms of the longitudinal fields. Because cylindrical  
4766 cavities are of interest, it is advantageous to write the field solutions in cylindrical  
4767 coordinates. After performing this transformation, the set of four equations for the  
4768 transverse field components are

$$H_\rho = \frac{i}{k_c^2} \left( \frac{\omega\epsilon}{\rho} \frac{\partial E_z}{\partial\phi} - \beta \frac{\partial H_z}{\partial\rho} \right), \quad (6.5)$$

$$H_\phi = \frac{-i}{k_c^2} \left( \omega\epsilon \frac{\partial E_z}{\partial\rho} + \frac{\beta}{\rho} \frac{\partial H_z}{\partial\phi} \right), \quad (6.6)$$

$$E_\rho = \frac{-i}{k_c^2} \left( \beta \frac{\partial E_z}{\partial\rho} + \frac{\omega\mu}{\rho} \frac{\partial H_z}{\partial\phi} \right), \quad (6.7)$$

$$E_\phi = \frac{i}{k_c^2} \left( \frac{-\beta}{\rho} \frac{\partial E_z}{\partial\phi} + \omega\mu \frac{\partial H_z}{\partial\rho} \right), \quad (6.8)$$

4769 where  $k_c$  is the cutoff wavenumber defined by  $k_c^2 = k^2 - \beta^2$  with  $k = \omega\sqrt{\mu\epsilon}$  being the  
4770 wavenumber of the EM radiation.

4771 This set of equations can be used to solve for a variety of different modes, which can  
4772 be obtained by setting conditions on  $E_z$  and  $H_z$ . For cylindrical cavities two types of  
4773 modes are allowed, which correspond to solutions where  $E_z = 0$  and  $H_z = 0$  respectively.

### 4774 6.2.2 TE and TM Modes

4775 The TE family of modes corresponds to the case where  $E_z = 0$ . This implies that  $H_z$  is  
4776 a solution to the Helmholtz wave equation

$$(\nabla^2 + k^2)H_z = 0. \quad (6.9)$$

4777 For solutions of the form  $H_z(\rho, \phi, z) = h_z(\rho, \phi)e^{-i\beta z}$ , Equation 6.9 can be solved using  
 4778 the standard technique of separation of variables. Rather than reproduce the derivation  
 4779 here I shall simply quote the solutions for the transverse fields [92], which are

$$H_\rho = \frac{-i\beta}{k_{c_{nm}}} (A \sin n\phi + B \cos n\phi) J'_n(k_{c_{nm}}\rho) e^{-i\beta_{nm}z}, \quad (6.10)$$

$$H_\phi = \frac{-i\beta n}{k_{c_{nm}}^2 \rho} (A \cos n\phi - B \sin n\phi) J_n(k_{c_{nm}}\rho) e^{-i\beta_{nm}z}, \quad (6.11)$$

$$E_\rho = \frac{-i\omega\mu n}{k_{c_{nm}}^2 \rho} (A \cos n\phi - B \sin n\phi) J_n(k_{c_{nm}}\rho) e^{-i\beta_{nm}z}, \quad (6.12)$$

$$E_\phi = \frac{i\omega\mu}{k_{c_{nm}}} (A \sin n\phi + B \cos n\phi) J'_n(k_{c_{nm}}\rho) e^{-i\beta_{nm}z}. \quad (6.13)$$

4780 One observes that the solutions have a periodic dependence on  $\phi$ , and radial profiles  
 4781 given by the Bessel functions of the first kind. The integer indices  $n$  and  $m$  arise from  
 4782 continuity conditions on the EM fields in the azimuthal and radial directions. For the  
 4783 TE modes, the indices range from  $n \geq 0$  and  $m \geq 1$ .  $k_{c_{nm}}$  is the cutoff wavenumber for  
 4784 the TE<sub>nm</sub> mode given by

$$k_{c_{nm}} = \frac{p'_{nm}}{b}, \quad (6.14)$$

4785 where  $b$  is the radius of the cavity or waveguide and  $p'_{nm}$  is the  $m$ -th root of the derivative  
 4786 of the  $n$ -th order Bessel function (see Table 6.1).

**Table 6.1.** A table of the values of  $p'_{nm}$ .

$n$	$p'_{n1}$	$p'_{n2}$	$p'_{n3}$
0	3.832	7.016	10.174
1	1.841	5.331	8.536
2	3.054	6.706	9.970

4787 The TM mode family corresponds to the case where  $H_z = 0$ , and  $(\nabla^2 + k^2)E_z = 0$ .  
 4788 Again, solutions are assumed of the form  $E_z(\rho, \phi, z) = e_z(\rho, \phi)e^{-i\beta z}$ , for which the general  
 4789 form of the solutions is the same as for the TE modes. However, the different boundary  
 4790 conditions for the TM modes results in particular solutions with a different form, which I  
 4791 shall quote here without derivation. The transverse fields of the TM modes are given by

$$H_\rho = \frac{-i\omega\epsilon n}{k_{c_{nm}}^2 \rho} (A \cos n\phi - B \sin n\phi) J_n(k_{c_{nm}}\rho) e^{-i\beta_{nm}z}, \quad (6.15)$$

$$H_\phi = \frac{-i\omega\epsilon}{k_{c_{nm}}} (A \sin n\phi + B \cos n\phi) J'_n(k_{c_{nm}}\rho) e^{-i\beta_{nm}z} \quad (6.16)$$

$$E_\rho = \frac{-i\beta}{k_{c_{nm}}} (A \sin n\phi + B \cos n\phi) J'_n(k_{c_{nm}}\rho) e^{-i\beta_{nm}z}, \quad (6.17)$$

$$E_\phi = \frac{-i\beta n}{k_{c_{nm}}^2 \rho} (A \cos n\phi - B \sin n\phi) J_n(k_{c_{nm}}\rho) e^{-i\beta_{nm}z}, \quad (6.18)$$

<sup>4792</sup> which one may notice are the same solutions as the TE modes with  $H$  and  $E$  flipped.

<sup>4793</sup> The cutoff wavenumber for the TM modes is given by,  $k_{c_{nm}} = p_{nm}/b$ , where the values of

<sup>4794</sup>  $p_{nm}$  correspond to the  $m$ -th zero of the  $n$ -th order Bessel function (see Table 6.2).

**Table 6.2.** A table of the values of  $p_{nm}$ .

$n$	$p_{n1}$	$p_{n2}$	$p_{n3}$
0	2.405	5.520	8.654
1	3.832	7.016	10.174
2	5.135	8.417	11.620

### <sup>4795</sup> 6.2.3 Resonant Frequencies of a Cylindrical Cavity

<sup>4796</sup> A cylindrical cavity is constructed by taking a section of cylindrical waveguide and

<sup>4797</sup> shorting both ends with conductive material. This means that the electric fields inside a

<sup>4798</sup> cylindrical cavity are exactly those derived in Section 6.2.2 with the additional condition that the electric fields must go to zero at  $z = 0$  and  $z = L$  (see Figure 6.2).

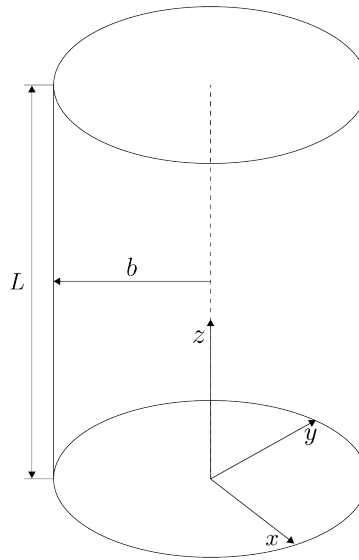


**Figure 6.2.** The geometry of a cylindrical cavity with length  $L$  and radius  $b$ .

<sup>4799</sup>

4800 The transverse electric field solutions for a cylindrical waveguide are of the form

$$\mathbf{E}(\rho, \phi, z) = \mathbf{e}(\rho, \phi) (A_+ e^{-i\beta_{nm}z} + A_- e^{i\beta_{nm}z}), \quad (6.19)$$

4801 where  $A_+$  and  $A_-$  are arbitrary amplitudes of forward and backward propagating waves.

4802 In order to enforce that  $\mathbf{E}$  is zero at both ends of the cavity it is required that

$$\beta_{nm}L = 2\pi\ell, \quad (6.20)$$

4803 where  $\ell = 0, 1, 2, 3, \dots$ . Using this constraint on the propagation constant one can solve

4804 for the resonant frequencies of the  $\text{TE}_{nml}$  and the  $\text{TM}_{nml}$  modes in a cylindrical cavity.

4805 For the TE modes the resonant frequencies are

$$f_{nml} = \frac{c}{2\pi\sqrt{\mu_r\epsilon_r}} \sqrt{\left(\frac{p'_{nm}}{b}\right)^2 + \left(\frac{\ell\pi}{L}\right)^2}, \quad (6.21)$$

4806 and the frequencies of the TM modes are

$$f_{nml} = \frac{c}{2\pi\sqrt{\mu_r\epsilon_r}} \sqrt{\left(\frac{p_{nm}}{b}\right)^2 + \left(\frac{\ell\pi}{L}\right)^2}. \quad (6.22)$$

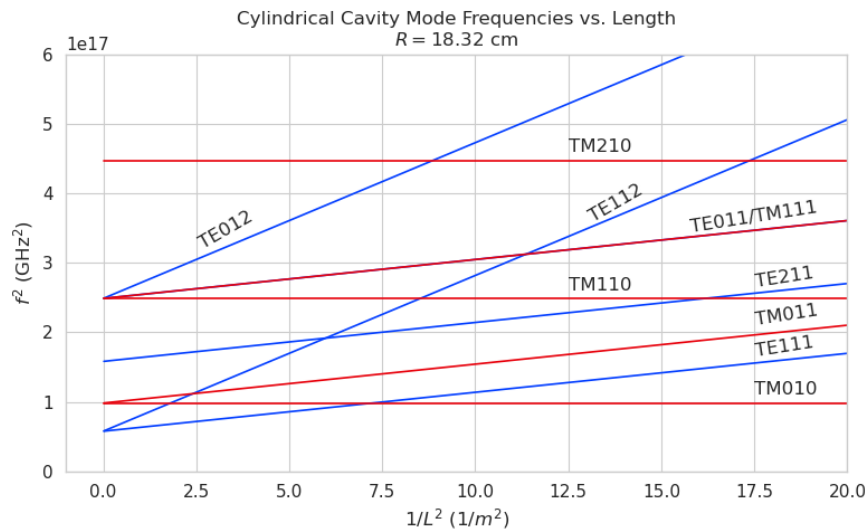


**Figure 6.3.** Relation of mode frequency to cavity length for a cylindrical cavity with a radius of 18.32 cm.

## 4807 6.2.4 Cavity Q-factors

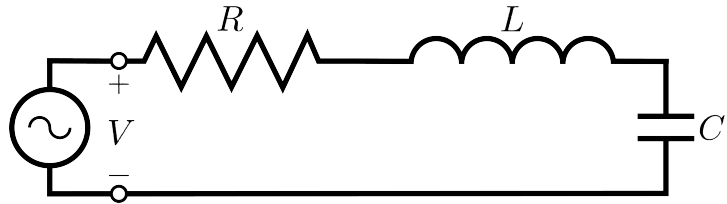


**Figure 6.4.** A series RLC circuit.

4808 The resonant behavior of cylindrical cavities can be modeled as a series RLC circuit  
 4809 (see figure 6.4). The input impedance of the circuit can be obtained by applying  
 4810 Kirchhoff's laws to calculate the impedance of the equivalent circuit. For a series RLC  
 4811 circuit the input impedance is

$$Z_{\text{in}} = \left( \frac{1}{R} + \frac{1}{i\omega L} + i\omega C \right). \quad (6.23)$$

4812 The resistance in the circuit represents all sources of loss in the cavity, which is primarily  
 4813 caused by the finite conductivity of the cavity walls. The inductor and capacitor represent  
 4814 the energy stored in the cavity in the form of electric and magnetic fields. If the circuit  
 4815 is being driven by an external power source the input power can be written in terms of  
 4816 the circuit input impedance and the source voltage

$$P_{\text{in}} = \frac{1}{2} Z_{\text{in}} |I|^2 = \frac{1}{2} |I|^2 \left( \frac{1}{R} + \frac{1}{i\omega L} + i\omega C \right). \quad (6.24)$$

4817 The resistor introduces a loss into the system with a power given by

$$P_{\text{loss}} = \frac{1}{2} |I|^2 R, \quad (6.25)$$

4818 and the capacitor and inductor store energies given by

$$W_e = \frac{1}{4} \frac{|I|^2}{\omega^2 C}, \quad (6.26)$$

$$W_m = \frac{1}{4} |I|^2 L, \quad (6.27)$$

4819 respectively. Using these expressions the input power and input impedance can be written

4820 in terms of the lost power and stored energy

$$P_{\text{in}} = P_{\text{loss}} + 2i\omega(W_m - W_e), \quad (6.28)$$

$$Z_{\text{in}} = \frac{P_{\text{loss}} + 2i\omega(W_m - W_e)}{\frac{1}{2}|I|^2}. \quad (6.29)$$

4821 The condition for resonance in the RLC circuit is that the stored magnetic energy  
 4822 is equal to the stored electric energy ( $W_e = W_m$ ). When this occurs  $Z_{\text{in}} = R$ , which is a  
 4823 purely real impedance, and  $P_{\text{in}} = P_{\text{loss}}$ . The resonant frequency of the circuit can be  
 4824 determined from the condition  $W_e = W_m$  from which one finds that

$$\omega_0 = \frac{1}{\sqrt{LC}}. \quad (6.30)$$

4825 An important performance parameter for any resonant system is the Q-factor, which  
 4826 quantifies the quality of the resonator as the ratio of the stored energy multiplied by the  
 4827 resonant frequency to the average energy lost per second. For the series RLC circuit, the  
 4828 Q-factor is given by the expression

$$Q_0 = \omega \frac{W_e + W_m}{P_{\text{loss}}} = \frac{1}{\omega_0 RC}, \quad (6.31)$$

4829 from which one observes that as the resistance of the RLC circuit is decreased the quality  
 4830 factor of the resonator increases. From the perspective of cylindrical cavities this implies  
 4831 that as one decreases the resistance of the cavity walls it is expected that the Q-factor of  
 4832 the cavity should increase, which is indeed the case. In certain applications where a high  
 4833 Q is desireable it is possible to manufacture a cavity out of superconducting materials in  
 4834 order to minimize the power losses of the system.

4835 The Q-factor of the resonator also determines with bandwidth (BW) of the system. A  
 4836 cavity with a high Q-factor will resonant with a smaller range of frequencies than a cavity  
 4837 with a low Q-factor. To see this examine the behavior of the RLC circuit when driven by  
 4838 frequencies near the resonance. For a frequency  $\omega = \omega_0 + \Delta\omega$ , where  $\Delta\omega = \omega - \omega_0 \ll \omega_0$ ,  
 4839 the input impedance can be written as

$$Z_{\text{in}} = R + i\omega L \left( \frac{\omega^2 - \omega_0^2}{\omega^2} \right), \quad (6.32)$$

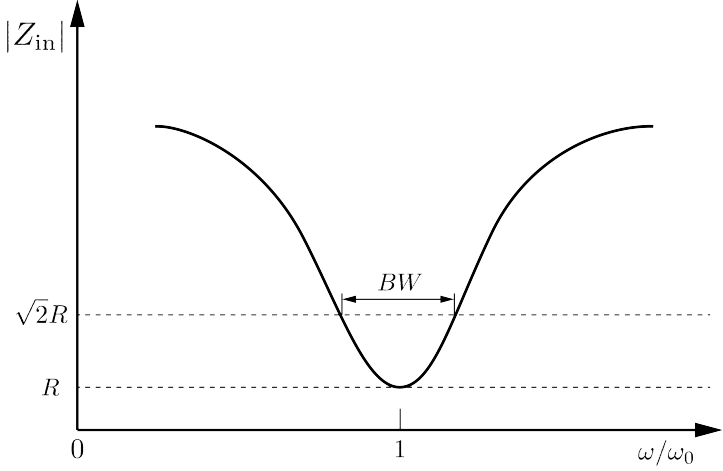


**Figure 6.5.** Illustration of the behavior of the input impedance of the series RLC circuit as a function of the driving frequency. The BW is proportion to the width of the resonance, which is inversely proportional to Q.

4840 and by expanding  $(\omega^2 - \omega_0^2)/\omega^2$  to first order in  $\Delta\omega$ , one obtains

$$Z_{in} \approx R + i \frac{2RQ_0\Delta\omega}{\omega_0}. \quad (6.33)$$

4841 Therefore, the magnitude of the input impedance near the resonance is given by

$$|Z_{in}| = R \sqrt{1 + 4Q_0^2 \frac{\Delta\omega^2}{\omega^2}}, \quad (6.34)$$

4842 from which it is seen that for the series RLC circuit the input impedance is minimized  
 4843 at the resonant frequency, which corresponds to the maximum input power (see Figure  
 4844 6.5). The half-power BW is the range of frequencies over which the input power drops to  
 4845 half the input power on resonance. This occurs when  $|Z_{in}| = \sqrt{2}R$ , which corresponds to  
 4846  $\Delta\omega/\omega = BW/2$ . Using Equation 6.34 one can find that

$$2R^2 = R^2(1 + Q_0^2BW^2), \quad (6.35)$$

4847 which implies

$$BW = \frac{1}{Q_0} \quad (6.36)$$

4848 It is important to emphasize that the Q-factor defined here,  $Q_0$ , is technically the  
 4849 unloaded Q. It reflects the quality of the cavity or resonant circuit without the influence  
 4850 of any external circuitry. In practice, however, a cavity is invariably coupled to an

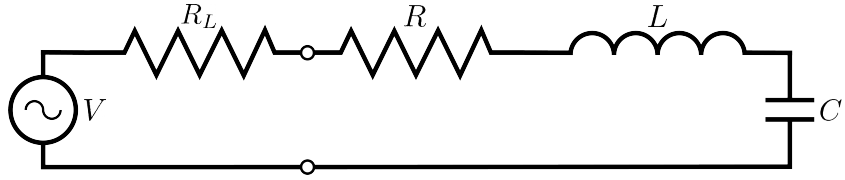


**Figure 6.6.** A series RLC circuit coupled to an external circuit with input impedance  $R_L$ .

4851 external circuit to drive a cavity resonance or to measure the energy of a resonant mode.  
 4852 Coupling a cavity to an external circuit changes the Q by loading the equivalent cavity  
 4853 RLC circuit (see Figure 6.6). The Q-factor of the cavity when it is loaded by an external  
 4854 circuit is called the loaded Q, which is the quantity that one actually measures when  
 4855 exciting a resonance in the cavity. Using the series RLC circuit model one can see that  
 4856 the load resistor in Figure 6.6 will add in series with the resistor in the circuit for a total  
 4857 equivalent resistance of  $R + R_L$ . Therefore, the loaded Q is given by

$$Q_L = \frac{1}{\omega_0(R + R_L)C}, \quad (6.37)$$

4858 from which one observes that the loaded Q is always less than the intrinsic Q of the  
 4859 cavity.

4860 The amount of coupling that is desireable depends on the specific application of  
 4861 the resonator. If one wants a resonator that is particular frequency selective then it  
 4862 makes sense to limit the amount of coupling to the cavity to maintain a small BW,  
 4863 alternatively, if a larger BW is need one can increase the cavity coupling by tuning the  
 4864 input impedance of the external circuit. The critical point, where maximum power is  
 4865 transferred between the cavity and the external circuit, occurs when the input impedance  
 4866 of the cavity matches the input impedance of the external transmission line. For the  
 4867 series RLC circuit on resonance, this matching condition corresponds to

$$Z_0 = Z_{in} = R, \quad (6.38)$$

4868 where  $Z_0$  is the impedance of the transmission line. The loaded Q at this critical point  
 4869 is, therefore,

$$Q_L = \frac{1}{2\omega_0 Z_0 C} = \frac{Q_0}{2}. \quad (6.39)$$

4870 One can describe the degree of coupling between the cavity and an external circuit by

<sup>4871</sup> defining a coupling factor,  $g$ , such that,

$$g = \frac{Q_0}{Q_L} - 1. \quad (6.40)$$

<sup>4872</sup> When  $g = 1$  then  $Q_L = Q_0/2$ , and the cavity is said to be critically coupled. If  
<sup>4873</sup>  $Q_L < Q_0/2$ , then the cavity is undercoupled to the transmission line, corresponding to  
<sup>4874</sup>  $g < 1$ . Alternatively, if  $Q_L > Q_0/2$ , then  $g > 1$ , and the cavity is overcoupled to the  
<sup>4875</sup> transmission line. Various specialized circuits can be used to tune the input impedance  
<sup>4876</sup> of the external circuit as seen by the cavity to achieve a wide range of different coupling  
<sup>4877</sup> factors based on the desired application of the cavity.

## <sup>4878</sup> 6.3 The Cavity Approach to CRES

### <sup>4879</sup> 6.3.1 A Sketch of a Molecular Tritium Cavity CRES Experiment

<sup>4880</sup> Resonant cavities can be used to perform CRES measurements, and they represent the  
<sup>4881</sup> current preferred technology by the Project 8 collaboration. The basic approach to a  
<sup>4882</sup> neutrino mass measurement using a resonant cavity and molecular tritium beta-decay  
source is illustrated by Figure 6.7.

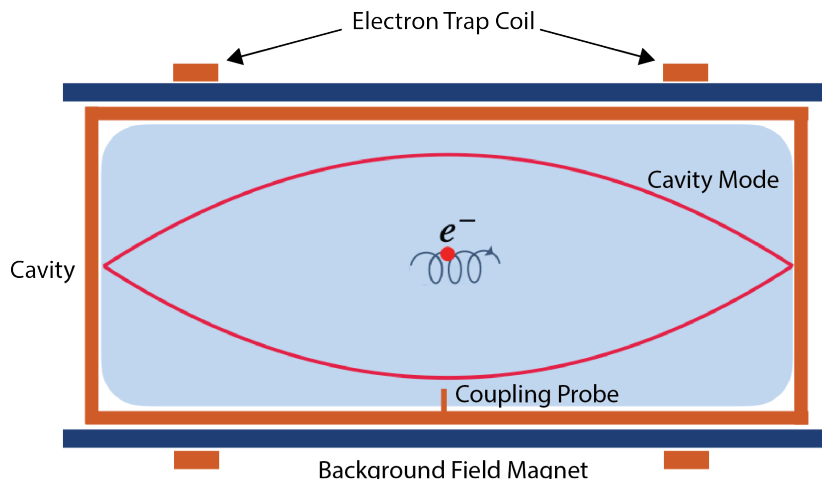


**Figure 6.7.** A cartoon depiction of a cavity CRES experiment. A metallic cavity filled with tritium gas is inserted into a uniform background magnetic field to perform CRES measurements. Electrons from beta-decays inside the cavity can be trapped and used to excite a resonant mode(s). By coupling to the cavity mode with a suitable probe one can measure the cyclotron frequency of the electron and perform CRES.

<sup>4883</sup>

4884 At the core of the experiment is a large resonant cavity filled with tritium gas. The  
4885 filled cavity is then placed in a uniform magnetic field provided by a primary magnet,  
4886 which provides the background magnetic field. The value of the background magnetic field  
4887 sets the range of cyclotron frequencies for electrons emitted near the tritium spectrum  
4888 endpoint. When a beta-decay electron is produced in the cavity it is trapped using a set  
4889 of magnetic pinch coils that keep electrons inside the cavity volume.

4890 Electrons trapped inside the cavity do not radiate in the same way as electrons  
4891 in free-space. Effectively, the same boundary conditions that were used to derive the  
4892 resonant modes of a cylindrical cavity in Section 6.2 apply to the radiation of the electron  
4893 as well. The coupling of an electron performing cyclotron motion in a cavity has been  
4894 studied in detail for measurements of the electron’s magnetic moment [101–103]. If an  
4895 electron is emitted with a kinetic energy that corresponds to a cyclotron frequency that  
4896 matches a resonant frequency of the cavity, then energy radiated by the electron excites  
4897 a corresponding resonance in the cavity. The strength of the electron’s coupling to the  
4898 cavity is given to first order by the dot product between the electrons trajectory and  
4899 the electric field vector of the resonant mode. Additional effects, such as the Purcell  
4900 enhancement [104], alter the emitted power from the free-space Larmor equation [50]. If  
4901 an electron is moving with a cyclotron frequency that is far from any resonant modes  
4902 in the cavity, then radiation from the electron is suppressed. One can interpret this  
4903 somewhat surprising effect as the metallic walls of the cavity reflecting the radiated  
4904 energy back to the electron.

4905 Detecting an electron in the cavity is accomplished by coupling the cavity to an  
4906 external transmission line that leads to an amplifier and RF receiver chain [105]. The  
4907 coupling of the cavity resonance to the amplifier occurs through a coupling probe or  
4908 aperture designed to read out the excitation of the mode(s) excited by the electron. For  
4909 CRES measurements, the placement of a wire antenna coupling probe inside the cavity  
4910 volume leads to unacceptable losses of tritium atoms due to recombination to molecular  
4911 tritium on the antenna surface, therefore, apertures are the preferred coupling method  
4912 for cavity CRES experiments.

4913 One of the attractive features of the CRES technique for neutrino mass measurement  
4914 is the gain in statistics that comes from the differential nature of the tritium spectrum  
4915 measurement. Initially, this seems incompatible with cavities, due to the narrow reso-  
4916 nances of cavity modes giving relatively small bandwidth. However, by intentionally  
4917 over-coupling to a single cavity mode one can achieve bandwidths of a few 10’s of MHz  
4918 (see Section 6.2), which is sufficient for a measurement of the tritium spectrum endpoint

4919 region.

### 4920 **6.3.2 Magnetic Field, Cavity Geometry, and Resonant Modes**

#### 4921 **Magnetic Field and Volume Scaling**

4922 For a CRES experiment, cylindrical cavities are a natural choice since they match  
4923 the geometry of standard solenoid magnets, which are needed in order to produce the  
4924 background magnetic field for CRES measurements. Furthermore, the cylindrical shape is  
4925 compatible with a Halbach array, which is the leading choice of atom trapping technology  
4926 for future atomic tritium experiments by the Project 8 collaboration. Cylindrical cavities  
4927 also benefit from well-established machining practices that are able to achieve high  
4928 geometric precision at large lengths. More exotic cavity designs are under-consideration  
4929 and there are ongoing efforts to investigate the potential advantages these may have over  
4930 the standard cylindrical geometry.

4931 As shown in Section 6.2, the physical dimensions of the cavity are directly coupled to  
4932 the resonant frequencies of the cavity. This dependency links the size of the cavity to  
4933 the magnitude of the background magnetic field, because the magnetic field determines  
4934 the cyclotron frequencies of trapped electrons. Specifically, as the size of the cavity is  
4935 increased to accommodate larger volumes of tritium gas, the frequencies of the resonant  
4936 modes decrease proportionally. This requires that the magnetic field also decrease in  
4937 order to maintain coupling between electrons and the desired cavity mode.

4938 The required cavity size is ultimately determined by the required statistics in the  
4939 tritium spectrum endpoint region. Because the gas density must be kept below a certain  
4940 level to ensure that electrons have sufficient time to radiate before scattering, larger  
4941 volumes become the only way to achieve higher event statistics. To achieve the sensitivity  
4942 goals of Phase III and IV cavity volumes on the order of several cubic-meters are required,  
4943 which pushes one towards frequencies in the range of 100's of MHz.

#### 4944 **Single-mode Cavity CRES**

4945 It is tempting to consider maintaining a high magnetic field, while still increasing the size  
4946 of the cavity, in order to increase the radiated power from trapped electrons for better  
4947 SNR. However, if one were to maintain the same magnetic field while increasing the  
4948 size of the cavity, the electrons would begin to couple to higher order modes with more  
4949 complicated transverse geometries. The danger with this approach is that a complicated  
4950 mode structure could introduce systematic errors into the CRES signals. Example

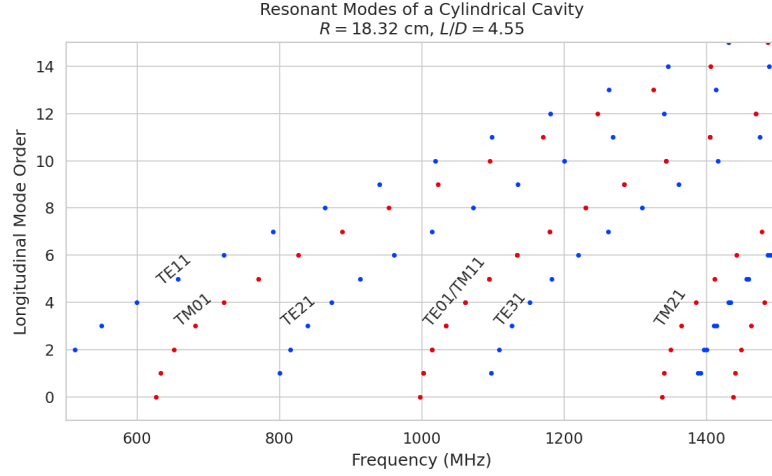
4951 systematics include unpredicted mode hybridization or changes in the mode shapes from  
4952 imperfections in the cavity construction, which would prevent reconstruction of the  
4953 electron's starting kinetic energies with adequate resolution. For this reason, it is ideal  
4954 to operate with magnetic fields that give cyclotron frequencies near the fundamental  
4955 frequency of the cavity, where the mode structure is relatively simple (see Figure 6.8).  
4956 In this frequency region it is possible to perform CRES by coupling to only a single  
4957 resonant mode; however, it is currently an open question if a single mode measurement  
4958 will provide enough information about an individual electron's position to reconstruct  
4959 the full event. Regardless, developing a solid understanding of the CRES phenomenology  
4960 when an electron is coupling to a single mode will be a necessary step towards a future  
4961 multimode cavity experiment.

## 4962 Considerations for Resonant Mode Selection

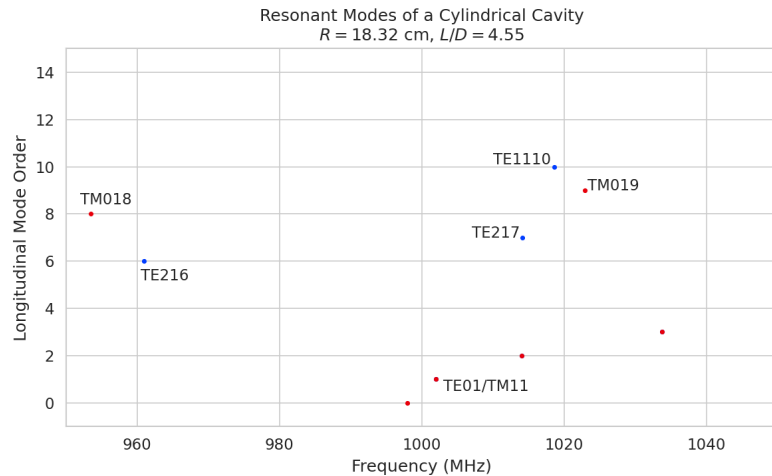
4963 A single-mode cavity experiment begs the question, which resonant mode is best for  
4964 CRES measurements? There is an immediate bias towards low order  $TE_{nm}$  and  $TM_{nm}$   
4965 modes due to the multimode considerations discussed above. Additionally, there is a  
4966 preference towards modes with longitudinal index  $\ell = 1$  with a single antinode along the  
4967 vertical axis of the cylindrical cavity. The reason for this is that there is a phase change  
4968 in the electric fields between antinodes that leads to modulation effects that destroy the  
4969 carrier frequency signal information.

4970 A second consideration for mode selection is the volumetric efficiency of the mode.  
4971 Volumetric efficiency can be thought of as an integral over the volume of the cavity  
4972 weighted by the relative amplitude of the mode. From the perspective of simply maximiz-  
4973 ing the volume useable for CRES measurements, this integral would be as close to unity  
4974 as possible. However, there is a requirement to reconstruct the position of the electrons  
4975 inside the cavity volume so that the local magnetic fields can be used to convert the  
4976 measured cyclotron frequency to a kinetic energy. With a single mode this necessarily  
4977 requires a variable transverse mode amplitude, which lowers the volumetric efficiency, so  
4978 that position of the electron in the cavity can be estimated from the average amplitude  
4979 of the CRES signal. Longitudinal indices of  $\ell = 1$  have an advantage in volumetric  
4980 efficiency over higher order  $\ell$  modes, since there are only two longitudinal nodes, one at  
4981 each end of the cavity. Therefore, the average coupling strength of trapped electrons as  
4982 they oscillate axially is higher for  $\ell = 1$  modes.

4983 An additional factor for mode selection is the intrinsic or unloaded Q of the mode.  
4984 In terms of SNR it is advantageous to use a mode with a very high  $Q_0$ , which is then



(a)



(b)

**Figure 6.8.** Examples of the resonant mode frequencies of a cylindrical cavity. This cavity has a radius of 18.32 cm and a length to diameter ratio of 4.55. Several families of resonant modes are relevant in the  $\approx 800$  MHz bandwidth of (a); however, after zooming in to a  $\sim 80$  MHz bandwidth centered on TE011 one sees that only a handful of resonant modes have frequencies close to TE011. Since the bandwidth required for a cavity CRES experiment is  $O(10)$ 's MHz, a significant number of resonant modes can be safely ignored since their resonant frequencies are far from the CRES bandwidth.

highly overcoupled to achieve the necessary bandwidth to cover the tritium endpoint spectrum. A high intrinsic Q ( $Q_0$ ) combined with a small loaded Q ( $Q_L$ ) requires a large cavity coupling factor ( $g$ , see Equation 6.40). Because of the impedance mismatch associated with large coupling factors, the noise power contributed by the physical cavity temperature is reduced by a factor proportional to  $1/g$ , which allows one to achieve

4990 adequate SNR without the requirement of cooling the entire cavity to single Kelvin  
4991 temperatures.

4992 An example of a resonant mode that exhibits these traits is the TE<sub>011</sub> mode. At present  
4993 the TE<sub>011</sub> mode is the preferred resonance for a single-mode cavity CRES experiment  
4994 by the Project 8 collaboration. TE<sub>011</sub> is a low order mode located in a region relatively  
4995 far from other cavity modes. Furthermore, the separation of the TE<sub>011</sub> mode can be  
4996 improved by various mode-filtering techniques discussed in Section 6.4.2 below. TE<sub>011</sub>  
4997 consists of a single longitudinal antinode that can provide pitch angle information in the  
4998 form of amplitude modulation, and has an electric field with a radial profile given by the  
4999  $J'_0$  Bessel function allowing for radial position estimation. Lastly, the TE<sub>011</sub> mode has a  
5000 relatively high intrinsic Q compared to nearby modes, which helps with SNR. Unloaded  
5001 Q's greater than 80000 are achievable for a 1 GHz TE<sub>011</sub> resonance using a copper walled  
5002 cavity.

### 5003 **6.3.3 Trade-offs Between the Antenna and Cavity Approaches**

5004 The choice between cavities and antennas for large-scale CRES measurements is not  
5005 without trade-offs. Both the antenna array and cavity approaches are relatively immature  
5006 techniques, and at present there are no known obstacles that would prevent either  
5007 approach from being used for a large scale neutrino mass experiment. The preference for  
5008 cavities is largely driven by important practical considerations that could make a cavity  
5009 based experiment significantly cheaper than an antenna experiment of similar size and  
5010 scope. However, the switch to cavities also introduces new challenges less relevant to the  
5011 antenna array, which must be solved in order for Project 8 to achieve its neutrino mass  
5012 measurement goals.

5013 One of the major relative drawbacks of the antenna array approach is the size and  
5014 complexity of the data-acquisition system. A large-scale antenna array experiment  
5015 requires  $O(100)$  antennas independently digitized at rates of  $O(10)$  to  $O(100)$  MHz. Since  
5016 there is insufficient information in a single antenna channel to detect or reconstruct the  
5017 CRES signal, the entire array output must be processed during the signal reconstruction.  
5018 Because data storage becomes an issue with these data volumes, there is a real-time  
5019 signal reconstruction requirement that allows one to detect CRES signals buried in the  
5020 thermal noise. As discussed in Section 4.4, the computational cost of these real-time  
5021 detection algorithms are potentially quite large for even a small scale antenna array  
5022 experiment. However, the operating principle of a cavity experiment allows the CRES  
5023 signal to be detected using only a single read-out channel digitized at rates of  $O(10)$  MHz,

5024 which reduces the cost of the data acquisition system by many orders of magnitude.

5025 From an engineering perspective, the simple geometry and thin-walls of a cylindrical  
5026 cavity are simpler to interface with the cryogenic and magnetic subsystems needed  
5027 for a CRES experiment. Conversely, the antenna array requires careful design and  
5028 engineering to accommodate the antenna array and receiver electronics in proximity to  
5029 the trapping magnets. Additionally, due to near-field interference effects, the antenna  
5030 array is unable to reconstruct CRES events within the reactive near-field distance of the  
5031 antennas. Because atom trapping requirements require magnetic fields which correspond  
5032 to cyclotron frequencies for endpoint electrons less than 1 GHz, the required stand-off  
5033 distance leads to a significant loss in useable experiment volume, necessitating larger and  
5034 more expensive magnets.

5035 Another advantage to the cavity approach is the relatively compact sideband structure,  
5036 which is a result of the low modulation index for cavity CRES signals. The axial motion  
5037 in an antenna array experiment leads to frequency modulation and sidebands. The shape  
5038 of the sideband structure is determined by the modulation index,  $h = \frac{\Delta f}{f_a}$ , where  $\Delta f$   
5039 is the size of the frequency deviation and  $f_a$  is the axial frequency. The large electron  
5040 traps required for a cubic-meter-scale experiment leads to high modulation indices, which  
5041 causes the signal spectrum to be made up of numerous low power sidebands that make  
5042 reconstruction and detection challenging. This behavior was observed in simulations  
5043 of the FSCD in which carrier power decreased with pitch angle due to the increase in  
5044 modulation index (see Figure 4.30). For cavities, however, the modulation index remains  
5045 near  $h = 1$  even for very long magnetic traps due to the high phase velocity in cavities  
5046 relative to the axial velocity of the electron. This results in an almost ideal spectrum  
5047 shape that has a strong carrier frequency with a few sidebands whose relative amplitudes  
5048 encode pitch angle information.

5049 A downside of the cavity approach is the apparent difficulty of estimating the position  
5050 of the electron using only the coupling of the electron to a single mode. The amplitude of  
5051 the TE<sub>011</sub> mode is completely independent of the azimuthal coordinate, and thus position  
5052 reconstruction using the TE<sub>011</sub> mode is only able to estimate the radial position of the  
5053 electron. This position degeneracy may lead to magnetic field uniformity requirements  
5054 that are too challenging to meet due to mechanical uncertainties in cavity and magnet  
5055 construction, as well as uncertainties caused by nuisance external magnetic fields such  
5056 as the Earth's field and magnetic fields from building materials. A multimode cavity  
5057 experiment may provide a way to extract more precise information on the position of  
5058 the electron by analyzing the coupling of the electron to several modes that overlap in

5059 different ways.

## 5060 **6.4 Single-mode Resonant Cavity Design and Simulations**

5061 The single-mode cylindrical cavities envisioned for the Phase III and IV experiments must  
5062 be carefully engineered in order to measure the neutrino mass with the desired sensitivity.  
5063 In this section I summarize some simulation studies performed to analyze early design  
5064 concepts for a single-mode cavity. The primary tool for these investigations was Ansys  
5065 HFSS, which was also used for the development of the SYNCA antenna described in  
5066 Section 5.3.

### 5067 **6.4.1 Open Cylindrical Cavities with Coaxial Terminations**

#### 5068 **Design Concept**

5069 A basic cavity design question relevant to Project 8's ultimate goal of an atomic tritium  
5070 CRES experiment is how to build a cavity that can be efficiently filled with atomic  
5071 tritium. To keep the rate of atom loss from recombination on surfaces low, it is ideal if  
5072 the ends of the cylindrical cavity are as open as possible so that tritium atoms can flow  
5073 inside unimpeded. Additionally, one of the primary calibration techniques planned for  
5074 future CRES experiments involves CRES measurements using electrons injected from  
5075 an electron gun source, which also requires an opening at the cavity end. Cylindrical  
5076 cavities with open ends can be manufactured, however, the intrinsic Q-factors of these  
5077 cavities are orders of magnitude less than their sealed counterparts, which reduces the  
5078 signal-to-noise ratio when that cavity is used for CRES measurement.

5079 Cylindrical cavities with mostly open ends that also exhibit Q values for the  $TE_{01\ell}$   
5080 modes similar to sealed cavities can be built by using coaxial endcaps to terminate the  
5081 cavity. Cavities of this type have been manufactured for specialized applications related  
5082 to the measurements of the dielectric constants of liquefied gasses (see Figure 6.9) [3, 4].  
5083 This cavity design leaves the ends of the cavity wide open, but retains high Q-values for  
5084 the  $TE_{01\ell}$  modes due to the coaxial endcap, which are designed to perfectly reflect the  
5085 electric fields of  $TE_{01\ell}$  modes. Coupling to the  $TE_{01\ell}$  mode is achieved via an aperture  
5086 located at the center of the cavity wall.

5087 A cavity similar to Figure 6.9 is a candidate design for the future CRES experiments  
5088 by Project 8, since it appears to elegantly solve many practical issues that arise when  
5089 combining cavity CRES and atomic tritium. The coaxial endcaps leave significant regions

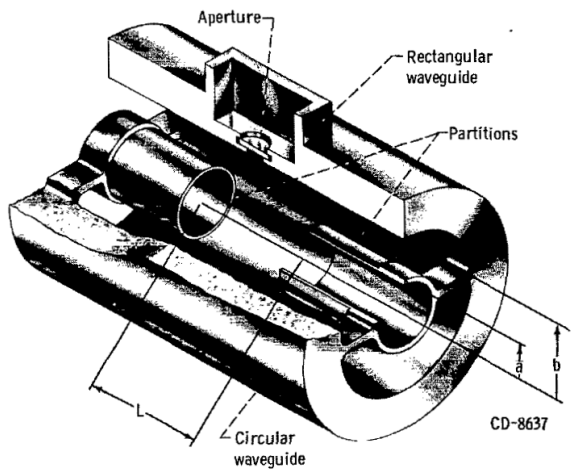


**Figure 6.9.** An image of an open cavity with coaxial terminations used for dielectric constant measurements. Figure from [3].

of the cavity ends completely open, which allows for the entrance of atomic tritium as well as the pumping away of molecular tritium that has recombined on the cavity walls. These open ends are achieved while preserving the high Q-values of the  $TE_{01\ell}$  modes, which is important for extracting as much signal power from the electron as possible. In subsequent sections this cavity design will be analyzed in more detail, primarily by using HFSS simulations to analyze the resonant mode structure of this cavity geometry.

#### Coaxial Terminator Constraints

The reason that coaxial endcaps can be used to achieve high Q-values for the  $TE_{01\ell}$  modes is that the electric fields for these modes are purely azimuthally polarized (see Equations 6.12 and 6.13). Therefore, the boundary conditions that require the electric field to go to zero at the cavity ends can be supplied using a coaxial partition of the correct radius (see Figure 6.10). Because the cylindrical shape enforced by the partition does not match the boundary conditions of other cavity modes, these terminations also significantly suppress the Q-factors of non- $TE_{01\ell}$  modes, which is potentially beneficial for a single-mode cavity CRES experiment.

The correct radius of the cylindrical partition is derived by setting up the boundary value problem in Figure 6.10, and analyzing the reflection and transmission coefficients for waves incident on the coaxial terminators. The basic problem is to identify the radius  $a$  where the reflection coefficient for the  $TE_{01\ell}$  modes becomes equal to 1. One can show that if the coaxial partitions are made sufficiently long relative to the wavelength of the

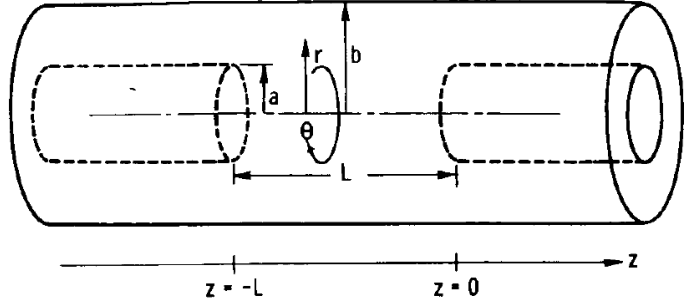


**Figure 6.10.** The simplified geometry of an open cavity with coaxial terminations. Figure from [4].

5110 TE<sub>01</sub> modes then perfect reflection can be achieved. This derivation is quite lengthy  
 5111 and complex and is presented in full in [4]. Here, I shall simply explain the resulting  
 5112 conditions on the partition radius for perfect reflection.

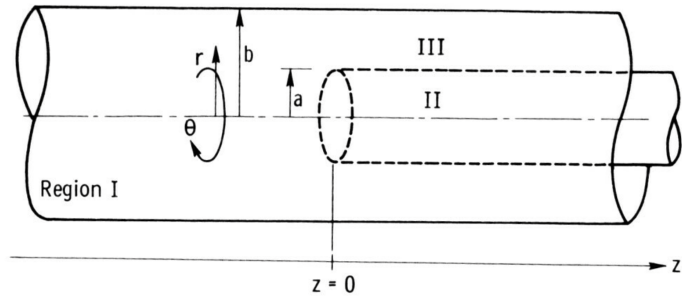


**Figure 6.11.** Electric field regions for the open cavity boundary value problem. Figure from [4].

5113 The open cavity boundary value problem is solved by expressing the forms of the  
 5114 electric fields in the different regions of the cavity and requiring that the electric fields are  
 5115 continuous. There are effectively three distinct regions in the open cavity corresponding  
 5116 to the central cavity volume, the inner coaxial volume, and the outer coaxial volume (see  
 5117 Figure 6.11).

5118 In Region I, the boundary conditions are those of a cylindrical waveguide, and it  
 5119 is required that  $E_\phi$  for the TE<sub>0m</sub> modes go to zero at the cavity wall ( $r = b$ ). This  
 5120 necessitates  $J'_{0m}(k_{c0m}b) = 0$ . A solution for the radius  $a$  is desired such that the TE<sub>01</sub>  
 5121 mode propagates, but other TE<sub>0m</sub> modes are below the cutoff frequency for the circular  
 5122 waveguide. This is equivalent to requiring

$$3.832 < k_{c0m}b < 7.016, \quad (6.41)$$

5123 where the numbers 3.832 and 7.016 correspond to the first and second zeros of the Bessel  
 5124 function (see Table 6.1).

5125 In Region II the boundary conditions are those of a cylindrical waveguide, but with  
 5126 a smaller radius. The condition that  $E_\phi = 0$  at the cylindrical partition radius is that  
 5127  $J'_{0m}(k_{c0m}a) = 0$ . To ensure perfect reflection, all modes in Region 1 of the cavity must be  
 5128 below the cutoff frequency of the circular waveguide formed by the inner volume of the  
 5129 coaxial terminator. Therefore, solutions where the condition

$$k_{c0m}a < 3.832, \quad (6.42)$$

5130 is true are required.

5131 Finally, in Region III the boundary condition are those of a coaxial waveguide. One  
 5132 needs to guarantee that  $E_\phi = 0$  at both  $r = b$  and  $r = a$ , which involves finding the  
 5133 eigenvalues of the following equation

$$J'_0(k_{c0m}a)Y'_0(k_{c0m}b) - J'_0(k_{c0m}b)Y'_0(k_{c0m}a) = 0, \quad (6.43)$$

5134 where  $Y'_0$  the zeroth-order derivatives of the Bessel function of the second kind. The  
 5135 solutions to this equation depend on the value of the ratio  $b/a$ . The approximate solution  
 5136 is given by

$$\delta_n a \simeq \frac{n\pi}{b/a - 1}, \quad (6.44)$$

5137 where  $\delta_n$  are eigenvalues of Equation 6.43. Similar to Region II, solutions for which  
 5138 the TE<sub>01</sub> modes of Region I are below the cutoff frequency of Region III are needed.  
 5139 Therefore, it is required that

$$k_{c0m} < \delta_1. \quad (6.45)$$

5140 In general, one has some freedom in specifying the value of  $b/a$ . A value typically used  
 5141 in practice is  $b/a = 2.082$ , which corresponds to positioning the radius of the cylindrical  
 5142 partition at the maxima of the TE<sub>01</sub> electrical fields.

5143 Using the constraints from the three field regions one can develop a coaxial terminator  
 5144 that acts as a virtual perfectly conducting surface for the TE<sub>01</sub> modes. The only required  
 5145 inputs are the desired frequency of the TE<sub>011</sub> mode and a choice for the value of  $b/a$ .

## 5146 6.4.2 Mode Filtering

5147 The general case of an electron coupling to a resonant cavity is complicated. This is  
5148 because cavities contain an infinite number of resonant modes, which for higher order  
5149 modes, have couplings to the electron with a complex spatial dependence. The danger is  
5150 that improper modeling of the electron's coupling to the cavity can lead to systematic  
5151 errors in the CRES measurements that prevent a high-resolution measurement of the  
5152 electron's kinetic energy. This in part drives the preference for a single-mode cavity  
5153 experiment that uses only the electron's coupling to the TE<sub>011</sub> mode to perform CRES,  
5154 assuming that sufficient information on the electron's position can be obtained with a  
5155 single mode.

5156 The TE<sub>011</sub> mode is in a region where there are relatively few other modes to which  
5157 the electron could couple(see Figure 6.8). However, one can see that the frequency of  
5158 the TE<sub>011</sub> is perfectly degenerate with the TM<sub>111</sub> mode, which means that electrons will  
5159 inevitably couple to both modes if they have the correct cyclotron frequency.

5160 The magnitude of the impact of the electron coupling to both TE<sub>011</sub> and TM<sub>111</sub> is  
5161 currently unknown. To first order an electron coupling to both modes will lose more  
5162 energy over time, which can be measured by observing the frequency chirp rate of the  
5163 signal. This effect may be small enough to be negligible or simple enough to model, so  
5164 that the cavity can be treated as an effective single-mode cavity. Alternatively, one could  
5165 consider devising a coupling scheme that is sensitive to both the TE<sub>011</sub> and the TM<sub>111</sub>  
5166 modes. By measuring the coupling of the electron to both modes more information on  
5167 the position of the electron could be obtained, which could improve the position and  
5168 energy resolution of the CRES measurements.

5169 A different approach is the mode filtering approach, which seeks to obtain a single  
5170 TE<sub>011</sub> mode cavity using perturbations to the cavity walls that selectively suppress the  
5171 TM modes, while leaving the TE modes mostly unperturbed. The type of perturbations  
5172 required can be determined by visualizing the surface currents induced in the cavity  
5173 walls by each type of mode (see Figure 6.12). By definition, all TM have electric fields  
5174 directed along the vertical axis of the cylindrical cavity, which means that perturbations  
5175 that impede currents in this direction will modify TM resonances. On the other hand,  
5176 the TE<sub>01</sub> modes induce azimuthal currents in the cavity walls; therefore, it is possible  
5177 to break the degeneracy between TE<sub>01</sub> and TM<sub>11</sub> by using a cavity perturbation that  
5178 suppresses axial currents, but does not affect the flow of azimuthal currents.

5179 Figure 6.12 shows two cavity design concepts that achieve this selective current  
5180 perturbation. The resistive approach inserts a series of thin dielectric rings into the walls

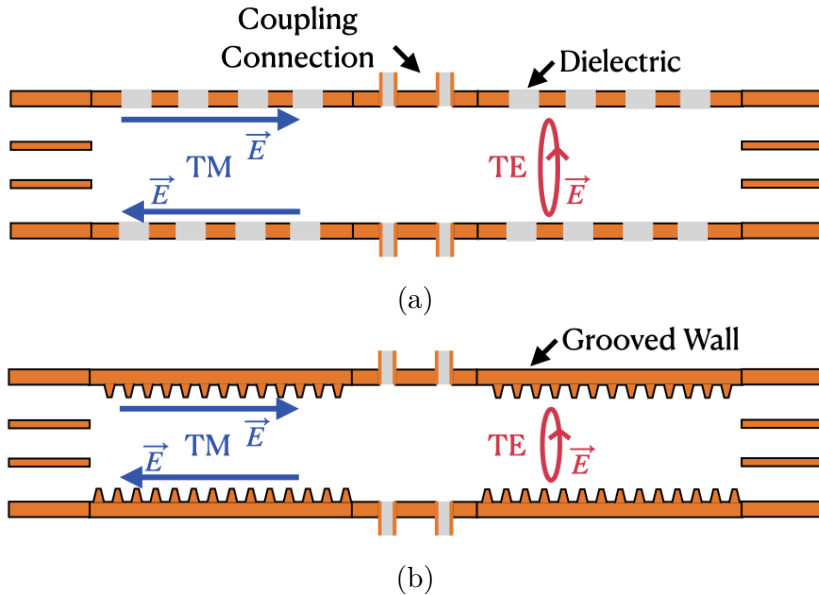


**Figure 6.12.** Two mode filtering concepts to break the degeneracy of  $TE_{01}$  and  $TM_{11}$  modes. The resistive approach uses dielectric materials to impede currents that travel vertically along the cavity while leaving azimuthal currents unperturbed. An alternative approach is to impede the currents using grooves cut into the cavity wall, which achieve the same effect with an inductive impedance.

of the cavity that introduces a resistive and capacitive impedance to the longitudinal currents, while leaving azimuthal current paths intact. Cavities of this type with high  $TE_{01}$  Q's have also been constructed by tightly wrapping a thin, dielectric coated wire around a mold to form the cavity wall. An alternative method is to introduce an inductive impedance by cutting grooves or a thread pattern on the inside wall of the cavity. For reasons of manufacturability and compatibility with tritium the grooved cavity approach is the preferred method for mode-filtered cavity construction by Project 8.

#### 6.4.3 Simulations of Open, Mode-filtered Cavities

A candidate design for a single  $TE_{011}$  mode CRES experiment is a cavity that utilizes the coaxial terminations combined with a mode-filtering wall. The first step towards validating that a cavity that combines these two design features will operate as expected is a thorough simulation effort for which finite element method (FEM) simulation software is invaluable. The primary tool for electromagnetic FEM calculations inside Project 8 is Ansys HFSS, which has a robust and well-established eigenmode solver that can identify the resonant frequencies and associated Q-factors for given structure.

Four variations of a cavity design with a  $\sim 1$  GHz  $TE_{011}$  resonance were implemented

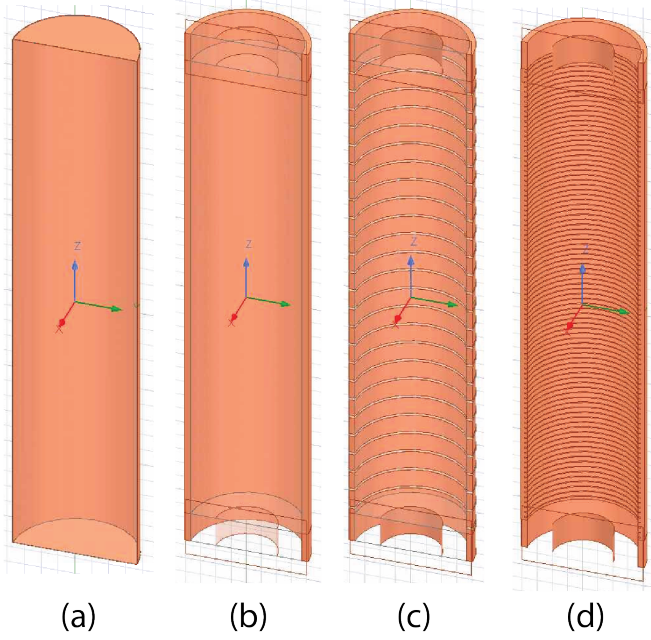


**Figure 6.13.** Four cavity design variations. (a) is a standard sealed cylindrical cavity, (b) is an open cavity with smooth walls, (c) is an open cavity with walls made of alternating conductor and dielectric, and (d) is an open cavity with grooved walls. The main cavity and coaxial terminator parameter are identical for all four cavities.

in HFSS (see Figure 6.13). The four designs include a standard cylindrical cavity, an open cavity with smooth walls, an open cavity with walls made of alternating conductor and dielectric, and an open cavity with grooved walls. The relevant design parameters are summarized in Table 6.3. All cavities were simulated using copper walls and filled with a vacuum dielectric. The identities of the resonant modes found by HFSS were validated by visual inspection of the electric and magnetic field patterns and by comparison to analytical calculations of the mode frequencies.

**Table 6.3.** A table of cavity design parameters used for HFSS simulations.

Name	Qty.	Unit	Description
$D_{\text{cav}}$	326.4	mm	Cavity diameter
$L_{\text{cav}}$	1668.0	mm	Cavity length
$D_{\text{term}}$	200.2	mm	Inner diameter of coaxial terminator
$L_{\text{term}}$	100.0	mm	Terminator length
$l_{\text{die}}$	8.3	mm	Dielectric spacer thickness
$\Delta l_{\text{die}}$	66.7	mm	Distance between dielectric spacers
$l_{\text{groove}}$	3.0	mm	Groove height
$d_{\text{groove}}$	9.0	mm	Groove depth
$\Delta l_{\text{groove}}$	18.3	mm	Distance between grooves

5204 The results of the HFSS simulations validate our predictions of the resonant behavior  
of an open, mode-filtered cavity developed in the preceding sections (see Figure 6.14) One

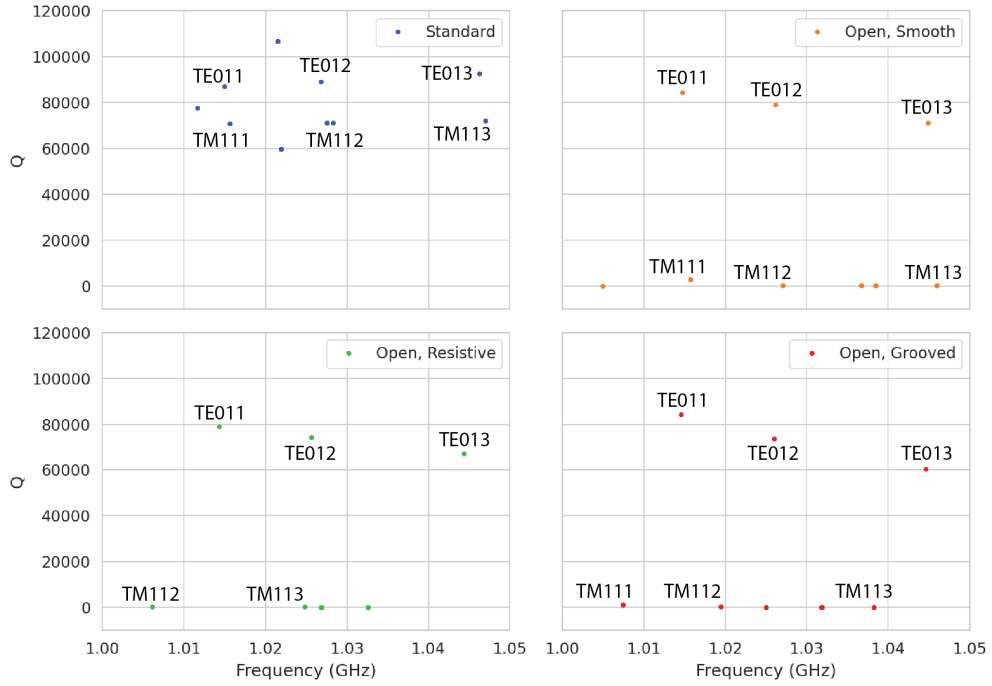


**Figure 6.14.** The frequencies and Q-factors of the resonant modes identified by HFSS for the cavity variations shown in Figure 6.13. The fully-sealed cavity with smooth walls has several high-Q modes near the  $TE_{011}$  resonance. Introducing the open-termination preserves the Q-factors of the  $TE_{01\ell}$  modes and suppresses the Q-factors of the modes whose boundary conditions do not match the cylindrical partition. Both the resistive and grooved wall perturbations shift the resonant frequencies of the TM modes away from the  $TE_{011}$  mode. By properly tuning the geometry of the grooves or the resistive spacers several MHz of frequency separation can be achieved.

5205  
5206 can see that for a standard cavity the  $TE_{01}$  and the  $TM_{11}$  are degenerate in frequency  
5207 with relatively high Q-factors. The open-ended cavity preserves the high Q-factors of  
5208 the  $TE_{01}$  modes, while the other modes, since their boundary conditions do not match  
5209 the coaxial geometry, have their Q-factors suppressed. One can see that the effect of  
5210 the resistive and inductive mode-filtering schemes is to effectively shift the resonant  
5211 frequencies of the  $TM_{11}$  modes below those of the associated  $TE_{01}$  modes, which breaks  
5212 the degeneracy. Optimization of the dielectric spacer or groove parameters can ensure  
5213 that the  $TE_{011}$  mode is isolated from other modes by  $O(10)$  MHz, which provides sufficient  
5214 bandwidth for a measurement of the tritium spectrum endpoint.

5215 Further optimization of the cavity design requires a more detailed cavity simulation  
5216 that includes the cavity coupling mechanism as well as other geometry modifications

5217 required for integration into the magnetic and tritium gas subsystems. Perhaps more  
5218 important is the development of the capability to simulate the interaction of electrons  
5219 with the cavity so that simulated CRES signals can be generated using cavities designed  
5220 for CRES measurements. Simulated CRES signals can then be used to estimate the  
5221 neutrino mass sensitivity of the experiment, which allows for the optimization of the cavity  
5222 design towards the configuration that provides the best measurement of the neutrino  
5223 mass.

## 5224 **6.5 Single-mode Resonant Cavity Measurements**

5225 Measurement test stands play an important role in the research and development process  
5226 that cannot be replaced by simulations. For example, constructing a prototype CRES  
5227 cavity forces one to consider important practical issues such as manufacturability and  
5228 machine tolerances that may require modifications to the design. Furthermore, by  
5229 comparing laboratory measurements of a real cavity to simulations, one can quantify  
5230 the impact of imperfections and real-life measurement systematics, which allows for  
5231 more accurate sensitivity estimates of the experiment. Lastly, the development of these  
5232 prototypes helps to build the necessary experience and expertise within the collaboration  
5233 required for more complicated experiments to succeed.

5234 With these objectives in mind a prototype cavity was constructed to demonstrate the  
5235 open, mode-filtered cavity concept explored in the previous sections. The primary goal  
5236 of the measurements was to validate that an open, mode-filtered cavity suppressed the  
5237 TM<sub>11</sub> modes as predicted by HFSS simulations.

### 5238 **6.5.1 Cavities and Setup**

5239 Two rudimentary cavities were constructed using segments of copper pipe available from  
5240 McMaster-Carr (see Figure 6.15). The design consists of copper pipes of two diameters.  
5241 The larger diameter pipe forms the main cavity wall and the smaller diameter pipe is  
5242 used to create a coaxial termination. The diameter of the outer pipe was chosen to  
5243 produce a TE<sub>011</sub> resonance of approximately 6 GHz, while the diameter of the smaller  
5244 pipe was selected based on the open termination criteria introduced in Section 6.4.1. The  
5245 approximate diameters and lengths of the copper pipe are summarized in Table 6.4.

5246 Coupling to the cavity was achieved using a hand-formable segment of coaxial cable  
5247 stripped at one end to form a loop antenna. This was inserted into a small hole located

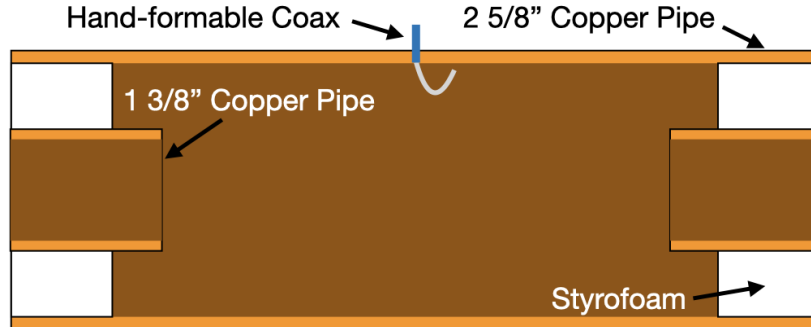


**Figure 6.15.** A cartoon depicting the design of the open-ended cavity prototype designed to operate at approximately 6 GHz. The main cavity wall was composed of a single copper pipe. A mode-filtered version of this cavity was constructed by

5248 at the center of the main cavity wall. The coaxial terminators were supported inside the  
 5249 main cavity by carving a spacer from polystyrene foam (styrofoam), so that they could  
 5250 be easily inserted into the cavity and repositioned. The dielectric constant of styrofoam  
 5251 is quite close to air at microwave frequencies, so this is expected to have minimal impact  
 5252 on the resonant properties of the cavity.

**Table 6.4.** A table of parameters describing the cavity prototypes. Certain values such as the cavity length and the distance between dielectric spacers are approximate due to variation in the machining of the copper. In particular, the filtered cavity was constructed from conducting copper segments that varied in size from 1.50" to 1.85".

Name	Qty.	Unit	Description
$D_{\text{cav}}$	2.625	in	Cavity diameter
$L_{\text{cav}}$	$\approx 13$	in	Cavity length
$D_{\text{term}}$	1.375	in	Inner diameter of coaxial terminator
$L_{\text{term}}$	1.575	in	Terminator length
$l_{\text{die}}$	0.75	in	Dielectric spacer thickness
$\Delta l_{\text{die}}$	$\approx 1.50$ to $1.85$	in	Distance between dielectric spacers

5253 The effective length of the cavity is given by the distance between the inner edges of  
 5254 the coaxial terminations. The length of the outer section of pipe that forms the main wall  
 5255 of the cavity is approximately 16" in length which leads to a cavity length of  $\approx 13"$  when  
 5256 both terminators are inserted in the cavity. Because the terminators were not rigidly  
 5257 mounted this distance is only approximate, but the uncertain length of the cavity will  
 5258 not prevent us from validating the open cavity design.

5259 Along with the smooth-walled open cavity, a resistively mode-filtered cavity was  
 5260 constructed by creating dielectric spacers out of segments of clear PVC pipe (see Figure  
 5261 6.16). The spacers were machined such that the conductive segments of the cavity would

5262 be separated by 0.75" when the cavity was fully assembled. Due to variations in the  
 5263 lengths of the copper segments that make up the cavity wall the distance between spacers  
 5264 has significant variation with average value of about 1.7". Eight total spacers were used  
 5265 to build the cavity, which when assembled was approximately 16" in total length similar  
 to the non-filtered cavity.

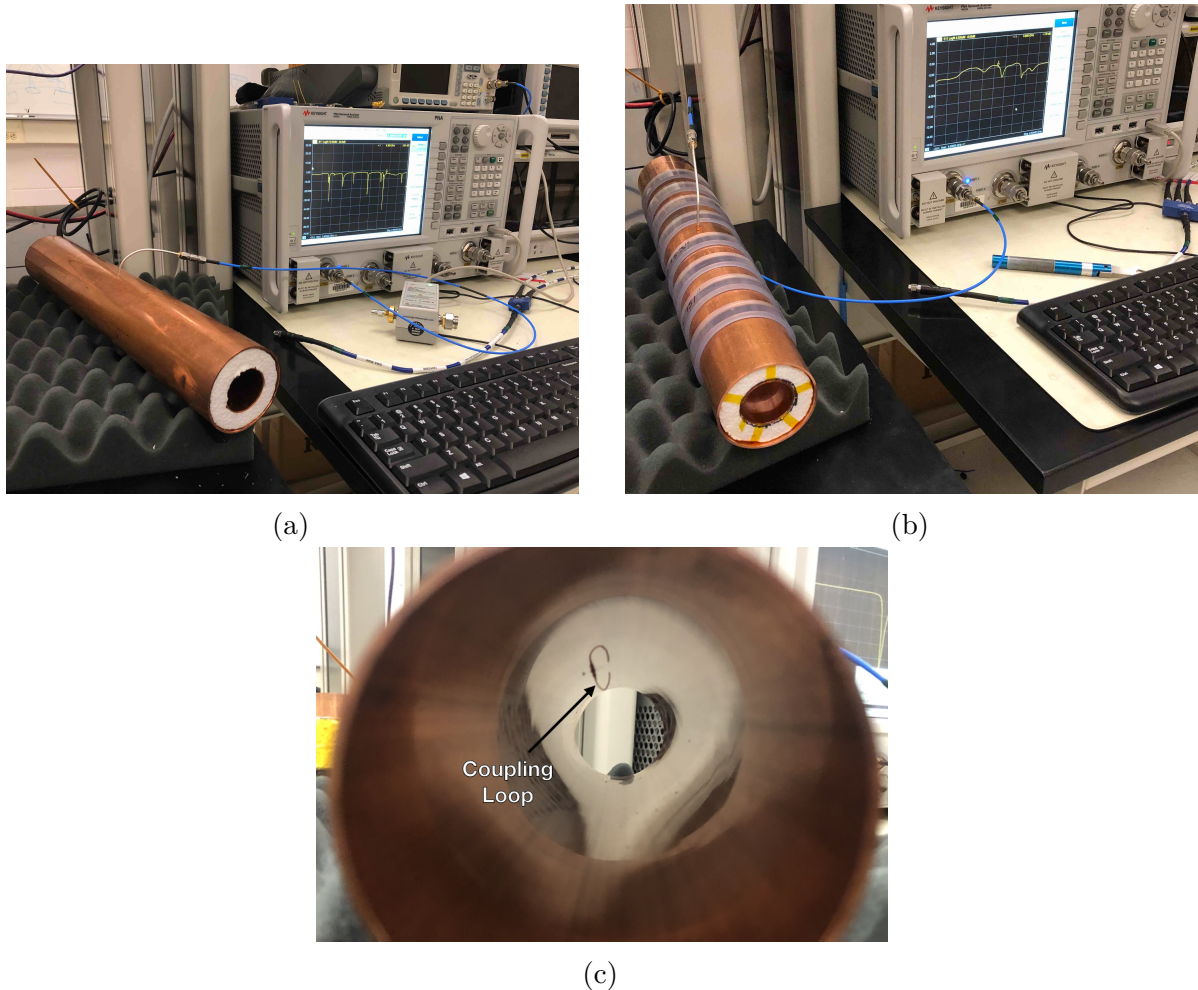


**Figure 6.16.** Images depicting the measurement of the filtered and non-filtered open cavities using the VNA. The coupling loop in the figure is shown in the TE orientation.

5266 Measurements of both cavities were performed using a VNA connected to the cavity  
 5267 coupling probe (see Figure 6.16). By measuring the return loss over a range of frequencies  
 5268 one can measure the frequencies and relative Q-factors of the resonant modes in the  
 5269 cavity. Due to the opposite polarity of the electric fields for the TE and TM modes,  
 5270 the loop coupling probe must be rotated 90° to change the polarity of the loop antenna.  
 5271 When the antenna is oriented such that the loop opening faces the ends of the cavity, it  
 5272

5273 couples primarily to the TE modes which have magnetic fields directed along the long  
 5274 axis of the cavity (see Figure 6.16). If the coupling loop is turned by  $90^\circ$  from where  
 5275 it is shown in the image then it will couple to the TM modes which have azimuthally  
 5276 directed magnetic fields. In this way both the TE and TM resonances can be measured  
 5277 independently.

## 5278 **6.5.2 Results and Discussion**

5279 The primary analysis for the prototype cavities involved a simple visualization of the return loss as measured by the VNA and a comparison between the filtered and non-  
 5280 filtered variations. Since the resonances measured by the VNA are not labeled, there is an uncertainty about the true identities of the modes measured by the VNA. To resolve  
 5281 this I performed a simulation of the simplest possible cavity that could be created from the prototype components, which is a fully open cavity created by removing the coaxial  
 5282 inserts. The fully-open cavity with the as-built dimensions was simulated in HFSS to get  
 5283 estimates on the positions of the  $\text{TE}_{011}$  and  $\text{TM}_{111}$  modes (see Figure 6.17).

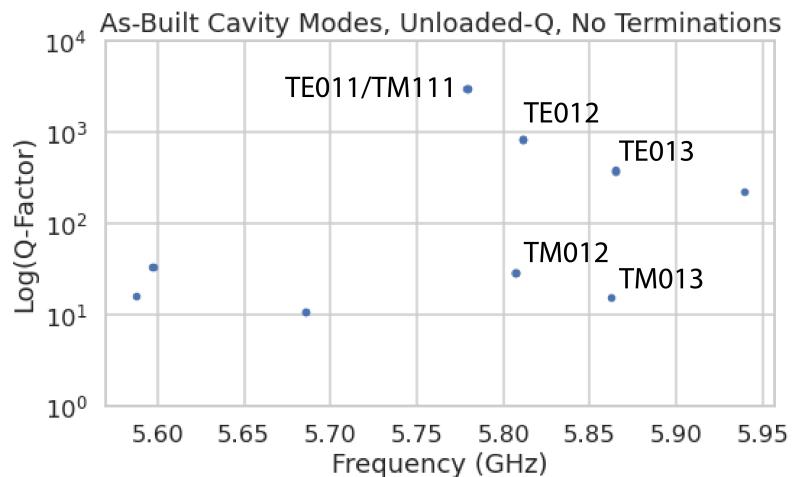


**Figure 6.17.** HFSS simulation results for the as-built cavity with the coaxial terminators removed. The  $\text{TE}_{011}/\text{TM}_{111}$  frequency is approximately 5.78 GHz.

5287 Simulation of the fully open cavity shows that the  $\text{TE}_{011}/\text{TM}_{111}$  modes have a  
 5288 frequency of approximately 5.78 GHz in the fully open cavity. If the frequency of this  
 5289 mode is compared to the measurements of the filtered and non-filtered cavities with the  
 5290 terminators removed one can easily identify the  $\text{TE}_{011}$  mode at approximately 5.75 GHz  
 5291 (see Figure 6.18).

5292 In both variations of the non-filtered cavities one sees that the  $\text{TE}_{011}$  mode is degen-  
 5293 erate with what appears to be a doublet of TM modes located at the  $\text{TM}_{111}$  frequency  
 5294 position. This doublet is actually the  $\text{TM}_{111}$  mode, which has two polarizations with  
 5295 opposite polarizations. Because any real pipe used to construct a cavity will not be  
 5296 perfectly round due to manufacturing tolerances, it is likely that the frequency degeneracy  
 between the two polarizations is broken, which results in the doublet peaks.

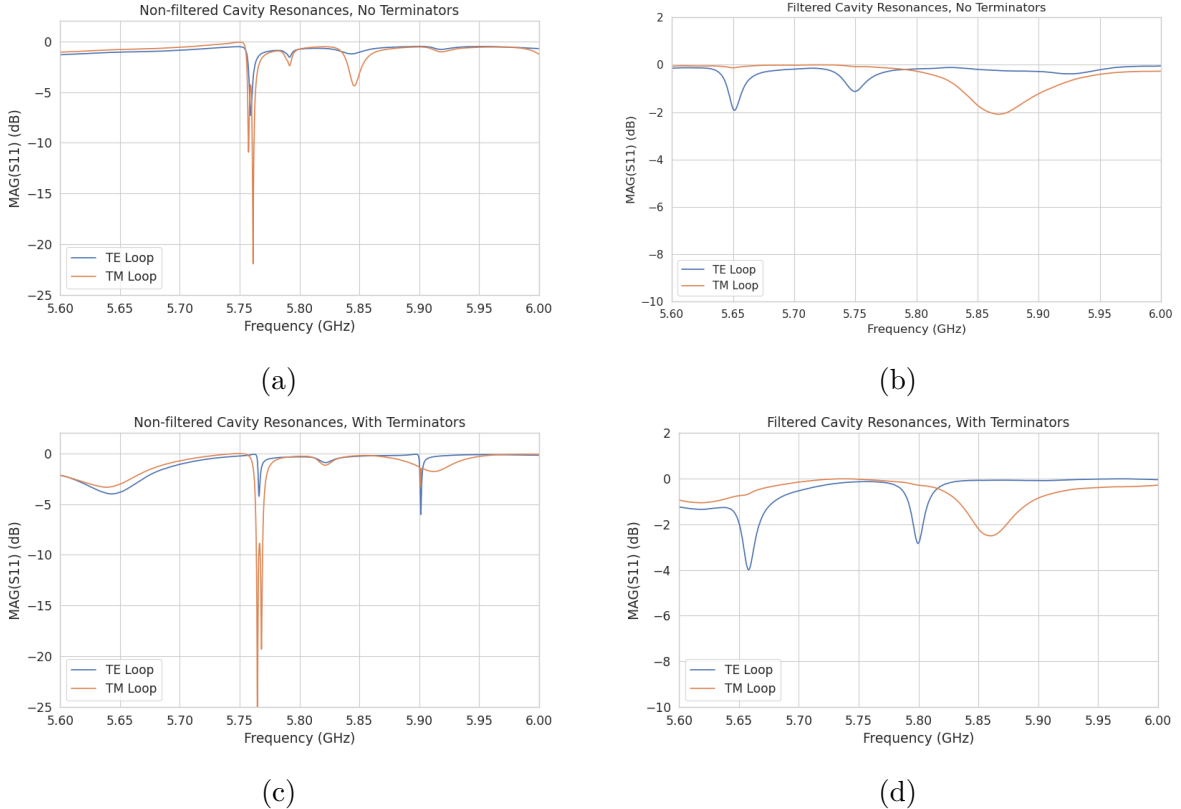


**Figure 6.18.** Measurements of the filtered and non-filtered prototype cavities acquired with the VNA.

5297  
 5298 The S-parameter plot for the filtered cavity without terminators has an isolated TE  
 5299 resonance at 5.65 GHz, associated with the  $\text{TE}_{011}$  mode. The frequency of this mode  
 5300 is lower than the non-filtered cavity due to a difference in the overall lengths of the  
 5301 cavities. An obvious difference between the filtered and non-filtered cavities is that  
 5302 there is no  $\text{TM}_{111}$  doublet at the  $\text{TE}_{011}$  frequency. This is what one would expect if  
 5303 the mode-filtering was suppressing the TM modes. There appears to be a noticeable  
 5304 difference in the Q of the  $\text{TE}_{011}$  resonance between non-filtered and filtered variations as  
 5305 indicated by the increased resonance depth for the filtered cavity. Overall, the Q-factors  
 5306 of the filtered cavity appear significantly smaller than the non-filtered cavity due to the

5307 increase in resonance width. This is likely caused by the relatively large widths of the  
5308 dielectric spacers, which are partially impeding the TE modes.

5309 One can see from these cavity measurements that, in principle, resistive mode-filtering  
5310 can be used to separate the  $TE_{011}$  resonance from the degenerate  $TM_{111}$  modes in  
5311 combination with the open cavity endcaps. This finding agrees with the expectations  
5312 from HFSS, which should provide confidence that the eigenmode solver is correctly  
5313 modeling the behavior of the cavity. Although I did not perform a similar study using  
5314 a cavity with grooved walls, it is expected that the resonant mode structure would be  
5315 similar to the cavity studied here.

5316 While this prototype cavity is a good first step, several deficiencies prevent this setup  
5317 from providing more than qualitative information to the design of cavities for CRES. This  
5318 includes the rudimentary approach to cavity coupling using a stripped coax antenna and  
5319 the inability to map the field density in the cavity volume. Improvements in these areas  
5320 are required so that measurements from a real cavity can provide useful information to  
5321 cavity CRES simulations that will ultimately inform neutrino mass sensitivity estimates.

5322 Future work with prototype cavities must include an improved cavity coupling scheme,  
5323 which is robust and compatible with atomic tritium. Since the cavity will ultimately  
5324 be filled with atomic tritium, a coupling antenna cannot be used due to the losses of  
5325 atomic tritium caused by recombination on the antenna surfaces. Possible non-invasive  
5326 coupling schemes include aperture coupling, where the cavity is coupled to an external  
5327 waveguide structure through an aperture, or a split-ring coupling approach, where the  
5328 center segment of the cylindrical cavity wall is replaced an isolated conductive ring with  
5329 a small vertical slit. The aperture coupling approach is a standard coupling scheme [92]  
5330 used in a wide range of applications, but at low frequencies the size of the external  
5331 waveguide conflicts with design of the atom trapping magnet and cryogenics system.  
5332 The split-ring approach could potentially be coupled to a small coaxial transmission line  
5333 which is more compatible with the rest of the experiment design. A challenge with this  
5334 coupling scheme is achieving a large enough coupling factor by correctly engineering  
5335 the geometry of the split-ring and the connection to the coax transmission line. The  
5336 design and optimization of this coupling scheme is an area of current research in the  
5337 collaboration.

5338 The robustness of the coupling mechanism is relevant due to the difficulty in modeling  
5339 its effect on the cavity modes. Small changes in geometry can have a large influence on  
5340 the coupling and hence the performance of the cavity, therefore, correctly modeling the  
5341 cavity coupling is critical for accurate CRES simulations. Coupling schemes that rely on

5342 connections to coaxial lines are potentially at a disadvantage in this regard due to the  
5343 effect of soldering imperfections or unintended bends in the coax on the coupling. Future  
5344 work will identify a coupling scheme for the cavity compatible with the neutrino mass  
5345 goals of Project 8.

5346 Imperfections in the geometry of a real cavity will necessarily distort the resonant  
5347 modes away from simulation predictions. This will change the coupling of an electron  
5348 to the cavity and thus change the expected signal structure. Ultimately, this effect will  
5349 limit the achievable energy resolution of the experiment unless the differences between  
5350 simulation and a real cavity can be sufficiently characterized and calibrated. One possible  
5351 approach to this is to utilize a "bead puller" system [106] to strategically perturb the  
5352 cavity by moving a conductive bead through the cavity volume. The small perturbation  
5353 caused by the bead affects the phase of the cavity resonances proportional to the total  
5354 magnitude of the electric field at that position, so by moving the bead through the  
5355 cavity volume the total electric field can be mapped and compared to simulation. This  
5356 information can provide bounds on the relative perturbations to the cavity mode structure  
5357 from real-life imperfections compared to the idealized cavity in HFSS.

5358 **Chapter 7 |**

5359 **Conclusion and Future Prospects**

5360 In this dissertation I have discussed research and development efforts towards the  
5361 development of a scalable CRES (cyclotron radiation emission spectroscopy) measurement  
5362 technology that can be used to build a CRES experiment at cubic-meter scales with  
5363 sensitivity to neutrino masses of 40 meV. The primary contributions of my dissertation  
5364 are the development and analysis of signal reconstruction algorithms for an antenna-based  
5365 CRES experiment [62], which are vital to estimating the neutrino mass sensitivity of the  
5366 experiment; the development of a synthetic cyclotron radiation antenna (SYNCA) [78],  
5367 which allowed for laboratory validation of antenna array CRES simulation models [44];  
5368 and the development of an open-ended cavity design compatible with atomic tritium for a  
5369 cavity based CRES experiment. A measurable impact of this work is the transition of the  
5370 Project 8 collaboration’s experimental plan from an antenna array based approach to a  
5371 cavity based approach, after my work played a key role in demonstrating the significantly  
5372 higher cost and complexity of the antenna array experiment.

5373 The transition from antenna arrays to cavities requires a new set of demonstrator  
5374 experiments to make incremental progress towards a 40 meV measurement of the neutrino  
5375 mass. At the time of writing, the near-term plan of Project 8 is to design and construct a  
5376 small-scale cavity CRES experiment utilizing the 1 T magnet installed in the UW-Seattle.  
5377 This cavity is designed to have a TE011 resonance with a frequency of about 26 GHz with  
5378 a length-to-diameter ratio that mimics the larger cavities intended for the pilot-scale and  
5379 Phase IV experiments. The goal of this experiment is to demonstrate cavity CRES as  
5380 well as validate models of CRES systematics using electrons from  $^{83m}\text{Kr}$  and an electron  
5381 gun. Though the primary goal is demonstration, near-term physics measurements are  
5382 available in the form of high-resolution measurements of the  $^{83m}\text{Kr}$  conversion spectrum  
5383 of interest to the KATRIN collaboration.

5384 Furthermore, Project 8 is currently constructing a low-frequency CRES setup located  
5385 at Yale University to better understand the principles of cavity based CRES at lower

5386 magnetic fields. The Low, UHF Cavity Krypton Experiment at Yale (LUCKEY) is  
5387 a 1.5 GHz cavity CRES experiment that will use conversion electrons from  $^{83m}\text{Kr}$  to  
5388 perform CRES measurements at the lowest frequencies ever attempted with the technique.  
5389 LUCKEY will validate frequency scaling models developed by Project 8 and will pave  
5390 the way for the future Low-Frequency Apparatus (LFA), which will be a larger, 1 GHz  
5391 cavity CRES experiment that possibly includes a molecular tritium source. The target  
5392 for the LFA is a measurement of the neutrino mass with a sensitivity of approximately  
5393 0.2 eV, which will build towards the atomic pilot-scale CRES experiment.

5394 In parallel to the development of cavity CRES is the development of the atomic  
5395 tritium source. Recent demonstrations of the production of atomic hydrogen are excellent  
5396 steps towards the atomic tritium production needed for the pilot-scale experiment. One  
5397 area of future study includes the development of a more detailed understanding of the  
5398 efficiency of atomic hydrogen production. Near-term plans include the development  
5399 of a magnetic, evaporatively cooled beamline, as well as the prototyping of a Halbach  
5400 array atom trap. Nearly all the components of the atomic tritium system will require  
5401 demonstration before the complete system can be built. The long-term goal of the  
5402 atomic tritium work is to construct a full atomic tritium prototype that demonstrates  
5403 the production, cooling, trapping, and recycling of tritium at the rates needed for the  
5404 pilot-scale experiment.

5405 More broadly, the long-term goal of the Project 8 collaboration is to fully develop  
5406 both the atomic tritium and cavity CRES technologies so that both can be combined in  
5407 a pilot-scale CRES experiment. It is envisioned that this process will take approximately  
5408 10 years for both atomic tritium and cavity CRES. After these developments comes the  
5409 pilot-scale experiment, which will be the first CRES experiment that simultaneously  
5410 demonstrates all the required technologies for Phase IV. Scaling to Phase IV with cavity  
5411 CRES will require the construction of multiple copies (approximately 10) of the pilot-scale  
5412 experiment to obtain sufficient statistics for 40 meV sensitivity.

5413 Development of the CRES experimental technique by Project 8 has led to new  
5414 experiments utilizing the CRES technique for basic physics research, such as the  $^6\text{He}$ -  
5415 CRES collaboration [107], and has also found applications as a new approach to x-ray  
5416 spectroscopy [108]. Recently, a new experimental effort called CRESDA has begun in  
5417 the UK to develop new quantum technologies applied to CRES measurements for the  
5418 neutrino mass [109]. This flourishing of new experimental efforts based on the CRES  
5419 technique is likely to continue as Project 8 continues to develop the technique towards  
5420 its neutrino mass measurement goal.

5421        The work described in this dissertation represents important R&D steps towards  
5422        a next-generation neutrino mass measurement with CRES. A direct neutrino mass  
5423        measurement, which sets both an upper and lower bound on the neutrino mass will be  
5424        important to several physics subfields. For example, fixing the neutrino mass scale with  
5425        an independent measurement will enable cosmological fits to use the neutrino mass as  
5426        a fixed parameter, which will allow current data to provide more information on other  
5427        parameters in cosmological models. Additionally, a precise measurement of the neutrino  
5428        mass scale will be important for constraining the energy-scales of possible mechanisms  
5429        responsible for the relative smallness of the neutrino mass, showing the path towards  
5430        new physics beyond the standard model.

# 5431 Bibliography

- 5432 [1] CAHN, R. N., D. A. DWYER, S. J. FREEDMAN, W. C. HAXTON, R. W. KADEL,  
5433 Y. G. KOLOMENSKY, K. B. LUK, P. McDONALD, G. D. OREBI GANN, and  
5434 A. W. P. POON (2013) “White Paper: Measuring the Neutrino Mass Hierarchy,”  
5435 in *Snowmass 2013: Snowmass on the Mississippi*, 1307.5487.
- 5436 [2] AGOSTINI, M., G. BENATO, and J. DETWILER (2017) “Discovery probability of  
5437 next-generation neutrinoless double-  $\beta$  decay experiments,” *Phys. Rev. D*, **96**(5), p.  
5438 053001, 1705.02996.
- 5439 [3] WENGER, N. C. and J. SMETANA (1972) “Hydrogen Density Measurements Using  
5440 an Open-Ended Microwave Cavity,” *IEEE Transactions on Instrumentation and*  
5441 *Measurement*, **21**(2), pp. 105–114.
- 5442 [4] WENGER, N. (1967) “Resonant Frequency of Open-Ended Cylindrical Cavity,”  
5443 *IEEE Transactions on Microwave Theory and Techniques*, **15**(6), pp. 334–340.
- 5444 [5] DAS, A. and T. FERBEL (2003) *Introduction to Nuclear and Particle Physics*,  
5445 World Scientific.
- 5446 [6] CURIE, P. (1898) “Sur une nouvelle substance fortement radioactive, contenue  
5447 dans la pechblende,” *Comptes rendus de l’Academie des Sciences, Paris*, **127**, pp.  
5448 1215–1217.
- 5449 [7] RUTHERFORD, E. (1899) “Uranium radiation and the electrical conduction pro-  
5450 duced by it,” *Philos. Mag.*, **47**, p. 109.  
5451 URL <https://cds.cern.ch/record/261896>
- 5452 [8] GERWARD, L. (1999) “Paul Villard and his Discovery of Gamma Rays,” *Physics*  
5453 *in Perspective*, **1**, pp. 367–383.
- 5454 [9] BECQUEREL, H. (1900) “Deviation du rayonnement du radium dans un champ  
5455 électrique,” *C.R.*, **130**, pp. 809–815.
- 5456 [10] D.Sc., E. R. M. and F. S. B.A. (1902) “XLI. The cause and nature of ra-  
5457 dioactivity.—Part I,” *The London, Edinburgh, and Dublin Philosophical Mag-*  
5458 *azine and Journal of Science*, **4**(21), pp. 370–396, <https://doi.org/10.1080/14786440209462856>.  
5459 URL <https://doi.org/10.1080/14786440209462856>

- 5461 [11] CHADWICK, J. (1914) *Intensitätsverteilung im magnetischen Spektrum der  $\beta$ -*  
5462 *Strahlen von Radium B+C*, Druck von Friedr. Vieweg und Sohn.  
5463 URL <https://books.google.com/books?id=8s8UmQEACAAJ>
- 5464 [12] BROWN, L. M. (1978) “The idea of the neutrino,” *Physics Today*, **31**(9).
- 5465 [13] PAULI, W. (1978) “Dear radioactive ladies and gentlemen,” *Phys. Today*, **31N9**,  
5466 p. 27.
- 5467 [14] AMALDI, E. (1984) “From the discovery of the neutron to the discovery of nuclear  
5468 fission,” *Physics Reports*, **111**(1), pp. 1–331.  
5469 URL <https://www.sciencedirect.com/science/article/pii/037015738490214X>
- 5470 [15] CHADWICK, J. (1932) “The existence of a neutron,” *Proceedings of the Royal  
5471 Society of London. Series A, Containing Papers of a Mathematical and Physical  
5472 Character*, **136**(830), pp. 692–708, <https://royalsocietypublishing.org/doi/pdf/10.1098/rspa.1932.0112>.  
5473 URL <https://royalsocietypublishing.org/doi/abs/10.1098/rspa.1932.0112>.
- 5474 [16] WILSON, F. L. (1968) “Fermi’s Theory of Beta Decay,” *American Journal of  
5475 Physics*, **36**(12), pp. 1150–1160, [https://pubs.aip.org/aapt/ajp/article-pdf/36/12/1150/11891052/1150\\_1\\_online.pdf](https://pubs.aip.org/aapt/ajp/article-pdf/36/12/1150/11891052/1150_1_online.pdf).  
5476 URL <https://doi.org/10.1119/1.1974382>
- 5477 [17] CRANE, H. R. and J. HALPERN (1938) “New Experimental Evidence for the  
5478 Existence of a Neutrino,” *Phys. Rev.*, **53**, pp. 789–794.  
5479 URL <https://link.aps.org/doi/10.1103/PhysRev.53.789>
- 5480 [18] COWAN, C. L., F. REINES, F. B. HARRISON, H. W. KRUSE, and A. D.  
5481 McGUIRE (1956) “Detection of the Free Neutrino: a Confirmation,” *Science*,  
5482 **124**(3212), pp. 103–104, <https://www.science.org/doi/pdf/10.1126/science.124.3212.103>.  
5483 URL <https://www.science.org/doi/abs/10.1126/science.124.3212.103>
- 5484 [19] ANICIN, I. V. (2005) “The Neutrino - Its Past, Present and Future,” *arXiv e-prints*,  
5485 physics/0503172, [physics/0503172](https://arxiv.org/abs/physics/0503172).
- 5486 [20] DAVIS, R. (2003) “Nobel Lecture: A half-century with solar neutrinos,” *Rev. Mod.*  
5487 *Phys.*, **75**, pp. 985–994.
- 5488 [21] McDONALD, A. B. ET AL. (2002) “Direct evidence for neutrino flavor transfor-  
5489 mation from neutral-current interactions in SNO,” *AIP Conf. Proc.*, **646**(1), pp.  
5490 43–58.
- 5491 [22] FUKUDA, Y. ET AL. (1998) “Evidence for oscillation of atmospheric neutrinos,”  
5492 *Phys. Rev. Lett.*, **81**, pp. 1562–1567, [hep-ex/9807003](https://arxiv.org/abs/hep-ex/9807003).
- 5493
- 5494
- 5495
- 5496
- 5497

- 5498 [23] GIGANTI, C., S. LAVIGNAC, and M. ZITO (2018) “Neutrino oscillations: The rise  
 5499 of the PMNS paradigm,” *Prog. Part. Nucl. Phys.*, **98**, pp. 1–54, 1710.00715.
- 5500 [24] WORKMAN, R. L. and OTHERS (2022) “Review of Particle Physics,” *PTEP*, **2022**,  
 5501 p. 083C01.
- 5502 [25] AN, F. ET AL. (2016) “Neutrino Physics with JUNO,” *J. Phys. G*, **43**(3), p. 030401,  
 5503 1507.05613.
- 5504 [26] BIAN, J. ET AL. (2022) “Hyper-Kamiokande Experiment: A Snowmass White  
 5505 Paper,” in *Snowmass 2021*, 2203.02029.
- 5506 [27] ABI, B. ET AL. (2020) “Long-baseline neutrino oscillation physics potential of the  
 5507 DUNE experiment,” *Eur. Phys. J. C*, **80**(10), p. 978, 2006.16043.
- 5508 [28] ZUBER, K. (2020) *Neutrino Physics*, CRC Press.
- 5509 [29] XING, Z. Z. and S. ZHOU (2011) *Neutrinos in Particle Physics, Astronomy and*  
 5510 *Cosmology*, Springer.
- 5511 [30] MOHAPATRA, R. N. ET AL. (2007) “Theory of neutrinos: A White paper,” *Rept.  
 5512 Prog. Phys.*, **70**, pp. 1757–1867, hep-ph/0510213.
- 5513 [31] DE GOUVÉA, A. (2016) “Neutrino Mass Models,” *Ann. Rev. Nucl. Part. Sci.*, **66**,  
 5514 pp. 197–217.
- 5515 [32] WONG, Y. Y. Y. (2011) “Neutrino mass in cosmology: status and prospects,”  
 5516 *Ann. Rev. Nucl. Part. Sci.*, **61**, pp. 69–98, 1111.1436.
- 5517 [33] ADE, P. A. R. ET AL. (2016) “Planck 2015 results. XIII. Cosmological parameters,”  
 5518 *Astron. Astrophys.*, **594**, p. A13, 1502.01589.
- 5519 [34] CARLSTROM, J. ET AL. (2019) “CMB-S4,” in *Bulletin of the American Astronomical  
 5520 Society*, vol. 51, p. 209, 1908.01062.
- 5521 [35] ELLIOTT, S. R. and P. VOGEL (2002) “Double beta decay,” *Ann. Rev. Nucl. Part.  
 5522 Sci.*, **52**, pp. 115–151, hep-ph/0202264.
- 5523 [36] DOLINSKI, M. J., A. W. P. POON, and W. RODEJOHANN (2019) “Neutrinoless  
 5524 Double-Beta Decay: Status and Prospects,” *Ann. Rev. Nucl. Part. Sci.*, **69**, pp.  
 5525 219–251, 1902.04097.
- 5526 [37] FORMAGGIO, J. A., A. L. C. DE GOUVÉA, and R. G. H. ROBERTSON (2021)  
 5527 “Direct measurements of neutrino mass,” *Physics Reports*, **914**, pp. 1–54, direct  
 5528 measurements of neutrino mass.  
 5529 URL [https://www.sciencedirect.com/science/article/pii/  
 5530 S0370157321000636](https://www.sciencedirect.com/science/article/pii/S0370157321000636)

- 5531 [38] AKER, M. ET AL. (2022) “New Constraint on the Local Relic Neutrino Background  
 5532 Overdensity with the First KATRIN Data Runs,” *Phys. Rev. Lett.*, **129**(1), p.  
 5533 011806, 2202.04587.
- 5534 [39] FORMAGGIO, J. A., A. L. C. DE GOUVÊA, and R. G. H. ROBERTSON (2021)  
 5535 “Direct Measurements of Neutrino Mass,” *Phys. Rept.*, **914**, pp. 1–54, 2102.00594.
- 5536 [40] MONREAL, B. and J. A. FORMAGGIO (2009) “Relativistic cyclotron radiation  
 5537 detection of tritium decay electrons as a new technique for measuring the neutrino  
 5538 mass,” *Phys. Rev. D*, **80**, p. 051301.  
 5539 URL <https://link.aps.org/doi/10.1103/PhysRevD.80.051301>
- 5540 [41] ESFAHANI, A. A. ET AL. (2022) “The Project 8 Neutrino Mass Experiment,”  
 5541 2203.07349.
- 5542 [42] ——— (2023) “Cyclotron Radiation Emission Spectroscopy of Electrons from  
 5543 Tritium Beta Decay and  $^{83m}\text{Kr}$  Internal Conversion,” 2303.12055.
- 5544 [43] ——— (2023) “Tritium Beta Spectrum and Neutrino Mass Limit from Cyclotron  
 5545 Radiation Emission Spectroscopy,” 2212.05048.
- 5546 [44] “Antenna Arrays for Physics Measurements with Large-scale CRES Detectors,” *In  
 5547 preparation*.
- 5548 [45] NICHOLSON, T. ET AL. (2015) “Systematic evaluation of an atomic clock at 2 x  
 5549 10-18 total uncertainty,” *Nature Communications*, **6**(6896).
- 5550 [46] HÄNSCH, T. W. (2006) “Nobel Lecture: Passion for precision,” *Rev. Mod. Phys.*,  
 5551 **78**, pp. 1297–1309.  
 5552 URL <https://link.aps.org/doi/10.1103/RevModPhys.78.1297>
- 5553 [47] GABOR, D. (1946) “Theory of communication. Part 1: The analysis of information,”  
 5554 *Journal of the Institution of Electrical Engineers-part III: radio and communication  
 5555 engineering*, **93**(26), pp. 429–441.
- 5556 [48] ESFAHANI ASHTARI, A. ET AL. (2022) “Viterbi decoding of CRES signals in  
 5557 Project 8,” *New J. Phys.*, **24**(5), p. 053013, 2112.05265.
- 5558 [49] JACKSON, J. D. (1999) *Classical electrodynamics*, 3rd ed., Wiley, New York, NY.  
 5559 URL <http://cdsweb.cern.ch/record/490457>
- 5560 [50] F.R.S., J. L. D. (1897) “LXIII. On the theory of the magnetic influence on  
 5561 spectra; and on the radiation from moving ions,” *The London, Edinburgh, and  
 5562 Dublin Philosophical Magazine and Journal of Science*, **44**(271), pp. 503–512,  
 5563 <https://doi.org/10.1080/14786449708621095>.  
 5564 URL <https://doi.org/10.1080/14786449708621095>

- 5565 [51] ESFAHANI, A. A. ET AL. (2022) “The Project 8 Neutrino Mass Experiment,” in  
5566 *2022 Snowmass Summer Study*, 2203.07349.
- 5567 [52] KRAUS, C. ET AL. (2005) “Final results from phase II of the Mainz neutrino mass  
5568 search in tritium beta decay,” *Eur. Phys. J. C*, **40**, pp. 447–468, [hep-ex/0412056](#).
- 5569 [53] ASEEV, V. N. ET AL. (2011) “An upper limit on electron antineutrino mass from  
5570 Troitsk experiment,” *Phys. Rev. D*, **84**, p. 112003, [1108.5034](#).
- 5571 [54] SAENZ, A., S. JONSELL, and P. FROELICH (2000) “Improved Molecular Final-  
5572 State Distribution of HeT+ for the  $\beta$ -Decay Process of T2,” *Phys. Rev. Lett.*, **84**(2),  
5573 p. 242.
- 5574 [55] BODINE, L. I., D. S. PARNO, and R. G. H. ROBERTSON (2015) “Assessment  
5575 of molecular effects on neutrino mass measurements from tritium  $\beta$  decay,” *Phys.  
5576 Rev. C*, **91**(3), p. 035505, [1502.03497](#).
- 5577 [56] ASNER, D. M. ET AL. (2015) “Single electron detection and spectroscopy via  
5578 relativistic cyclotron radiation,” *Phys. Rev. Lett.*, **114**(16), p. 162501, [1408.5362](#).
- 5579 [57] VÉNOS, D., J. SENTKERESTIOVÁ, O. DRAGOUN, M. SLEZÁK, M. RYŠAVÝ, and  
5580 A. ŠPALEK (2018) “Properties of 83mKr conversion electrons and their use in the  
5581 KATRIN experiment,” *JINST*, **13**(02), p. T02012.
- 5582 [58] LAGENDIJK, A., I. F. SILVERA, and B. J. VERHAAR (1986) “Spin exchange and  
5583 dipolar relaxation rates in atomic hydrogen: Lifetimes in magnetic traps,” *Phys.  
5584 Rev. B*, **33**, pp. 626–628.  
5585 URL <https://link.aps.org/doi/10.1103/PhysRevB.33.626>
- 5586 [59] SILVERA, I. and J. WALRAVEN (1986) “Spin-polarized atomic hydrogen,” *Prog.  
5587 Low Temp. Phys.*, **X**, pp. 139–370.
- 5588 [60] PRITCHARD, D. E. (1983) “Cooling Neutral Atoms in a Magnetic Trap for Precision  
5589 Spectroscopy,” *Phys. Rev. Lett.*, **51**, pp. 1336–1339.  
5590 URL <https://link.aps.org/doi/10.1103/PhysRevLett.51.1336>
- 5591 [61] HALBACH, K. (1980) “Design of permanent multipole magnets with oriented rare  
5592 earth cobalt material,” *Nuclear Instruments and Methods*, **169**(1), pp. 1–10.  
5593 URL <https://www.sciencedirect.com/science/article/pii/0029554X80900944>
- 5595 [62] “Real-time Signal Detection for Cyclotron Radiation Emission Spectroscopy Mea-  
5596 surements using Antenna Arrays,” *In preparation*.
- 5597 [63] FURSE, D. ET AL. (2017) “Kassiopeia: a modern, extensible C++ particle tracking  
5598 package,” *New Journal of Physics*, **19**(5), p. 053012.  
5599 URL <https://doi.org/10.1088/1367-2630/aa6950>

- 5600 [64] ESFAHANI, A. A. ET AL. (2019) “Electron radiated power in cyclotron radiation  
 5601 emission spectroscopy experiments,” *Phys. Rev. C*, **99**, p. 055501.  
 5602 URL <https://link.aps.org/doi/10.1103/PhysRevC.99.055501>
- 5603 [65] ASHTARI ESFAHANI, A. ET AL. (2019) “Locust: C++ software for simulation of  
 5604 RF detection,” *New J. Phys.*, **21**, p. 113051, 1907.11124.
- 5605 [66] WIECHERT, E. (1901) “Elektrodynamische Elementargesetze,” .  
 5606 URL <https://doi.org/10.1002/andp.19013090403>
- 5607 [67] LIÉARD, A. (1898) “Champ électrique et Magnétique,” *Léclairage électrique*, **16**(27-  
 5608 29).
- 5609 [68] BALANIS, C. (2015) *Antenna Theory: Analysis and Design*, Wiley.  
 5610 URL <https://books.google.com/books?id=PTFcCwAAQBAJ>
- 5611 [69] <https://www.ansys.com/products/electronics/ansys-hfss>.
- 5612 [70] [https://en.wikipedia.org/wiki/Linear\\_time-invariant\\_system](https://en.wikipedia.org/wiki/Linear_time-invariant_system).
- 5613 [71] NYQUIST, H. (1928) “Certain Topics in Telegraph Transmission Theory,” *Transactions of the American Institute of Electrical Engineers*, **47**(2), pp. 617–644.
- 5614
- 5615 [72] BRUN, R. and F. RADEMAKERS (1997) “ROOT: An object oriented data analysis  
 5616 framework,” *Nucl. Instrum. Meth. A*, **389**, pp. 81–86.
- 5617 [73] ASHTARI ESFAHANI, A. ET AL. (2021) “Bayesian analysis of a future  $\beta$  decay  
 5618 experiment’s sensitivity to neutrino mass scale and ordering,” *Phys. Rev. C*, **103**,  
 5619 p. 065501.  
 5620 URL <https://link.aps.org/doi/10.1103/PhysRevC.103.065501>
- 5621 [74] KAY, S. (1998) *Fundamentals of Statistical Signal Processing: Detection Theory*,  
 5622 *Volume II*, Pearson.
- 5623 [75] NEYMAN, J. and E. PEARSON (1933) “On the problem of the the most efficient  
 5624 tests of statistical hypotheses,” *Phil. Trans. R. Soc. Lond. A*, **231**.
- 5625 [76] STUMPF, M. (2018) *Electromagnetic Reciprocity in Antenna Theory*, Wiley.
- 5626 [77] BUZINSKY, N. (2021) *Statistical Signal Processing and Detector Optimization in*  
 5627 *Project 8*, Ph.D. thesis, Massachusetts Institute of Technology.
- 5628 [78] ESFAHANI, A. A. ET AL. (2023) “SYNCA: A Synthetic Cyclotron Antenna for  
 5629 the Project 8 Collaboration,” *Journal of Instrumentation*, **18**(01), p. P01034.  
 5630 URL <https://dx.doi.org/10.1088/1748-0221/18/01/P01034>
- 5631 [79] BISHOP, C. (2016) *Pattern Recognition and Machine Learning*, Springer.

- 5632 [80] PLEHN, T., A. BUTTER, B. DILLON, and C. KRAUSE (2022) “Modern Machine  
5633 Learning for LHC Physicists,” 2211.01421.
- 5634 [81] GEORGE, D. and E. A. HUERTA (2018) “Deep Learning for Real-time Gravitational  
5635 Wave Detection and Parameter Estimation: Results with Advanced LIGO Data,”  
5636 *Phys. Lett. B*, **778**, pp. 64–70, 1711.03121.
- 5637 [82] GABBARD, H., C. MESSENGER, I. S. HENG, F. TONOLINI, and R. MURRAY-  
5638 SMITH (2022) “Bayesian parameter estimation using conditional variational au-  
5639 toencoders for gravitational-wave astronomy,” *Nature Phys.*, **18**(1), pp. 112–117,  
5640 1909.06296.
- 5641 [83] REIMANN, R. (2022) “Project 8: R&D for a next-generation neutrino mass experi-  
5642 ment,” *PoS, PANIC2021*, p. 283.
- 5643 [84] ASHTARI ESFAHANI, A. ET AL. (2020) “Cyclotron radiation emission spectroscopy  
5644 signal classification with machine learning in project 8,” *New J. Phys.*, **22**(3), p.  
5645 033004, 1909.08115.
- 5646 [85] BALANIS, C. A. (2016) *Antenna Theory: Analysis and Design, 4th Edition*, Wiley.
- 5647 [86] STANKOVIĆ, L. and D. MANDIC (2023) “Convolutional Neural Networks Demys-  
5648 tified: A Matched Filtering Perspective-Based Tutorial,” *IEEE Transactions on  
5649 Systems, Man, and Cybernetics: Systems*, **53**(6), pp. 3614–3628.
- 5650 [87] <https://www.nvidia.com/en-us/data-center/v100/>.
- 5651 [88] <https://www.nvidia.com/en-us/data-center/h100/>.
- 5652 [89] HE, K., X. ZHANG, S. REN, and J. SUN (2016) “Deep Residual Learning for  
5653 Image Recognition,” in *2016 IEEE Conference on Computer Vision and Pattern  
5654 Recognition (CVPR)*, pp. 770–778.
- 5655 [90] SIMONYAN, K. and A. ZISSERMAN (2015) “Very Deep Convolutional Networks  
5656 for Large-Scale Image Recognition,” in *3rd International Conference on Learning  
5657 Representations, ICLR 2015, San Diego, CA, USA, May 7-9, 2015, Conference  
5658 Track Proceedings* (Y. Bengio and Y. LeCun, eds.).  
5659 URL <http://arxiv.org/abs/1409.1556>
- 5660 [91] FRIIS, H. (1946) “A Note on a Simple Transmission Formula,” *Proceedings of the  
5661 IRE*, **34**(5), pp. 254–256.
- 5662 [92] POZAR, D. M. (2005) *Microwave engineering*; 3rd ed., Wiley, Hoboken, NJ.  
5663 URL <https://cds.cern.ch/record/882338>
- 5664 [93] AKER, M. ET AL. (2022) “Direct neutrino-mass measurement with sub-electronvolt  
5665 sensitivity,” *Nature Physics*, **18**(2), pp. 160–166.  
5666 URL <https://doi.org/10.1038/s41567-021-01463-1>

- 5667 [94] MONREAL, B. and J. A. FORMAGGIO (2009) “Relativistic Cyclotron Radiation  
 5668 Detection of Tritium Decay Electrons as a New Technique for Measuring the  
 5669 Neutrino Mass,” *Phys. Rev. D*, **80**, p. 051301, 0904.2860.
- 5670 [95] ASHTARI ESFAHANI, A. ET AL. (2017) “Determining the neutrino mass with  
 5671 cyclotron radiation emission spectroscopy—Project 8,” *J. Phys. G*, **44**(5), p. 054004,  
 5672 1703.02037.
- 5673 [96] ESFAHANI, A. A. ET AL. (2022) “The Project 8 Neutrino Mass Experiment,” in  
 5674 *2022 Snowmass Summer Study*, 2203.07349.
- 5675 [97] ASHTARI ESFAHANI, A. ET AL. (2019) “Locust: C++ software for simulation of  
 5676 RF detection,” *New Journal of Physics*, **21**(11), p. 113051.  
 5677 URL <https://doi.org/10.1088/1367-2630/ab550d>
- 5678 [98] FURSE, D. ET AL. (2017) “Kassiopeia: a modern, extensible C++ particle tracking  
 5679 package,” *New Journal of Physics*, **19**(5), p. 053012.  
 5680 URL <https://doi.org/10.1088/1367-2630/aa6950>
- 5681 [99] BALANIS, C. (2011) *Modern Antenna Handbook*, Wiley.  
 5682 URL <https://books.google.com/books?id=UYpV8L8GNCwC>
- 5683 [100] WIRTH, W. (2001) *Radar Techniques Using Array Antennas*, Institution of Engi-  
 5684 neering and Technology.  
 5685 URL <https://books.google.com/books?id=ALht42gkzLsC>
- 5686 [101] BROWN, L. S., G. GABRIELSE, K. HELMERSON, and J. TAN (1985) “Cyclotron  
 5687 motion in a microwave cavity: Lifetime and frequency shifts,” *Phys. Rev. A*, **32**,  
 5688 pp. 3204–3218.  
 5689 URL <https://link.aps.org/doi/10.1103/PhysRevA.32.3204>
- 5690 [102] HANNEKE, D., S. FOGWELL HOOGERHEIDE, and G. GABRIELSE (2011) “Cavity  
 5691 control of a single-electron quantum cyclotron: Measuring the electron magnetic  
 5692 moment,” *Phys. Rev. A*, **83**, p. 052122.  
 5693 URL <https://link.aps.org/doi/10.1103/PhysRevA.83.052122>
- 5694 [103] HANNEKE, D. A. (2007) *Cavity control in a single-electron quantum cyclotron: an  
 5695 improved measurement of the electron magnetic moment*, Ph.D. thesis, Harvard U.
- 5696 [104] PURCELL, E. (1946) “Spontaneous Emission Probabilities at Radio Frequencies,”  
 5697 *Phys. Rev.*, **69**, pp. 674–674.  
 5698 URL <https://link.aps.org/doi/10.1103/PhysRev.69.674>
- 5699 [105] MOSKOWITZ, B. E. and J. ROGERS (1988) “ANALYSIS OF A MICROWAVE  
 5700 CAVITY DETECTOR COUPLED TO A NOISY AMPLIFIER,” *Nucl. Instrum.  
 5701 Meth. A*, **264**, pp. 445–452.

- 5702 [106] RAPIDIS, N. M. (2018) “Application of the Bead Perturbation Technique to a  
5703 Study of a Tunable 5 GHz Annular Cavity,” *Springer Proc. Phys.*, **211**, pp. 45–51,  
5704 [1708.04276](#).
- 5705 [107] BYRON, W. ET AL. (2022) “First observation of cyclotron radiation from MeV-scale  
5706  $e^{pm}$  following nuclear beta decay,” [2209.02870](#).
- 5707 [108] KAZKAZ, K. and N. WOOLLETT (2021) “Using Cyclotron Radiation Emission  
5708 for Ultra-high Resolution X-Ray Spectroscopy,” *New J. Phys.*, **23**(3), p. 033043,  
5709 [1911.05869](#).
- 5710 [109] CANNING, J. A. L., F. F. DEPPISCH, and W. PEI (2023) “Sensitivity of future  
5711 tritium decay experiments to New Physics,” *JHEP*, **03**, p. 144, [2212.06106](#).

5712

## Vita

5713

**Andrew Douglas Ziegler**

5714

### Education

5715

- Doctor of Philosophy, Physics, The Pennsylvania State University, University Park, Pennsylvania, USA, 2023
- Bachelor of Science, Physics, The University of Minnesota, Minneapolis, Minnesota, USA, 2017

5716

5717

5718

5719

### Selected Publications

5720

5721

- Astari Esfahani, A. et al. (2023) "Antenna Arrays for CRES-based Neutrino Mass Measurement", *Phys. Rev. C*, In preparation.
- Astari Esfahani, A. et al. (2023) "Real-time Signal Detection for Cyclotron Radiation Emission Spectroscopy Measurements using Antenna Arrays", *Journal of Instrumentation*, In preparation.
- Astari Esfahani, A. et al. (2023) "Tritium Beta Spectrum and Neutrino Mass Limit from cyclotron Radiation Emission Spectroscopy", *Phys. Rev. Lett.*, Accepted.
- Astari Esfahani, A. et al. (2022) "SYNCA: A Synthetic Cyclotron Antenna for the Project 8 Collaboration", *Journal of Instrumentation*, **18**(01).

5722

5723

5724

5725

5726

5727

5728

### Selected Presentations

5729

5730

5731

5732

- *New Developments in the CRES Technique for Neutrino Mass Measurement*, Invited Talk, Fall 2022 Meeting of the APS Division of Nuclear Physics, New Orleans, Louisiana, USA, 2022
- *Signal Detection Algorithms for Phase III of the Project 8 Experiment*, Contributed Talk, APS April Meeting 2022, New York, New York, USA, 2022
- *Synthetic Electron Antenna for Calibrating the Project 8 Neutrino Mass Experiment*, Contributed Talk, Fall 2021 Meeting of the APS Division of Nuclear Physics, Virtual, 2021

5733

5734

5735

5736

5737